Photomonomers and Photoinitiators for Light-Induced Polymerizations in Metal-Organic Frameworks

Zur Erlangung des akademischen Grades eines

DOKTORS DER NATURWISSENSCHAFTEN

(Dr. rer. nat.)

von der Fakultät für Chemie und Biowissenschaften

des Karlsruher Instituts für Technologie (KIT)

genehmigte

DISSERTATION

von

M. Sc. Silvana Hurrle, geb. Röse

aus Böblingen

„It may be that you are not yourself luminous,
but you are a conductor of light.“

Sir Arthur Conan Doyle,
The Hound of The Baskervilles

Kurzzusammenfassung

Die vorliegende Doktorarbeit beschreibt die Synthese von Initiatoren und Monomeren für licht-induzierte Polymerisationen in (oberflächengebundenen) metallorganischen Gerüstverbindungen ((SUR)MOFs). Zunächst wurden SURMOFs als potentielle Template für licht-induzierte freie radikalische Polymerisation hergestellt und untersucht. Grundlegende Studien für die Beladung solcher Gerüststrukturen mit Polybromstyrol wurden durchgeführt und mittels Röntgendiffraktometrie (XRD) und Flugzeit-Sekundärionen-Massenspektrometrie (ToF-SIMS) untersucht. Dabei wurden die SURMOFs am effizientesten über die Gasphase beladen und Modelpolymerisationen durchgeführt. Außerdem wurden die analytischen Möglichkeiten mittels Massenspektrometrie untersucht. Des Weiteren wurde festgestellt, dass hochauflösende Elektrosprayionisations-massenspektrometrie angemessen für die Charakterisierung von Polymerisationen in SURMOFs ist. Anschließend wurde ein bifunktionaler Photoinitiator entwickelt und über Azid-Alkin-Cycloaddition in einer SURMOF-Gerüststruktur verankert, was mittels Infrarot-Reflektions-Absorptions-Spektroskopie (IRRAS) und ToF-SIMS bestätigt wurde. Der funktionalisierte SURMOF wurde in einer Quartzmikrowaage (QCM) unter Polymerisationbedingungen beobachtet und es wurde gezeigt, dass die Polymerisation von Methylmethacrylat initiiert werden konnte. Das Herauslösen des Polymers aus der Struktur und die anschließende Analyse durch Massenspektrometrie ist Gegenstand zukünftiger Untersuchungen.

Der Photoinitiator, der für die Funktionalisierung von SURMOFs entwickelt wurde, wurde zudem für die Herstellung von Blockcopolymeren mittels λ-orthogonaler Chemie verwendet. Zunächst wurde Polyethylenglykol (PEG), ausgestattet mit einer Azid-Endgruppe, in einer kupferkatalysierten Azid-Alkin-Cycloaddition (CuAAC) bei sichtbarem Licht ($\lambda = 420\,\mathrm{nm}$) an die terminale Dreifachbindung des Photoinitiators gebunden. Der erhaltene PEG-Makroinitiator wurde mittels Massenspektrometrie charakterisiert und in Laserpuls-Polymerisationen (PLP) mit Methylmethacrylat umgesetzt ($\lambda = 351\,\mathrm{nm}$). Das erhaltene Blockcopolymer PEG-*b*-PMMA wurde mittels hochauflö-

sender Größenausschlusschromatographie-Elektrosprayionisations-Massenspektrometrie (SEC-ESI-MS) analysiert. Für den Nachweis der λ-Orthogonalität des Systems wurde die Reihenfolge der Herstellungsschritte umgekehrt. Das heißt, die PLP wurde vor der Funktionalisierung mittels CuAAC durchgeführt. Beide Reaktionswege resultierten in vergleichbaren Massenspektren in der SEC-ESI-MS und die spezifischen Isotopenmuster konnten den entsprechenden Strukturen zugeordnet werden.

Für licht-induzierte Stufenwachstumspolymerisationen in MOFs war die Synthese von Photomonomeren erforderlich, die eine AB Polycycloaddition eingehen. Zwei Monomere wurden entwickelt, die sowohl eine α-Methylbenzaldehyd-Einheit, als auch einen Fumarsäureester als Endgruppe tragen. Bei der Bestrahlung mit UV-Licht (λ_{max} = 350 nm) in Dichlormethan polymerisieren beide Monomere, jedoch mit erheblichen Unterschieden in der Polymerisationsgeschwindigkeit und -Effizienz. Das Monomer mit dem aliphatischen Rückgrat wies eine höhere Zyklisierungstendenz als das Monomer mit dem aromatischen Rückgrat auf. Außerdem ergab die SEC-ESI-MS Analyse, dass das aliphatische Monomer anfällig für Endgruppenfragmentierung ist. Durch die Herstellung von Copolymeren beider Monomere wurde die Labilität der Endgruppen des aliphatischen Monomers bestätigt. Theoretische Berechnungen der Bindungsenergien der Monomere in ausgewählten MOF-Strukturen lassen vermuten, dass beide Monomere in die Strukturen diffundieren und damit vielversprechend für erfolgreiche MOF-Polymerisationen sind.

Abstract

The current thesis reports the synthesis of initiators and monomers for light-induced polymerizations in (surface-mounted) metal-organic frameworks ((SUR)MOFs). First, SURMOFs were examined for the potential application as templates for light-induced free radical polymerization. Fundamental studies on the loading of such structures with polybromostyrene have been performed and investigated via X-ray diffraction (XRD) and time of flight-secondary ion mass spectrometry (ToF-SIMS). The SURMOFs were most efficiently loaded via the gas phase and model polymerizations were carried out. Furthermore, the analytical possibilities and limitations of polymers obtained from SUR-MOFs via mass spectrometry were examined. The limits of the mass spectrometric analysis were found to be in an adequate range for SURMOF polymerization. Subsequently, a bifunctional photoinitiator was developed and successfully anchored to the SURMOF structure via azide-alkyne cycloaddition, which was confirmed via infrared reflection-absorption spectroscopy (IRRAS) and ToF-SIMS. The functional SURMOF was observed under polymerization conditions in a quartz crystal microbalance (QCM) and was able to initiate the polymerization of methyl methacrylate. The release of the polymer from the SURMOF and subsequent analysis via mass spectrometry is the subject of further investigations.

The photoinitiator that was developed for SURMOF polymerization was employed in λ-orthogonal chemistry for the preparation of block copolymers. First, polyethylene glycol (PEG) functionalized with an azide was attached to the terminal triple bond of the photoinitiator via visible-light copper-catalyzed azide-alkyne cycloaddition (CuAAC) at $\lambda = 420$ nm. The resulting PEG-macroinitiator was analyzed via mass spectrometry and was subsequently employed in pulsed-laser polymerization (PLP) of methyl methacrylate at $\lambda = 351$ nm. The obtained block copolymer PEG-b-PMMA was characterized via high resolution size exclusion chromatography-electrospray ionization-mass spectrometry (SEC-ESI-MS). The λ-orthogonal character of the system was investigated by reversing the order of the preparation steps, i.e. the PLP was performed prior to the

visible light CuAAC. Both reaction routes result in similar mass spectra in SEC-ESI-MS and the unique isotopic patterns of the system were simulated and assigned to the corresponding species.

For light-induced step-growth polymerization in MOFs, the synthesis of photomonomers was designed that undergo AB-type polycycloaddition. Two monomers were synthesized that carry both an α-methyl benzaldehyde moiety, as well as a fumaric acid ester as end groups. Upon irradiation with UV-light ($\lambda_{max} = 350\,\text{nm}$) in dichloromethane, both monomers polymerize, yet with major differences in polymerization rate and efficiency. The monomer with an aliphatic backbone showed a higher cyclization tendency than the monomer with the aromatic backbone. Furthermore, SEC-ESI-MS revealed that the end groups of the aliphatic monomer are sensitive to end group fragmentation. The synthesis of copolymers from both monomers confirms the lability of the end group with the aliphatic backbone. Theoretical calculations of the binding energies of the monomers in selected MOF structures suggest that both monomers might diffuse into the structures, and may result in successful interlace polymerizations.

Publications

Arising from the Thesis

(1) **Hurrle, S.**; Goldmann, A. S.; Gliemann, H.; Mutlu, H.; Barner-Kowollik, C., Light-Induced Step-Growth Polymerization of AB-Type Photo-Monomers at Ambient Temperature. *ACS Macro Lett.* **2018**, *7*, 201-207.

(2) **Hurrle, S.**; Lauer, A.; Gliemann, H.; Mutlu, H.; Wöll, C.; Goldmann, A. S.; Barner-Kowollik, C., Two-in-One: λ-Orthogonal Photochemistry on a Radical Photoinitiating System. *Macromol. Rapid Commun.* **2017**, *38*, 1600598.

Additional Publications

(3) **Hurrle, S.**; Friebe, S.; Wohlgemuth, J.; Wöll, C.; Caro, J.; Heinke, L., Sprayable, Large-Area Metal–Organic Framework Films and Membranes of Varying Thickness. *Chem. Eur. J.* **2017**, *23*, 2294-2298.

(4) Nayab, S.; Trouillet, V.; Gliemann, H.; **Hurrle, S.**; Weidler, P. G.; Rashid Tariq, S.; Goldmann, A. S.; Barner-Kowollik, C.; Yameen, B., Chemically Reprogrammable Metal Organic Frameworks (MOFs) Based on Diels-Alder Chemistry. *Chem. Commun.* **2017**, *53*, 11461-11464.

(5) Best, J. P.; Michler, J.; Liu, J.; Wang, Z.; Tsotsalas, M.; Maeder, X.; **Röse, S.**; Oberst, V.; Liu, J.; Walheim, S.; Gliemann, H.; Weidler, P. G.; Redel, E.; Wöll, C., Nanomechanical Investigation of Thin-Film Electroceramic/Metal-Organic Framework Multilayers. *Appl. Phys. Lett.* **2015**, *107*, 101902.

Contents

Contents

Introduction

Polymer chemists strive to achieve control over polymerization procedures in order to enable a generation of macromolecules with defined shape, size, and morphology. Polymerization processes are typically performed in organic solutions or aqueous emulsions, which under typical conditions lead to rather ill-defined polymers.[1–3] The methods invented to obtain control over polymerizations so far are invariably chemical, and employ the addition of controlling agents that prevent radicals from permanently terminating.[1,2,4] In the current thesis, however, a different approach is followed by conducting chain-growth and step-growth polymerizations inside confined environments, thereby controlling the macromolecular growth process through the highly ordered geometry of

frameworks. Metal-organic frameworks (MOFs) are highly ordered crystalline structures, which are formed by self-assembly, consisting of metal nodes and organic linkers.[5–7] The variety of metals and linkers allows the exact tuning of pore size and shape, as well as the introduction of functional moieties.[8,9] The spatial entrapment of individual chains inside the MOF pores is envisaged to enhance the molecular weight control and to minimize dispersities via suppression of chain interactions and termination reactions.[10]

MOFs have been known for 20 years[8,11,12] and find applications in gas storage and separation,[13–16] catalysis,[17,18] and biology.[19–21] MOFs can be prepared, in addition to crystalline powders or surface-coatings,[22] in a layer-by-layer process that has been developed by Wöll and Shekhah and results in homogeneous MOF thin films, termed surface-mounted MOFs or SURMOFs.[5] The growth of the SURMOFs in a step-by-step fashion allows the precise adjustment of layer thickness and, furthermore, enables the introduction of functionalities in specific layers of the structure.[23–25] Such post-synthetic modifications are the basis for the strategy of SURMOF interlace polymerization in the current thesis.

One of the aims is the development of a functional photoinitiator that can be anchored to SURMOF structures via post-synthetic modification (Figure 1.1, Steps 1 and 2). The characterization of the successful functionalization of the SURMOFs is crucial for the
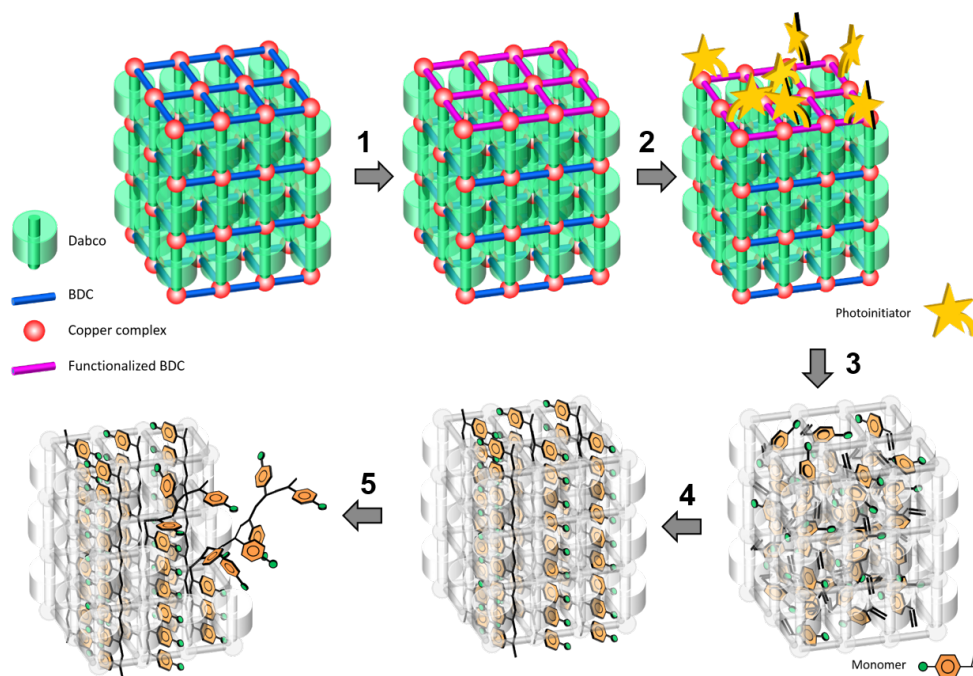
Figure 1.1: Concept of polymerizations in SURMOFs. 1) A functional linker is introduced into or on top of the structure. 2) The SURMOF is functionalized with a photoinitiator (the initiator is not shown in further steps for simplicity). 3) The SURMOF is filled with a monomer. 4) The polymerization is performed and the chains fill the SURMOF structure. 5) The SURMOF is dissolved with EDTA or acid and the polymer chains are released.

development of SURMOFs as polymerization templates. Furthermore, the loading of the SURMOF structures with monomers has to be investigated and optimized (Step 3). Moreover, the analysis of the resulting polymer is a keypoint in the current thesis. It is critical to analyze the polymer before (Step 4) and after (Step 5) releasing it from the structure in order to exclude any polymer growth outside of the channels. The characterization of the initiation and termination processes can enhance to understand the influence of confined space on polymerizations.

On the other hand, step-growth polymerization has not been implemented in MOFs so far, possibly because most step-growth polymerizations follow a condensation process, which releases small molecules such as water during the process. In MOFs, however, small molecules may block the pores of the structure, thereby hindering polymerization. Furthermore, step-growth polymerizations are often performed between two monomers, each carrying one type of functional group. Yet, the diffusion of two monomers in an ordered manner into the MOF structure for the successful polymerization is not readily achievable. Therefore, the preparation of a photoreactive monomer carrying two functionalities (Figure 1.2, red and blue) is required, since it needs to react with itself to form the polymer without a catalyst or any other form of additive. Hence, a monomer that reacts in high yield and selectivity, yet is stable at ambient temperature, is critically required. Premature reaction due to the high reactivity of the functional groups towards each other is a challenge in bifunctional monomer synthesis in general.

The step-growth polymerization in MOF structures should reduce cyclization reactions of the growing polymer chains,[26] as the probability of end groups from the same chain to interact is highly reduced.

In conclusion, the aims of the current thesis are the synthesis of a functional photoinitiator for free radical polymerization in SURMOF structures, as well as the identifica-

Dabco
BDC
Copper complex
Monomer
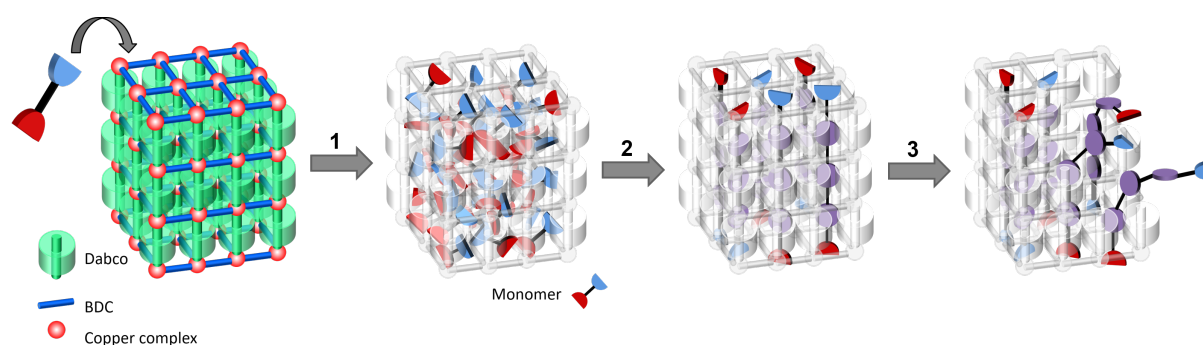
Figure 1.2: Concept of step-growth polymerizations in MOFs. 1) The MOF is filled with an AB-type monomer. 2) The polymerization is performed and the polymer chains fill the MOF structure. 3) The MOF is dissolved with EDTA or acid and the polymer chains are released.

tion of analytical limitations. Furthermore, the synthesis of a photoreactive step-growth monomer is required that fulfills the above mentioned criteria and, in addition, can be loaded into MOF structures for interlace polymerizations.

Theoretical Background

2.1 Photochemistry

Reactions are considered as light-induced reactions when the necessary activation energy is provided by light irradiation rather than thermal activation by heat. Furthermore, thermal reactions proceed in the electronic ground state, while photoreactions involve one or more electronic excited states along the reaction coordinate.[27] As a consequence, there are more processes involved in photochemical reactions, i.e., fluorescence and phosphorescence, chemoluminescence, and photoelectrochemical processes. Light-induced chemistry has several advantages and, unfortunately, disadvantages compared to thermal chemistry. On the one hand, light can exert spatial and temporal control; spatial control by focusing through lenses or by employing a laser, and temporal control by turning the energy on or off merely by the push of a button. For thermal reactions, the mixture is heated or cooled through a large range of temperatures, whereas for photochemistry, the wavelength and the photon intensity can be chosen and monochromatic light can be produced. On the other hand, for most photoreactions, UV-light is necessary for the activation of the functional moieties. The intensity of the near-UV-visible wavelength range of the sun, an inexpensive source of light, is low ($< 5\,\mathrm{mW\,cm}^{-2}$), rendering sunlight-induced reactions a challenge, but not impossible.[28–30]

Selectivity of photoreactions is a major goal in the research of photo-induced processes. To understand the structural and environmental conditions that have to be designed in photochemistry, we will have a closer look into the basics of photophysics.

2.1.1 Basics of Photochemistry and Photophysics

Light is electromagnetic radiation characterized by a frequency f and a wavelength λ. The frequency f is proportional to the wavenumber ν and the latter inversely proportional to λ.[28]

$$f = \frac{c}{\lambda} = c\nu \tag{2.1}$$

c: speed of light in vacuum

Table 2.1 lists the energy of electromagnetic radiation of various wavelengths. A comparison of the energy of the photons with typical binding energies (C-C: $341\,\mathrm{kJ\,mol^{-1}}$; C-H: $413\,\mathrm{kJ\,mol^{-1}}$; C-Cl: $328\,\mathrm{kJ\,mol^{-1}}$; C-Br: $276\,\mathrm{kJ\,mol^{-1}}$)[31] shows that light in the near-UV-visible range is indeed able to break covalent bonds. Yet, the theory behind the absorption of photons by molecules and if a photon can be absorbed at all, cannot be answered simply by comparing energies.

The absorption of a molecule depends on the molecular orbitals (MOs) and the corresponding energy levels. The MOs of a molecule are constructed from the atomic orbitals (AOs) of the atoms that form the bond. The molecule exists in two states: singlet state (S_n) or triplet state (T_n). In the singlet state, the electrons within the molecule are all paired (Pauli principle: the electrons have opposite spins $+\frac{1}{2}$ and $-\frac{1}{2}$), whereas for triplet states, the spins are parallel.[31,32] The absorption of light by a molecule is the in-

Table 2.1: Energy E of electromagnetic radiation depends on the wavelength λ and the frequency f. Reproduced with permission from John Wiley and Sons.[32]

Color	λ [nm]	f [Hz]	E [$\mathrm{kJ\,mol^{-1}_{photons}}$]
IR	1000	3.00×10^{14}	120
red	700	4.28×10^{14}	171
orange	620	4.84×10^{14}	193
yellow	580	5.17×10^{14}	206
green	530	5.66×10^{14}	226
blue	470	6.38×10^{14}	254
violett	420	7.14×10^{14}	285
near-UV	300	1.00×10^{14}	400
far-UV	200	1.50×10^{14}	598

teraction of the electric field component E of the light with the permanent dipole moment μ (or μ^* for induced dipole moment) of the molecule. The absorption of light causes a transition of the molecule from the ground state (S_0) to an excited state (S_1), which is equivalent to an electron transfer from an occupied MO to an unoccupied MO.[32]

In the UV/vis range for organic chemistry, three main transitions occur:

nπ^* transitions. These transitions are symmetry-forbidden. They occur, for example, in carbonyl groups as n corresponds to the non-binding electron pairs of the oxygen atom. The absorption wavelengths are usually located between 300 nm to 380 nm.

$\pi\pi^*$ transitions. They are symmetry-allowed and therefore result in high absorption coefficients. The transition happens between π orbitals, therefore affecting double bonds or conjugated π systems. The absorption can occur either at short wavelengths for small conjugated systems or higher wavelengths for larger conjugated π systems.

Charge-Transfer transitions. They arise in strongly delocalized and polarized molecules. The excitation energy is delocalized over the entire molecule and the absorption coefficients are high. The transitions can also occur in donor/acceptor systems.[32]

The absorption and emission of a photon proceeds in 10^{-15} s, thereby being 1000 to 10 000 times faster than a molecular vibration. Thus, the nuclei do not change their position and the potential energy surfaces of both states before and after the excitation lie vertically above each other. Hence, the absorption and emission processes occur vertically, known as the Franck-Condon-Principle (Figure 2.1).[31] The probability of a certain nuclear assembly is the highest in the center of the zero-point energy, consequently leading to the most probable and the most intense absorption. The probability of nuclear assemblies to the left and to the right of the center of the zero-point energy decreases, hence resulting in lower intensities. The various absorption and emission processes cause broad bands in UV-Vis spectroscopy rather than thin signals.[31]

The processes that take place in an excited molecule can be illustrated in a Jablonski diagram (Figure 2.2). In the diagram, the electronic states are depicted with the rotational and vibrational energy levels. After the molecule is excited to the S_1 state, it will first relax to the vibrational ground state of S_1 (10^{-12} s). Excitation into higher excited states S_2 or S_3 will result in internal conversion (IC) to the lowest excited state S_1 rapidly, followed by the relaxation into the ground state of the S_1 state. The *Kasha*
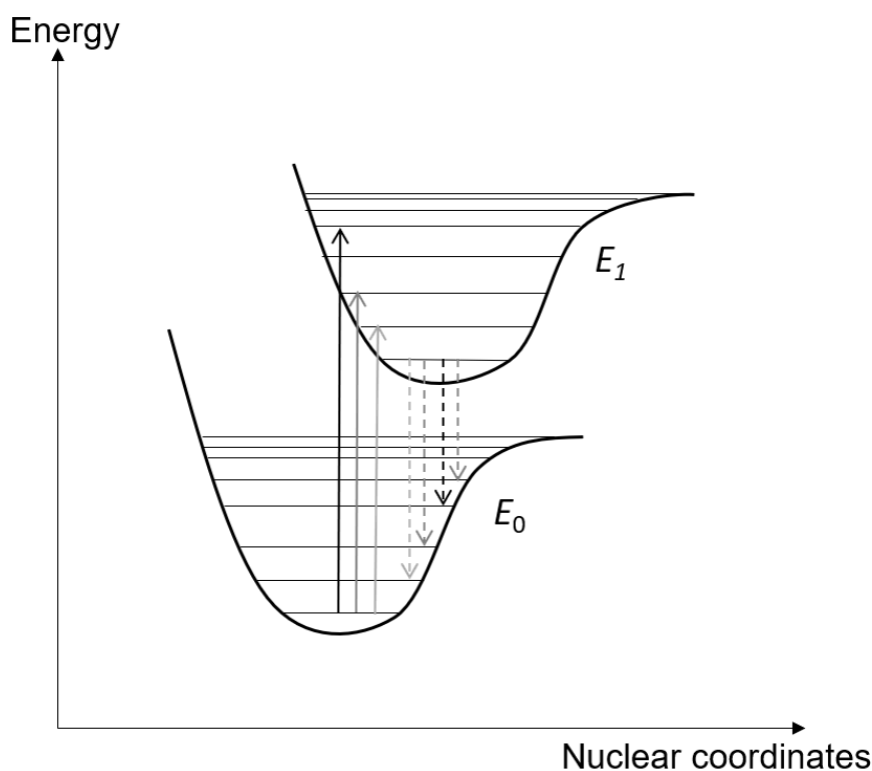
Figure 2.1: Franck-Condon-allowed absorption (solid line) from the ground state into the excited state and emission (dashed line) from the excited state to the ground state.[31]

rule says that all processes following the absorption will proceed from the vibrational ground state of S_1. From here, the molecule can undergo IC back to S_0 or intersystem crossing (ISC) to T_1. Exceptions from the *Kasha* rule appear in systems with a similar energy difference between S_2 and S_1 as between S_1 and S_0, for example in the case for azulenes and thioketones. Here, the vibrational ground state of S_2 is the basis for the following processes.[31,32]

Fluorescence: Fluorescence describes the photon release during the deactivation to an excited vibrational state of S_0. The relaxation to the ground state again occurs in 10^{-12} s. The lifespan of S_1 during Franck-Condon-allowed fluorescence accounts for ca. 10^{-8} s.

Phosphorescence: Phosphorescence describes the release of a photon during the transition from an excited state into S_0 under spin inversion.

Internal conversion (IC): IC describes the isoenergetic transformation from an excited state into a lower state, e.g., from S_2 to S_1. The relaxation into the vibrational
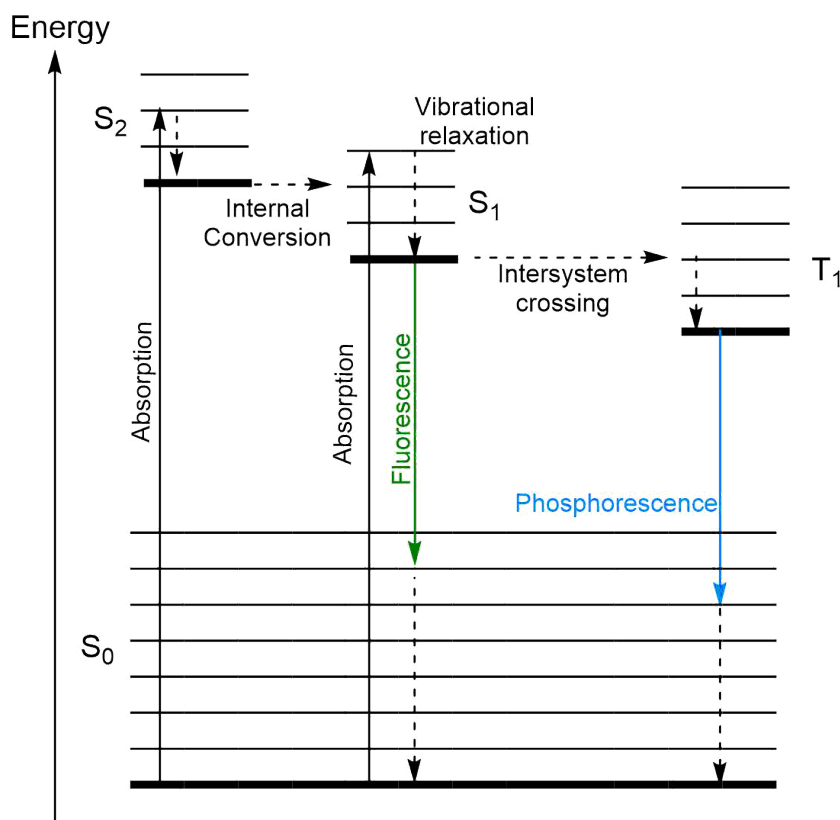
Figure 2.2: Photophysical processes involved in an electronically excited molecule.[31,32]

ground state proceeds under the release of thermal energy. The lifespan of an excited state during IC depends strongly on the observed system.

Intersystem Crossing (ISC): ISC describes the transition from the ground state of S_1 into an excited state of T_1 under spin reversion, followed by the relaxation to the ground state of T_1. With increasing spin-orbit interaction of the system, the probability for this spin-forbidden transition increases.

Chemical reactions can occur from both the S_1 state and the T_1 state. The lifespan of T_1 is far longer than the lifespan of S_1, regardless of the deactivation being thermal or with radiation, as the deactivation in all cases involves spin inversion. The longer lifespan of T_1 allows for bimolecular reactions to proceed, while the lifespan of S_1 is usually only sufficient for monomolecular reactions.

Additionally to the deactivation processes depicted in Figure 2.2, the following deactivation reactions can be described:[31]

Energy transition: $D^* + A \longrightarrow D + A^*$

Electron transfer: $D^* + A \longrightarrow D\cdot^+ + A\cdot^-$

Exciplex formation: $D^* + A \longrightarrow [D\cdots A]^*$

All cases describe how the excited energy donor D* can be deactivated by bimolecular interaction with an energy acceptor A. In case of energy transition, the energy of D* can be transferred to A, if the excitation energy of the acceptor is equal or smaller than the excitation energy of the donor. Electron transition can proceed from the SOMO (single-occupied MO) of an excited donor D* into the LUMO (lowest unoccupied MO) of the acceptor A, or after the excitation of A to A*, the electron can be transferred from the HOMO (highest occupied MO) of D to the electron hole that was created during the activation of A. Exciplexes are complexes that only exist in the excited state.[31]

2.1.2 Photoinitiation

Photoinitiators (PI) lead to initiating species upon irradiation, most commonly radicals. The initiation can proceed after the following mechanisms:[32]

$$PI \longrightarrow PI^* \longrightarrow radicals \tag{1}$$
$$PI \longrightarrow PI^* + co{-}I \longrightarrow radicals \tag{2}$$
$$PS \longrightarrow PS^* + PI \longrightarrow radicals \tag{3}$$
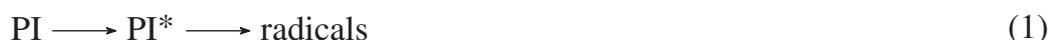
The initiator alone can lead to radicals (1) or react with a co-initiator (co-I) to form initiating species (2). In other cases (3), the light is absorbed by a photosensitizer (PS), followed by either energy or electron transfer. The formation of radicals by PI can occur by homolytic cleavage or hydrogen transfer.[32] The reactivity of a photoinitiating system depends not only on the initiation step, but also on the deactivation processes and the lifespans of the intermediates that moreover depend on the reaction conditions, e.g., solvent and temperature. Figure 2.3 depicts the processes that compete with the formation of radicals. The overall efficiency of an initiator includes the quantum yields of the ISC Φ_{ISC} and radical formation Φ_R, respectively, excited state life times τ_S and τ_T, and rate coefficient of deactivation k_d and cleavage processes k_c. The inclusion of photosensitizers can result in very complex mechanisms.[32]

Many efficient photoinitiators are based on the benzoyl chromophore (Figure 2.4). They absorb in the near-UV range from 310 to 365 nm.[33] The carbonyl group of the benzoyl moiety entails three orbitals: the non-binding MO (n) of the oxygen, the bind-
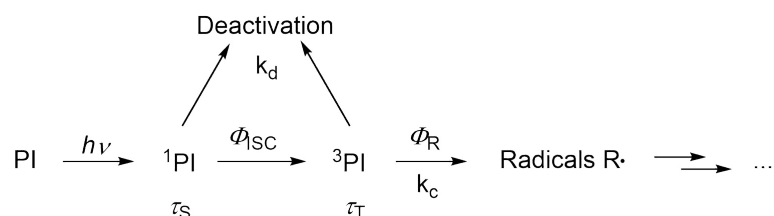
Figure 2.3: Schematic mechanism of light-induced photoinitiation. *PI:* photoinitiator, Φ: (quantum) yield, *k:* rate coefficient, τ: life time.[32]

ing (π) and non-binding (π^*) MO of the carbonyl double bond. The possible excitation result in five possible states: the ground state S_0 ($n^2\pi^2$) with two possible excited singlet states S_1 ($n\pi^*$) and S_2 ($\pi\pi^*$), as well as two triplet states T_1 ($n\pi^*$) and T_2 ($\pi\pi^*$). From the theoretical point of view, only the $\pi\pi^*$ transitions are allowed and $n\pi^*$ transitions are forbidden, observable by the extinction coefficients that are high for $\pi\pi^*$ ($\sim 10\,000\,\mathrm{L\,mol^{-1}\,cm^{-1}}$) and low for $n\pi^*$ transitions ($\sim 100\,\mathrm{L\,mol^{-1}\,cm^{-1}}$). The excitation to the states S_1 and S_2 can be observed by UV-Vis absorption spectroscopy. Here, the structure of the benzoyl chromophore leads to two bands between 280 and 300 nm, as well as 320 and 360 nm. The absolute positions of the bands' maxima depend on the polarity of the solvent, and the attached groups R and R' that can interact with the MOs of the benzoyl moiety.[33]

The cleavage of the initiator into two radicals can follow two basic mechanisms: Norrish-type I and Norrish-type II.[31,33] Both mechanisms include the triplet state of the carbonyl bond which results in a quasi-biradical (Figure 2.5). The radical can (next to other deactivation and recombination processes) undergo α-cleavage of the adjacent C-C bond (Norrish-type I, Figure 2.5a), or intramolecular H-abstraction (Norrish-type II,
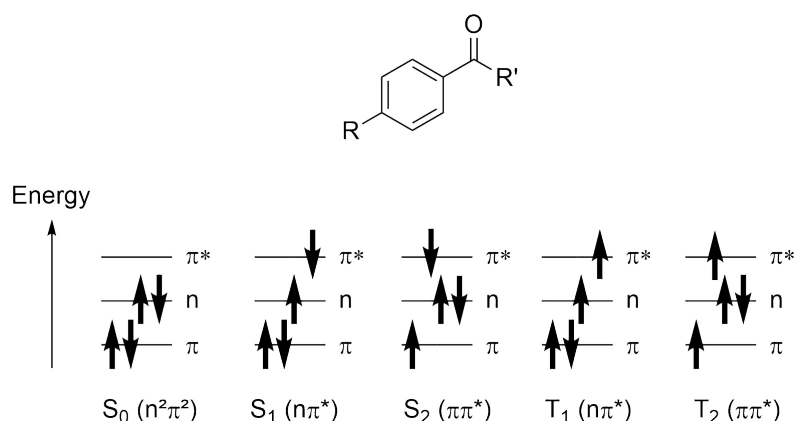
Figure 2.4: Structure of benzoyl chromophore, as well as the five molecular states of the MOs of the carbonyl moiety. Reproduced and adapted with permission from John Wiley and Sons.[33]

11
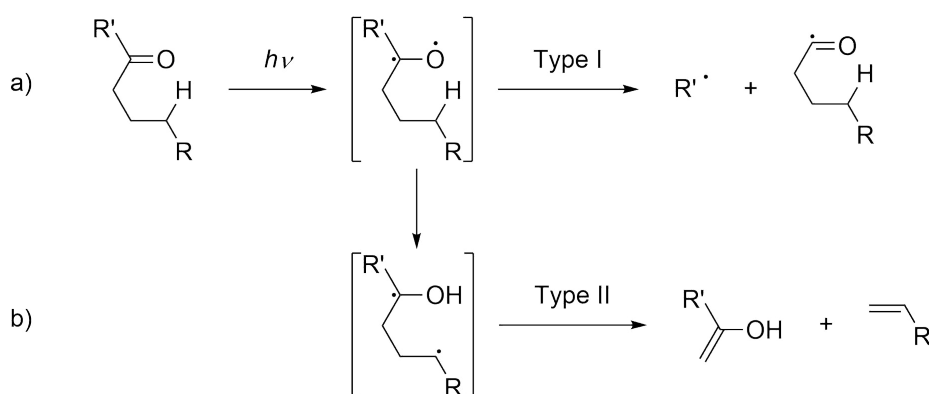
Figure 2.5: Basic principle of Norrish-type I (a) and II (b) reactions on carbonyl containig compounds.[31]

Figure 2.5b). Furthermore, photoreduction, *Yang*-cyclization[34] and the *Paterno-Büchi* reaction[35] are competing processes of the *Norrish* reactions.

The initiators based on the benzoyl chromophore mostly undergo Norrish-type I reactions in α-, β- or γ-position. The aryloyl radical has been found to be an initiating species, while the reactivity of the partner radical depends on its substituents.[36]

A class of very efficient initiators are hydroxy alkyl acetophenones (HAPs) (Figure 2.6). The triplet states of HAPs can be observed via picosecond absorption spectroscopy. The triplet state life time of HAP $\tau_T = 450\,ps$ in benzene and is heavily reduced with increasing polarity, e.g. in methanol ($\tau_T = 55\,ps$). Hence, the solvent plays an important role in stabilizing the triplet state, which can be attributed to the hydroxy group in close proximity to the carbonyl group, capable of forming hydrogen bonds. The efficiency of the α-cleavage depends on the substituents of the phenyl group, as well as on the possible functionalization of the hydroxy moiety.[33,37]
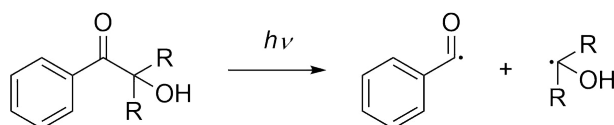
Figure 2.6: α-Cleavage of hydroxy alkyl acetophenones into two radicals.[33]

A class of newly developed photoinitiators are acylgermanes (Figure 2.7) that form radicals at visible light. They were developed for dental materials.[38,39]
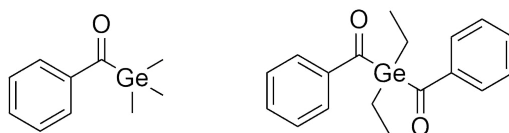
Figure 2.7: Acylgermane photoinitiators for polymerizations at visible light.[38]

2.2 Cycloadditions

Cycloadditions belong to the class of pericyclic reactions. Pericyclic reactions describe reactions with a continuous flow of π-electrons in a cyclic transition state by breaking and forming bonds without the appearance of an intermediate. The subtypes of pericyclic reactions are electrocyclic reactions, sigmatropic rearrangemants, group transfer reactions, and cycloadditions.[40–42] The reactions are concerted and can be triggered either thermally or photochemically. Woodward and Hoffmann in-depth investigated the processes of pericyclic reactions and summarized their findings in the *Woodward-Hoffmann* rules (Table 2.2).

Table 2.2: *Woodward-Hoffmann* rules for cycloadditions that proceed suprafacial.[I]

πe	thermal	photochemical
4n	Forbidden	Allowed
4n+2	Allowed	Forbidden

The rules allow to predict the reactivity of a system and which product is more favorably depending on the reaction, if the orbital symmetries during concerted reactions are maintained.[40]

To understand the *Woodward-Hoffmann* rules, it is important to understand how the linear combination of atomic orbitals (LCAO) constitutes MOs. First, the combination of AOs will result in the same number of MOs. For example, a diatomic molecule with the AOs ϕ_A and ϕ_B yields two wave functions ψ_+ and ψ_- as shown in Equations 2.2 and 2.3.[40]

$$\psi_+ = \phi_A + \phi_B (bonding) \tag{2.2}$$

$$\psi_- = \phi_A - \phi_B (antibonding) \tag{2.3}$$

[I]A reaction proceeds *suprafacial* when the bond cleavage and the new bond formation occur on the same side of the conjugated π-system. *Antarafacial* includes the opposite site of the π-system.
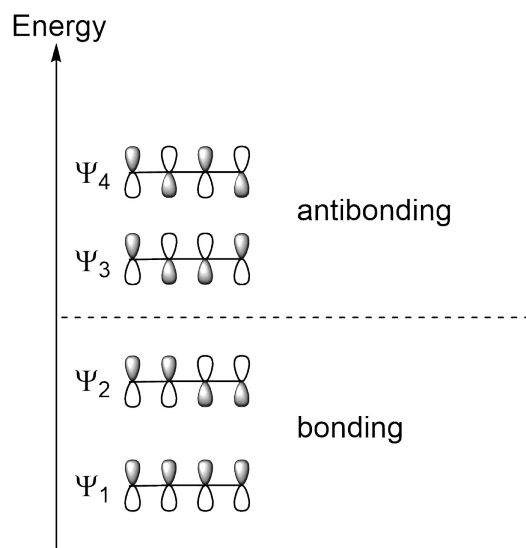
Figure 2.8: Molecular orbital scheme of 1,3-butadiene and their symmetry.[40]
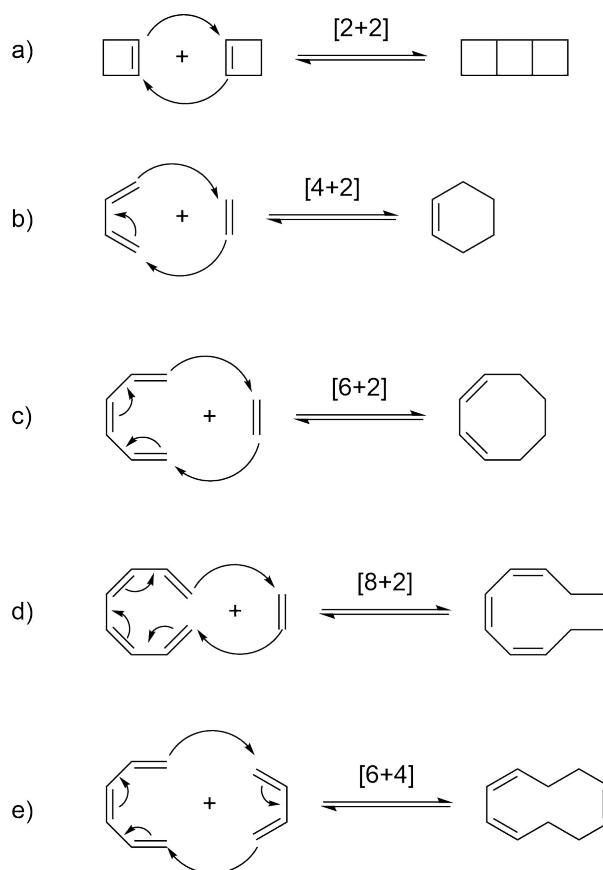
Figure 2.9: Examples for cycloadditions with varying numbers of π-electrons involved.[40]

The energy of the antibinding MO is higher than of the binding MO. The MO scheme for the π-electron system of 1,3-butadiene is depicted in Figure 2.8, which includes four MOs and thereby generates two binding and two antibinding MOs, respectively.

Cycloaddition reactions, in general, are characterized by the formation of two new σ-bonds between two molecules. They are characterized by the number of π-electrons included in the transition state, e.g. [2+2], [4+2], [6+2], [8+2]- and [6+4]-cycloaddition. Excamples for all major classes are depicted in Figure 2.9. The *Woodward-Hoffmann* rules (Table 2.2) state that cycloadditions (suprafacial) which include $4n$ electrons are photochemically triggered, while reactions with ($4n$+2) electrons are only thermally activated. [40]

2.2.1 [2+2]-Cycloaddition

Suprafacial [2+2]-Cycloadditions are thermally forbidden according to the *Woodward-Hoffmann* rules. This can be explained by examining the resulting MOs of the reaction. Figure 2.10a describes the thermal cycloaddition between two ethene molecules. The HOMO of one ethene and the LUMO of the other ethene would react suprafacial with each other, resulting in a binding σ- and a nonbinding σ^*-orbital. However, two new σ bonds are necessary to form the cycle. Figure 2.10b shows the situation under light irradiation. Here, an electron of the HOMO of one ethene is excited into the LUMO, threreby creating a SOMO that can react with the LUMO of the other ethene and results in two binding σ-orbitals. [40]
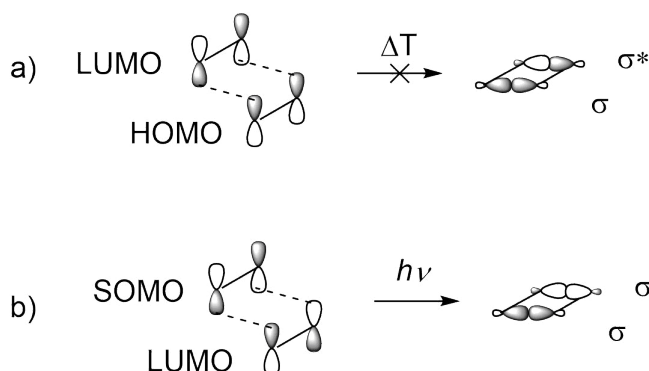
Figure 2.10: Frontier orbital interactions of the [2+2]-cycloaddition between two ethene molecules under thermal (a) and photochemical (b) conditions. [40]

2.2.2 [4+2]-Cycloaddition

[4+2]-Cycloadditions involve six π-electrons in the formation of two new σ-bonds and a π-bond. The *Diels-Alder* (DA) reaction, featuring a diene and a dienophile, and 1,3-

dipolar cycloaddition between a 1,3-dipole and a dipolarophile are examples for this class of cycloadditions.[40–42]

Diels-Alder Reactions

The DA reaction was first described by O. P. H. Diels and K. Alder in 1928[43] and both were awarded the Nobel Prize in 1950. DA reactions describe the cycloaddition of a diene with an alkene or alkyne in bulk or inert solvents by thermal activation. The cycloaddition between 1,3-butadiene and ethene is conducted in the gasphase at 200 °C. The LUMO of the diene reacts with the HOMO of the dienophile as depicted in Figure 2.11. The yield of the DA reaction between 1,3-butadiene and ethene results in low
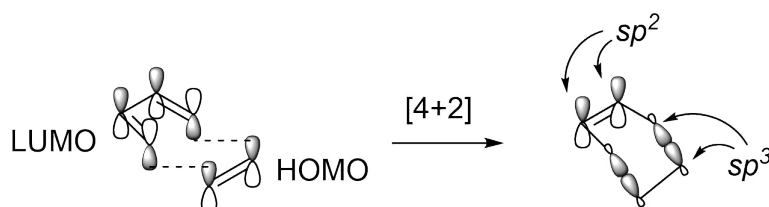
Figure 2.11: Orbitals involved in the *Diels-Alder* reaction between 1,3-butadiene and ethene.[42]

yields of ca. 20% and the high temperature limits the possible applications in, e.g., biological systems. High temperatures are required as the energy gap between the HOMO of the dienophile and the LUMO of the diene is large.[41,42] The stabilization of the transition state of a DA reaction can be estimated by the simplified Equation 2.4.[41] The energy gaps between the ethylene HOMO and the butadiene LUMO is $-1326\,\text{kJ mol}^{-1}$ and between the ethylene LUMO and the butadiene HOMO is $-1305\,\text{kJ mol}^{-1}$, thus leading to a small ΔE_TS (TS = transition state) additionally to the high energy differences between the orbitals.

$$\Delta E_\text{TS} \propto \frac{1}{E_\text{HOMO,diene} - E_\text{LUMO,dienophile}} + \frac{1}{E_\text{HOMO,dienophile} - E_\text{LUMO,diene}} \quad (2.4)$$

The introduction of electron-withdrawing or electron-donating groups shifts the energy levels of the frontier orbitals and thereby enables DA reactions with high yields at lower temperatures. Figure 2.12 depicts the frontal orbital interactions between unsubstituted butadiene and ethene (column 2) and after the introduction of pendant groups. A DA reaction proceeds under so-called "normal" electron-demand between an electron-poor

dienophile and an electron-rich diene (column 1). The electron-withdrawing group (EWG) on the ethene lowers the energy of both binding and non-binding orbitals, hence, reducing the gap between the HOMO of the diene and the LUMO of the dienophile. Electron-donating groups (EDG) can also be attached to the π-system, thereby decreasing the gap between HOMO and LUMO.

The introduction of EWG groups onto the dienophile also enhances the reactivity of the system, as the energy of the orbitals of the dienophile are lowered, and the energy gap between the HOMO of the dienophile and the LUMO of the diene is reduced, referred to as "inverse" electron demand (column 3).[40,41]
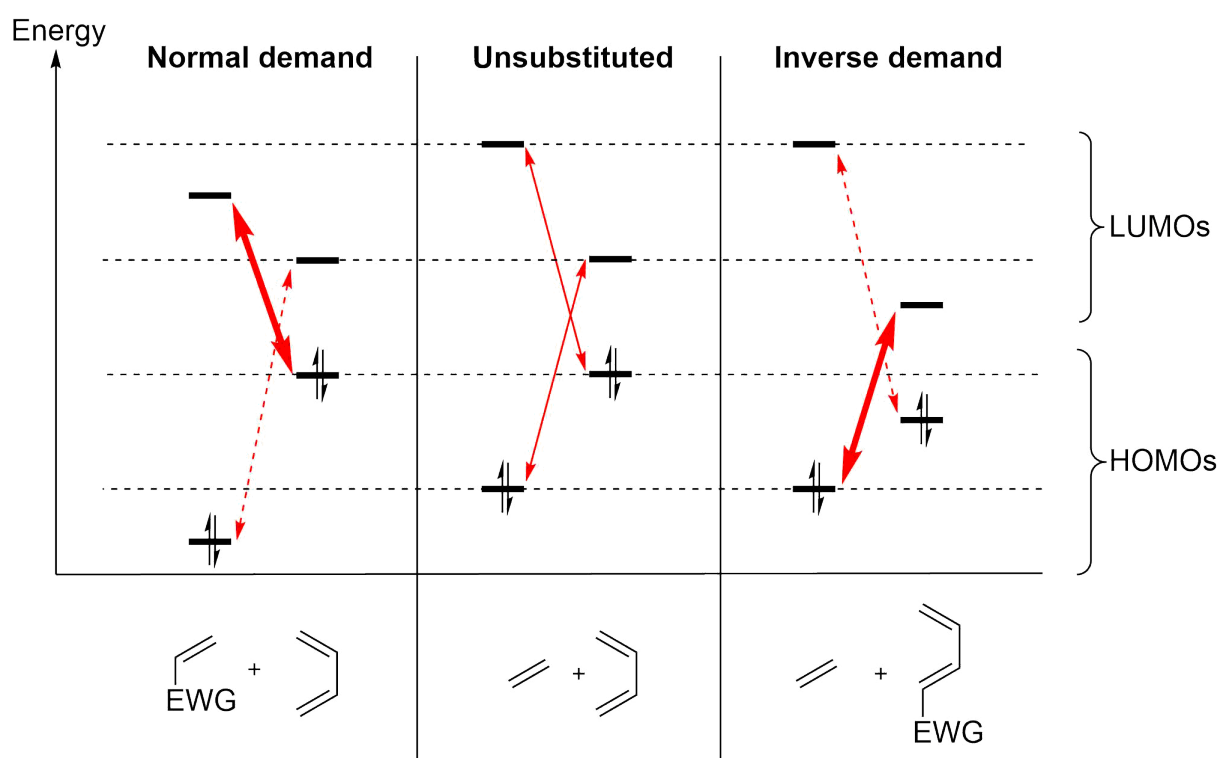
Figure 2.12: Frontier orbital interactions of *Diels-Alder* reactions between unsubstituted and EWG-substituted 1,3-butadiene and ethene.[40,41]

1,3-Dipolar Cycloadditions

1,3-Dipoles are zwitterionic molecules with heteroatoms that are described with all-octet resonance structures. Figure 2.13 gives an overview of a small selection of 1,3-dipoles. The 1,3-dipolar cycloaddition is an important tool for the synthesis of heterocycles.[41]
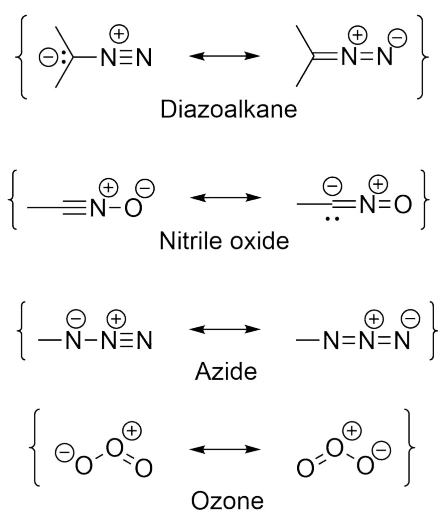
Figure 2.13: Selection of important 1,3-dipoles in organic synthesis.[41]

1,3-Dipoles can be characterized as propargyl-anion-type (linear) and allyl-anion-type (angled). The central ion of propargyl-anion-type dipoles is nitrogen which carries the positive charge in all resonance structures. Dipoles of the allyl-anion-type can possess oxygen, sulfur or nitrogen as central atom.

A convenient 1,3-dipolar cycloaddition is the *Huisgen* azide-alkyne cycloaddition.[44] Azides are stable towards dimerization and hydrolysis, can be readily introduced by substitution reactions, and can be reduced to amino groups. The azide-alkyne cycloaddition gained substantial interest after Tornøe and Meldal introduced Cu(I)-catalysis and thereby accelerated the reaction rate by seven orders of magnitude.[45] Figure 2.14 depicts the postulated mechanism of the copper-catalyzed azide-alkyne cycloaddition (CuAAC). First, the copper catalyst coordinates to the alkyne bond (**1**). It is suggested that copper can coordinate to more than one alkyne (**2**), thereby increasing the local concentration of alkynes.[45] The catalytic step in the mechanism of the CuAAC is still not fully understood. Based on DFT (density functional theory) calculations[46,47] and crystal structure datas of copper-acetylide complexes,[45] the azide and the alkyne are most probably coordinated to more than one copper ion, depicted as structures **3A** and **3B**. Both intermediate copper complexes maintain the favored structural coordination of copper-acetylide complexes while entailing a six membered transition state. However, the intermediate **3A** cannot explain the absolute regioselectivity of the cycloaddition.[45,48]

Complex **4** describes the possible intermediate complexes after one bond between the azide and the alkyne was formed. After the triazole was generated, the product is still coordinated to a copper complex (**5**), before being released (**6**) by the substitution with an electrophile (H$^+$).
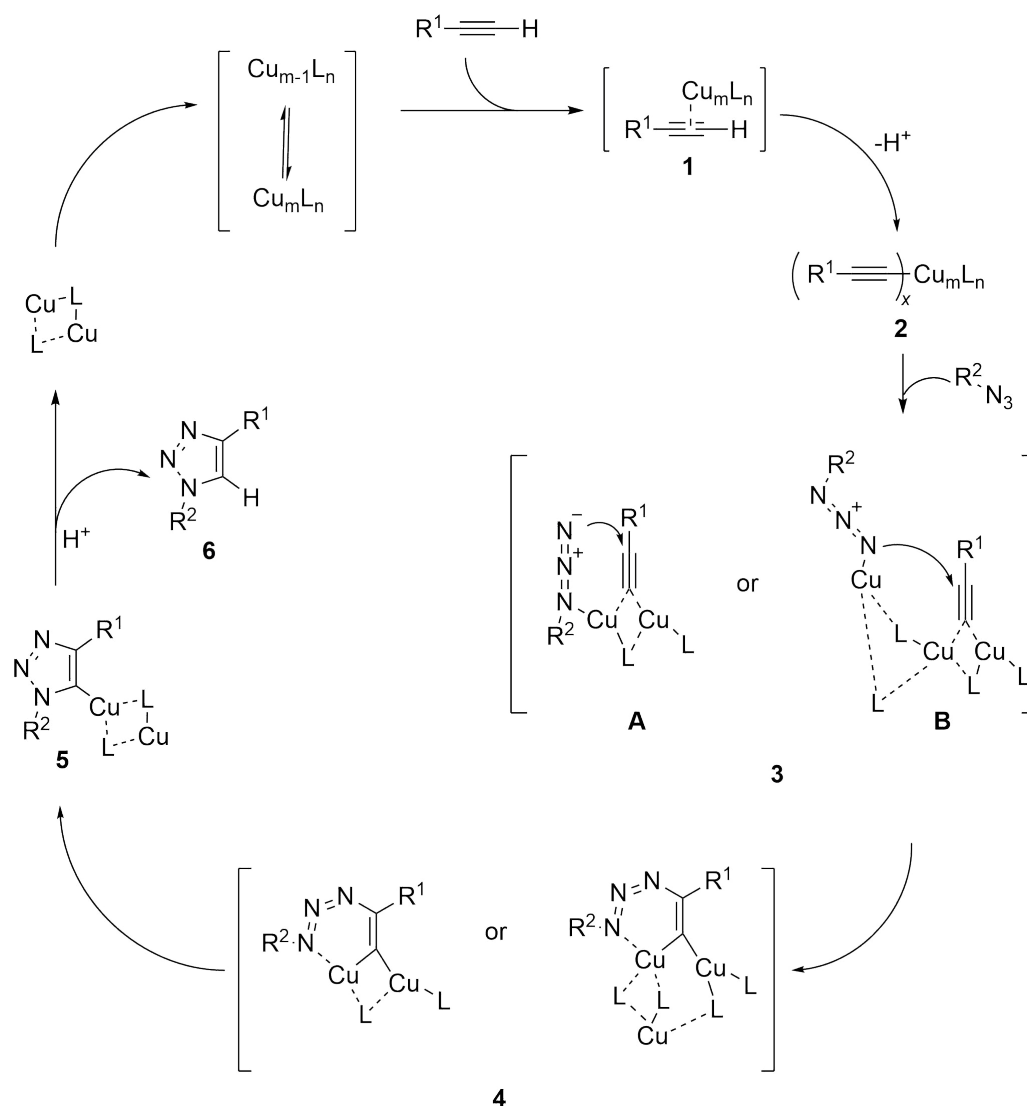
Figure 2.14: Mechanism of the copper-catalyzed azide-alkyne cycloaddition.[45]

2.3 Photoenolization

Photoenolization describes the tautomerization process of light sensitive aldehydes or ketones. First reported by Yang *et al.*,[49] the photoenolization of *o*-substituted benzophenones (first generation photoenols) was more closely investigated by Porter and Tchir,[50,51] and reviewed by Sammes.[52] The accepted mechanism for the photoenolization process of *o*-methyl benzaldehydes (second generation photoenols), including the life times determined by Porter and Tchir, is depicted in Figure 2.3.

The irradiation with near-UV light generates the excited singlet state via the $n \rightarrow \pi^*$ transition with a short life time of $\tau < 10$ ns. ISC results in the reactive triplet state which has a longer life time than the singlet state of $\tau = 40$ ns. The aldehyde moiety of the molecule is able to rotate, thereby forming two biradical isomers by the Norrish-
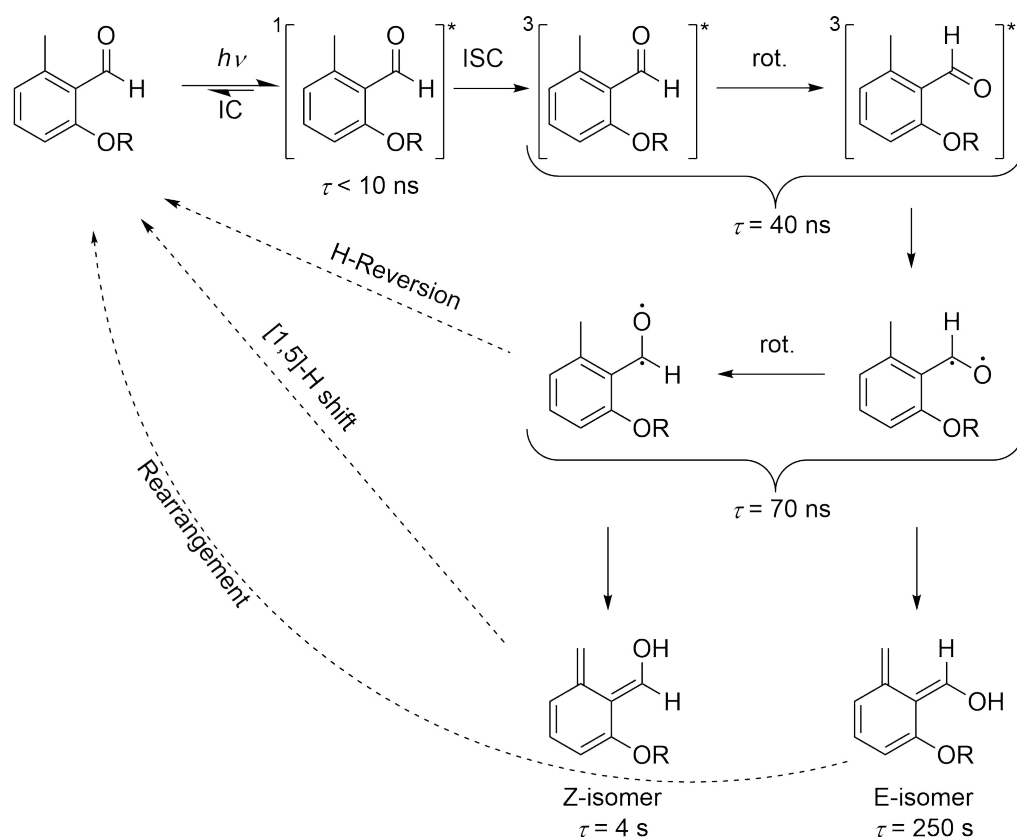
Figure 2.15: Mechanism of the photoenolization process of *o*-substituted *α*-methylbenzaldehydes.

type II *γ*-hydrogen abstraction. The isomers can either react back to the ground state or rearrange into two diene isomers, the Z- and the E-isomers. The E-isomer has a life time of close to 60 times longer than the life time of the Z-isomer. The Z-isomer is readily transformed into the ground state by a [1,5]-H shift[53] and is therefore unreactive in cycloadditions with dienophiles. In contrast, the E-isomer cannot undergo an H-shift which results in the longer life time, and thus, the E-isomer can easily react with dienophiles in DA reactions.[54]

The photoenols can be employed in fast DA reactions with electron-poor alkenes. Reactions have been performed, for example, with maleimides[55,56] and fumarates.[57,58] Furthermore, the reaction was employed for surface functionalization and patterning,[59-61] polymer conjugation and the formation of nanoparticles,[56,62-64] and stimulated-emission depletion direct laser writing (STED-DLW).[65]

The photoenolization was also employed in light-induced step-growth polymerizations.[57] Here, a difunctional photoenol monomer was polymerized with a difumarate monomer. During the polymerizations, the photoenol group underwent a side reaction towards dimerization of two photoenol groups as depicted in Figure 2.16. The concen-
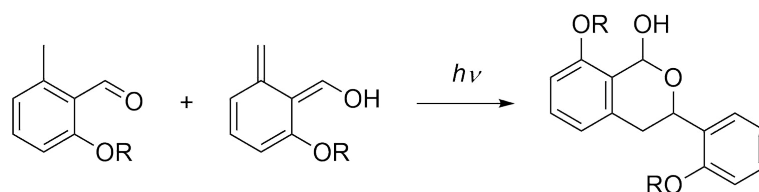
Figure 2.16: Possible dimerization reaction of *o*-methyl benzaldehydes under UV-irradiation and without the presence of a dienophile.[57]

tration of the photoenol as well as the concentration of available dienophiles can supress the side product formation.

2.4 Properties and Applications of Porous Materials

Porous materials are solids with pores which are employed in various applications from daily necessities to industrial uses, e.g., purifying water or gases. Pores are defined as closed (isolated from the solid's surface), open (connected to the solid's surface), and penetrating (open pores with at least two openings on two sides of the material), as depicted in Figure 2.17. Closed porous materials are mainly applied as sonic or thermal insulators. Open pores find application as carriers for catalysts or as bioreactors. For the application as filters or for gas distribution, penetrating open pores are required.[66]
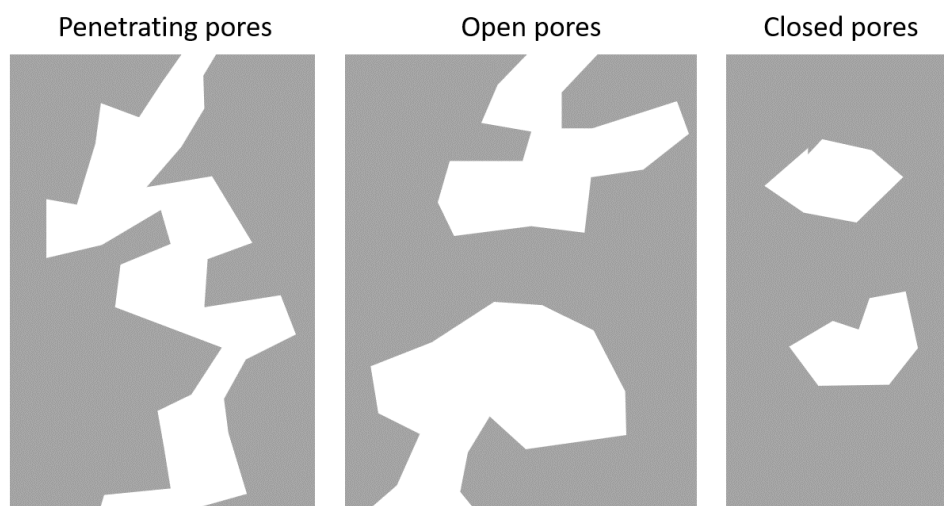
Figure 2.17: Schematic description of pores classified as: *penetrating:* pores with minimum two openings on two sides of the material; *open:* pores with openings on the material's surface; *closed:* pores with no contact to the material's surface.[66]

In general, porous materials feature lower densities and higher surface areas than the pore-free solids. The high surface areas are interesting in terms of catalysis, however, increasing porosity involves decreasing mechanical strength and the material has to be carefully designed for specific conditions. The desired application also requires specific pore sizes. Zeolites, silica gels and intercalated layered materials have atomic scale pores which are necessary for gas separation and catalysis. Water purification requires pore sizes between 0.1 and 100 μm, which are usually prepared by sintering. The pore sizes are classified by the International Union of Pure and Applied Chemistry (IUPAC) nomenclature, namely in micropores (up to 2 nm), mesopores (up to 50 nm), and macropores (> 50 nm).[66]

2.4.1 Metal-Organic Frameworks

Metal-organic frameworks (MOFs) are crystalline inorganic-organic hybrid structures that consist of metal nodes and organic linkers (Figure 2.18). As variable metal nodes (e.g. copper, zinc, chromium, etc.) or metal-containing secondary building units (SBU, yellow), and linkers (e.g. nitrogen- or carboxylic acid containing multifunctional organic molecules, blue and red)[7,67–70] can be used and combined, over 70 000 different MOF structures have been reported over the last decade.[67] As MOFs are highly crystalline materials, they consist of unit cells that combine to a large lattice with regular sized, permanent pores. Pore sizes and geometry are defined by the length and the properties of the linker molecules and can therefore be readily controlled with the largest reported pores of close to 12 nm[71] and the lowest density of approx. 0.13 g cm^{-3}.[67] Due to their lattice structure, MOFs are highly porous materials and can have specific *Brunauer-Emmett-Teller* (BET) surface areas of up to 6500 m^2 g^{-1}. Therefore, they can be used as gas storage or separation devices as well as for heterogeneous catalysts.[6,7,67,68,70–72]
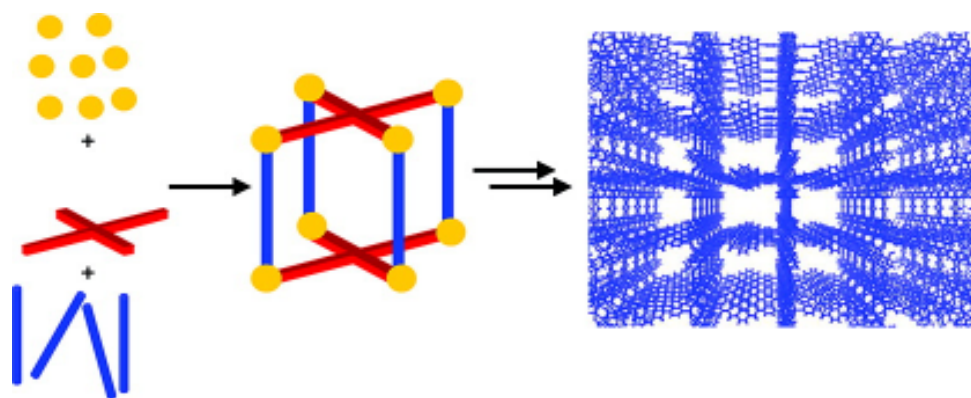
Figure 2.18: Schematic description of MOF preparation. Reprinted with permission from Ref. 69. Copyright (2010) American Chemical Society.
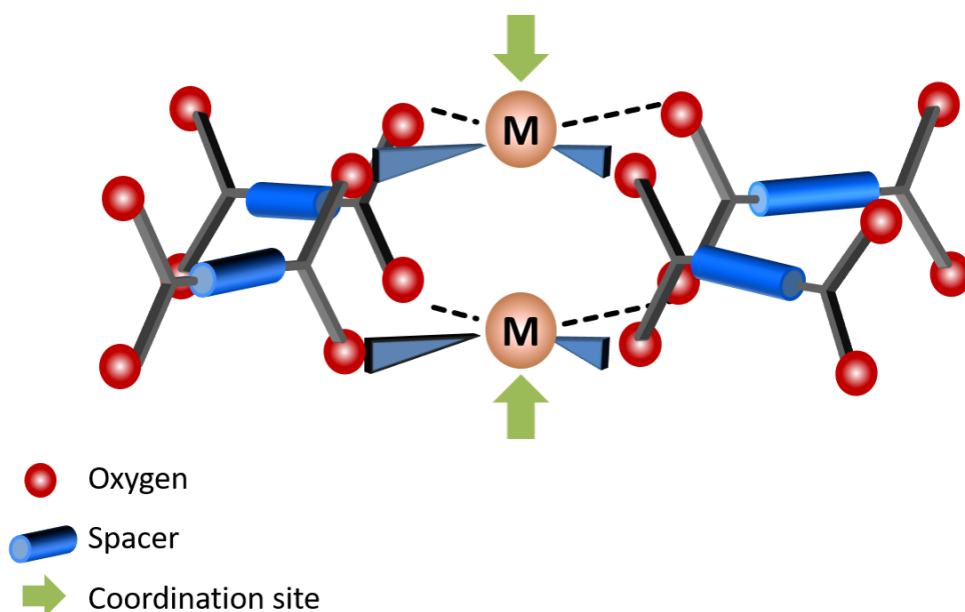
Figure 2.19: Paddle wheel complex of two metal ions (M) with four dicarboxylic acid linkers. The green arrows mark free coordination sites.[73]

A popular SBU for MOF preparation is the paddle wheel-shaped metal dimer complex that many transition metals can form (Figure 2.19). The paddle wheel contains two coordination sites at the axial position of the metal ions and are usually occupied by the solvent in which the MOF was prepared. The solvent can be easily exchanged or removed, generating free coordination sites that are of interest for gas absorption and heterogeneous catalysis.[73]

The first reported MOF containing the paddle wheel complex is HKUST-1,[70] consisting of copper ions and benzene-1,3,5-tricarboxylic acid (BTC) linkers.[73] HKUST-1 has been investigated in molecule absorption and separation,[74–77] as carrier for ion loading,[78] for the preparation of photocatalysts,[79] and as surface coating.[80,81] The paddle wheel complex can also be formed by W, Fe, or Cr. In fact, $Cr_3(BTC)_2$ shows high oxygen absorption at low pressure, while the N_2 uptake under the same conditions is negligible.[82–84] The shape and size of the pores depends on the metal nodes and organic linkers employed (Figure 2.20). HKUST-1 and $Cr_3(BTC)_2$ possess 3D channels. MOFs with the structure $M_2(DHBDC)$ (DHBDC = 2,5-dihydroxytherephthalic acid); M = Mg, Mn, Co, Ni, Zn) form hexagonal 1D channels and contain a high amount of unsaturated metal sites.[73] Al(BDC)(OH) (BDC = therephthalic acid), also known as MIL-53, possesses diamond-shaped 1D channels that are highly flexible. One axis of the framework is connected via Al-OH-Al chains which angles change upon guest absorption and are applied for the selective absorption of xylene isomers, and drug delivery.[85–87]
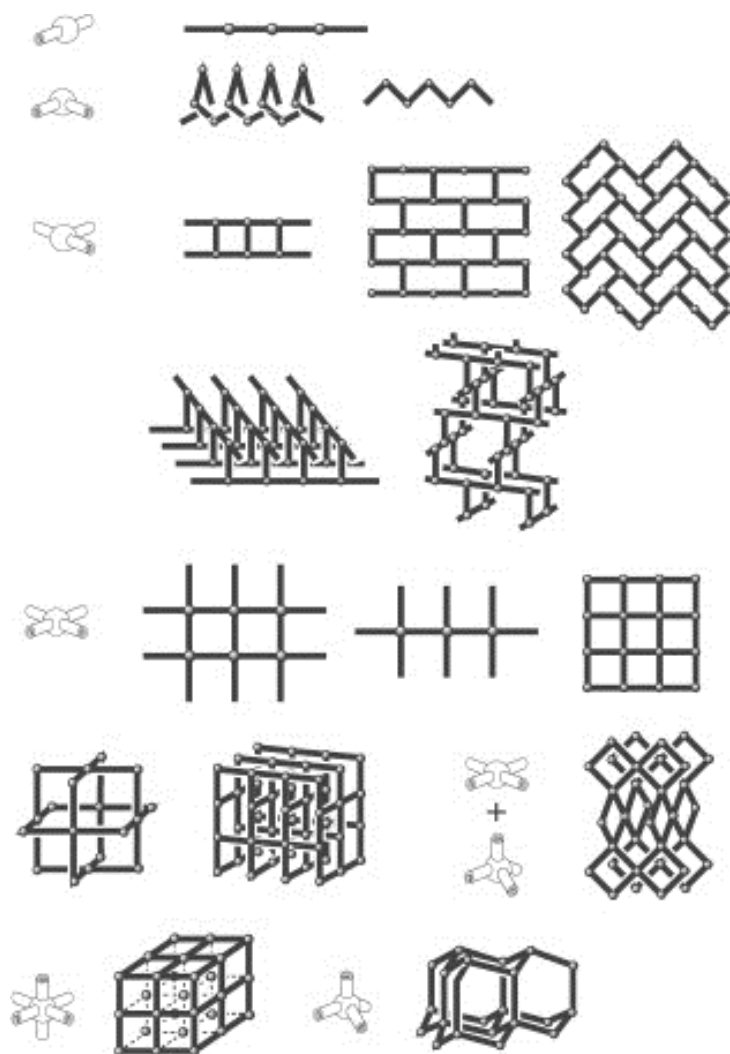
Figure 2.20: Structural frameworks that can be constructed by combining various connectors and linear linkers. Reprinted with permission from John Wiley and Sons.[8]

Post-Synthetic Modification

The wide variety of MOF structures allows the introduction of specific functional groups for post-synthetic modification.[9,88–90] Zeolites, in comparison, are not only restricted to the pore size, but also are limited to modifications by ion exchange or silanation. MOF structures possess the advantage that the pore size and shape can be adjusted to specific applications and, furthermore, various functional groups can be attached to the organic linkers.[91]

Fundamentally, there are two major access routes to functional MOF structures, as depicted in Figure 2.21. The desired functionality can be attached to the organic linker before the framework formation, resulting in the functional framework in one step. The functional group can also be attached after the framework preparation as post-synthetic modification (PSM). On the one hand, the self-assembly method can only be performed
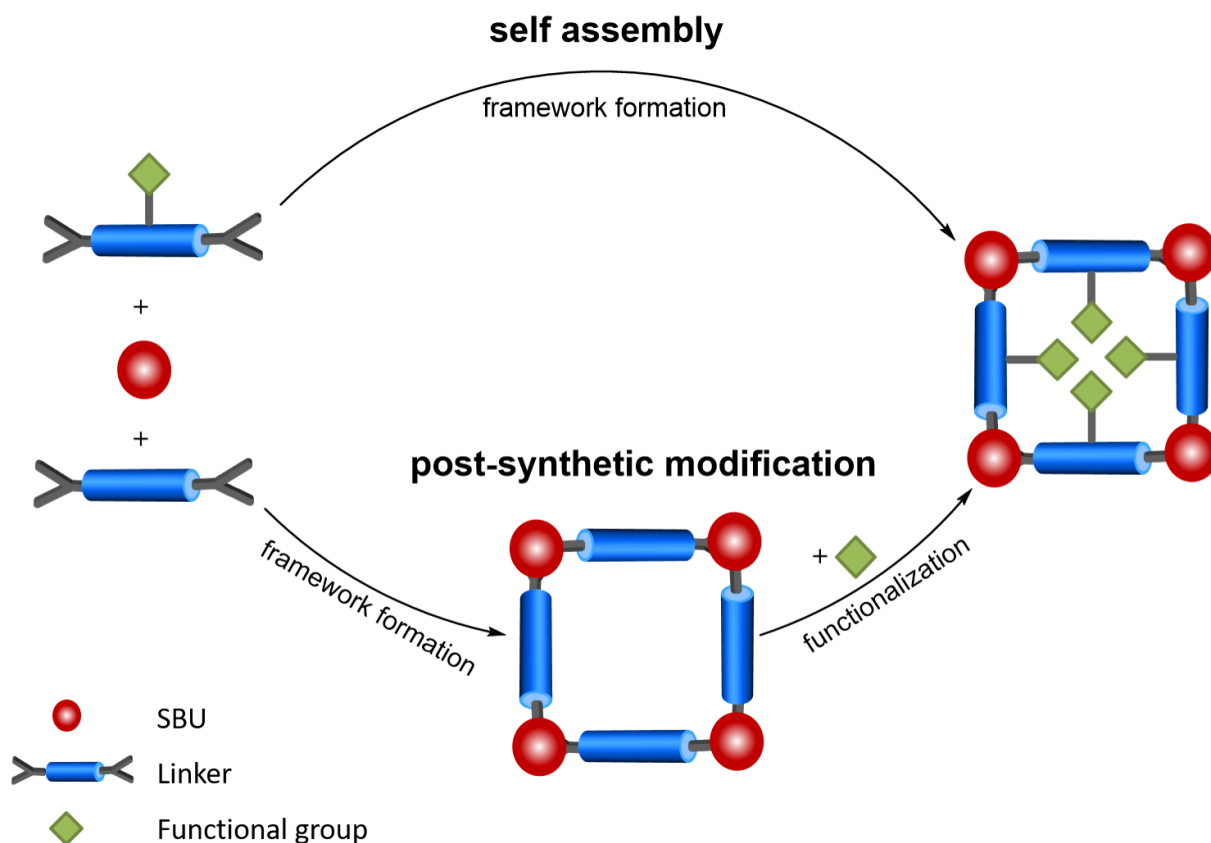
Figure 2.21: Functionalization of metal-organic frameworks via self-assembly or post-synthetic modification.[91]

with functional moieties that do not interfere with the framework growth. On the other hand, the PSM approach requires robust MOF structures that are stable under the PSM reaction conditions. Via PSM, one single MOF can be tranformed into various isotopological structures that may change the physical and chemical properties of the porous solid without changing the crystallinity.[91]

Cohen and coworkers investigated the reactivity of amine-functionalized MOFs towards a variety of alkyl anhydrides ($O[CO(CH_2)_nCH_3]_2$, n = 1-18) on NH_2-BDC containing MOFs (Figure 2.22).[91–93] The reaction yield was determined by ^{1}H NMR spec-

$R = (CH_2)_nCH_3$, n = 1-18
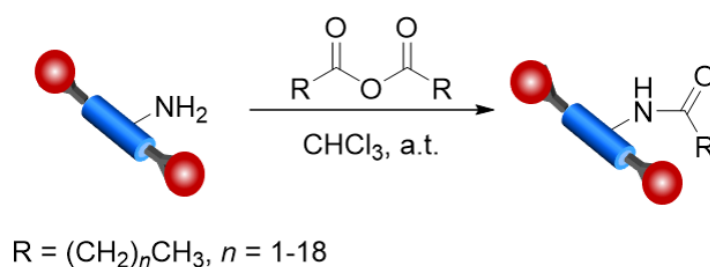
Figure 2.22: Post-synthetic modification of amine-containing MOF structures with alkyl anhydrides.[92]

troscopy after dissolving the MOF structures. Quantitative modification was achieved for anhydrides with $n \leq 5$, with decreasing yields down to 10% for $n = 18$.

CuAAC has been investigated as MOF functionalization procedure by several groups. For example, Hupp and coworkers produced a MOF structure with pendant alkyne groups which were applied in CuAAC with ethidium bromide monoazide, as depicted in Figure 2.23. As the azide provided a fluorescent reactant, the reaction was followed by fluorescence spectroscopy and revealed that the surface of the MOF was indeed functionalized, yet, the inner sites of the material remained unreacted. The observation led to the development of polymer-coated MOF particles which influences the stability and dispersion quality of MOFs in various media.[94]
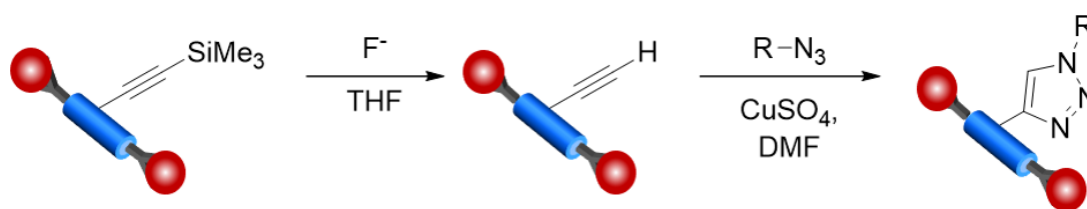
Figure 2.23: Post-synthetic modification of alkyne-containig MOF structures.[94]

Furthermore, the CuAAC was performed on azide-functionalized MOF structures.[95] Furrasseng and coworkers developed mild conditions for the transformation of amine groups into azide functionalities that can be applied on acidic-sensitive MOFs.[96] The azide formation as well as the successful triazole synthesis was analysed via IR and NMR spectroscopy. The method was applied to four different MOF types with various terminal alkynes, evidencing that the CuAAC can be employed for quantitative functionalization of MOFs, even with bulky reactants.
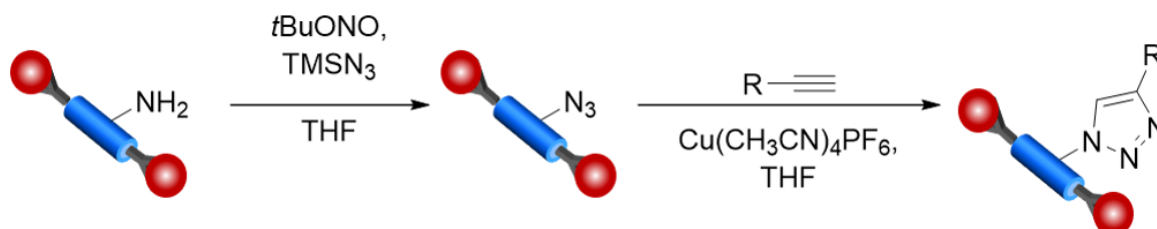
Figure 2.24: Two-step triazole functionalization of amino-containing MOF structures.[96]

2.4.2 Surface-Mounted Metal-Organic Frameworks

Surface-mounted metal-organic frameworks (SURMOFs) are a specific type of MOF-coating on surfaces. Figure 2.25 depicts various methods for the coating of MOF thin films. In Figure 2.25a, the preparation of thin films is achieved by dipping surfaces into a MOF mother solution. The crystals are formed and are deposited on a surface, resulting in a polycrystalline film. If the mother solution is filtered to remove the crystals, a surface with a self-assembled monolayer (SAM) can be immersed into the solution, which results in crystal growth directly on the surface and thereby produces oriented single crystals.[22] Both methods yield heterogenous films which do not uniformly coat the substrate, because the films consist of small individual particles with various thickness. The diffusion of guest molecules into these heterogeneous MOF layers are therefore likewise heterogeneous which limits the application of these films, e.g. as sensors or membranes.

The orientation of crystal growth can be enhanced by the layer-by-layer (LBL) method (Figure 2.25b) by immersing the SAM-functionalized surface into the metal precursor solution and the ligand solution consecutively.[97] The SAM layer hereby provides functional groups for the complexation of the metal ions and creates an ideal template for epitaxial growth. The first SURMOF that was prepared by this method was HKUST-1.[5] A gold-coated surface was functionalized with mercaptohexadecanoic acid (MHDA), providing carboxylic acid groups for the complexation of Cu_2^{2+} SBUs. The surface was coated by immersing the substrate into the copper precurser solution ($Cu_2(OAc)_4$ in ethanol), followed by intensive rinsing with ethanol, and subsequent immersion into the BTC solution (in ethanol). After a further rinsing step, the cycle can be repeated to achieve the desired SURMOF thickness. In contrast to the polycrystalline films, HKUST-1 SURMOF prepared by the LBL method showed only reflexes of the (111) growth direction in out-of-plane X-ray diffraction (XRD), while the polycrystalline surfaces also produce reflexes of the (100) and (110) orientation.[97]

(a)

(b)
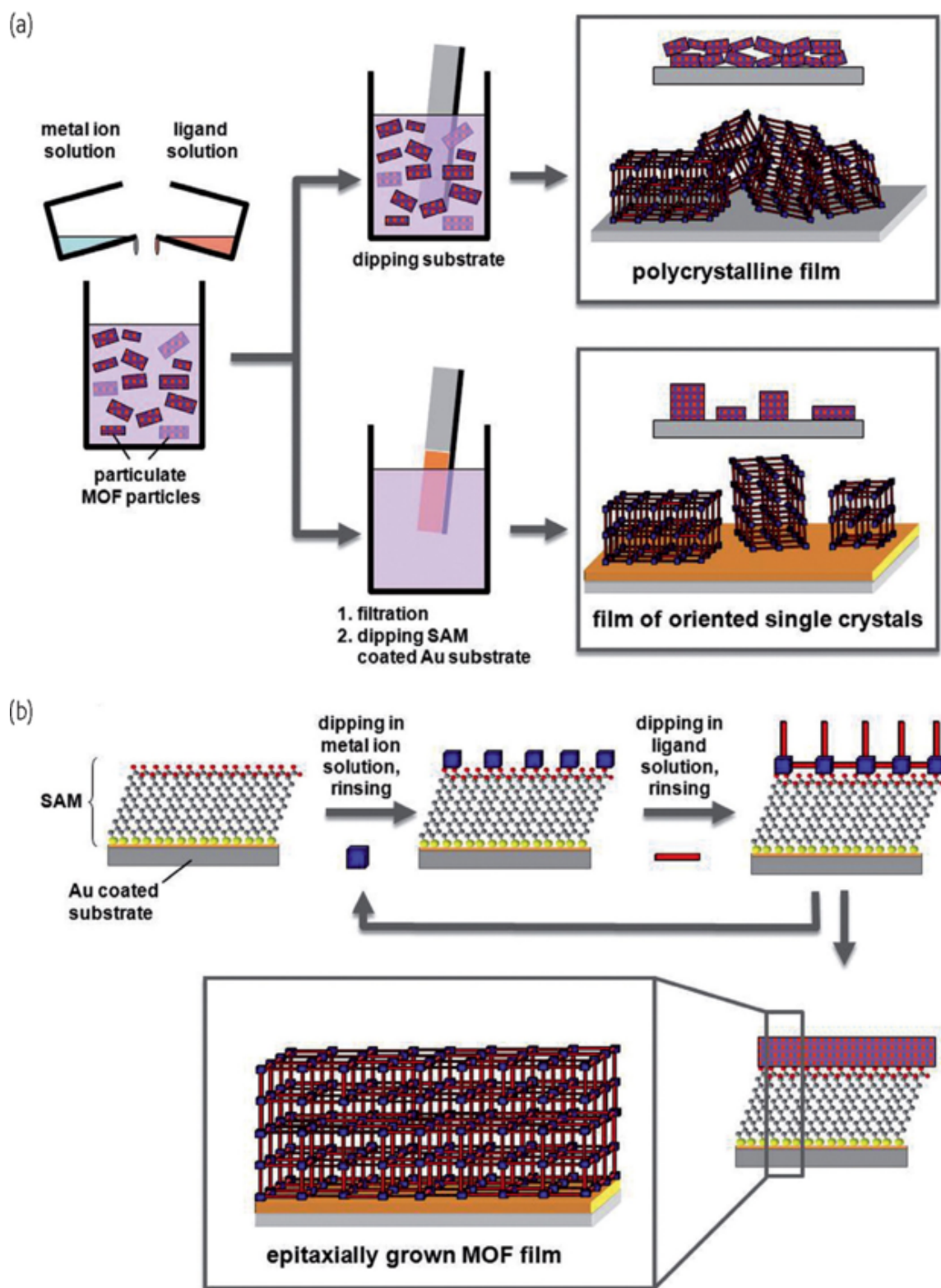
Figure 2.25: Schematic depiction of the formation of MOF thin films. (a) The coating of a substrate with particulate MOF, which was precipitated before (above), and the growth of MOF crystals directly on a SAM-terminated gold surface, after the precipitated MOF-crystals in solution were removed (below). (b) Demonstration of the epitaxial layer-by-layer growth of SURMOF on a gold coated substrate, which was functionalized with a SAM before the deposition of the SURMOF. The thickness of the SURMOF layer depends on the number of coating cycles. Reprinted from Ref. 97, with permission from Elsevier.
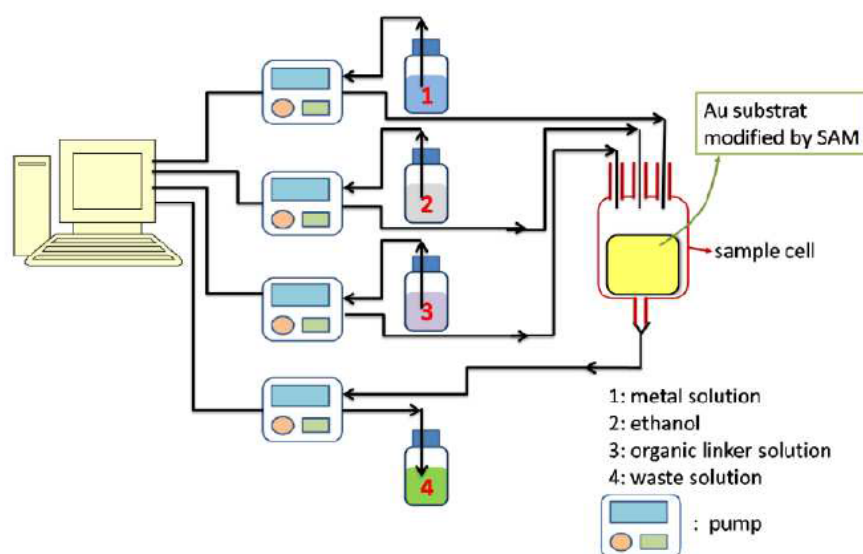
Figure 2.26: Schematic depiction of the automated layer-by-layer preparation of MOF thin films. SAM-functionalized samples are placed into a tempered sample cell and the cell is consecutively filled with the precursor and rinsing solutions. Reprinted with permission from Ref. 98. Copyright (2011) American Chemical Society.

Wöll and coworkers employ an automated system for the preparation of SURMOFs.[98] Figure 2.26 depicts the setup of the automatic pump system. The SAM-functionalized substrate is placed into a sample holder that is equipped with three inlets and one outlet. Through the individual inlets, the solutions for the MOF preparation are pumped into the sample cell, remain there for a preset time, and are subsequently removed through the outlet into the waste container. Unfortunately, the pumping method requires long reaction times. The preparation of a SURMOF with 100 nm thickness requires ca. 100 cycles, thus 400 immersion steps, which results in 3 d preparation time. Most applications for storage and separation are in need of μm thicknesses which is not practical with the pumping method.[97]

A faster procedure is the spray method (Figure 2.27).[99] The precursor solutions are deposited on the SAM-functionalized surface from spray nozzles. The deposition cycle here also consists of rinsing steps in between the metal and linker solution application. The spray method likewise results in highly crystalline and oriented films comparable to the pump method. The spray method has the advantage that the deposition times are reduced from minutes to seconds and thereby the overall preparation time of MOF thin films is reduced. However, the individual deposition methods are not suitable for every MOF structure. HKUST-1 and SURMOFs with 2D channels like Cu-BDC can be produced by the spraying method. For MOFs with two linkers, resulting in 3D channels
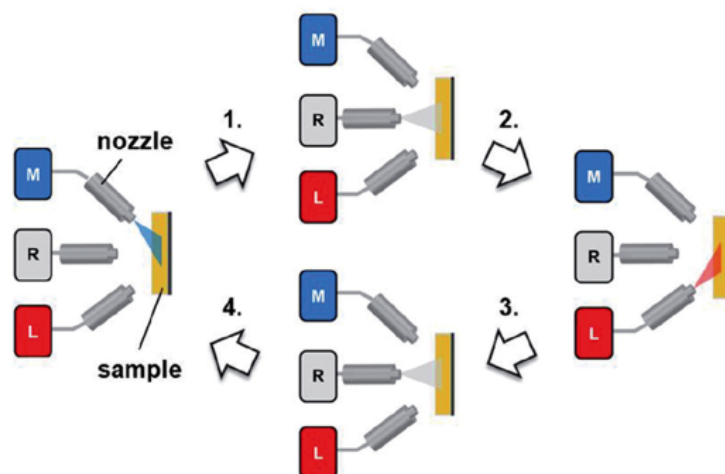
Figure 2.27: Scheme of the production of SURMOFs by spray method:[99] In the first step, the metal solution (M) is sprayed on the substrate subsequently followed by the rinsing liquid (R), the linker solution (L) and again the rinsing liquid. The number of spraying cycles determines the final thickness of the deposited SURMOF layer. Reprinted from Ref. 97, with permission from Elsevier.

like Cu-BDC-dabco (dabco = 1,4-diazabicyclo[2.2.2]octane), the pumping method is required to yield the highest quality of the SURMOF films, as the crystallization during the spray time is not fast enough for these materials.[97,99]

The growth of MOFs by the layer-by-layer method results in a unique structure orientation, as is evidenced for Cu-BDC (also known as MOF-2) and similar structures. The SURMOF preparation on COOH-terminated SAMs yields perfectly stacked lamellae of MOF sheets resulting in channels with a squared cross section (Figure 2.28).
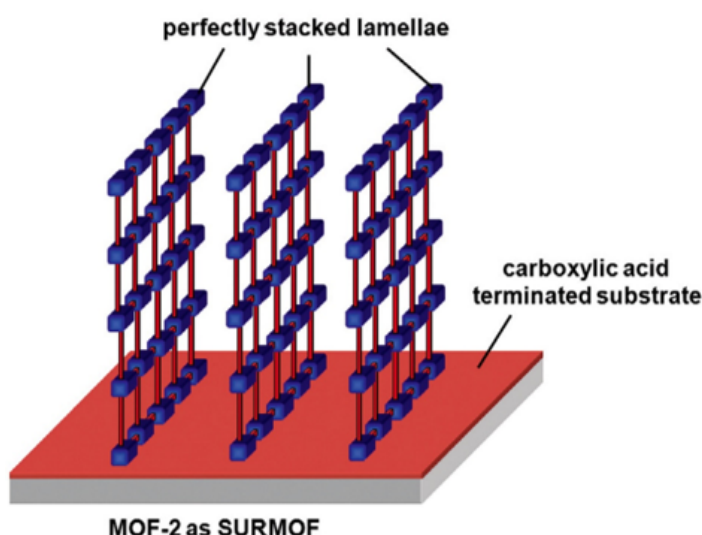
Figure 2.28: Cu-BDC and related structures form stacked lamellae perpendicular to the COOH-terminated surface. Reprinted from Ref. 97 with permission from Elsevier.

The SURMOF growth direction for 3D channels, as in Cu-BDC-dabco or HKUST-1, can be adjusted by the employed SAM.[22,100] Depending on the complexation between the metal ions and the functional groups of the SAM, the growth of a SURMOF can be directed into one specific orientation. If the surface carries SAM molecules with one heteroatom for complexation, e.g., OH or tertiary amines, the copper paddle wheel complexes will coordinate with the axial position to the surface. For SURMOFs like Cu-BDC-dabco, the BDC-linkers will consequently be oriented parallel to the surface, resulting in (001) orientation (Figure 2.29). A surface functionalized with COOH-groups will yield the structure in (110) orientation, thus, the dabco molecules are oriented parallel to the surface.
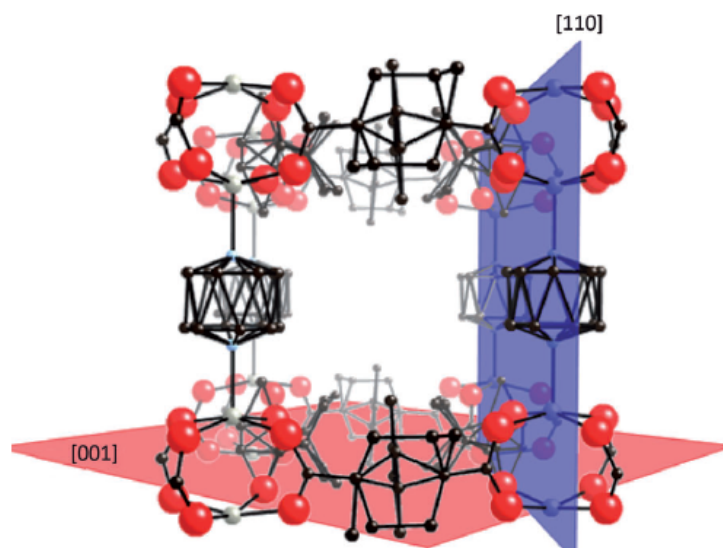
Figure 2.29: Two principle growth directions of $[Zn_2(cam)_2(dabco)]_n$ (cam = (1*R*, 3*S*)-(+)-camphoric acid). Schematic illustrations of oriented growth in the (001) orientation on pyridyl-terminated and the (110) orientation on COOH-terminated SAMs on gold substrates. Reprinted with permission from John Wiley and Sons.[100]

2.5 Polymerization Mechanisms and Processes

Polymers are macromolecules that are built by a large number of small molecules, termed monomers. The molecular weight of those macromolecules may reach into the millions of $g \, mol^{-1}$.

Important for the physical properties of any polymer is the molecular weight. However, the majority of synthetic polymers do not possess one chain length and thereby one

molecular weight, but a *molecular weight distribution*. Thus, average molecular weight and polydispersity are required to characterize polymeric materials.[1,2]

Number-average molecular weigth M_n is defined as the total weigth of all molecules divided by the total number of molecules:

$$M_n = \frac{\sum N_x M_x}{\sum N_x} \tag{2.5}$$

where N_x is the number of molecules (chain length x) with a weigth M_x.

Weigth-average molecular weigth M_w is defined as the weigth fraction w_x of molecules whose weigth is M_x:

$$M_w = \sum w_x M_x = \frac{\sum N_x M_x^2}{\sum N_x M_x} \tag{2.6}$$

For monodisperse materials, the average molecular weights M_n and M_w are equal. For polymers, however, $M_w > M_n$ and the distance between the molecular weights increases with increasing broadening of the distribution as depicted in Figure 2.30. The ratio of the two molecular weights indicates the width of the distribution, as M_n is biased towards low molecular weigth fractions, and M_w is biased towards high molecular weigth fractions. The ratio is termed *polydispersity* and is calculated via Equation 2.7:[1,2]

$$Đ = \frac{M_w}{M_n} \tag{2.7}$$
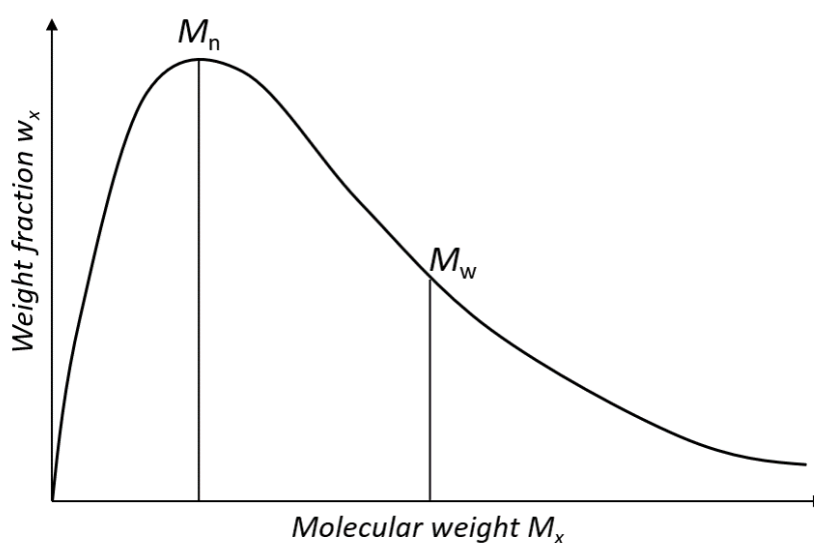
Figure 2.30: Distribution of molecular weigths in a polymer. Adapted with permission from John Wiley and Sons.[2]

The applied polymerization method has an impact on the shape of the distribution and the length of the polymers. Polymers are classified by two different systems. They can be categorized based on polymer structure into *condensation* and *addition* polymers,[101] or on the polymerization process into *step* and *chain* polymerizations.[2]

Depending on the polymerization process and the desired polymer structure, more than one monomer can be emloyed in the process. As an example, Figure 2.31 depicts the general approach of synthesizing polyesters from diacids and diols. The polymeriza-

$$n\,HO-R-OH \;+\; n\,HOOC-R'-COOH \;\longrightarrow\; H{\left(O^{\,R}{}_{O}\overset{O}{\underset{}{C}}{}^{\,R'}\overset{O}{\underset{}{C}}\right)}_{n}OH \;+\; (2n\text{-}1)\,H_2O$$

Figure 2.31: Preparation of polyesters from diols and diacids. R and R' can be aliphatic or aromatic groups.[1,2]

tion follows a step-growth process and is also referred to as polycondensation due to the elimination of water during the reaction. The unit in the parentheses repeats throughout the polymer structure and is therefore termed the *repeating unit*.[1,2]

Condensation reactions are widely employed in industrial processes for the preparation of many important polymers, e.g. polyamides (Nylon), polycarbonates, and polyurethanes. All these structures have in common that two functional groups are

Polymer type	Linkage
Polyamide, protein	
Polycarbonate	
Polyurethane	
Polyacetal	
Polysiloxane	
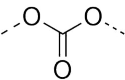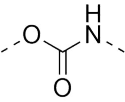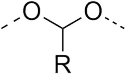
Figure 2.32: Typical polymers that are produced by a condensation process and the corresponding linkage moiety.[2]

required to form the bond between the monomers. Figure 2.32 lists a few polymer types and the resulting linkage moiety in the repeating unit that are synthesized by condensation reactions.[2]

Polymers can also be generated by only one functional group in chain growth mechanisms. The most common type of monomer in this category contains double bonds that are transformed into saturated linkages usually by radical mechanisms (Figure 2.33).[1,2]

$$n\,H_2C=CHR \longrightarrow$$

Figure 2.33: Transformation of vinyl monomers into polymers with the resulting saturated repeating unit.

In the following, the step *vs* chain classification will be introduced for the categorization of polymerization mechanisms.

2.5.1 Polymerization Mechanisms

Free Radical Polymerization

Radical polymerization is the most employed synthetic procedure in industry.[1,2,10,102,103] The process follows a chain growth mechanism consisting of initiation, propagation, termination and chain transfer reactions as depicted in Figure 2.34. First, an initiator produces radicals that can react with the monomer (M) successively in the propagation step. There are two possibilities of termination reactions: combination (1) and disproportionation (2). In case (1), two active chains ($P_i^{\cdot}$ and $P_j^{\cdot}$) react with each other and, consequently, the spins of the electrons are annihilated, resulting in a dead polymer. The term dead polymer describes a species that is not able to react further with monomer. In case (2), a hydrogen radical is transferred from the chain $P_j^{\cdot}$ to another chain $P_i^{\cdot}$, resulting in a saturated polymer P_iH and an unsaturated polymer chain P_j'. The hereby created double bond of P_j' cannot further polymerize. In transfer reactions, a small species (X), in most cases a proton, is transferred to a chain $P_i^{\cdot}$, producing a radical $A^{\cdot}$ and a deactivated polymer chain P_iX.[1,2]

The polymerization rate can be expressed by the change in monomer concentration (Equation 2.8). The concentration of all radicals can be summarized in one concentra-

Initiation   Initiator I $\xrightarrow{k_i}$ 2R$^\bullet$

Propagation   R$^\bullet$ + M $\xrightarrow{k_p}$ RM$^\bullet$ $\xrightarrow{M}$ $\xrightarrow{M}$ P$_i^\bullet$

Termination   (1)   P$_i^\bullet$ + P$_j^\bullet$ $\xrightarrow{k_{t,c}}$ P$_{i+j}$

             (2)   P$_i^\bullet$ + P$_j^\bullet$ $\xrightarrow{k_{t,d}}$ P$_i$H + P$_j'$

Transfer   P$_i^\bullet$ + AX $\xrightarrow{k_{tr}}$ P$_i$X + A$^\bullet$
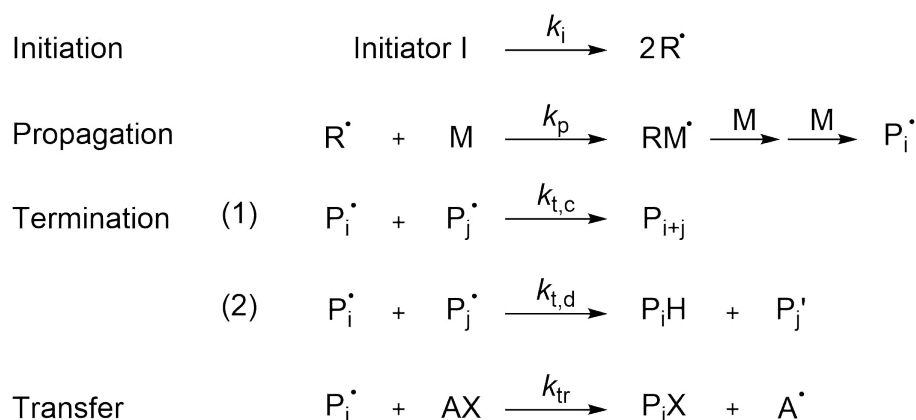
Figure 2.34: Mechanism of free radical polymerizations. *Initiation:* The initiator decomposes into two radicals R$^\bullet$. *Propagation:* The polymer chain grows by adding monomers. *Termination:* (1) by combination of two propargating chains P$_i^\bullet$ and P$_j^\bullet$ resulting in one inactive chain P$_{i+j}$. (2) by disproportionation forming a polymer P$_i$H and an inactive double bond on P$_j'$. *Transfer:* The radical moiety from an active polymer chain is transferred onto another species AX. [1,2]

tion P$^\bullet$ if one assumes that the propagation rate coefficient k_p and the termination rate coefficients $k_{t,c}$ and $k_{t,d}$ do not depend on the chain length of the polymer. [1,2]

$$\frac{-d[M]}{dt} = R_p = k_p[P^\bullet][M] \tag{2.8}$$

Due to their high reactivity, the concentration of the radicals [P$^\bullet$] has very low values and quantitative measurement is not practical in everyday polymerization. For a more practical solution of the polymerization rate R_p, it is necessary to eliminate the radical concentration from Equation 2.8 by applying the *steady-state* assumption. Therefore, it is assumed that the radical concentration [P$^\bullet$] stays constant throughout the reaction process by assuming that the initiation rate R_i and the termination rate R_t are equal. Thus, for each radical that is produced, another one is terminated. [1,2]

$$R_i = R_t = 2k_t[P^\bullet]^2 \tag{2.9}$$

$$\Rightarrow [P^\bullet] = \left(\frac{R_i}{2k_t}\right)^{\frac{1}{2}} \tag{2.10}$$

The resulting term for [P$^\bullet$] (Equation 2.10) can now be inserted into R_p, yielding Equation 2.11 for the polymerization rate R_p.

$$R_p = k_p[M]\left(\frac{R_i}{2k_t}\right)^{\frac{1}{2}} \tag{2.11}$$

Hence, the polymerization rate R_p depends on the square root of the initiation rate R_i. However, the assumption that R_i and R_t are equal is a simplification that does not describe the mechanism adequately. A careful examination of the termination processes reveals that the reaction between two propagating chains is in fact diffusion controlled. Figure 2.35 displays the steps that constitute the termination process of a polymerization. First, two propagating polymer chains are required to reach close proximity by *translational diffusion* in order to interact. For a termination reaction to occur, the chain ends of the individual polymers have to diffuse close to each other by *segmental diffusion*. In the last step, the end groups of the polymers can terminate in either combination reactions (as shown in Figure 2.35) or disproportionation.[2] Thus, the termination rate
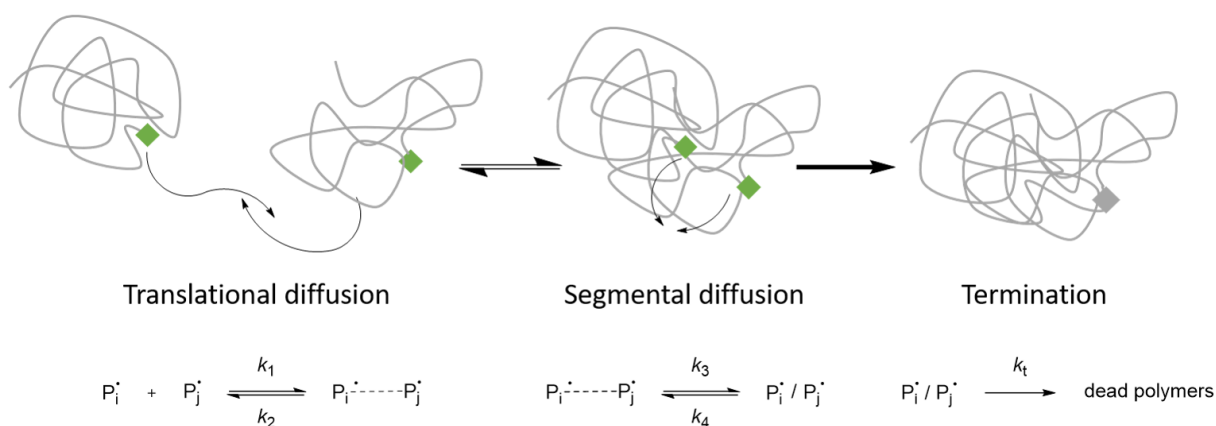
Figure 2.35: Diffusion processes involved in termination reactions of free radical polymerizations.[2]

R_t also depends on the diffusion rate coefficients k_1, k_2, k_3, and k_4. With progressing polymerization, the chain length of the polymers increase, as well as the viscosity of the polymerization mixture. A higher viscosity decelerates the translational diffusion, however, the segmental diffusion is enhanced as the polymer chains become more and more entangled. The ratio of translational to segmental diffusion influences the polymerization rate R_p. If the viscosity of a polymerization system is too high, the translational diffusion decreases faster than the segmental diffusion increases, which results in uncontrolled acceleration of the polymerization, the so-called *gel-effect*. The termination rate R_t is decreased with increasing viscosity, hence, R_p is accelerated, which in turn leads to a higher viscosity and, thus, decelerates R_t further. The auto-acceleration due to the gel-effect can lead to strong exothermic temperature raise. A proper dissipation of the heat cannot prevent the *gel effect*, thus, it is required to keep the viscosity of the polymerization mixture below a critical value.

The termination reactions have a major impact on the molecular weight distributions of polymerizations. This can be explained by examining the kinetic chain length v. v is defined as the average number of monomers consumed per radical, and is described as the ratio between the propagation rate and the initiation rate or the termination rate, respectively, as the latter two are assumed equal:[2]

$$v = \frac{R_p}{R_i} = \frac{R_p}{R_t} \tag{2.12}$$

The number-average degree of polymerization X_n is the average number of monomers in a polymer chain, and is related to v. If the termination reactions in a polymerization proceed exclusively via combination, X_n is double the value of v:[2]

$$X_n = 2v \tag{2.13}$$

If the termination reactions proceed exclusively via disproportionation, X_n is equal to v:

$$X_n = v \tag{2.14}$$

Therefore, M_n depends on the termination processes, as M_n is directly related to X_n, which in turn depends on v:

$$M_n = M_0 X_n = M_0 a v \tag{2.15}$$

M_0: Molecular weight of monomer
a: Factor that depends on the ratio of combination to disproportionation

Other processes that have an influence on the molecular weight are the chain-transfer processes. Transfer reactions entail the premature termination of propagating chains via the transfer of hydrogen or small molecule species onto the propagating chain. Molecules involved can be monomers, initiators, solvents or other additives. The transfer rate R_{tr} is given by Equation 2.16 and depends on the concentrations of radical species [P˙] and reaction partners [AX].[2]

$$R_{tr} = k_{tr}[P˙][AX] \tag{2.16}$$

The resulting radical A˙ can initiate the growth of a new polymer chain. Chain transfer reactions lead to a decrease in the length of the propagating polymers, and influence the propagation rate R_p. Depending on the reinitiation rate of species A˙, the effect on

the polymerization degree X_n can be large, and may yield to the exclusive formation of oligomers ($X_n \simeq$ 1-5). The magnitude of the decrease of X_n depends on the ratio of k_{tr} to k_p.

The degree of polymerization X_n has to be redefined to include all termination and transfer processes. The *Mayo* equation (Equation 2.17) includes the rates for transfer to monomer C_M, transfer to solvent C_S, and transfer to initiator C_I.[1,2]

$$\frac{1}{X_n} = \frac{R_i}{2R_p} + C_M + C_S\frac{[S]}{[M]} + C_I\frac{[I]}{[M]} \tag{2.17}$$

$C_M = \frac{k_{tr,M}}{k_p}; C_S = \frac{k_{tr,S}}{k_p}; C_I = \frac{k_{tr,I}}{k_p}$

Thus, termination and transfer reactions are responsible for the outcome and molecular weight development of a free radical polymerization.

Step-Growth Polymerization

There are two types of step-growth polymerizations (Figure 2.36): the AA, BB-type (1), where every monomer possesses one type of functional group, and the AB-type (2), where both functional groups are attached to one monomer.[2]

(1) n A–R–A + n B–R'-B $\longrightarrow$ $-(A-R-AB-R'-B)_n$

(2) n A–R–B $\longrightarrow$ $-(A-R-B)_n$
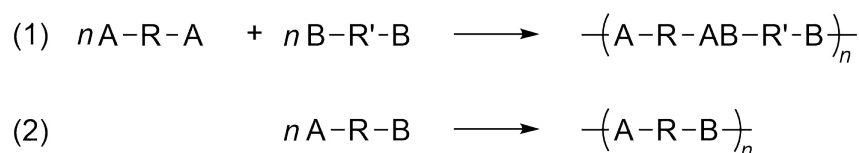
Figure 2.36: Basic illustration of AA, BB-type and AB-type step growth polymerization.[2]

The molecular weight increases slower in step-growth polymerizations than in chain growth polymerizations. There is indeed no initiation step in step-growth processes and all monomers can theoretically react at the same time. However, high conversions of > 99% are required for high polymerization degrees. Figure 2.37 displays the individual steps that are involved in the step-growth process. The molecular weight increases in a stepwise manner continuously with time.[2]

monomer	+	monomer	$\longrightarrow$	dimer
monomer	+	dimer	$\longrightarrow$	trimer
dimer	+	dimer	$\longrightarrow$	tetramer
trimer	+	monomer	$\longrightarrow$	tetramer
trimer	+	dimer	$\longrightarrow$	pentamer
trimer	+	trimer	$\longrightarrow$	hexamer
tetramer	+	monomer	$\longrightarrow$	pentamer
tetramer	+	dimer	$\longrightarrow$	hexamer
tetramer	+	trimer	$\longrightarrow$	heptamer

.
.
.
.
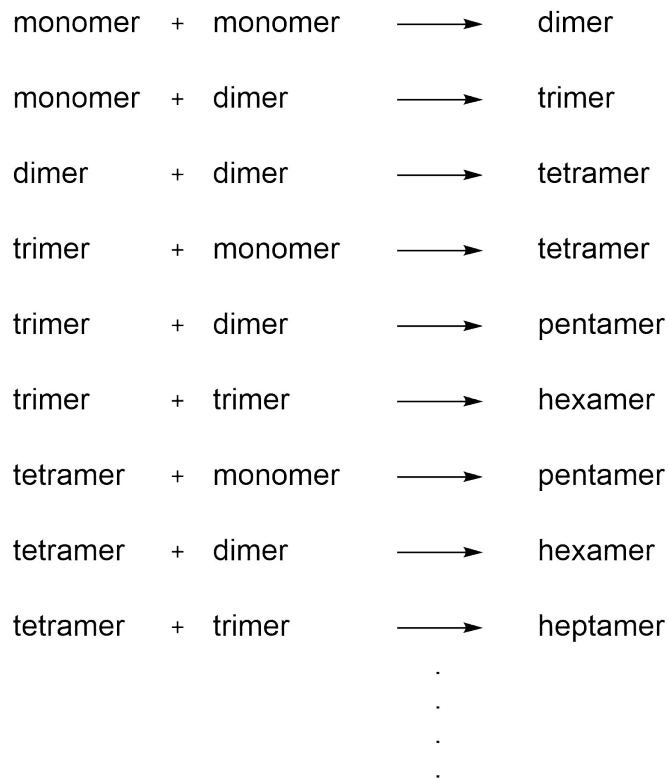
Figure 2.37: Selection of individual reaction steps in a step-growth polymerization.[2]

The individual reaction steps can be summarized as:

$$n\text{-}mer + m\text{-}mer \longrightarrow (n+m)\text{-}mer$$
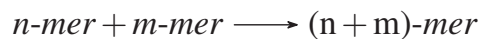
Therefore, the polymerization rate of a step-growth polymerization is composed of the reaction rates of all individual steps. Thus, the kinetics of such a system are usually difficult to calculate. Therefore, it can be assumed that the reactivity of the functional groups is the same regardless of the length of the polymer chain. Thereby, the kinetics are simplified and comparable with the kinetics of the corresponding small molecule reaction.[2]

$$A + B \longrightarrow A{-}B$$

The rates for the consumption of functional groups A and B are equal:

$$\frac{-d[A]}{dt} = \frac{-d[B]}{dt} = k[A][B] \tag{2.18}$$

Equation 2.18 can be rewritten, if a stoichiometric ratio between A and B is assumed:

$$\frac{-d[M]}{dt} = k[M]^2 \tag{2.19}$$

with M as the concentration of functional groups.[2]

The concentration $[M]$ at a specific reaction time t can be expressed as the initial monomer concentration $[M]_0$ minus the amount of consumed functional groups, which can be determined by the conversion p:[2]

$$[M] = [M]_0 - [M]_0 p = [M]_0(1 - p) \tag{2.20}$$

Thus, the polymerization degree X_n, which can be described as the initial number of monomer molecules divided by the number of molecules at time t depends on the conversion p:

$$X_n = \frac{N_0}{N} = \frac{[M]_0}{[M]} = \frac{1}{1 - p} \tag{2.21}$$

Equation 2.21 is also known as the *Carothers Equation* and was originally introduced 1936 by W. H. Carothers.[104] Figure 2.38 depicts the molecular weight development of step-growth polymerizations (b) according to the Carothers Equation in comparison to chain-growth polymerizations (a) and non-terminating chain-growth polymerization (c), e.g. protein synthesis. For normal chain-growth polymerization, the reactive species, e.g. radicals, have short life times of seconds and terminate fast after initiation. Thus, the molecular weight reaches high values after a very short time period as is depicted in 2.38a. Higher conversion leads to a higher number of polymers in the reaction mixture, but does not lead to a higher molecular weight. The nature of stepwise polymerization in step-growth processes leads to a very different molecular weight development (Figure 2.38b). The molecular weight does not reach high values until the polymerization reaches above 99%. Hence, the organic reaction that is employed in the polymerization process is required to have a high selectivity and result in high yields in order to produce high molecular weight material.[2]
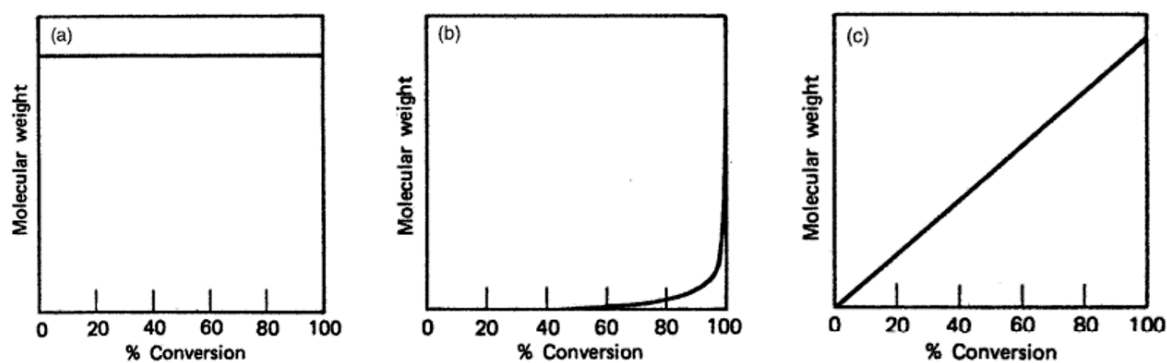
Figure 2.38: Molecular weight development of chain polymerization (a), step-growth polymerization (b), and non-terminating polymerization (c). Adapted with permission from John Wiley and Sons.[2]

There are polymerization processes, apart from protein synthesis, that result in a linear development of the molecular weight with conversion (Figure 2.38c), e.g. anionic and cationic polymerization, as well as ring-opening polymerization. The main feature in all these polymerizations is that initiation is a fast process and termination reactions are almost completely suppressed. The life time of the reactive species is increased from seconds to hours and the molecular weight can be controlled easily by the conversion and results in narrow polydispersities below 1.4.[2,4]

Reversible Deactivation Radical Polymerization (RDRP)

Control in radical polymerizations is achieved by minimizing bimolecular termination reactions and thereby prolonging the life time of the radicals from seconds to hours. The concept of reducing termination reactions is realized by transforming the propagating chains into a dormant state P_n-X by either *reversible termination* (Figure 2.39a) or *reversible transfer* (b) with a control agent $X^\cdot$. In both cases, the concentration of $X^\cdot$ is at
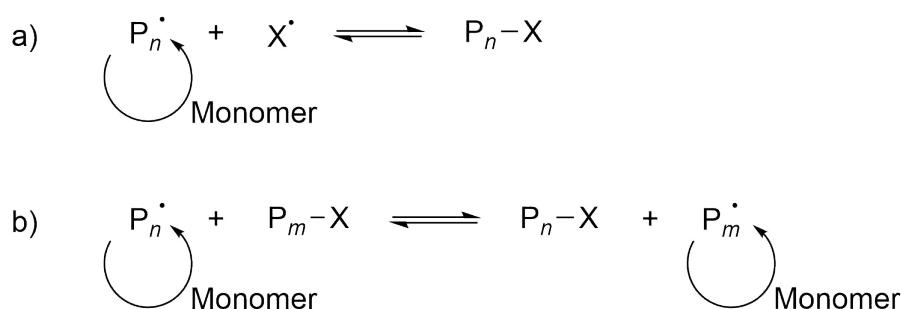
Figure 2.39: Mechanisms of controlled polymerizations. a) Reversible deactivation. b) Reversible chain transfer.[4]

least 4 orders of magnitude higher than the concentration of growing radicals. Thereby, the reaction rate for the combination of $P_n^\cdot$ and $X^\cdot$ is larger than for the combination of two $P_n^\cdot$. The equilibrium favors the dormant species by several orders of magnitude and results in higher concentrations for the dormant species (10^{-1} to 10^{-3} M) than for the reactive radicals (10^{-7} to 10^{-8} M). Reversible deactivation decreases the concentration of propagating radicals compared to free radical polymerization, while reversible transfer processes retain the overall radical concentration. The control agents that can be introduced into radical polymerizations are depicted in Figure 2.40.[2]

CuBrL		
for ATRP	for NMP	for RAFT
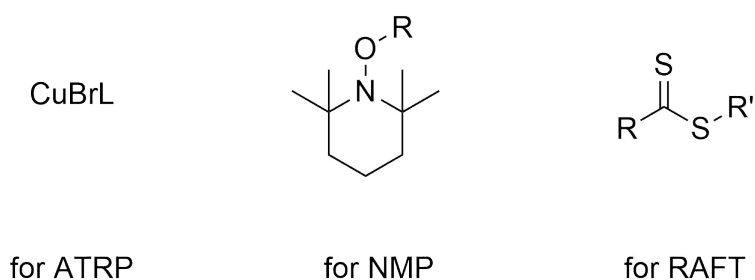
Figure 2.40: Structures of controlling agents for various controlled polymerization processes. *L:* Ligand; *ATRP:* Atom transfer radical polymerization; *NMP:* Nitroxide-mediated polymerization; *RAFT:* Reversible addition-fragmentation chain transfer.[1,2]

Atom Transfer Radical Polymerization (ATRP): is a reversible deactivation process. Transition metal compounds, usually copper halides, are employed in combination with a halogen-containing initiator. A ligand L is required to enhance the solubility of the copper salt. The reversible deactivation proceeds via the transfer of a halide radical from the copper complex to the propagating chain.
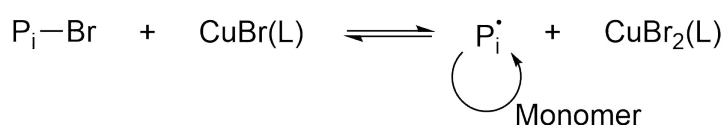
Figure 2.41: Mechanism of the reversible deactivation process in atom transfer radical polymerization (ATRP).[2]

Nitroxide-Mediated Polymerization (NMP): is a reversible deactivation process. An alkoxyamine is introduced into the polymerization and functions as initiator and control agent. Upon heat, the alkoxyamine is homolytically cleaved into an initiating radical and a stable nitroxide radical. The nitroxide radical undergoes reversible deactivation with the propagating radicals. It is also possible to use a conventional initiator in combination with nitroxide radicals.
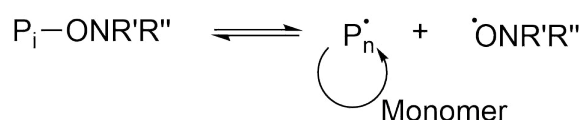
Figure 2.42: Mechanism of reversible deactivation in nitroxide-mediated polymerization (NMP).[2]

Reversible Addition-Fragmentation Chain Transfer (RAFT): is a reversible transfer process. The propagating radicals add to the thiocarbonyl group of a thioester, thereby releasing the R' group as a radical, which itself starts propagating.[2,4]
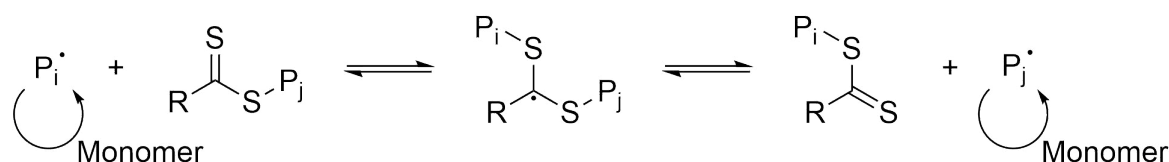
Figure 2.43: Mechanism of reversible transfer in reversible addition-fragmentation chain transfer (RAFT) polymerization.[2]

Polymerizations in MOFs

Termination reactions can also be suppressed by physical methods. The group of Kitagwa from the Kyoto University in Japan applied MOFs in the free radical polymerizations[10] and copolymerizations[105] of various monomers. They observed narrow molecular weight distributions for vinyl monomers,[102,106] and investigated the effect of various pore sizes on polymerizations of standard monomers such as styrene and methyl methacrylate.[103] The strongest effect on the chain growth process was observed in the polymerization of vinyl acetate (VAc). Poly(vinyl acetate) (PVAc) finds application as adhesive for paper, textiles, and wood, as well as water-based paints. It is also the precursor for the preparation of poly(vinyl alcohol). Vinyl alcohol (ethenol) is not stable as it tautomerizes into ethanal fast and can therefore not be readily polymerized.[2,103]

PVAc can be prepared solely by radical procedures. The propagating radicals of VAc tend to fast transfer and termination reactions, which results in a broad distribution with a polydispersity $Đ > 10$ (Figure 2.44). The above presented RDRP procedures are not successful as the radical of the monomer is insufficiently stabilized. The polymerization in Cu-BDC-dabco channels, however, yielded PVAc with a more narrow distribution of $Đ = 1.7$.[103] The group of Kitagawa suggested that the enhanced polymerization control is associated with the entrapping of the propagating chains in the MOF channels. Interactions between individual chains is hindered and termination reactions are reduced. Via electron paramagnetic resonance (ESR) spectroscopy, these authors were able to evidence an increased life time of active radicals in the MOF system. Polystyrene radicals were still detectable after three weeks at 70 °C.[103]

43
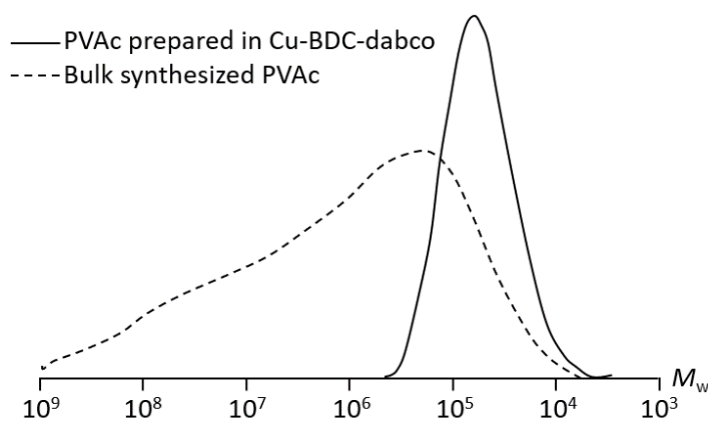
Figure 2.44: SEC profiles of PVAc prepared in Cu-BDC-dabco (solid line) and in the bulk condition (dashed line). The trace of the bulk synthesized PVAc is extremely broad ($Đ > 10$) containing high molecular weight material over the exclusion limit ($M_\mathrm{w} > 5\,000\,000$) of the SEC system. Adapted with permission from Ref. 102. Copyright (2007) American Chemical Society.

2.5.2 Pulsed-Laser Polymerization

Pulsed-laser polymerization (PLP) is a standardized method, developed by IUPAC, to determine the polymerization rate coefficient k_p of radical polymerizations. The procedure of PLP is depicted in Figure 2.45. A solution of monomer with a photoinitiator is irradiated with a laser pulse. The first pulse initiates radical formation at a high concentration ($\sim 10^{-6}\,\mathrm{mol\,L^{-1}}$) and the polymer chains begin to grow. During the dark time after the pulse, a few radical chains will terminate via combination or disproportionation, yet the majority of propagating chains will grow until the second laser pulse hits the sample. The second laser pulse will again initiate radical formation at a high concentration, thereby leading to instant termination of most of the propagating polymer chains.

The number of pulses is preset to result in a conversion of 2-3%, thereby keeping the monomer concentration constant throughout the polymerization process. Via size-exclusion-chromatography (SEC), the polymerization degrees of the polymer chains that grew for one, two or three dark periods can be determined and with that, the polymerization rate coefficient k_p can be deduced.

Usually, free radical polymerization can hardly be stopped at low conversions and low molecular weights, since the propagation of the polymer chains is fast and reaches high molecular weights within seconds. The polymers that result from PLP, however, have molecular weights that are adequate for mass spectrometric analysis (refer to Chapter 2.6).
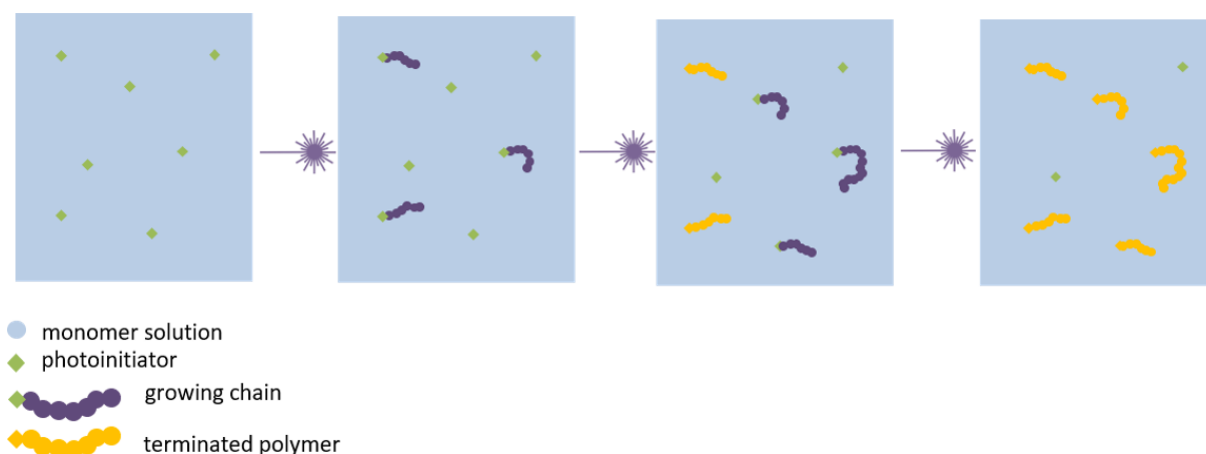
Figure 2.45: Schematic illustration of pulsed-laser polymerization. A monomer solution (blue), which contains initiator (green) is irradiated with a laser pulse that initiates polymerization. The propagating chains (purple) start to grow until a second laser pulse hits the sample. The second laser pulse terminates the growth of most of the chains (orange) and initiates new polymer growth.

2.6 Mass Spectrometry of Polymers

Mass spectrometry is an analytical method with unrivaled detection limits and sensitivity. It is applied in biochemistry, food control, forensic science, reaction physics and kinetics, and process monitoring.[107] The method requires the transfer of the sample into the gasphase while ionizing the molecules. The ionization process usually leads to fragmentation of the molecule into smaller species, which themselves can fragment again, and so on. The molecule fragments are separated according to their mass-to-charge ratio (*m/z*) and are detected in proportion to their abundance. For the analysis of polymers and biomacromolecules, however, the fragmentation process is usually undesired. Thus, new soft ionization techniques were developed, namely electrospray ionization (ESI) and matrix-assisted laser desorption ionization (MALDI).[107,108]

2.6.1 Ionization Techniques

The Matrix-Assisted Laser Desorption Ionization (MALDI)

The MALDI technique was introduced by Karas and Hillenkamp in 1988.[107,109,110] It is a widespread tool for the ionization of large molecules, such as polymers, proteins, and oligonucleotides. The technique impresses by simple sample preparation and has a high tolerance towards additives like salts and buffers.[107,111]

The MALDI process involves two steps. The first step is the introduction of the sample into a matrix, usually by dissolving the sample and the matrix in a volatile solvent
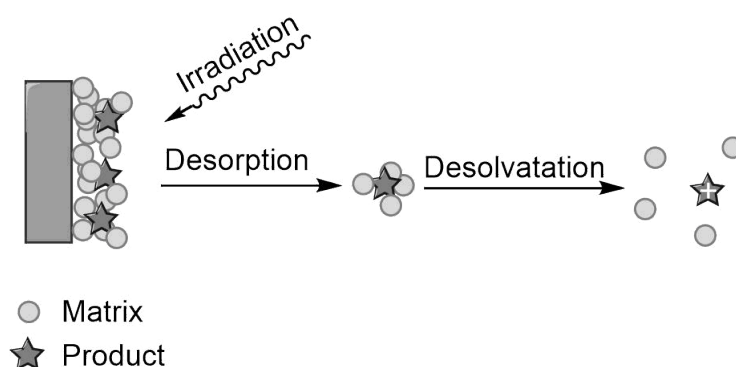
Figure 2.46: Diagram of the principle of MALDI. Adapted with permission from John Wiley and Sons.[107]

with subsequent drying on a substrate. The resulting matrix crystals are doped with the sample molecules in a low concentration to avoid agglomeration of the molecules of interest. In the second step, the substrate is irradiated with strong laser pulses under vacuum (Figure 2.46). The laser induces strong heat and thereby fast, localized sublimation of the matrix crystals. The ionization process during MALDI is not fully understood, yet the most accepted mechanisms involve proton transfer in the solid phase, or gaspase proton transfer from the matrix molecules. The resulting ions are transferred to the analyzer by an electric field.[107]

The Electrospray Ionization (ESI)

The ESI technique was introduced as a protein characterization method by Fenn and coworkers,[112–114] but was later extended to other bio- and synthetic polymers.[107,115] J. B. Fenn was awarded the Nobel Prize for the ESI technique in 2002.[116] The ESI process can be divided into three steps: the nebulization of the sample, the ion release from the droplets, and the detection of the ions.

Nebulization: of a sample solution, resulting in electrically charged droplets. The sample solution is passed trough a capillary tube (1 to $10\,\mu\mathrm{L\,min^{-1}}$) as depicted in Figure 2.47. An electric field is applied between the capillary and a counter-electrode,
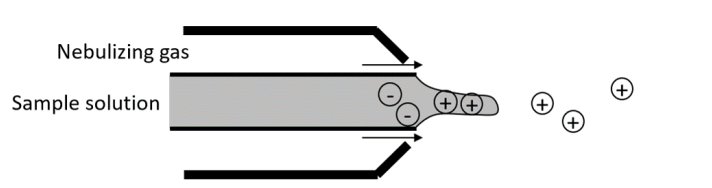
Figure 2.47: Electrospray of a sample solution with assistance by pneumatic nebulization. Reproduced from Ref. 117 with permission from Elsevier.

separated by 0.3-2 cm. The liquid that is located at the end of the capillary will be atomized into highly charged droplets upon the charge accumulation due to the electric field (10^6 V m^{-1}).[118] The onset voltage for droplet formation depends on the solvent and varies between 2 and 6 kV.[107,115,117]

Ion release: When the droplets are released, they are carried through either a heated flux of inert gas, or a heated capillary to induce solvent evaporation. The droplet sizes are reduced due to the evaporation of the solvent, leading to an increase in the charge-to-volume ratio of the droplets. The increased forces on the droplet surface leads to a deformation into a *Taylor* cone, which releases smaller droplets of ~100 nm (Figure 2.48). The volume of the offspring droplets are ca. 2% of the volume of the parent droplet, but they carry 15% of the charge. The droplets will further decrease in size via solvent evaporation, until the electric field on the droplet surface becomes sufficiently strong enough for the ions to desorp from the droplet's surface. Molecules with molecular weights higher than 5000 to 10000 Da do not desorp from the droplet, but are released by the complete evaporation of the solvent.[107,115]
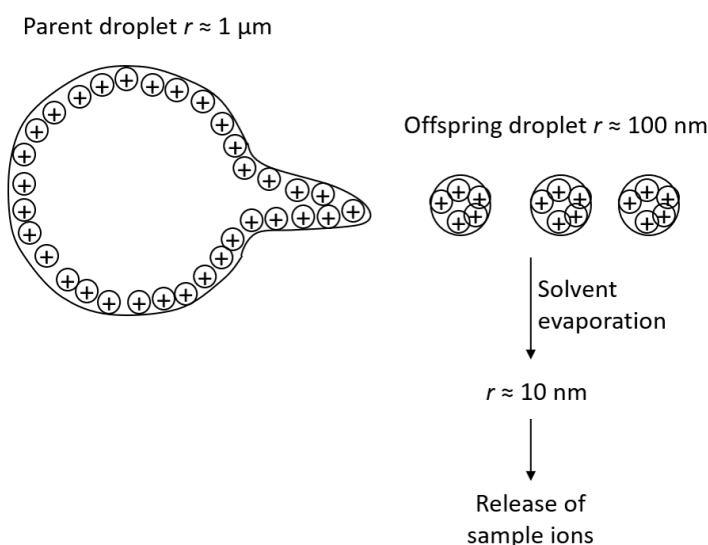
Figure 2.48: Droplet disintegration by release of offspring droplets from a *Taylor* cone at the surface of a parent droplet, followed by size reduction through solvent evaporation, and release of sample ions from a 10 nm radius droplet. Reproduced from Ref. 115 with permission from Elsevier.

The third step in the ESI process is the separation and detection of the ions that can be achieved by several methods, two of which are described in detail below.

2.6.2 Ion Detection

Time-of-Flight

The ions are accelerated into a drift region with defined length. All ions (of the same charge) receive the same kinetic energy E_{kin}. The velocity v of the ions depends on the mass m of each ion according to Equation 2.22.[119]

$$v = \sqrt{\frac{2E_{kin}}{m}} \qquad (2.22)$$

Ions with lower masses will therefore travel faster than the heavier ions. Figure 2.49 displays the basic principle of a time-of-flight (ToF) analyzer. Deviations in the ionization process are corrected by an ion mirror, which reflects the ions into a second drift path towards the detector. The complete flight time is increased without increasing the size of the instrument.[107,119]
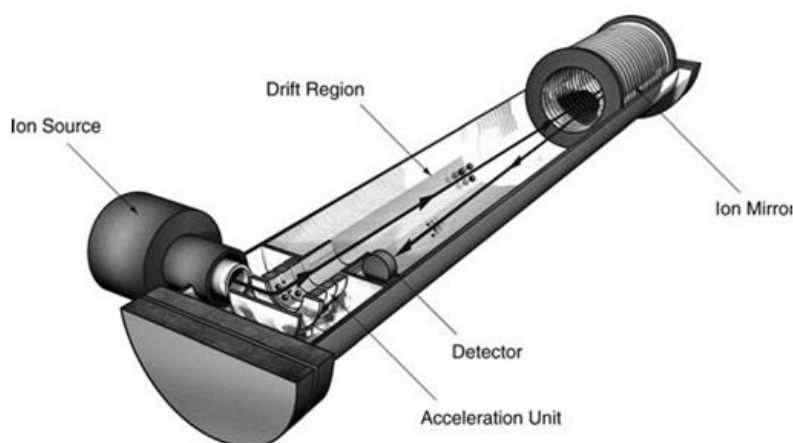
Figure 2.49: Illustration of a time-of-flight analyzer featuring an ion mirror. Reprinted with permission from John Wiley and Sons.[119]

ToF analyzers can be highly sensitive by employing orthogonal acceleration. Ions are collected in the acceleration unit, and released altogether into the drift region. While the ions are seperated along the flight distance, the acceleration unit is again filled with ions. The mass resolving power of ToF analyzers can reach values up to 40000 with a mass accuracy of 5-50 ppm.[119]

Orbitraps

Orbitraps are ion trapping devices that consist of a barrell-like electrode and an inner axial spindle (Figure 2.50). The ions are trapped by a purely electrostatic field that attracts them towards the spindle electrode. The spindle is shaped to balance the electrostatic forces by the centrifugal forces. Thus, the ions orbit around the spindle while harmonically oscillating. The frequency of the oscillation depends on the mass of the ions:[119]

$$f \sim \sqrt{\frac{m}{z}} \qquad (2.23)$$

On the one hand, orbitraps can reach a mass resolving power of up to 150 000 and a mass accurancy of 2-5 ppm, thereby exceeding the resolving powers of ToF analyzers. On the other hand, the mass range that can be detected is 6000 to 8000 , which is far lower than for ToF-analyzers (> 100 000).[119]
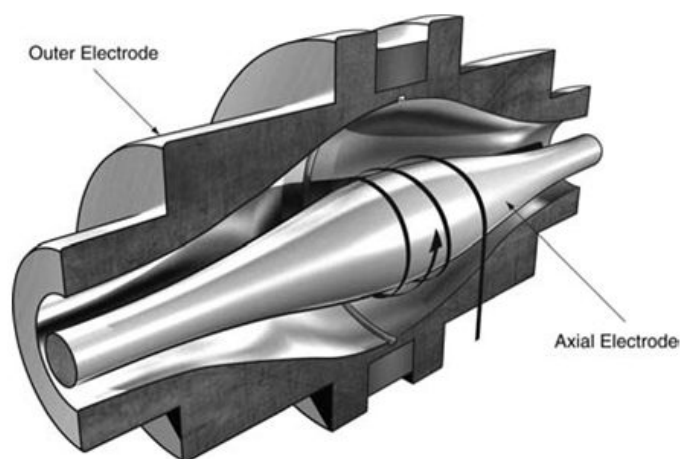
Figure 2.50: Illustration of an orbitrap mass analyzer. The black arrow represents an ion path. Reprinted with permission from John Wiley and Sons.[119]

2.7 Surface Characterization

2.7.1 X-ray Diffraction

Crystalline surfaces and surface coatings can be analyzed via X-ray diffraction (XRD). X-rays are diffracted at atomic electron shells. If the atoms are aligned in a crystal structure, the X-rays are reflected in the lattice distance d (Figure 2.51). The reflected rays
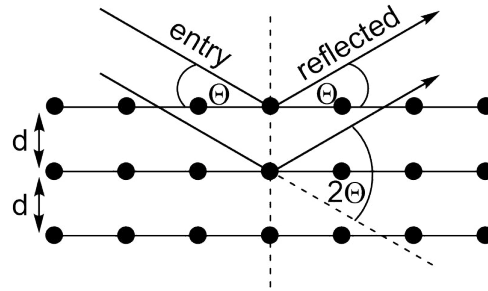
Figure 2.51: Diffraction of X-rays on the lattice of a crystal structure.[120]

from various crystal layers interfer with each other and result in addition or extinction of the reflected rays. The *Bragg* equation (Equation 2.24) describes the geometric association between d and the wavelength λ of the X-rays. The angle of reflection is equal to the angle of entry Θ.[120]

$$2d \sin \Theta = n\lambda \tag{2.24}$$

The intensity of the reflected radiation depends on the form factor of the crystal structure. The form factor describes the relationship between the atom position and the crystal structure and is the *Fourier* transformation of the electron density distribution in a unit cell. For detailed information, the reader is referred to literature about crystal structure characterization.[120,121]

Via the form factor, the addition and cancellation of the reflexes can be predicted. Table 2.3 lists the reflection conditions for non-cancellation for various lattice types.

With the reflection conditions, changes in crystal structures, e.g. due to shape changes or loading as in the case of porous materials, the resulting X-ray diffractogram can be

Table 2.3: Reflection conditions for the reflexes (hkl) in various lattices.[120]

Lattice type	Reflection condition
Primitive	all present
Body-centered	$h+k+l = 2n$
Face-centered	$h+k = 2n$ $k+l = 2n$ $h+l = 2n$
[100] faces centered	$k+l = 2n$
[010] faces centered	$h+l = 2n$
[001] faces centered	$h+k = 2n$

predicted. For example, a primitive lattice shows all reflexes, as there is no extinction. If a guest is introduced into the lattice, leading to a body-centered structure, the sum of h, k and l requires to be even, i.e. the (001), (010) and (100) reflexes are extinguished.

2.7.2 Quartz Crystal Microblance

Quartz crystal microbalances (QCM) are based on the inverse piezoelectric effect, i.e. the application of voltage on certain crystalline materials results in deformation and oscillatory motion of the crystals. A standing wave can be generated if the applied voltage matches the resonance frequency of the crystal. In the case of QCM, the crystal vibrates in the thickness-shear mode, i.e., the opposite surfaces of the crystal oscillate in an antiparallel fashion (Figure 2.52).[122]

QCMs can be run in two modes. One is the impendance analysis, where the polarization at the crystal's surface is observed as a function of the frequency of the voltage. The second is QCM-D, where the voltage is turned off and the oscillations of the crystals decay freely. The decaying oscillations produce voltage by the normal piezoelectric effect, which allows to record two parameters per overtone: the frequency f_n and the dissipation D_n. If the mass on the crystal surface is changed, the frequency of the oscillating crystal is changed according to Equation 2.25.[122]

$$\Delta f_n = -\frac{n}{C} m_f \tag{2.25}$$

m_f: mass per unit area of the absorbed film

C: mass sensitivity constant

Thus, the frequency of the quartz crystal depends on the absorbed mass on its surface. The mass sensitivity constant C depends on the fundamental resonance frequenzy f_F of the crystal.[122]
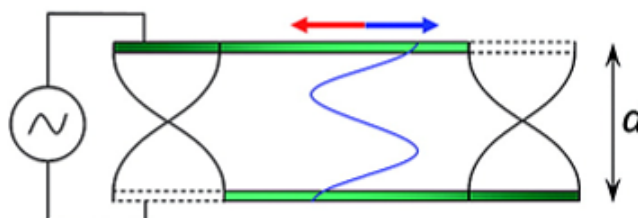
Figure 2.52: Side view of a quartz crystal in QCM. The application of voltage results in antiparallel deformation of the top and bottom surface. The fundamental frequency (black wave) and the third overtone (blue) are depicted. The amplitudes of the waves are in the order of a couple of nanometres. Reprinted with permission from Ref. 122. Copyright (2011) American Chemical Society.
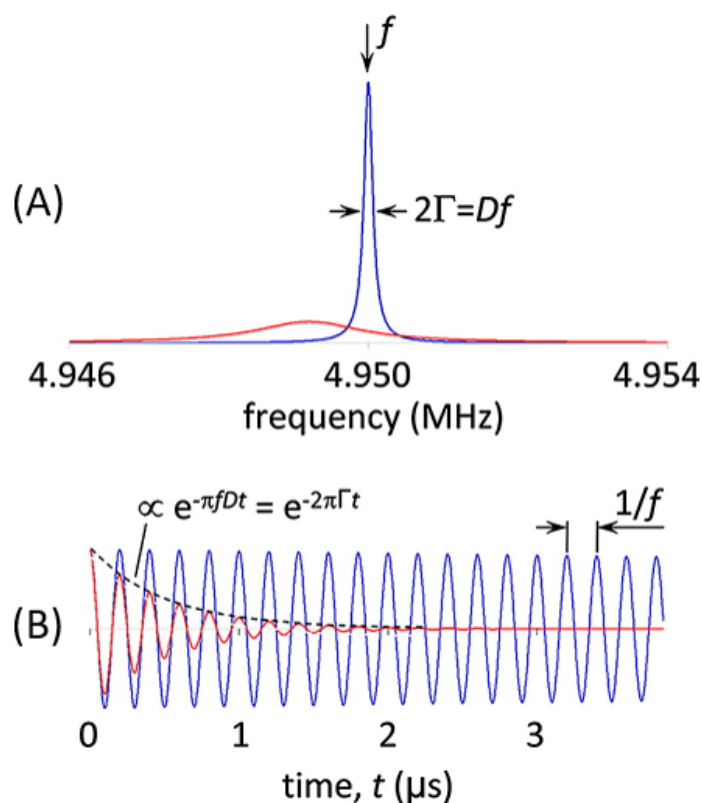
Figure 2.53: Decay curves of quartz crystals in QCM-D mode. The two curves illustrate crystals with low dissipation (blue) and with high dissipation (red) after (A) and before (B) Fourier transformation. The frequency f and the dissipation D, as well as the line width Γ can be determined. Reprinted with permission from Ref. 122. Copyright (2011) American Chemical Society.

QCMs are widely popular, because they work in liquids and enable *in situ* observation of the processes on surfaces.[122]

2.7.3 Secondary Ion Mass Spectrometry

Time of flight-secondary ion mass spectrometry (ToF-SIMS) is a powerful spatially resolving surface characterization method. SIMS describes the soft impact of primary ions on a sample *in vacuo* ($\sim 10^{-9}$ bar) which generates neutral and charged secondary species (Figure 2.54). The charged species are accelerated to the ToF analyzer, resulting in a high mass resolution of $>10\,000$. The lateral resolution of the ion maps can be as precise as $100\,\mathrm{nm}$.[123,124]

Various materials can generate sufficient primary ions for the bombardement of sample surfaces. The main primary ion beam is a liquid metal ion gun. Various metals have been employed over the last decades, e.g. gallium and gold, but the bismuth ion gun dominates nowadays.[125,126]
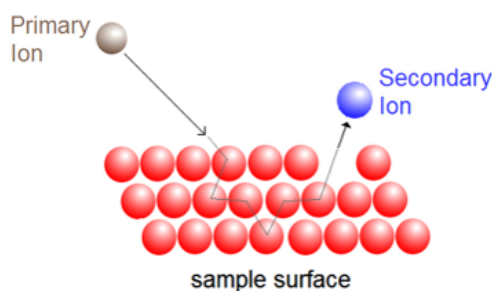
Figure 2.54: Schematic representation of the collision of a primary ion (grey) with a sample surface (red). Energy is transferred onto the surface and distributed through several atoms (grey lines) until a secondary ion (blue) is ejected. Reprinted with permission from Ref. 124. Copyright (2015) IOP Publishing.

For the analysis of biomolecules and organic molecules instead, large cluster ion beams are used. Here, charged particles of up to several hundreds atoms are emitted and upon impact with the surface, the kinetic energy of the ion clusters is distributed onto a large number of atoms, thereby reducing the impact energy per single atom. One of the first cluster ion guns with minimum destructive impact is the C_{60}^+ ion gun.[124]

The development of an Ar_n^+ cluster ion source enhanced the depth profiling of biological and polymeric materials. Since the gas ion clusters are large ($500 \leq n \leq 2500$), the destructive impact on the sample surface is even lower than for C_{60}^+.[124,127]

The basic components of a ToF-SIMS instrument are depicted in Figure 2.55. The sample is placed beneath the ToF analyzer and can be scanned with several ion sources, depending on the sample material and the required information. ToF-SIMS not only produces mass spectra from the surface, which can be translated into ion maps, it also allows the depth-profiling by sputtering, in which selected species and their intensities can be observed throughout the sputtering. Moreover, the combination of depth-profiling and ion maps enables the production of 3D maps of the analyzed volume.[124]

The instrument can be run in various modes, depending on the mass and spatial resolution required:[128]

Bunched mode: Short pulses ($\sim$600 ps) of a large number of primary ions ($\sim$2000) is employed to obtain high mass resolution. The spatial resolution, however, is reduced to 2 to 5 μm.

Burst alignment mode: A smaller number of ions ($\leq$ 600) is applied in longer pulses (20-100 ps), which results in an enhanced spatial resolution ($\sim$200 nm).
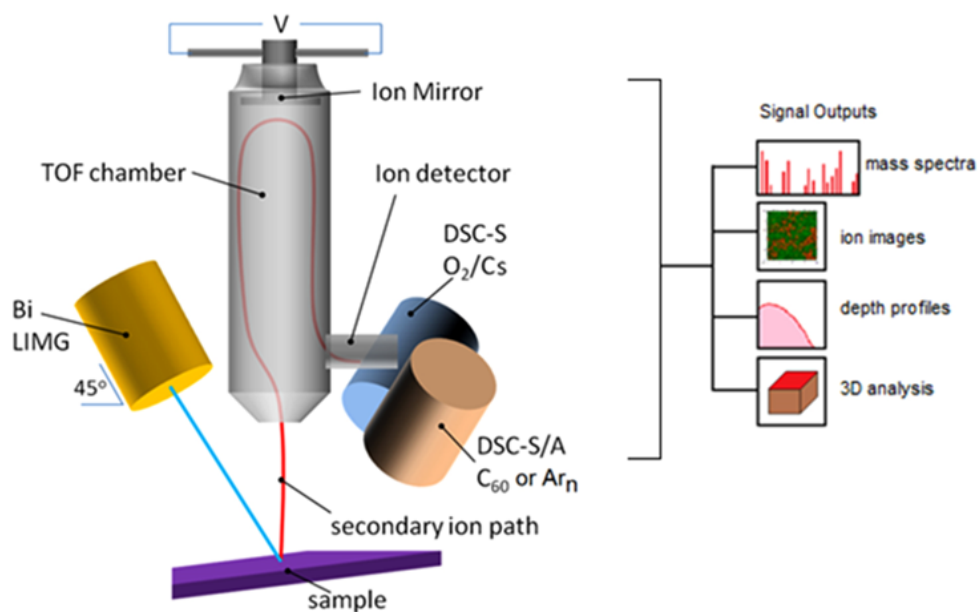
Figure 2.55: Schematic depiction of the main components of a time of flight-secondary ion mass spectrometre. Reprinted from Ref. 124. Copyright (2015) IOP Publishing.

Collimated mode: The spatial resolution is further increased ($\sim$100 nm) by reducing the number of primary ions (≤ 35).

In the current thesis, ToF-SIMS is employed for the analysis of the loading and the functionalization of SURMOFs via ion maps and depth-profiling.

<div align="right">CHAPTER 3</div>

Light-Induced Free Radical Polymerization in SURMOFs
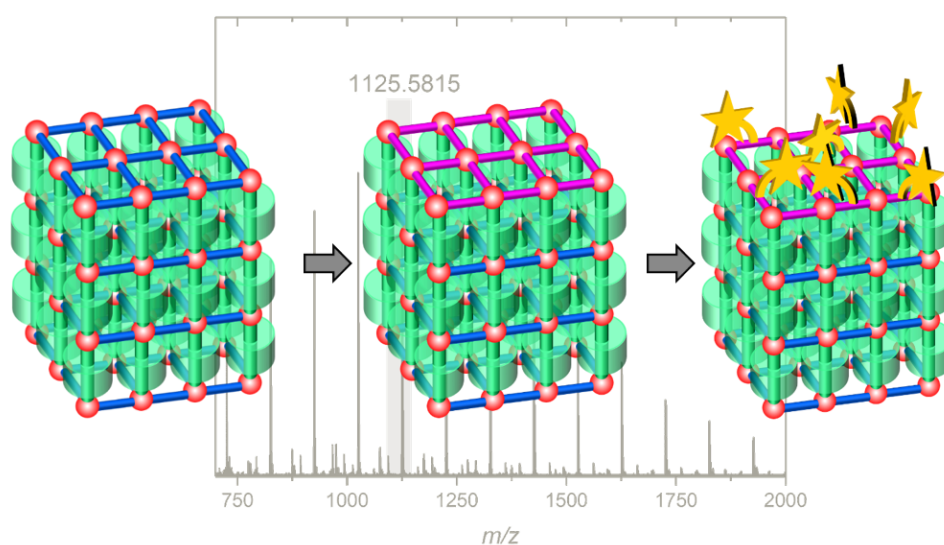
In the last decade, MOFs were introduced as templates for chain growth polymerization with major contributions by the group of Kitagawa and Uemura from Kyoto University, Japan.[10] These researchers employed free radical polymerization[102,103,106,129] and copolymerization[105] inside the channels of MOF structures, observing that the trapping of propagating chains in confined environments results in enhanced reaction control and

---

S. Hurrle designed and conducted the experiments unless otherwise stated. The SURMOFs were prepared and functionalized, as well as analyzed in QCM-D, in a cooperation with Z. Wang. ToF-SIMS characterization was performed and evaluated by S. O. Steinmüller and A. Welle. H. Gliemann, A. S. Goldmann, C. Barner-Kowollik and C. Wöll motivated and supervised the project.

narrow molecular weight distributions. Successful polymerizations were achieved by simply immersing the MOF powder in monomer/initiator solutions and, after removing excesses of monomer under low pressure, heating the powders to specific temperatures depending on the monomers employed. The conversions of the polymerizations were determined by thermogravimetrical analysis (TGA). During the TGA, residual monomer is released at higher temperatures and thereby allows the determination of the polymer conversion. So far, light-induced polymerization in MOFs was not investigated.

The goal of the project is the extension of MOF polymerization to SURMOFs. The layer-by-layer approach for the preparation of SURMOFs allows the adjustment of the thickness of the template homogeneously. Furthermore, specific functionalities can be introduced into the structure in the desired layers. Powder MOFs, on the other side, possess a distribution of particle sizes and the initiator is randomly distributed in the structure, thus leading to a variety of channel lengths for polymerization.

In the approach followed in the current thesis, a functional linker is introduced into SURMOFs[25,130] (Step 1, Figure 3.1) via layer-by-layer preparation. A photoinitiator is attached to the structure via PSM (Step 2),[9,88,90,131] resulting in a SURMOF as template for light-induced radical polymerizations. The implementation of a photoinitiator
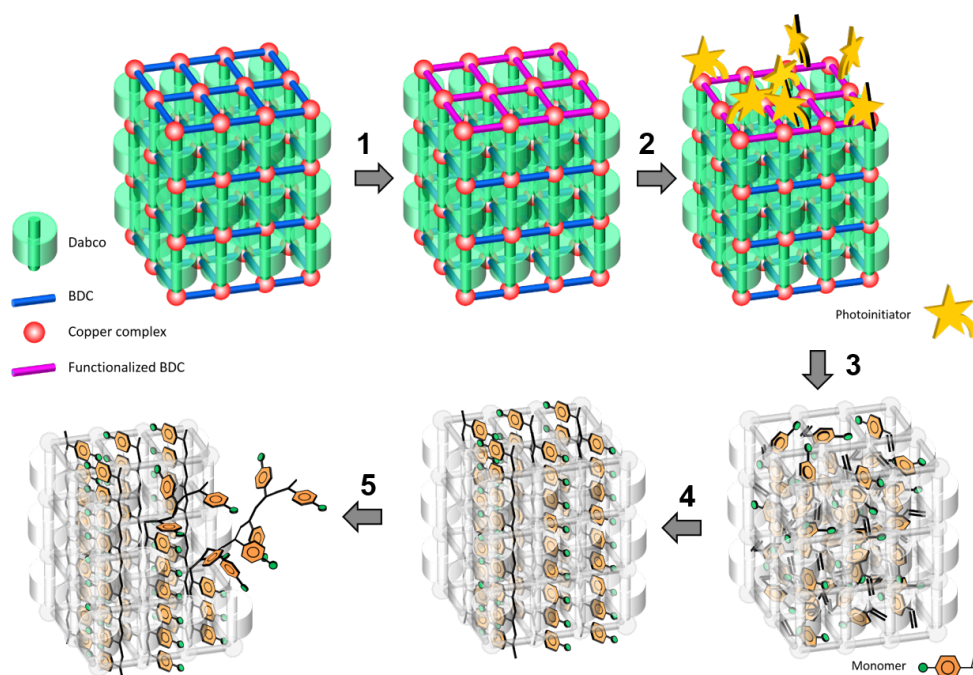
Figure 3.1: Schematic representation of polymerizations in Cu-BDC-dabco SURMOFs. *1)* Introduction of a functional azide linker (pink) into the SURMOF structure; *2)* Post-synthetic functionalization via azide-alkyne cycloaddition with an alkyne-photoinitiator (yellow); *3)* Loading of the SURMOF structure with monomer; *4)* Polymerization under UV-light irradiation and monitoring via quartz crystal microbalance; *5)* Dissolving of the SURMOF with EDTA solution and analysis of the polymer via mass spectrometry.

into the SURMOF structure offers the possibility to equip SURMOFs with polymers in specific areas by photo-patterning.[132–134]

The functional linker that is introduced in Step 2, Figure 3.1, contains an azide group which is capable of undergoing azide-alkyne cycloaddition. In fact, the successful functionalization of SURMOFs with similar structure motifs has been developed in the group of C. Wöll, and has been exploited for the preparation of SURGEL thin films and capsules.[20,135,136] By employing ring-strained cyclooctynes or alkynes with strong electron-withdrawing groups, the reactions were performed at ambient temperature without additional copper catalysts.[45,137] Thus, a photoinitiator that can be employed in azide-alkyne cycloaddition at ambient temperature for the functionalization of SURMOFs was developed. Furthermore, the successful characterization of the SURMOF with the implemented photoinitiator via ToF-SIMS was investigated for the potential interlatice polymerization within SURMOFs.

The SURMOFs that can be grown in the layer-by-layer fashion are mainly Zn- and Cu-based. Among those, the Cu-MOFs are the most consistent in growth and crystallinity. Furthermore, they show higher stability against humidity than the Zn-MOFs.[138] Respectively, Cu-BPDC and Cu-BDC-dabco were employed in the polymerization studies.

In addition, a mass spectrometry study is required for the detection of small traces of polymer since the amount of polymer that can be received via SURMOF polymerization is not sufficient for NMR spectroscopy or SEC analysis. In fact, mass spectrometry can also provide an insight into the initiation and termination process of the SURMOF polymerization. As it is not expected for propagating chains to accumulate inside the channels, termination by combination reactions should play a minor role in the polymer structure. However, understanding the termination procedures in SURMOF polymerization is crucial for the development of highly controlled polymerizations in MOFs, or efficient preparation of polymerMOF hybrid materials.[139,140]

3.1 Investigating the Lower Limits of the Mass Spectrometric Analysis of PMMA Traces

The polymerization in SURMOFs entails the challenge of analyzing the resulting polymer. In previous work by the Kitagawa team, the polymerization was performed in MOF powders and thus, the amount of powder can be easily adjusted, allowing to yield amounts of polymer that is sufficient for the analysis via SEC (2 mg).[103] SURMOFs,

however, are limited to the substrate to which they are attached and cannot be easily weighed and up-scaled. Kitagawa and colleagues calculated the size and space requirement for styrene in standard MOF systems[10] and stated that styrene can be assumed with a length of $l_{St} = 4.4\,\text{Å}$. Subsequently, the essential calculation for the maximum yield of polystyrene that can be expect from the polymerization in Cu-BDC-dabco SURMOF will be explained.

The substrate has an area of $A = 1\,\text{cm}^2$ and Cu-BDC-dabco has en elementary cell of $a = 10.803\,\text{Å}$ and $b = 9.481\,\text{Å}$. The SURMOF thickness was set to $D = 40\,\text{nm}$. The number of styrene molecules per cell $N_{St,cell}$ is given by Equation 3.1.

$$N_{St,cell} = \frac{a}{l_{St}} = 2.46 \tag{3.1}$$

The number of cells in the system depends on the substrate area A and the thickness of the SURMOF D, and is calculated by Equation 3.2.

$$N_{cell} = \frac{V_{MOF}}{V_{cell}} = \frac{A \times D}{a^2 \times b} = 3.615 \times 10^{15} \tag{3.2}$$

V_{MOF}: Volume of the SURMOF structure
V_{cell}: Volume of one unit cell

If all the monomer that can fit into the channels is converted into polymer, the maximum amount of polymer that can be expected is calculated by Equation 3.4

$$n_{St} = \frac{N_{cell} \times N_{St,cell}}{N_A} = 1.47 \times 10^{-8}\,\text{mol} \tag{3.3}$$

$$m_{poly} = n_{St} \times M_{St} = 1.53\,\mu\text{m} \tag{3.4}$$

The resulting maximum amount of polymer that results from the polymerization in Cu-BDC-dabco is ca. $1.5\,\mu\text{g}\,\text{cm}^{-2}$. Thus, the polymerization can neither be characterized via NMR nor SEC, as higher amounts of material are required for an adequate analysis (several mg). On the other hand, analyzing small amounts of polymeric material can be realized via mass spectrometry and thereby evidence successful polymerization processes in the SURMOF approach. Quantitative molecular weight distributions and polydispersities cannot be accessed via ESI-MS, however, the proof-of-principle of the SURMOF polymerization process is crucial before up-scaling can be realized. Therefore, a PMMA SEC calibration sample was employed in the following mass spectrometry study ($M_n = 1720\,\text{g}\,\text{mol}^{-1}$, $M_w = 1960\,\text{g}\,\text{mol}^{-1}$, $Đ < 1.15$). A stock solution of

PMMA in sodium-doped THF/MeOH analyte was diluted to obtain concentrations of $c = 100$, 10 and $1\,\mathrm{ng\,mL^{-1}}$. The solutions were introduced via direct-infusion into the ESI-MS system and analyzed for a prolonged scan time of 10 min. The long scan time provides a higher possibility to detect traces of PMMA, as all scans are coadded to provide a mass spectrum.

The mass spectrum of PMMA was first recorded under standard conditions with a concentration of $c = 1\,\mathrm{\mu g\,mL^{-1}}$ with a capillary temperature of $T = 320\,^\circ\mathrm{C}$ and a spray voltage of $V = 4.85\,\mathrm{kV}$. The spectrum (Figure 3.2) allows to clearly identify the polymer, including the repeating unit of ca. 100.05 Da as well as the highest intensity for the polymer chains with $m/z = 1125.58$ Da. The area of 1125 to 1129 Da will therefore be the focus of the following dilution experiments. The first parameter that was adapted for
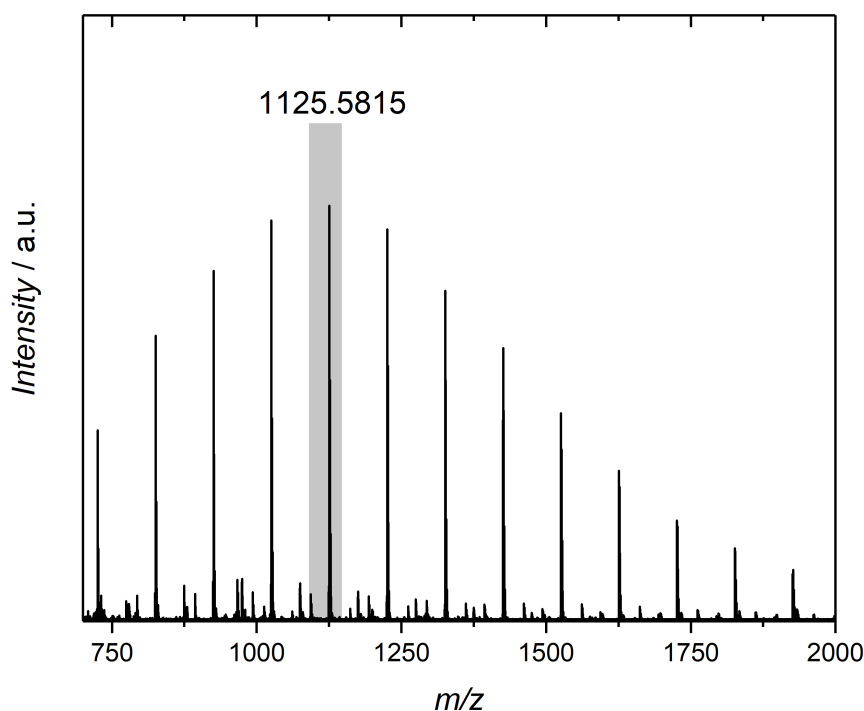
Figure 3.2: ESI mass spectrum of PMMA standard ($M_\mathrm{n} = 1720\,\mathrm{g\,mol^{-1}}$, $M_\mathrm{w} = 1960\,\mathrm{g\,mol^{-1}}$).

the analysis of small traces of PMMA was the capillary temperature T. The temperature was varied from 280 to $330\,^\circ\mathrm{C}$ in steps of $10\,^\circ\mathrm{C}$. The resulting mass spectra are collated in Figures C.1 and C.2 (page 145) for $c = 100$ and $10\,\mathrm{ng\,mL^{-1}}$, respectively. For a concentration of $c = 100\,\mathrm{ng\,mL^{-1}}$, one can observe that the intensity of the observed isotopic pattern increases with increasing T. However, the lower concentration of $c =$

$10\,\mathrm{ng\,mL^{-1}}$ does not follow the above observed trend and the intensities appear to be constant or slightly decrease. The intensity of the structures appears to be independent of the capillary temperature. At a concentration of $1\,\mathrm{ng\,mL^{-1}}$, there is no specific isotopic pattern distinguishable from the background species (Figure 3.3).

The second parameter that was varied for an enhanced ionization was the spray voltage. The spray voltage can have a major impact on the droplet charging in the spraying process (see Chapter 2.6.1). As a doped eluent is employed in the current experiment, higher spray voltages might be required to overcome the hindrance of droplet charging.[115] During the evaporation of the solvent of the droplets, the droplet charge is reduced by the release of ions from the droplet into the mass spectrometer. The abundance of analyte ions reaching the mass detector depends on the amount of charge on the droplets and the sensitivity of the analyte towards ionization. Hence, the spray voltage of the spray nozzle in the ESI-MS system was varied from $V = 5.0$ to $5.6\,\mathrm{kV}$, in order to enhance droplet charging and thereby increase the number of PMMA ions that could be detected in the mass spectrometer.
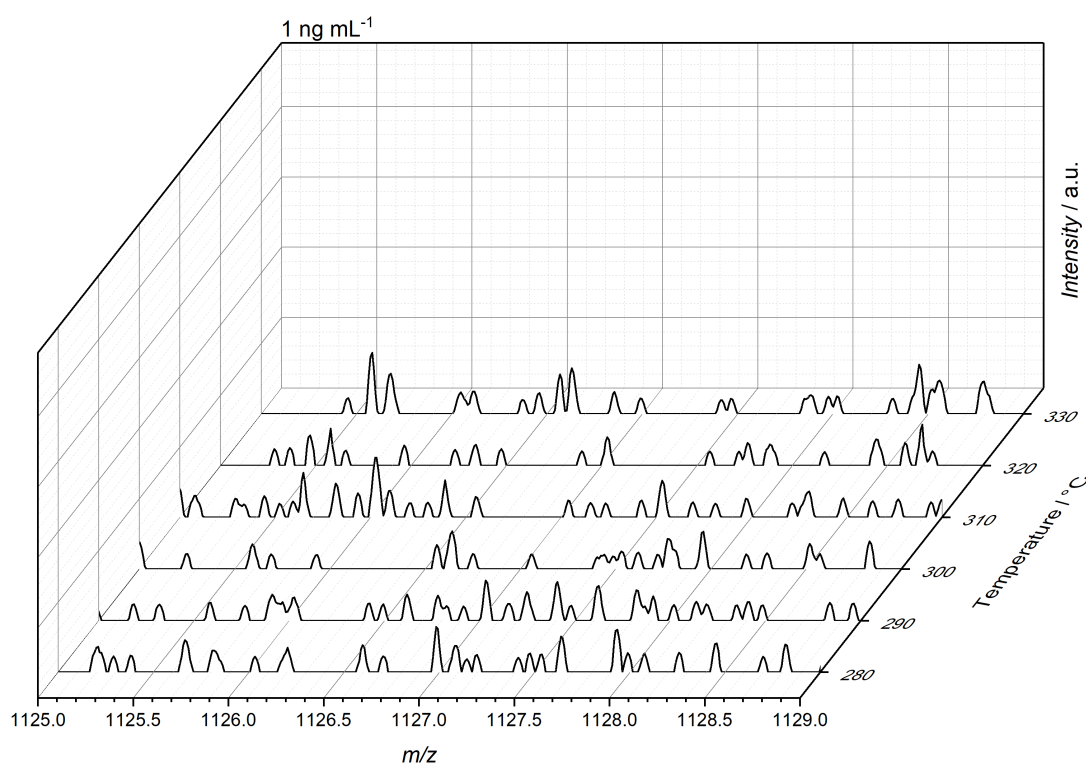
Figure 3.3: ESI mass spectra of a PMMA standard with a $c = 1\,\mathrm{ng\,mL^{-1}}$, analyzed with various capillary temperatures. Isotopic patterns cannot be distinguished.
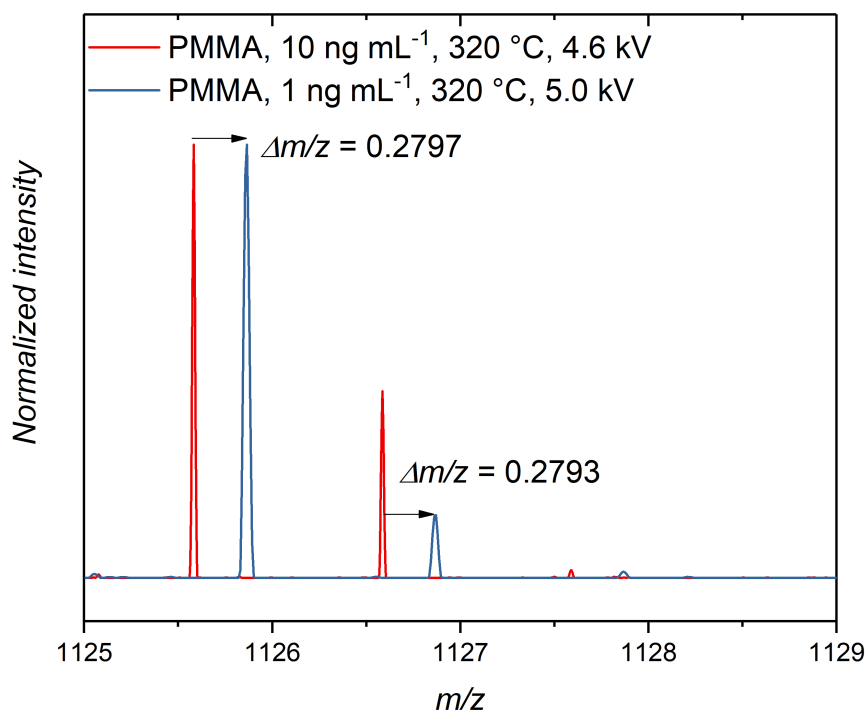
Figure 3.4: ESI mass spectra of PMMA with $c = 10 \, \mathrm{ng \, mL^{-1}}$ under standard conditions (red), and $c = 1 \, \mathrm{ng \, mL^{-1}}$ and a spray voltage of $V = 5.0 \, \mathrm{kV}$ (blue).

Increasing the spray voltage from the standard setting of 4.6 to 5.0 kV, resulted in the appearance of an isotopic pattern in the range of m/z = 1125 to 1129 Da as depicted in Figure 3.4. However, the pattern cannot be attributed to PMMA as the difference $\Delta m/z$ is approximately 0.279 Da, and thus, the pattern belongs to a background species. The capillary temperature was similarly varied in the same temperature range as mentioned above, yet, the isotopic pattern for PMMA is not detectable (Figure C.3, page 147).

Spray voltages of V = 5.4 and 5.6 kV (Figures C.5 and C.6, pages 149 and 150) did not enhance the ionization of PMMA and the polymer was not detected.

The ESI-MS system can detect PMMA in the range of the hypothetical yield of polymer in the μg range. The resulting material after polymerization in SURMOFs can be dissolved in a minimum of 50 μL of doped solvent to perform the characterization at the highest possible concentration.

3.2 Monomer-Loading in SURMOF Channels

One significant difference in MOFs and SURMOFs is the analytical opportunities. For powder MOFs, thermogravimetrical analysis (TGA) can be employed to determine the successful loading and the conversion of the polymerization. For the surface-anchored MOFs, however, TGA analysis is not applicable. Albeit, if a monomer with high eletron-density elements (e.g., bromine groups) is used, the loading can be determined by XRD as there will be a change in the reflexes that arises due to a form factor change. The form factor change will lead to a decrease in the [001] reflex, therefore influencing the ratio between [001] and [002] reflexes. Bromostyrene as monomer fulfills the criterium of carrying a high electron density element in the form of the bromine. For diffusion experiments, Cu-BPDC SURMOFs were prepared by the automatic spray method (refer to Chapter 2.4.2, page 30) on MHDA-functionalized surfaces, despite the channels' trend in horizontal instead of vertical orientation. The spray method provides a fast preparation with high crystallinity, which cannot be achieved as readily with Cu-BPDC-dabco. The pore size was chosen for simple and unhindered diffusion into the pores. The Cu-BPDC system thus provides suitable conditions for proof-of-principle experiments for the monomer loading.

The SURMOF sample was activated overnight at $60\,°C$ under vacuum (Figure 3.5), and was subsequently immersed into a degassed bromostyrene solution that contained benzoin as the photoinitiator. After 30 min, the sample was analyzed via XRD, however, no change in the reflexes' intensities can be detected. The monomer appears to diffuse fast from the SURMOF at ambient pressure, which does not correlate with the polymerization procedure in MOF powders that even involves low pressures to remove excesses of monomer.[103] The experiment was respectively changed to a gasloading approach. For this purpose, a THF solution of benzoin was added to the activated SURMOF under an Ar atmosphere for 10 min. After the sample was dried under vaccum, it was exposed to a constant stream of Ar/monomer by bubbling Ar through the bulk monomer solution as depicted in Figure 3.5. After 10 min of gas flow, the valve of the flask was closed and the sample was irradiated for 24 h with $\lambda_{max} = 366$ nm.

As can be seen in Figure 3.6, the change in form factor is clearly visible. The [001] reflex decreases strongly and one can therefore assume that a reaction between the monomers took place as the monomer itself rather diffuses from the structure. Poly(bromostyrene), however, cannot be easily detected via mass spectrometry. The

---

The preparation of SURMOFs by the spray method, and the loading and polymerization experiments with bromo styrene have been described in the Master thesis of S. Hurrle.[141]
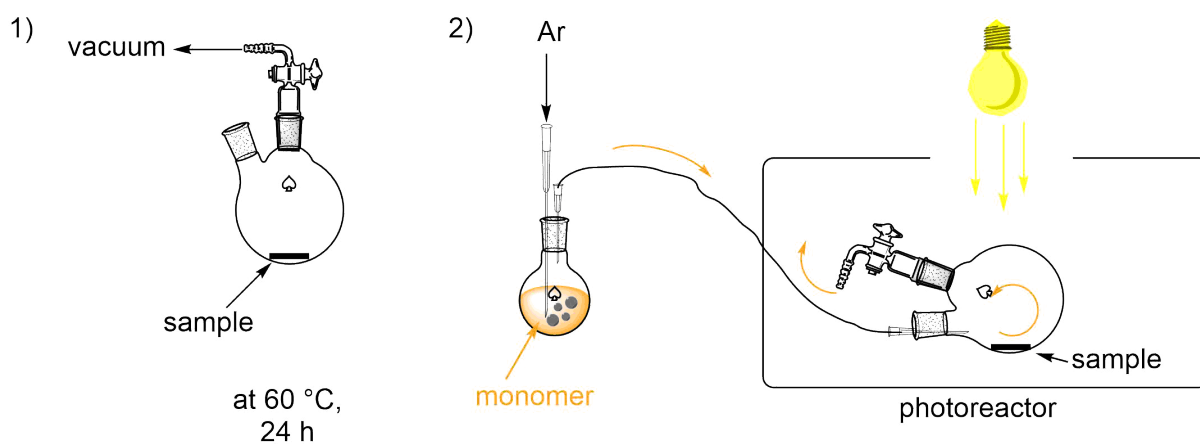
Figure 3.5: 1) Activation of SURMOF samples at 60 °C under vacuum. 2) Light-induced polymerization by gas phase-loading. The monomer is transferred into the flask with the sample by bubbling Ar through the bulk monomer. The flask with the sample is placed into a photoreactor and irradiated with $\lambda_{max} = 366$ nm.
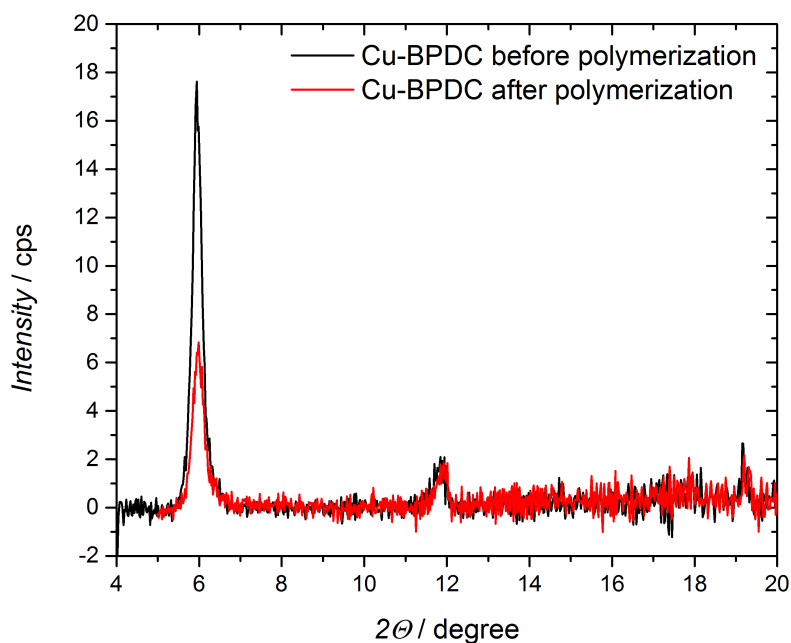
Figure 3.6: X-ray diffractogram of Cu-BPDC SURMOF before (black) and after (red) photopolymerization of bromostyrene inside the channels. The SURMOF was first loaded with benzoin in THF and subsequently loaded with the monomer via the gas phase. The sample was irradiated for 24 h with $\lambda = 366$ nm.

Br^- isotopes can be successfully detected via ToF-SIMS imaging (refer to Figure C.7, page 151), yet, the structure of the polymer is not fully characterizable via ToF-SIMS, as the polymer chains are fragmented during the ionization process. The gas phase approach was therefore repeated with MMA and the SURMOF dissolved in aqueous

EDTA solution. The MOF solution was extracted carefully with THF and subsequently the solvent evaporated under air. The residue, not visible to the naked eye, was dissolved in sodium-doped THF/MeOH solution and analyzed via ESI-MS. Unfortunately, PMMA was not detectable. As the diffusion of the initiator into the SURMOF structure proceeds with low control, the amount and the respective distribution of the initiator cannot be predicted. The radicals may be terminated fast during the initiation and, moreover, the distance between initiator molecules may not be sufficient for a successful polymerization.

In conclusion, the diffusion approach of Kitagawa is not applicable to SURMOFs, and the monomer requires to be loaded into the structure via the gas phase. Hence, the initiator has to be introduced into the SURMOF structure prior to polymerization in a controlled fashion. Therefore, it is essential to develop a functional photoinitiator, not only for an enhanced polymerization control, but also for a successful polymerization inside SURMOFs.

3.3 Design of a Functional Photoinitiator

The functional photoinitiator should be suitable for ring-strain promoted azide-alkyne cycloaddition.[137,142] By introducing electron-withdrawing groups to an alkyne moiety, the similar effect as ring-strain for cyclooctynes can be achieved and the cycloaddition can be triggered without an additional catalyst.[20] The designed initiator **PI-alkyne 1** consists of a photoinitiator unit, namely **Irgacure2959**, and a terminal triple bond with an adjacent ester group (see Table 3.1) that has an electron-withdrawing effect on the triple bond.

Table 3.1 shows the reaction conditions that were employed for the esterification between **Irgacure2959** and propiolic acid. Unfortunately, all procedures were unsuccessful and resulted in either no product formation, or many side products were observed in NMR spectroscopy that hindered a successful purification. Table 3.1, entries 1 and 2 describe esterifications under *Steglich* conditions with carbodiimides and *N,N*-dimethylpyridin-4-amin (DMAP) as catalysts. Both reactions did not result in any product formation (refer to Figures C.9 and C.10, page 152). The introduction of an alternative leaving group, namely CDI (1,1'-carbonyldiimidazole, Table 3.1, Entry 3), did also not yield any product (see Figure 3.7). Moreover, employing trimethylsilyl-protected propiolic acid (Table 3.1, Entry 4) did not yield the intermediate active ester in the first place.

Table 3.1: Esterification conditions of the synthesis of **PI-alkyne 1**.
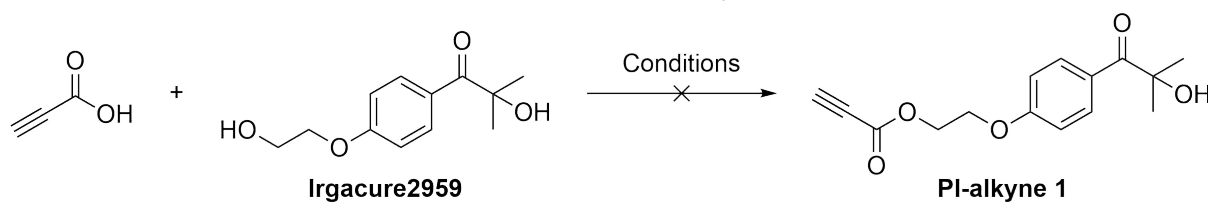
Entry	Catalyst	Base	Solvent	Temperature	t [h]
1	DCC	DMAP	DCM	a.t.	16
2	EDC	DMAP	DCM	a.t.	16
3	CDI	TEA	THF	a.t.	48
4[*]	CDI	-[a]	THF	a.t.	-[a]
5	pTsOH	-	toluene	reflux	16
6	PPh$_3$	DIAD	THF	a.t.	24

[*] TMS-protected propiolic acid was employed as reactant.
[a] Formation of active ester was not successful. Thus, the esterification reaction was not conducted.

Entry 5 in Table 3.1 describes an acid-catalyzed approach which indeed resulted in product formation when an excess of propiolic acid was employed. Via mass spectrometry of the crude product (refer to Figure C.14), the functional initiator was detected, however, the bifunctionalized photoinitiator was also observed. After the purification with column chromatography, analysis via NMR spectroscopy (refer to Figure C.13, page 154) revealed that the bifunctional product is present with ca. 20 mol%. The resonance of the terminal alkyne proton in the bifunctional product is slightly shifted by 0.1 ppm. For surface functionalization, the amount of impurity is too high. Further-
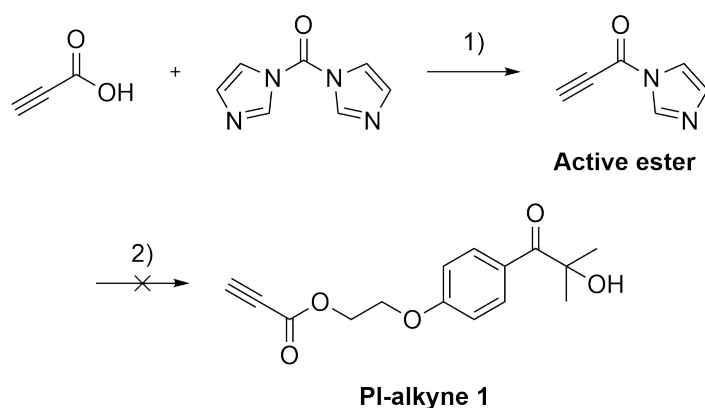
Figure 3.7: CDI esterification for the synthesis of **PI-alkyne 1**. *1) THF, a.t., 40 min; 2) THF, a.t., 48 h.*

more, with regard to successful polymerizations, the functionalization of the tertiary alcohol has an impact on the initiation efficiency of **PI-alkyne 1**. For clear kinetic studies and mass spectrometric analysis of the polymers retrieved from SURMOFs, the initiator must provide a high degree of purity.

As the mono- and bifunctional photoinitiators were not separable, *Mitsunobu* conditions (Entry 6, Table 3.1) were applied for the esterification. The *Mitsunobu* esterification allows the functionalization of primary and secondary alcohols. Tertiary alcohols are not affected, hence, the purification of the resulted product should result in pure monofunctionalized initiator. ^{1}H NMR spectroscopy of the crude product, however, suggests the existence of side products.[143] The ^{1}H NMR spectrum is depicted in Figure 3.8 and, in fact, the resonance of the methyl groups is shifted from 1.63 ppm to 1.43 and 1.26 ppm, indicating that the environment of the methyl groups has changed. Furthermore, additional resonances are detected between 4.8 and 5.4 ppm which can be attributed to olefinic protons. Thus, the photoinitiator **PI-alkyne 1** appears to be highly sensitive to the addition reaction between the terminal triple bond and the tertiary hydroxy group as depicted in Figure 3.9.
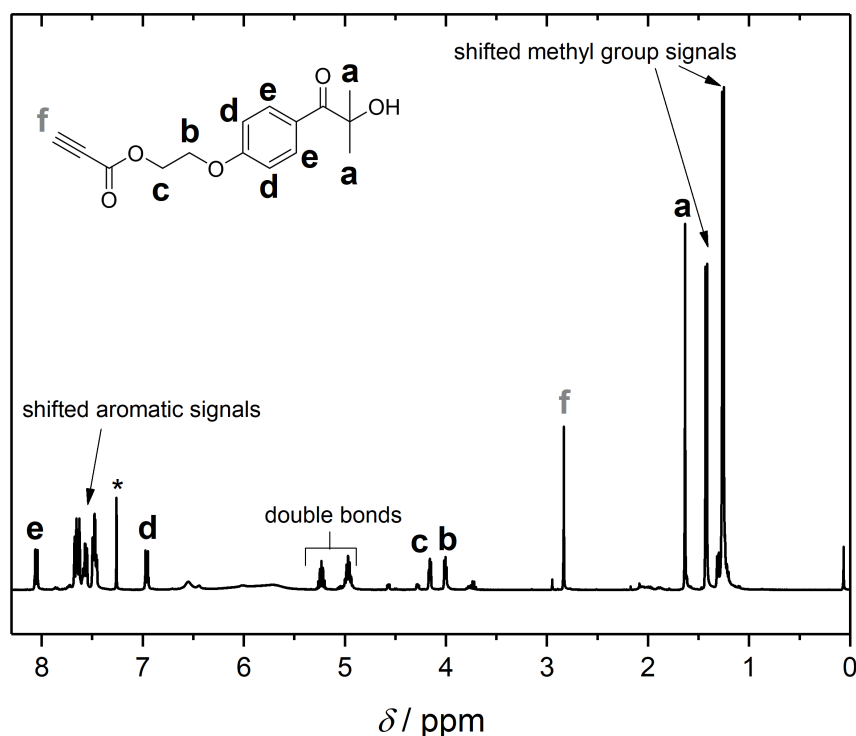
Figure 3.8: ^{1}H NMR spectrum in CDCl$_3$ of the *Mitsunobu* reaction of **Irgacure2959** and propiolic acid.
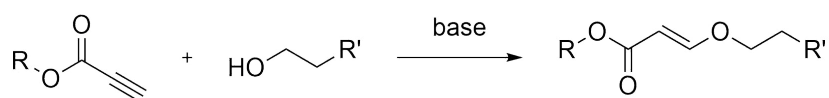
Figure 3.9: Side reaction during the Mitsunobu esterification. [143]

Because of the challenging synthesis of **PI-alkyne 1** and the concerns about the chemical stability, a propyl group was introduced as a spacer between the ester group and the triple bond (**PI-alkyne 2**, Figure 3.10), thereby reducing the side reaction of the terminal triple bond. **PI-alkyne 2** was synthesized by Steglich esterification with EDC between **Irgacure2959** and 5-hexynoic acid, resulting in a yield of 80% for the preparation of the desired photoinitiator.
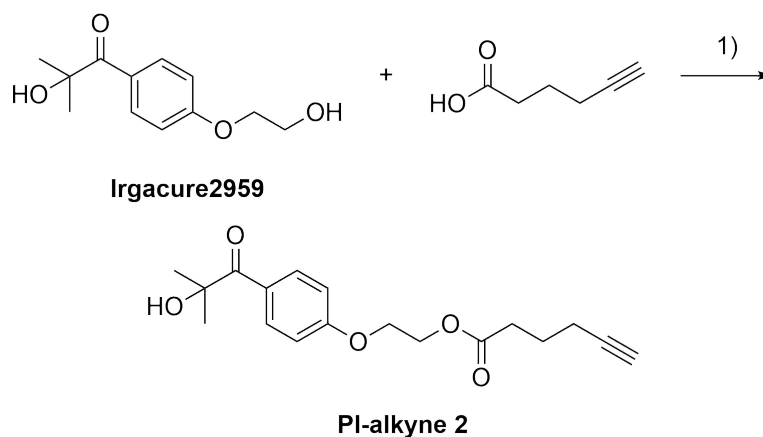
Figure 3.10: Synthesis of **PI-alkyne 2** via the esterification of **Irgacure2959** with 5-hexynoic acid. *1) EDC, DMAP, DCM, a.t., o.n., 80%.*

For the functionalization of SURMOFs with **PI-alkyne 2**, a copper catalyst is necessary, because the electronic situation of the terminal triple bond was significantly changed compared to **PI-alkyne 1**. The photoinitiator **PI-alkyne 2** was therefore tested for its stability in a copper-catalyzed azide-alkyne cycloaddition (CuAAC) in a model reaction. The azide functionalized linker N_3-BDC is not readily soluble in most organic solvents, thus, 4-azidobenzoic acid was selected as a test reactant.

The catalyst was $[\text{Cu(CH}_3\text{CN)}_4]\text{PF}_6$ as employed by Z. Wang *et al.* for SURMOF functionalization via CuAAC. [135] The product formation was confirmed by COSY NMR spectroscopy (see Figure B.3, page 130), clearly showing the resonance of the formed triazole ring which has no correlation with other protons in the molecule. A successful coupling was only achieved with 1.25 eq. of copper catalyst, clearly exceeding the molarity for the definition of catalytic amounts. It is likely that the catalyst is consumed by

PI-alkyne 2
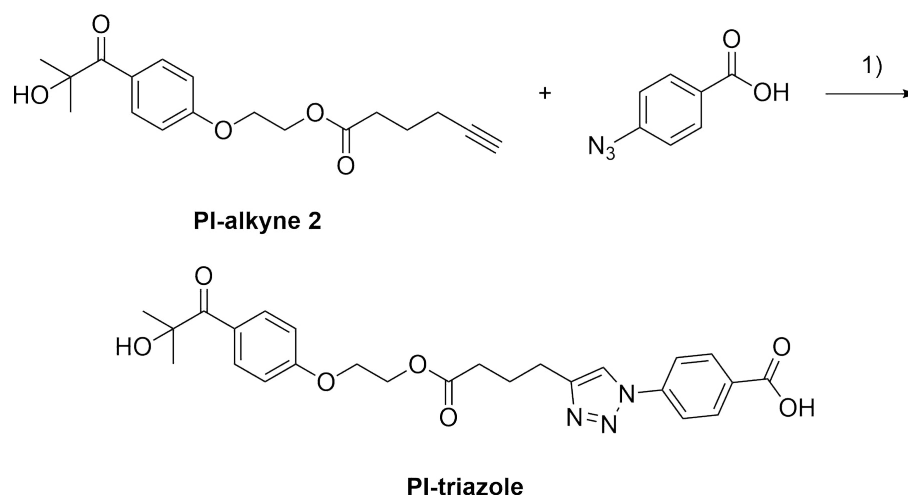
PI-triazole

Figure 3.11: Model reaction between **PI-alkyne 2** and 4-azidobenzoic acid. The successful formation of the product **PI-triazole** was confirmed by COSY NMR spectroscopy (Figure B.3). *1) [Cu(CH₃CN)₄]PF₆, THF, 70 °C, o.n.*

complexation with the carboxylic acid of the reactant, and therefore, the carboxylic acid has to be saturated with the catalyst in order to successfully catalyze the CuAAC.

The photoinitiator **PI-alkyne 2**, which will be referred to as **PI-alkyne** in the following chapters, undergoes successful CuAAC and was therefore employed in the functionalization of SURMOFs. Moreover, **PI-alkyne** was employed in the synthesis of block copolymers in a λ-orthogonal fashion. The copolymers were characterized in-depth via mass spectrometry, as is described in detail in Chapter 4.

3.4 Functionalization of SURMOFs

For the preparation of SURMOFs on gold-coated silicon wafers, a self-assembled monolayer (SAM) with suitable functional groups for the complexation of metal ions is required. Thiol groups attach covalently to gold and can readily be applied to substrates at ambient temperature.[68] For the desired [001] growth direction of Cu-BDC-dabco, substrates ($1\,\text{cm}^2$) were immersed into a solution of 11-mercaptoundecanol (MUD) in ethanol. After 24 h, the substrates were rinsed, dried with nitrogen, and coated with Cu-BDC-dabco in a layer-by-layer fashion by the automatic pump system (Chapter 2.4.2, page 29). The successful SURMOF growth can be detected via X-ray diffraction (XRD), and results in spectra with two reflexes (Figure 3.12), and a third reflex for the gold coating of the substrate. The XRD confirms the successful growth of Cu-BDC-dabco in the [001] orientation.
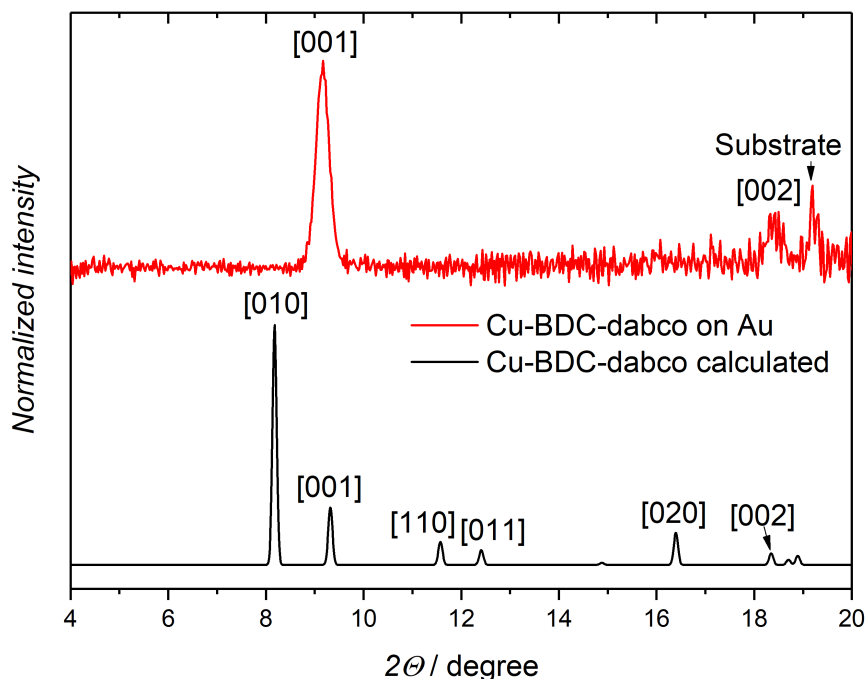
Figure 3.12: X-ray diffractogram of Cu-BDC-dabco SURMOF (red) grown in the layer-by-layer fashion (40 cycles) on gold-coated silicon substrates (MUD), compared to the calculated diffractogram (black).

The functionalization of the SURMOF can be carried out in any layer of the structure due to the layer-by-layer method, namely during the first cycles, in the middle, or on the top layer. However, the catalyzed cycloaddition of **PI-alkyne** and the azide groups tethered to the layers may be hindered in deeper areas of the SURMOF as both the catalyst and the photoinitiator need to diffuse into the pores and interact in a very small cavity. It was therefore considered to grow the SURMOF on top of a **PI-alkyne**-functionalized layer and thereby circumvent the diffusion difficulty. Thus, a model system was employed for the examination of the influence of the photoinitiator on the SUR-MOF growth. Cu-BDC-dabco was prepared with 40 cycles on a $1\,cm^2$ substrate and subsequently coated with 5 cycles Cu-(N_3-BDC)-dabco SURMOF. The resulting azide-functionalized SURMOF was exposed to the CuAAC with **PI-alkyne**. For the envisaged subsequent polymerizations, one photoinitiator layer would be sufficient, however, to facilitate the surface characterization, 5 cycles were applied with the aim of enhancing the signal intensity for IRRAS and ToF-SIMS analysis. The cycloaddition does not have an impact on the crystal structure, as is depicted in Figure C.15 on page 155. The successful functionalization was evidenced via IRRAS (Figure 3.13), which shows the decrease of the azide stretching vibration, yet, residual azide groups remain. Specific vibrations for
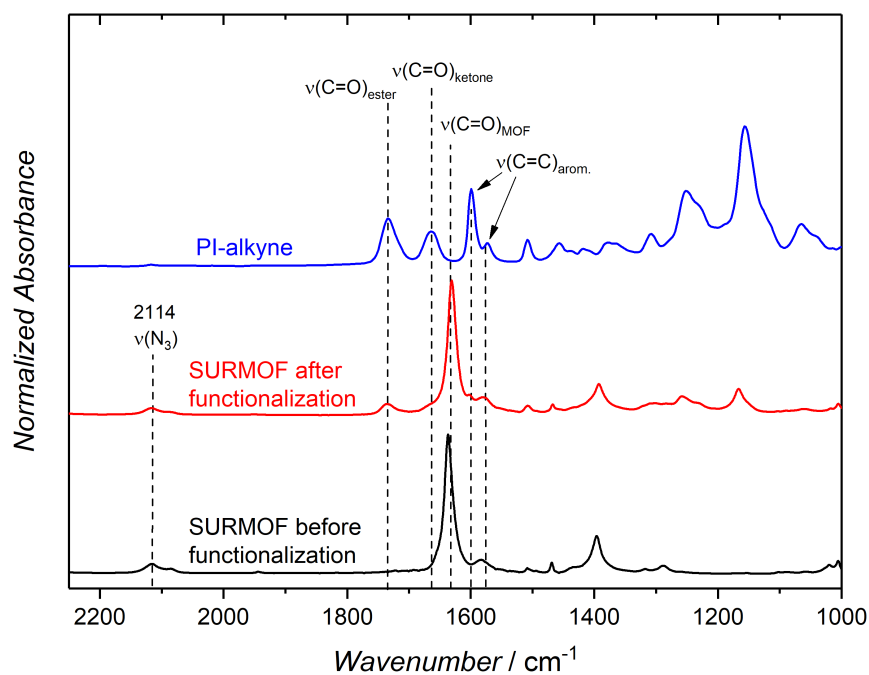
Figure 3.13: IRRA spectra of Cu-BDC-dabco (40 cycles) + Cu-(N_3-BDC)-dabco (5 cycles) before (black) and after (red) functionalization with **PI-alkyne** (blue).

PI-alkyne are detectable for the stretching vibrations of the ester and ketone moieties that are not present in the SURMOF prior to the functionalization.

Additionally, the functionalized SURMOF was characterized via ToF-SIMS. For the detection of successful layer functionalization, ToF-SIMS offers the possibility to depth-profile surfaces. The detection of a specific **PI-alkyne** fragment is crucial for the characterization of layer specific functionalization. Figure 3.14a depicts the mass spectrum that was retrieved during ToF-SIMS analysis. The spectrum shows a new mass value for the functionalized SURMOF, which can be attributed to a specific **PI-alkyne** fragment, i.e. $C_{10}H_{11}O_3^-$. The depth profile of the SURMOF structure (Figure 3.14b) underpins the increased occurrence of **PI-alkyne** at the top layers of the structure, as the signal decreases fast during the first 50 s sputter time. Detected gold clusters increase throughout the profiling as the substrate is exposed due to the sputtering of the SURMOF. Furthermore, the spectrum shows the signal for the fragment of dabco, C_2N^-, which remains constant until large amounts of SURMOF are removed and the gold surface is revealed continously. The successful functionalization is further underlined by the comparison of the images obtained by ToF-SIMS. For Cu-BDC-dabco and the azide-functionalized Cu-BDC-dabco, the fragment for the photoinitiator cannot be detected at all, as depicted in Figure 3.15.

Chemical Formula: $C_{10}H_{11}O_3^-$
Exact Mass: 179.0714
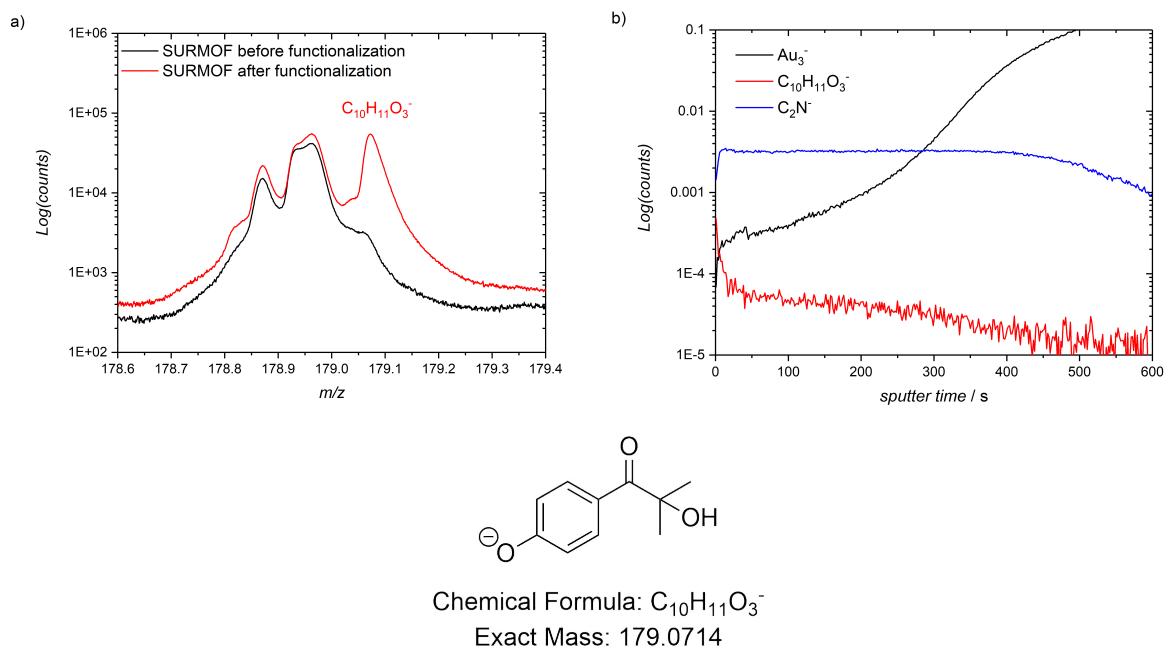
Figure 3.14: ToF-SIMS analysis of **PI-alkyne**-functionalized Cu-BDC-dabco. a) Mass spectrum of azide-functionalized Cu-BDC-dabco before (black) and after (red) functionalization with **PI-alkyne**. b) ToF-SIMS depth profile with MOF- and substrate-relevant mass values. The indicated mass can be attributed to a fragment of the photoinitiator.
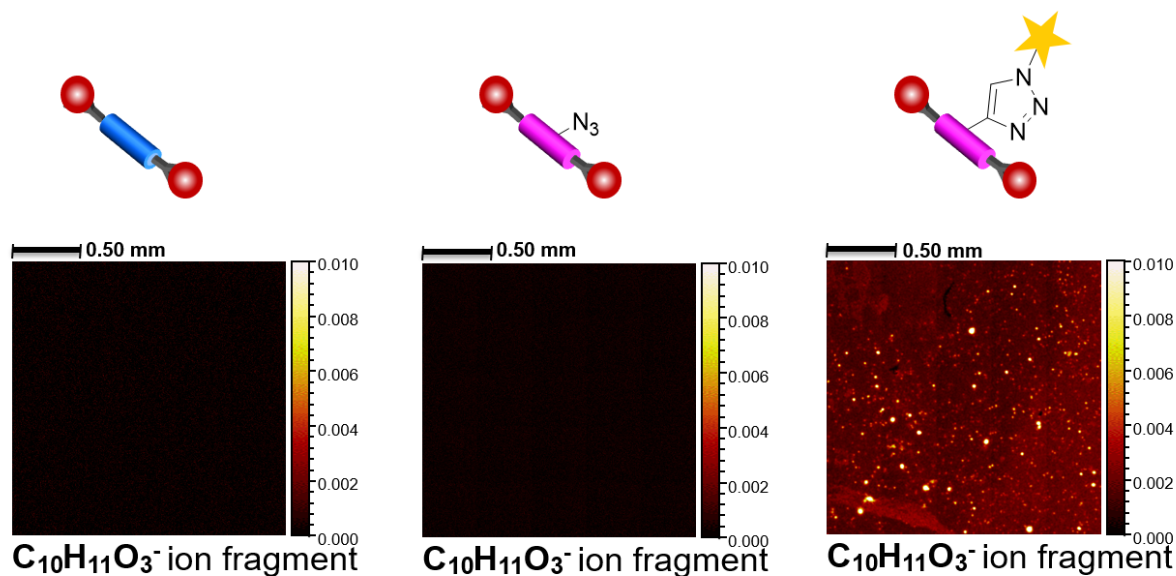
Figure 3.15: The photoinitiator fragment detected in ToF-SIMS images of Cu-BDC-dabco (left), functionalized with azide (middle), and after functionalization with **PI-alkyne** (right).

After the successful functionalization of the SURMOF, an additional 40 cycles of Cu-BDC-dabco were grown onto the functionalized SURMOF, resulting in a sandwich structure. The XRD of the sandwich SURMOF (Figure 3.16) displays an additional reflex for the crystal structure, and thus, evidences that **PI-alkyne** influences the crystal structure growth. In fact, a consistent growth direction is crucial for the purpose as polymerization scaffold. Therefore, the initiator **PI-alkyne** can be attached to the top layers of the SURMOF, yet, a functionalization of deeper layers of the SURMOF structure is not essential.
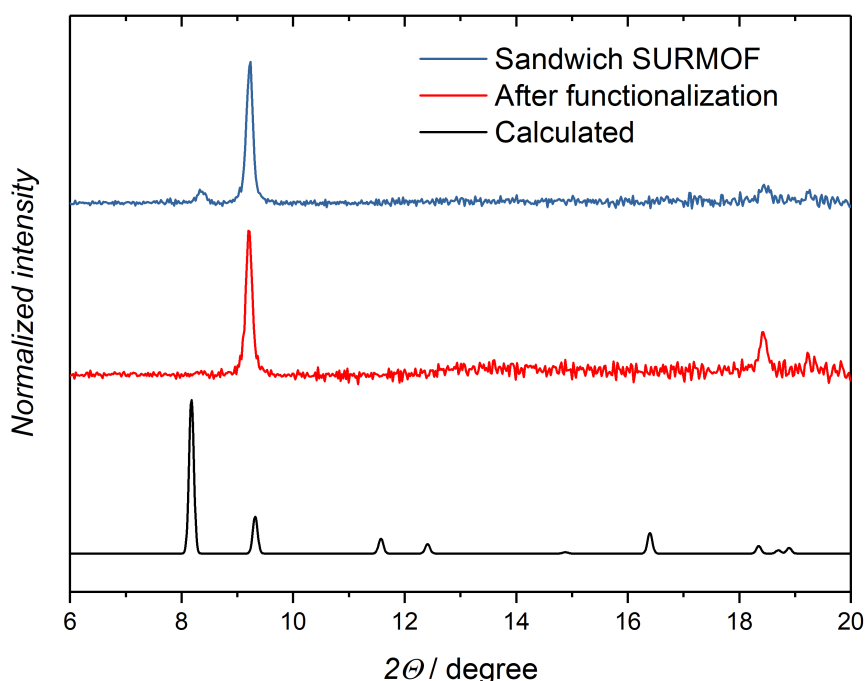
Figure 3.16: X-ray diffractogram of Cu-BDC-dabco after the functionalization (red) and of the sandwich SURMOF structure (blue), compared to the calculated diffractogram (black).

The functionalization of Cu-BDC-dabco with **PI-alkyne** is successful. However, the photoinitiator may reduce the diffusion of monomers into the SURMOF structure. The SURMOF was therefore grown and functionalized on QCM substrates. One sample consists of pure Cu-BDC-dabco (60 cycles); a second sample is additionally prepared with 1 cycle Cu-(N_3-BDC)-dabco with subsequent functionalization. The samples were activated in the QCM at 60 °C under Ar flow overnight and susequently cooled to ambient temperatures. The samples were exposed to methyl methacrylate (MMA) via bubbling Ar. The MMA containing Ar stream was carried to the samples and the weight gain Δm
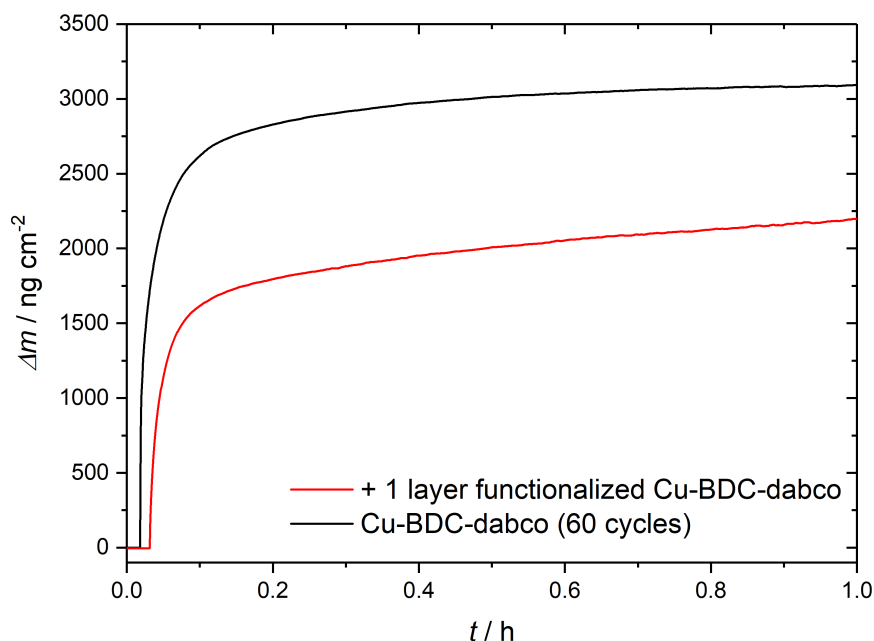
Figure 3.17: QCM-D signal for the loading of Cu-BDC-dabco (60 cycles, black) and after functionalization with **PI-alkyne** (1 cycle) with MMA via gas phase loading.

was monitored over 1 h (Figure 3.17). The maximum loading capacity is lower for the functionalized SURMOF, however, the loading speed of the SURMOFs is similar, as it is detectable via the slope of the graphs. Since the loading was tested on two separate samples, small differences in the total loading capacity can occur (see Figure C.16, page 155 for a third sample), however, an influence of the functionalization layer on the loading capacity cannot be fully excluded. Albeit, the amount of loaded monomer is in the μm range for all samples.

3.5 Free Radical Polymerization of MMA in SURMOFs monitored by QCM

As the functionalization of the SURMOF surfaces via CuAAC is successful, the polymerization process had to be investigated as the polymerizations in SURMOFs cannot be processed in the same manner as the polymerizations in bulk MOFs. The SURMOFs and their functionalization was therefore carried out on QCM samples to monitor the polymerization process. The samples were activated overnight at $60\,°C$ in the QCM chamber under a constant Ar flow.

The first sample was not functionalized with **PI-alkyne** as a blind sample for the polymerization process. The sample was loaded with MMA via bubbling Ar through
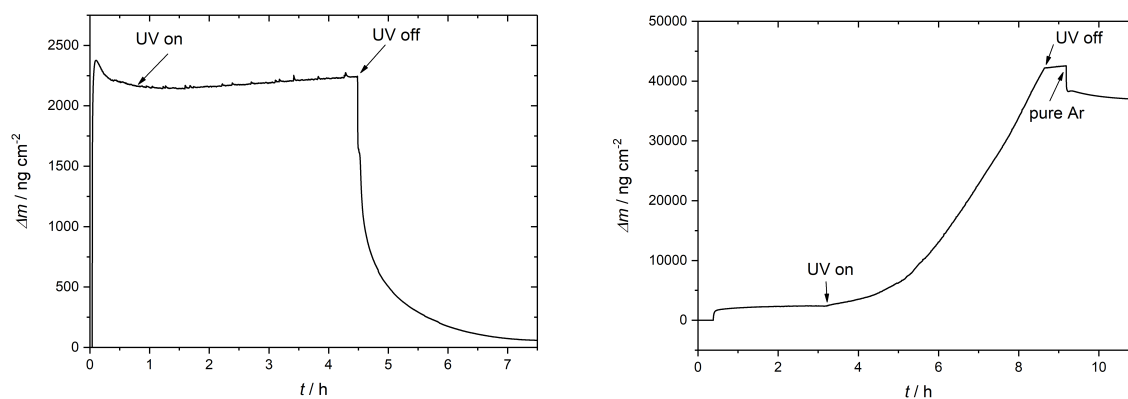
Figure 3.18: QCM results for the polymerization of MMA in SURMOF channels. The blind sample (left) does not show any sign of polymerization as there is no initiator present. The sample containing anchored initiator (right) does indeed show polymerization, yet the excessive mass increase indicates that the polymerization is taking place on top of the SURMOF surface.

a degassed solution of MMA. The sample was irradiated with UV-light ($\lambda = 366$ nm). After 3.5 h, the UV light was turned off and the Ar/MMA flow was switched to pure Ar to initiate the deloading. As there was no initiator present, a polymerization should not be possible and the monomer should diffuse from the structure. As can be seen in Figure 3.18 (left), the monomer is completely deloaded, thus, it can be assumed that the monomer does not polymerize in the absence of an initiator.

The next sample was functionalized with **PI-alkyne** on the top layer of the SURMOF. The sample was loaded with MMA for 1.5 h and subsequently irradiated with UV-light. During the irradiation process, the monomer gasflow continued, keeping the concentration of monomer constant in the gas phase above the substrate. The results are shown in Figure 3.18 (right). After the polymerization was initiated, the mass increased further, first slowly at the beginning, but then with a constant increase of $9.7\,\mu\mathrm{g\,cm^{-2}\,h^{-1}}$. According to the monomer loading, this gives a tenfold mass increase in the experiment, indicating that the polymerization cannot proceed just inside the SURMOF structure, but has also to take place outside of the channels. The polymerization was therefore stopped by shutting off the light source and switching to a pure Ar stream. Monomer that has not reacted diffused from the structure, resulting in a small mass decrease. The total mass increase of the sample is equal to polymeric material of $37\,\mu\mathrm{g\,cm^{-2}}$.

The sample was analyzed via ToF-SIMS, obtaining surface scan and depth profiling data, in order to gain an insight into the polymerization and to locate where it actually took place. The total ion distribution shows a general homogeneous surface intensity with several exceptions of lower intensity spots (Figure 3.19, top left). To clarify the composition of the dots, the surface distribution of residual PI-alkyne fragment
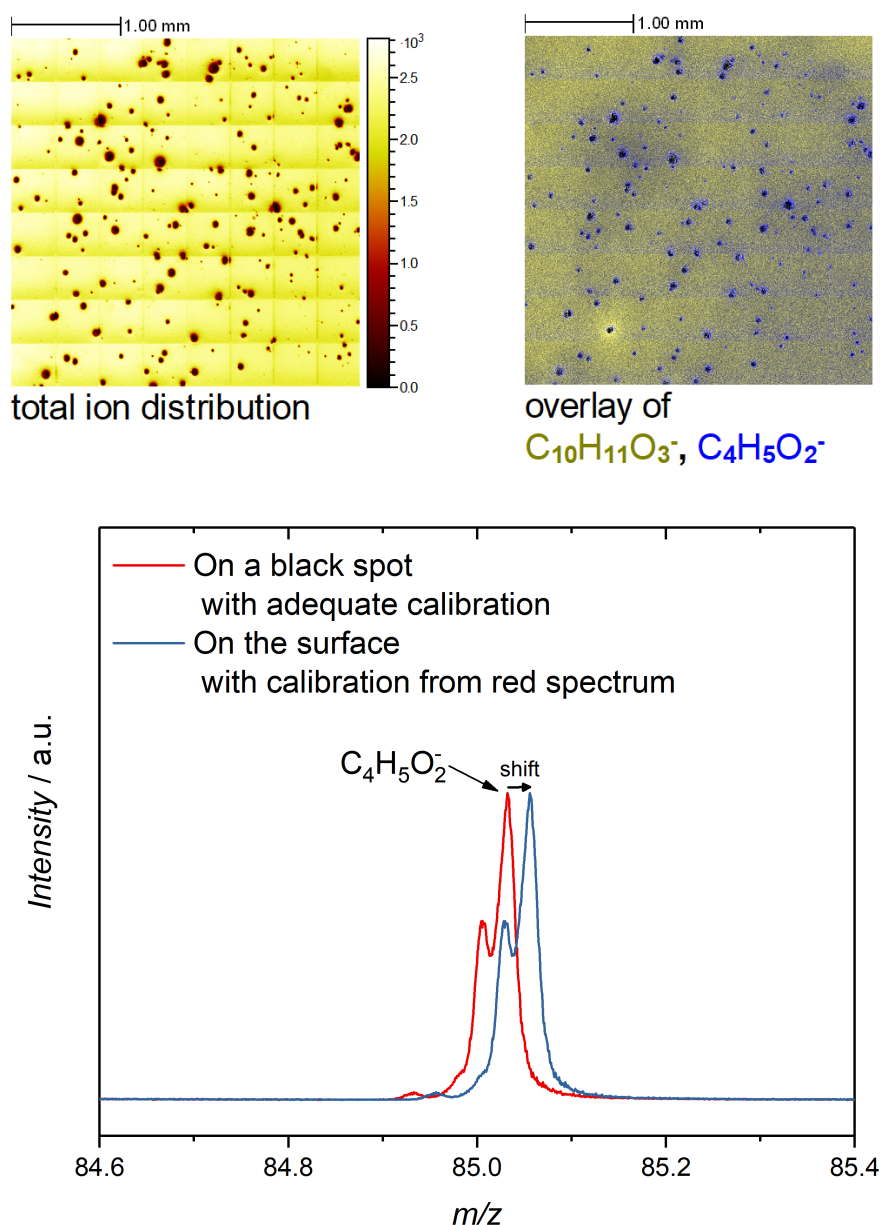
Figure 3.19: Sample of MMA polymerization on QCM-substrate. *Top, Left:* ToF-SIMS scan of total ion intensity. *Top, right:* Overlay of PI-alkyne fragment (yellow) and **PI-alkyne** fragment (blue). The surface shows black spots with very low intensity. *Bottom:* Mass spectra of PMMA fragment on one of the black dots (red) and on the SURMOF surface (blue) with reference in respect to the black spot. The shift in the mass values suggests that the spots possess a higher thickness than the SURMOF.

($C_{10}H_{11}O_3{}^-$) and a PMMA fragment ($C_4H_5O_2{}^-$) was checked. Thus, both signals were normalized to the total ion intensity and combined in an RGB overlay (Figure 3.19, top right) For a good contrast, the $C_{10}H_{11}O_3{}^-$-fragment was chosen for red and green, giving a yellow color, and the fragment $C_4H_5O_2{}^-$ for blue. It is clearly visible that the lower intensity spots in the normalized image contain PMMA.

In the next step, one of the spots including surrounding area was analyzed via depth profiling. The obtained summarized spectrum was calibrated using main elements of the SURMOF and the substrate: C^-, O^-, Cu^-, Au^{2-} and Au^{3-}. With this calibration, the PMMA fragment was identified. Now, a so-called *region of interest* (ROI) was chosen and reanalyzed, using just the area of the spot. Again, the same calibration method was employed to identify the PMMA fragment (Figure 3.19, red spectrum). The calibration of the ROI was applied on the depth-profile spectrum from before, resulting in a shift in the spectrum to higher masses (blue spectrum) which clearly indicates that the time of flight for the PMMA fragment was increased. Hence, the PMMA spot indeed is ontop of the SURMOF's topmost layer.

The total ion density distribution shows a lower intensity in the PMMA spots, thus, it can be assumed that the ionization probability is less than for the SURMOF itself. One possible explanation is that the PMMA in the spots is highly crosslinked. This theory was underpinned by dissolving the SURMOF with EDTA solution. The PMMA bubbles remained and were still visible with the naked eye. The bubbles were insoluble, even after treating the sample with various organic solvents (THF, chloroform, etc.) in the ultrasonic bath. Hence, there was no PMMA detected in the ESI-MS.

3.6 Summary

The resulting small amounts of polymer from polymerizations in SURMOFs will have to be characterized via mass spectrometry. A dilution experiment at an ESI-MS system evidenced that traces of PMMA up to $10\,ng\,mL^{-1}$ can be detected via ESI-MS. Mass spectrometry allows for the detailed clarification of the polymer structure and can give insight into the ionization process, and if the polymer is indeed attached to the linker of the SURMOF.

Polymerizations were performed according to the Kitagawa protocol by diffusing both the initiator (benzoin) and monomer into the structure by immersing the SURMOF into the monomer solution. The monomer did not remain in the SURMOF pores and diffused fast as was detected by XRD and ToF-SIMS. A gas phase approach was therefore developed that requires the initiator to be loaded into the SURMOF prior to the loading of the monomer. Initiator, solely diffused into the structure and not covalently bound, did result in a polymerization process according to XRD and ToF-SIMS, yet a successful characterization of the supposedly produced polymer via mass spectrometry was not achieved.

Consequently, a functional photoinitiator was developed that can be introduced into the structure of SURMOFs via post-synthetic functionalization. The highest crystallinity quality was achieved with the functionalization of the top layers, while further SURMOF growth upon a functionalized middle layer resulted in slight changes in crystallinity, presumably due to the size of the photoinitiator hindering the framework growth. The functionalization can be easily followed via ToF-SIMS analysis, simply by detecting a specific fragment of the photoinitiator. In fact, the photoinitiator did not result in blocked pores and the SURMOF can be loaded with monomer, as was shown via QCM experiments. Polymerization with functionalized SURMOFs were monitored as well via QCM, and a polymerization process was detected. Via ToF-SIMS, it was confirmed that the polymerization proceeded, however, resulted in insoluble PMMA that was polymerized on top of the SURMOF surface instead of inside the channels. Although the photoinitiator was detected evenly distributed over the surface, the polymerization proceeded in specific small areas, leading to droplets of insoluble PMMA on the SURMOF surface. Thus, a detection of PMMA from the SURMOF channels in ESI-MS was not successful.

In-Depth SEC-ESI-MS Characterization of λ-Orthogonal Block Copolymer Formation
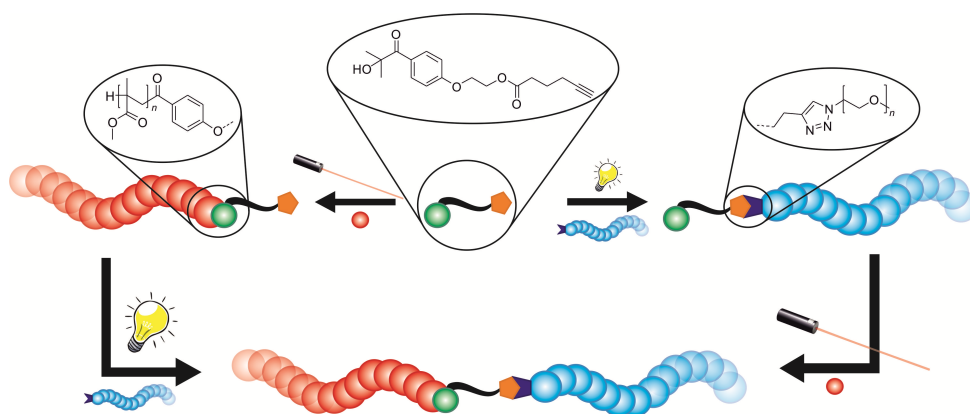
For the polymerization in SURMOFs via a framework attached photoinitiator, mass spectrometry will be crucial for understanding the initiation and, more importantly, the termination processes. Theoretically, termination by combination reactions is highly unlikely, yet, other analysis methods apart from mass spectrometry cannot give an insight into the specific end group structure. **PI-alkyne** was therefore applied in block copolymer synthesis with detailed mass spectrometric characterization by employing the concept of orthogonal reactions. While biological systems achieve selectivity through enzymatic catalysis, chemists seek for analogous results in synthetic protocols by developing

so-called orthogonal functionalities. Orthogonal groups or reactions describe synthetic procedures that involve only specific functional groups in a system without interfering with any other moieties present.[145–149] For example in our group, we demonstrated the λ-orthogonality of tetrazoles and benzaldehydes that can react with double bonds in pericyclic reactions.[56,64] By choosing suitable activation wavelengths, the benzaldehyde (λ = 350 nm) can be addressed individually without any cross-activation with tetrazole and perform cycloadditions with reactive double bonds. The tetrazole can subsequently be activated for pericyclic reactions at lower wavelengths. The drawback of the above mentioned photo-activated groups is the non-inversability. The benzaldehyde unit is activated at λ = 350 nm, however, it is also activated at λ = 310 nm, the wavelength that triggers the tetrazole. Therefore, the tetrazole unit cannot be addressed individually in the presence of unreacted benzaldehyde groups. To inverse the order of activation, it is necessary to employ a protection group for the benzaldehyde. The aldehyde unit can be transformed with amines into imines in a fast and simple way, the latter not being able to transform into a diene by irradiation. Thereby, the tetrazole can be activated at lower wavelengths, and after a deprotection step, the benzaldehyde can be transformed at higher wavelengths.[64] The concept of protection groups is widely applied in synthetic chemistry,[150] but the desire for fully λ-orthogonal functional groups remains.

The photoinitiator **PI-alkyne** that was synthesized for SURMOF-functionalization (see Chapter 3), was investigated for its stability and polymerizability while demonstrating λ-orthogonality for end group functionalization or block copolymer preparation. The concept of the project is depicted in Figure 4.1. On one hand, the initiating part of the molecule (α-end) is triggered in a pulsed-laser polymerization (PLP) at λ = 351 nm (Figure 4.1, Route A). The PLP method enables the preparation of short polymeric chains that can be detected in a high resolution ESI-MS setup. In fact, mass spectrometry facilitates end group analysis of polymers to a high degree and allows the identification of side reactions and degradations. The polymer of choice for PLP was PMMA, as it ionizes well in ESI-MS and can be detected in the nanogram range.

In addition, polyethylene glycol (PEG) ionizes effectively in ESI-MS comparable to PMMA, hence can be easily detected and analyzed. Therefore, PEG functionalized with an azide group was tethered to **PI-alkyne** by adopting a visible-light mediated CuAAC at λ = 420 nm[151] (Figure 4.1, Route B).

The resulting polymers obtained from both routes, namely **PMMA-alkyne** and **PEG-PI**, were each exposed in the second step to the opposing reaction protocol in order to verify the orthogonality of the photoinitiator part against the alkyne group of **PI-alkyne**.
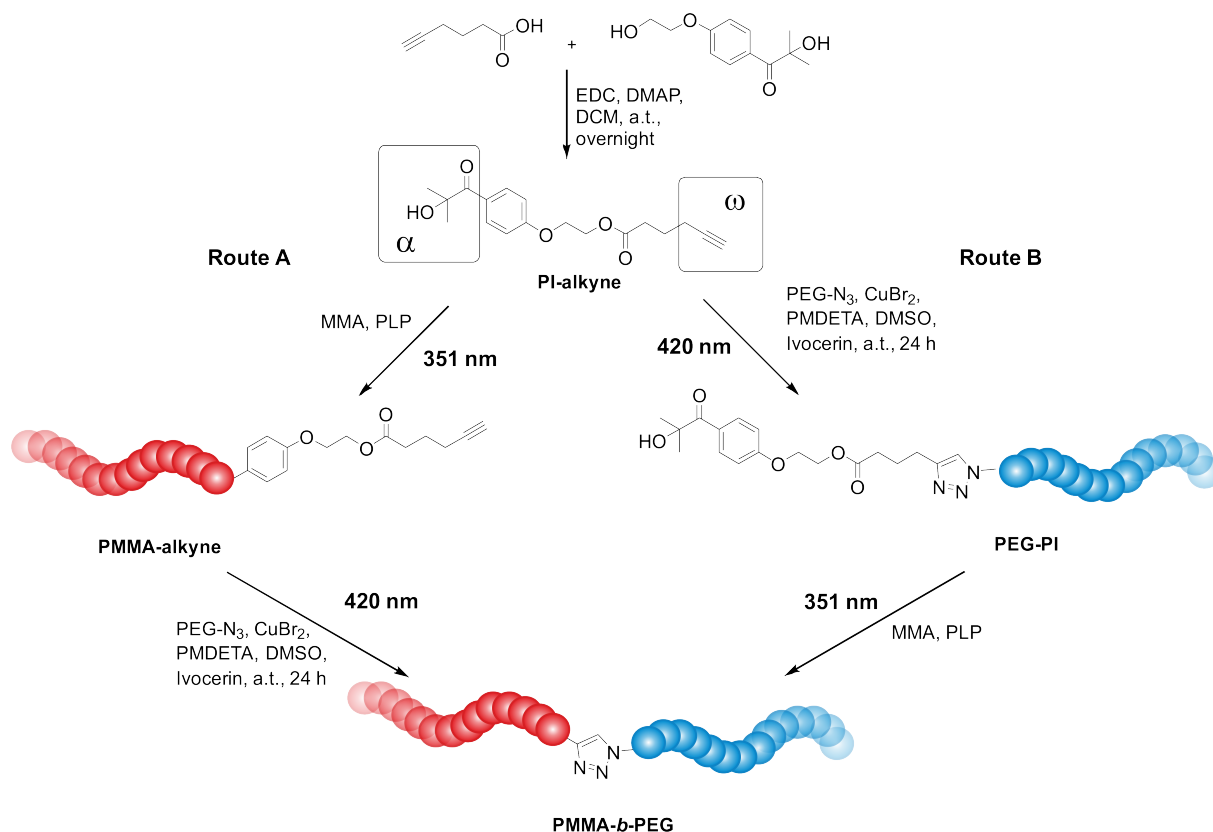
Figure 4.1: Concept of block copolymer formation in a λ-orthogonal fashion. Two routes are depicted where pulsed-laser polymerization (PLP) and visible-light copper catalyzed azide-alkyne cycloaddition (CuAAC) can be applied interchangeably. This figure was adapted with permission from John Wiley and Sons.[144]

4.1 Pulsed-Laser Polymerization of Methyl Methacrylate

The PLP studies on **PI-alkyne** were conducted at $\lambda = (351 \pm 1)$ nm with $0.35\,\mathrm{mJ\,pulse^{-1}}$ at a frequency of $200\,\mathrm{Hz}$ and with $90\,000$ pulses. All polymerizations were performed in bulk MMA with an initiator concentration of $3.7 \times 10^{-3}\,\mathrm{mol\,L^{-1}}$. The conversion was determined gravimetrically by evaporating the residual monomer and resulted in ca. 2%.

The low conversion and thereby resulting low molecular weight are crucial to allow for the characterization of the polymers via the hyphenated method size exclusion chromatography - electrospray ionization - mass spectrometry (SEC-ESI-MS).[152] In the SEC-ESI-MS, the polymer is analyzed through a conventional THF-based SEC system. The eluent, however, is diluted with methanol doped with sodium iodide and continuously passed through the ESI-MS. The resulting chromatogram is a sequence of time-dependent mass spectra and permits the examination of individual areas of the chromatogram. Our interest when analyzing the PLP generated PMMA was directed at the end group stability. The terminal triple bond was introduced for further post-
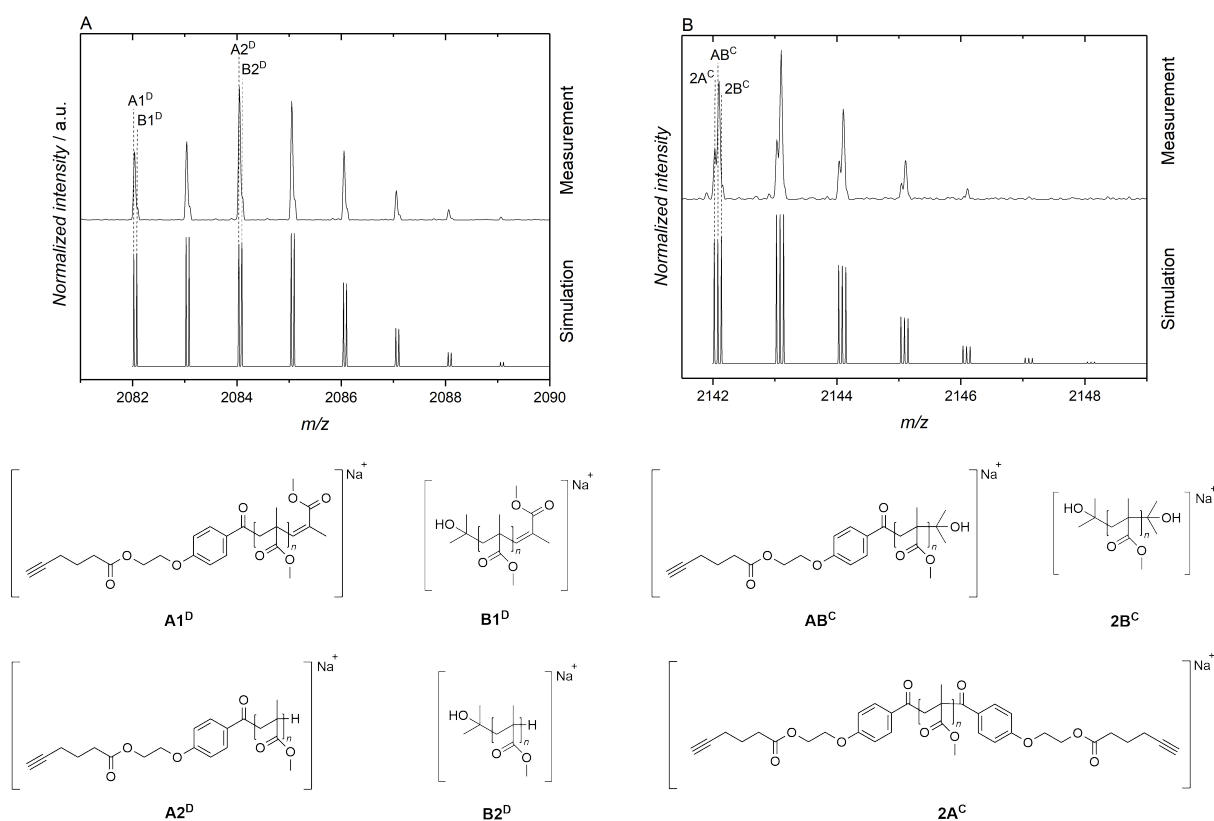
Figure 4.2: SEC ESI mass spectra for **PMMA-alkyne**. *Top:* Depicted are typical isotopic patterns for disproportionation (Spectrum A) and combination (Spectrum B) termination products. *Bottom:* Structures of the possible products. *A:* alkyne bearing end group; *B:* hydroxylpropyl end group; *D:* termination by disproportionation; *C:* termination by combination. This figure was adapted with permission from John Wiley and Sons. [144]

polymerization functionalization, therefore, its high stability is critical for a high end group fidelity.

As the initiator **PI-alkyne** forms two radicals upon irradiation, there is the possibility for two end groups forming, the alkyne (A) and the hydroxypropyl (B) end groups. Furthermore, as the polymers undergo either disproportionation (D) or combination (C), the mass spectrum will result in typical patterns for the termination mechanisms. Figure 4.2 shows exemplary the isotopic patterns and corresponding simulations for disproportionation (Graph A) and combination (Graph B) products as well as the structures that can be assigned to the signals. Interestingly, the masses of the end groups result in signals with very close proximity to each other. The simulations were therefore calculated with very high resolution of 1 ppm in order to assign the masses correctly.

Disproportionation yields four distinguishable products: two bearing a double bond (A1^D and B1^D) and two terminated with hydrogen (A2^D and B2^D). Disproportionation patterns can be identified by the difference of 2 Da between the double bond carrying

polymer chain and the hydrogen terminated polymer. Combination patterns refer solely to one polymer chain and do not interfere with the isotopic pattern of other species. On the one hand, the values for all experimental masses are in good agreement with the theoretical masses and can be found in Table 4.1. On the other hand, any reduction reaction on the alkyne moiety to alkene or alkane would have resulted in additional signals that were not observed in the present case. In the next section, the functionalization of PEG with **PI-alkyne** will be described.

Table 4.1: *m/z* values for patterns A and B depicted in Figure 4.2. Adapted with permission from John Wiley and Sons.[144]

Species	n	$(m/z)_{theo}$	$(m/z)_{exp}$	$\Delta(m/z)$
$2A^C$	16	2142.0222	2142.0344	0.0122
AB^C	18	2142.0797	2142.0989	0.0192
$2B^C$	20	2142.1380	2142.1589	0.0209
$A1^D$	17	2082.0222	2082.0356	0.0134
$B1^D$	19	2082.0797	2082.0960	0.0163
$A2^D$	18	2084.0378	2084.0481	0.0103
$B2^D$	20	2084.0953	2084.1082	0.0129

4.2 Functionalization of Poly(ethylenglycol) via Visible-Light CuAAC

The functionalization of PEG with **PI-alkyne** via visible-light CuAAC was conducted according to a procedure of Arslan *et al.*[151] In the case of light-induced copper-catalyzed click chemistry, the necessary Cu(I)-species (refer to Chapter 2.2.2) can be generated *in situ* by radicals that are introduced through photoinitiators. For the purpose of visible-light CuAAC, a photoinitiator that can be triggered with blue light, namely dibenzoyldiethylgermane (**DBDEG**) or Ivocerin®, was employed. The mechanism that was postulated by Arslan *et al.* is depicted in Figure 4.3.

Initially, the stability of **PI-alkyne** towards the visible-light irradiation was assessed. NMR samples of **PI-alkyne** in chloroform were analyzed before and after irradiation
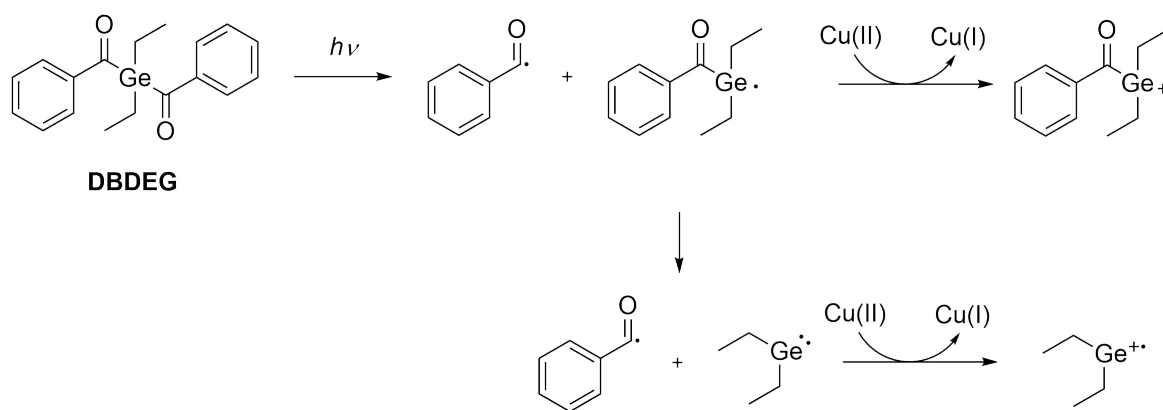
Figure 4.3: Reduction of Cu(II) to Cu(I) by radicals generated from **DBDEG** (Ivocerin®).[151]

with a 420 nm LED for 24 h. The ^{1}H NMR spectra do not indicate any changes and hence demonstrate the stability of **PI-alkyne** (Figure C.17, page 156). Additionally, **PI-alkyne** and **DBDEG** were dissolved each in MMA, and irradiated with visible light ($\lambda = 420$ nm). The conversion was determined gravimetrically. The results confirm the outcome of the NMR analysis as polymer formation is observed with **DBDEG**, whereas there is no sign of any polymerization for **PI-alkyne** (refer to Figure C.18, page 156). Therefore, it can be assumed that the photoinitiator is stable during the visible-light mediated click reaction.

The CuAAC between commercially available PEG-N$_3$ and **PI-alkyne** was performed in DMSO at ambient temperature for 24 h.[151] The crude product was purified by filtration over neutral alumina, and the successful azide-alkyne cycloaddition was verified via ESI-MS. The spectra before and after the functionalization are depicted in Figure 4.4 (A). The right hand side (B) shows a zoom into a specific area, proving that there
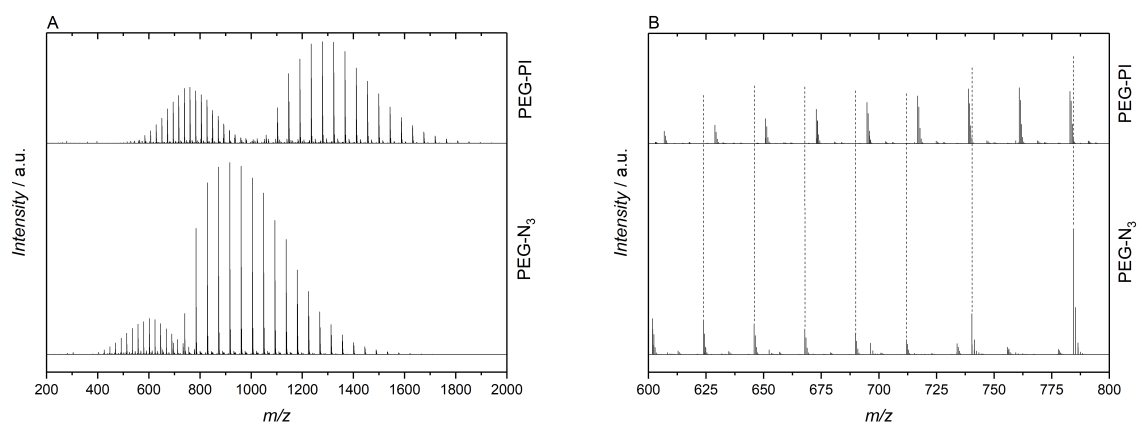
Figure 4.4: ESI mass spectra of PEG-N$_3$ before and after the functionalization with **PI-alkyne**. *A:* Overview of the mass spectra; *B:* Zoom into the mass spectra. This figure was adapted with permission from John Wiley and Sons.[144]

is no residual reactant present in the product. Since PEG is not produced by a radical polymerization process, there are no specific isotopic patterns assignable as mentioned above for the PLP process. For the exemplary isotopic pattern of PEG$_{18}$-PI and the corresponding simulation refer to Figure C.19, page 158.

4.3 λ-Orthogonal Block Copolymer Formation and Characterization by SEC-ESI-MS

The functional polymer **PEG-PI** was employed as a macroinitiator in the PLP of MMA under UV-light ($\lambda = 350$ nm). The polymerization was performed under the same conditions as mentioned previously for **PI-alkyne** and MMA. **PEG-PI** was soluble in the bulk monomer, hence, no additional solvent was necessary. The crude polymer was not precipitated and injected into the SEC-ESI-MS system without further purification. Here, the advantage of the combinatorial analysis method becomes evident. Since PEG ionizes strongly in the ESI-MS, the copolymer species would hardly be identifiable. Thus, by hyphenating the SEC to the ESI-MS, the shorter and unreacted PEG-chains are entering the mass spectrometer at longer retention times, thereby allowing a clearer identification of the polymers with higher molecular weight. Increasing the number of pulses up to 270 000 pulses decreased the amount of residual PEG macroinitiator (refer to Figure C.20, page 158), however, full removal of the macroinitiator was not achieved.

As the initiator cleaves into two radicals during the irradiation, the crude polymer mixture not only contains unreacted PEG, but also exclusively PMMA-containing chains that have been initiated with the hydroxy isopropyl radical. The complex mixture results in closely packed and overlayed isotopic patterns, as can be seen in Figure 4.5. The patterns shown here consist of double-charged polymer chains, because the elution volume of mono-charged masses contained residual **PEG-PI** and interfered with the ambiguous identification of the repeating units. In the spectrum of the copolymerization, the repeating units can be identified for both PMMA (50.0267 Da) and PEG (22.0081 Da) chains, respectively, and are shown exemplary for a few masses in Figure 4.5. Indeed, each single peak can be assigned to concomitant peaks in the appropriate distances of the repeating units for both PEG and PMMA.

During the PLP, the macroinitiator **PEG-PI** disproportionates into a macroradical that contains the PEG chain (A) and the hydroxy isopropyl radical (B). Further, both radicals are able to initiate the polymerization, and terminate by combination (C) and disproportionation (D) reactions. The possible products can therefore consist of PEG and PMMA,
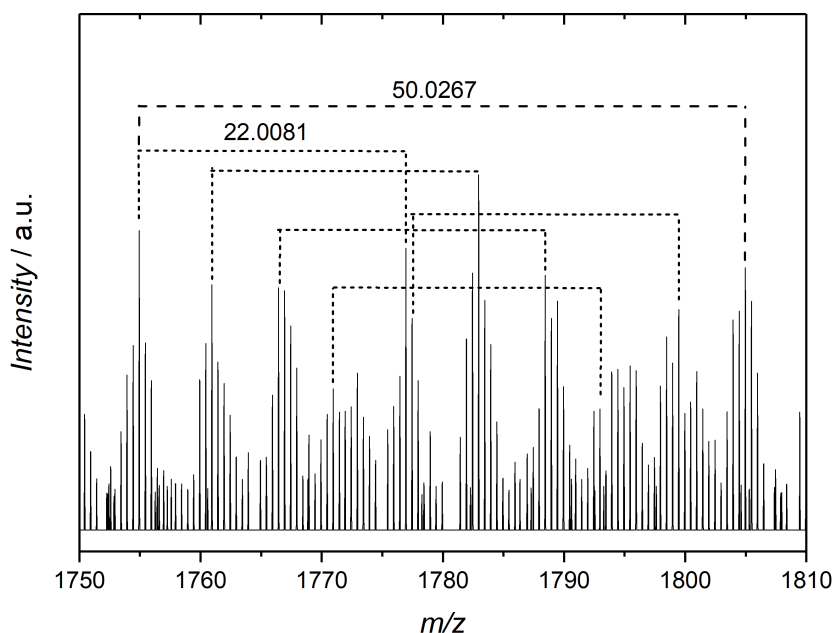
Figure 4.5: Section of the ESI mass spectrum of PEG-*b*-PMMA after PLP of **PEG-PI** with MMA. The repeating units for PMMA (50.0267 Da) and PEG (22.0081 Da) with a charge of $z = 2$ are marked exemplary. This figure was adapted with permission from John Wiley and Sons.[144]

or solely PMMA, as shown in Figure 4.6. In addition, the block copolymers also differ by the chain lengths of PEG and PMMA. Short and long chains are accessible for both species and thereby cause the rather complex spectrum (Figure 4.5). Hence, clear patterns for the termination products are not distinguishable and every pattern can consist of several isotopic patterns of various polymers. The first step in assigning the peaks was to assess the masses of each compound that could be detected. We also considered proton ionization throughout our simulations, and for pure PMMA compounds, it appears that it is possible to generate double charged molecules with one sodium ion and one proton, as shown for B2^{DH}.

The mass values were simulated with XCalibur^{TM} and the theoretical mass values were compared with the experimentally detected values. The simultaneous simulation of many structures is feasible, however, in some cases it does not result in a fitting pattern. In fact, the simulation gives for every species the same proportion, leading to peaks of the same intensity. In order to arrive at a more representative simulation, we changed the "amount", as it is termed in the software, of all species to define the correct pattern. As mass spectrometry is not a quantitative method, the parameters that we calculated are an exclusively mathematical solution, and should only be viewed as estimated proportions of the species in the system.
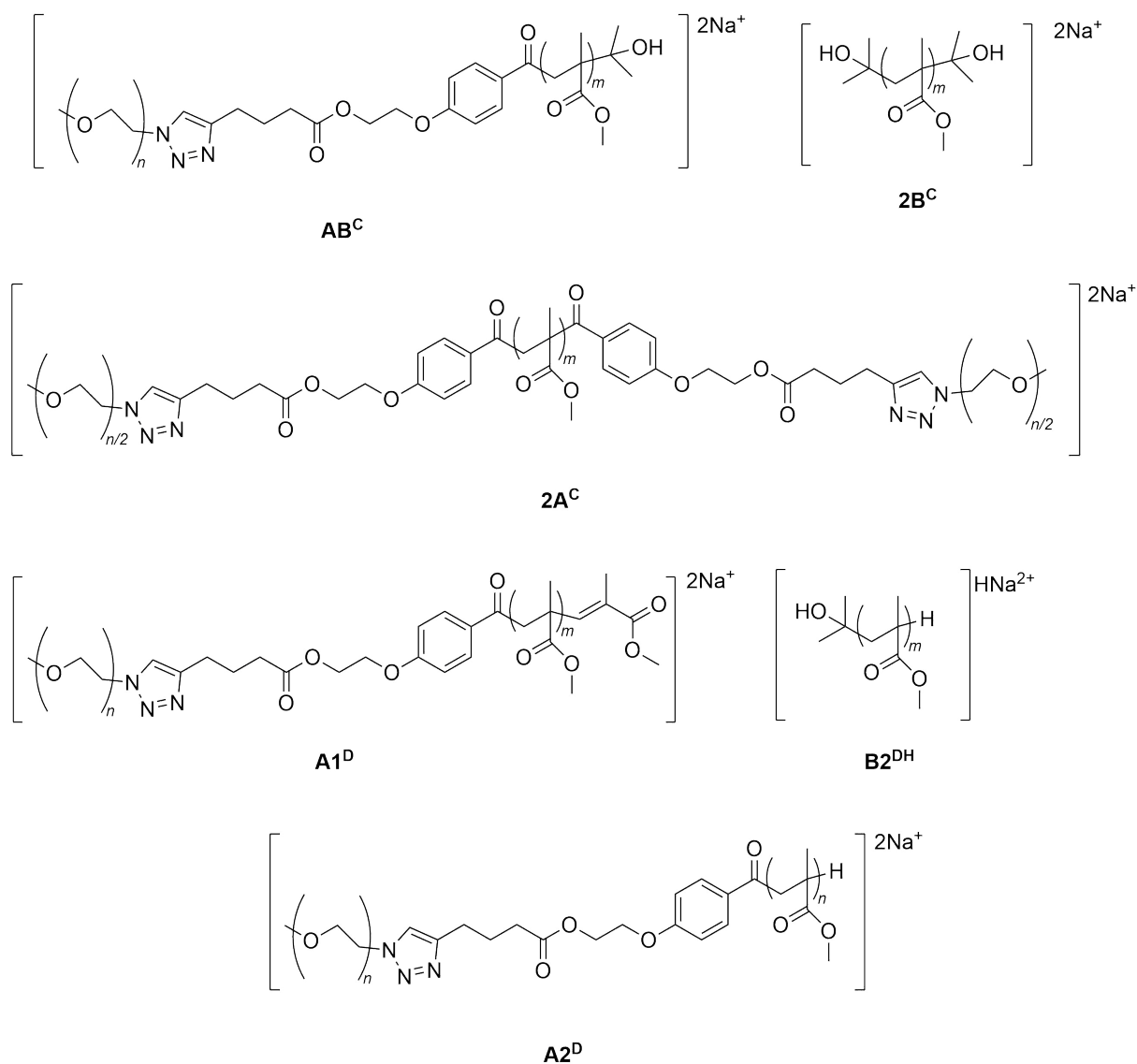
Figure 4.6: Structures of copolymer PMMA-*b*-PEG that were identified via SEC-ESI-MS. *A:* Species containing PEG; *B:* Species containing the hydroxy isopropyl end group of **PEG-PI**; *D:* Termination by disproportionation; *C:* Termination by combination. This figure was adapted with permission from John Wiley and Sons.[144]

In Figure 4.7, two patterns are depicted that repeat throughout the spectrum of PEG-*b*-PMMA (Figure 4.5). The patterns are, as mentioned above, more complex than for PMMA or PEG alone. The individual patterns of the species merge with each other as a consequence of the small differences in mass values. Nevertheless, the simulations can be adjusted to underpin the agreement of theoretical and experimental values. The exact mass values and their deviation from theoretical calculations for pattern A (Figure 4.7) are listed in Table 4.2, while the values for pattern B can be found in Table C.1 on page 157. To corroborate the λ-orthogonality in the present system, we performed the visible light-induced CuAAC on PMMA-alkyne that was generated during the PLP process.
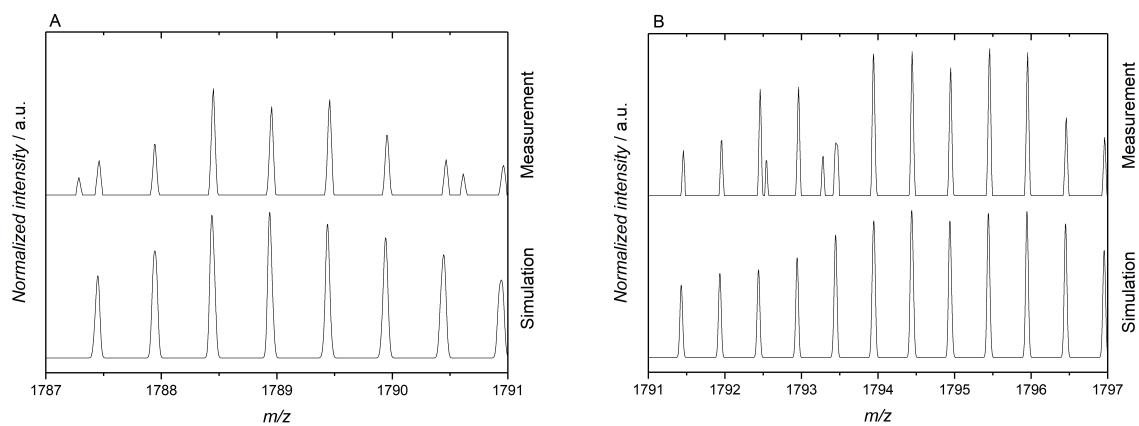
Figure 4.7: Zoom into the SEC-ESI mass spectrum in Figure 4.5 and the corresponding simulations. This figure was adapted with permission from John Wiley and Sons.[144]

The polymer was not soluble in DMSO, hence the reaction solvent was exchanged with DMSO/THF (1:1). The resulting copolymer was purified by filtration over basic alumina and was applied in the SEC-ESI-MS system for analysis without further purification.

Table 4.2: Theoretical and experimental *m/z* values for the copolymer PEG-*b*-PMMA generated with **PEG-PI** via PLP for pattern A in Figure 4.7. The right column provides the amount in which each species is present in the spectrum, yet other linear combination of the individual contributions may also result in the observed peak patterns. However, the absolute positions of each peak remain unaffected, confirming the presence of the expected species. Adapted with permission from John Wiley and Sons.[144]

Species	n	m	$(m/z)_{\text{theo}}$	$(m/z)_{\text{exp}}$	$\Delta(m/z)$	amount (eq.)
AB$^{\text{C}}$	35	16	1781.4571	1781.4407	0.0164	0.60
	33	17	1787.4571	1787.4608	0.0037	0.47
	16	25	1784.4231	1784.4583	0.0352	0.20
	24	21	1789.4440	1789.4567	0.0127	0.36
	26	20	1783.4440	1783.4551	0.0111	0.34
2A$^{\text{C}}$	27	17	1783.9185	1783.9519	0.0334	0.27
	34	14	1787.9316	1787.9439	0.0123	0.51
	43	10	1785.9447	1785.9544	0.0097	0.25
	50	7	1789.9687	1789.9548	0.0030	0.33
2B$^{\text{C}}$	0	34	1782.9302	1782.9532	0.0237	0.50
A1$^{\text{D}}$	14	25	1789.4153	1789.4567	0.0414	0.30
	16	24	1783.4253	1783.4551	0.0398	0.29
	23	21	1787.4284	1787.4608	0.0324	0.49
	25	20	1781.4284	1781.4407	0.0123	0.55
	32	18	1785.4415	1785.4498	0.0083	0.20
A2$^{\text{D}}$	14	26	1790.4231	1790.4651	0.0420	0.30
	16	25	1784.4231	1784.4583	0.0352	0.29
	23	22	1788.4362	1788.4493	0.0131	0.49
	25	21	1782.4362	1782.4469	0.0107	0.55
	32	18	1786.9510	1786.9591	0.0081	0.32

In Figure 4.8, the spectra of the copolymers, prepared by both routes, are depicted. Identical pattern sequences can be detected for the spectra. A closer look into the patterns (Figure C.21 and Figure C.22 on page 159) which were described previously for the first copolymer access route, confirms the successful functionalization of PMMA with PEG, as the patterns of both routes coincide.
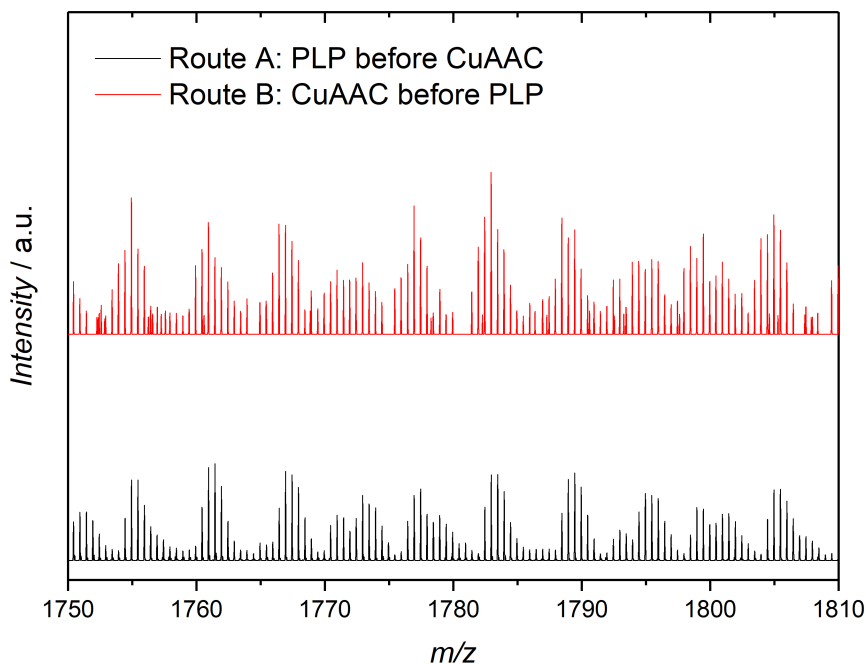
Figure 4.8: *Red:* High-resolution SEC-ESI-MS spectrum of the first orthogonal synthesis route: **PEG-PI** was synthesized via visible-light CuAAC and was subsequently employed as the photoinitiator in PLP of MMA. *Black:* High-resolution SEC-ESI-MS of the second orthogonal synthesis route: **Alkyne-PI** was used in the PLP of MMA. Subsequently, the alkyne containing PMMA was functionalized with PEG-N$_3$ in the visible-light CuAAC. Both routes result in the same isotopic patterns with slightly varying intensity ratios. This figure was adapted with permission from John Wiley and Sons.[144]

4.4 Summary

We investigated the identification of polymer end groups by the preparation of block copolymers via λ-orthogonal photochemistry. The resulting polymers and copolymers were analyzed via high-resolution SEC-ESI-MS, and the latter evidenced the stability of the functionalities during the reaction processes. Light-induced CuAAC and PLP can therefore be applied in any order, and thereby underline the λ- orthogonal character of the system. Our approach can be employed for the introduction of thermally unstable molecules by light induced reaction steps. In addition, the most convenient route can be selected based on the characteristics of the employed system, including UV-sensitive end group functionalization.

ESI-MS was proven to be an adequate characterization method for the in-depth understanding of initiation and termination on the developed functional photoinitiator.

AB-Type Photomonomers for Light-Induced Step-Growth Polycycloaddition
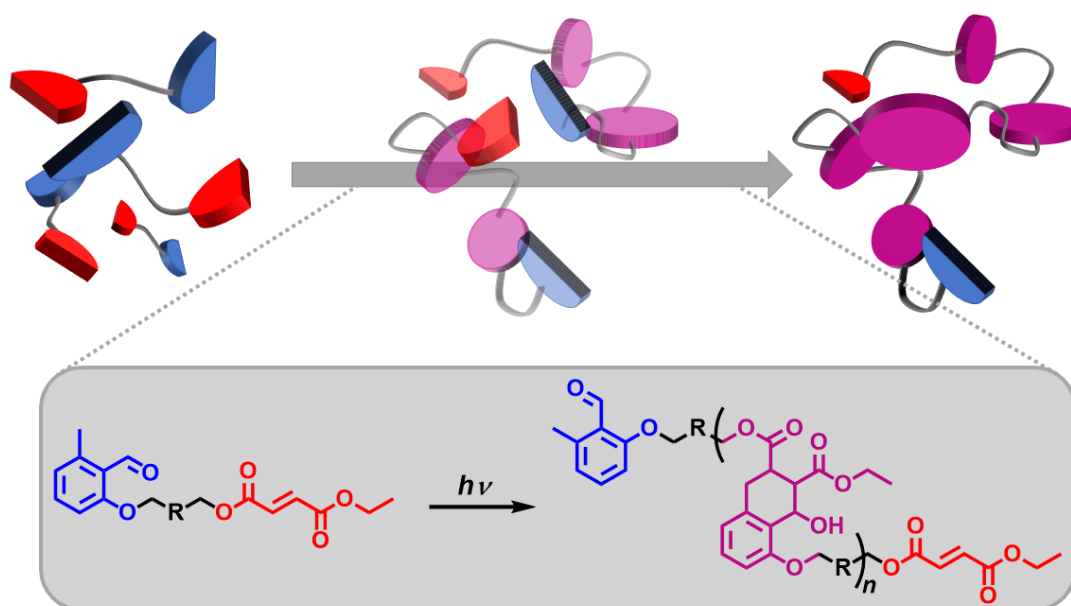
Many decades after the studies of Wallace H. Carothers on step-growth polymerizations,[153,154] polycondensations are still widely employed in industrial polymer production. Current research is focusing on introducing a vast range of organic reactions for step-growth processes. Among established ligation reactions (e.g., esterification, ami-

dation and urethane formation),[30,155] further reactions were adapted for step-growth polymerization, such as azide-alkyne 1,3-dipolar cycloaddition,[156–158] thiol-ene chemistry,[159–162] multi-component reactions,[163] and metathesis.[164] The vast range of functionalities, as well as the underlying mechanism of step-growth polymerizations, allows the introduction of various backbone structures and pendant groups which enable the precise tuning of the polymer's properties, e.g., solubility,[156] degradability,[16,160,165] fluorescence,[29,166] and thermo-mechanical behavior.[167–169]

As described in Chapter 1, the goal was the development of a monomer that can undergo light-induced polyaddition in an AB-type step-growth process. The AB-type concept is essential for polymerizations in confined environments as the monomers are deprived of their flexibility and mobility inside the channels. To ensure that the functional moieties are in close proximity, a monomer with AB structure is required. Within the context of polymerization in confined environments, the polymerization has to fulfill further criteria for kinetic studies in metal-organic frameworks (MOFs). The polymerization has to be a polyaddition, i.e., no small molecule (water, nitrogen,...) should be released during the irradiation. Any residual material would block the channels of the MOFs and thereby hinder the chain growth of the polymer. For the same reason, catalyst-free reactions are preferentially employed. Therefore, it is necessary to chose a system that can react fast and with high conversions, without the necessity of additional substances or the elimination of small molecules. An example of such a photo-induced addition reaction that meets the aforementioned criteria is the photo-induced Diels-Alder (DA) reaction[50,51] via the photo-enolization process of α-methyl benzaldehydes.[170] The photo-enolization describes a light-induced tautomerization,[52] which proved to be beneficial for synthetic organic chemistry,[171,172] ligation chemistry on macromolecules,[62,173–175] and surface functionalization.[59–61]

The monomer was designed in the AB-type fashion, as is depicted in Figure 5.1, consisting of 2-substituted α-methyl benzaldehyde as the photo-reactive group, and an

R: aliphatic or aromatic   **PhE-Mal**
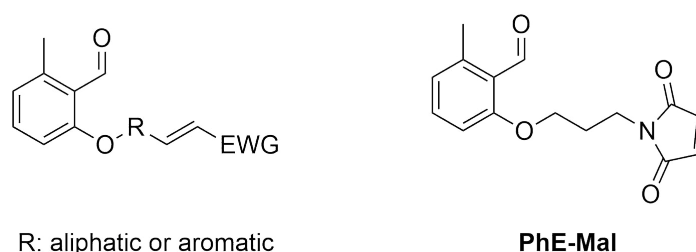
Figure 5.1: General structure of a photo-monomer with an electron-poor double bond and the design of a photo-monomer **PhE-Mal** with maleimide as reactive double bond. *EWG:* electron-withdrawing group; *R:* spacer group.

electron-poor alkene as highly reactive counterpart for the DA reaction. The two moieties are tethered via a spacer R which should be as short as possible to facilitate diffusion into MOF structures.

5.1 Syntheses of Step-Growth Monomers
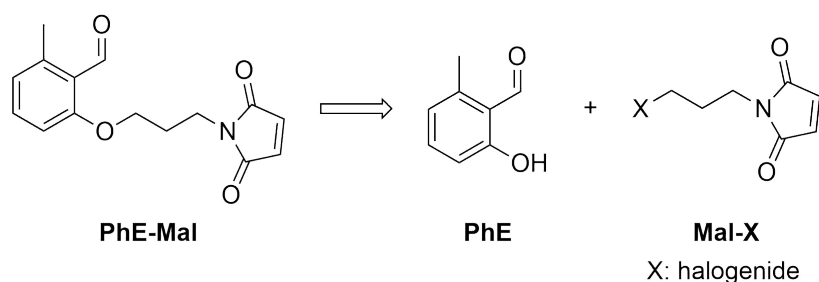
Figure 5.2: Retrosynthesis of **PhE-Mal** to the photoreactive **PhE** and a maleimide derivative **Mal-X**.

The schematic synthesis of a photo-monomer is depicted in Figure 5.2 and proceeds via an ether conjugation between **PhE**, namely 2-hydroxy-6-methylbenzaldehyde, and a maleimide derivative **Mal-X** which contains a halogenide capable of undergoing etherifications. The photoenol **PhE** was synthesized according to a literature protocol (Figure 5.3).[174] In a first step, the methyl group of 2,3-dimethyl anisole in *ortho* position to the methoxy group is selectively oxidized to an aldehyde by copper sulphate and potassium peroxodisulfate. The photo-active α-methyl benzaldehyde **PhE-OMe**, which can undergo tautomerization to a hydroxy-*ortho*-quinodimethane as described in Chapter 2.3 (page 19), is thereby generated. The methoxy protective group is cleaved in the second step and results in a hydroxy group (**PhE**), which can be exploited as a synthetic handle in subsequent transformations.

For the functionalization of **PhE** with maleimide, a maleimide derivative with a primary chloride (**Mal-Cl**) was synthesized according to a published procedure.[176] The ether synthesis between **PhE** and **Mal-Cl** (Figure 5.4) was adapted from a standard
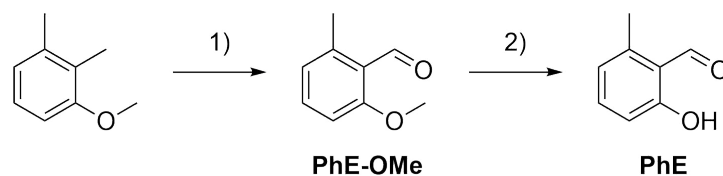
Figure 5.3: Synthesis of photoenol **PhE** in a two step procedure according to Oehlenschlaeger *et al.*[174] *1) CuSO$_4$·5H$_2$O, K$_2$S$_2$O$_8$, ACN/H$_2$O, 90 °C, 1 h; 2) AlCl$_3$, DCM, 0 °C, o.n.*

ether synthesis protocol by Hirschbiel *et al.* where potassium carbonate and 18-crown-6 are employed.[62] The reaction did not show any product formation in NMR spectroscopy, clearly detectable via the hydroxy group resonance of **PhE**. A prolonged reaction time
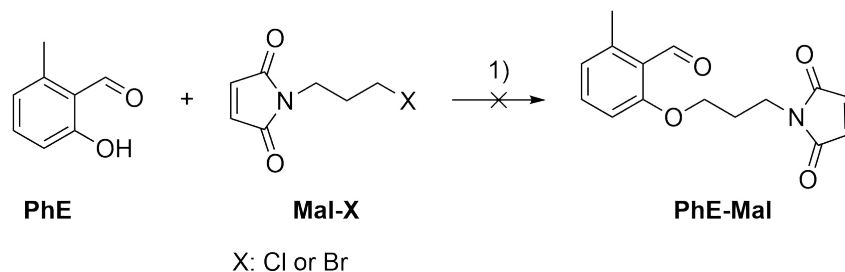
Figure 5.4: Attempted synthesis of monomer **PhE-Mal**. The reaction is performed between **PhE** and **Mal-Cl** or **Mal-Br**, respectively. The preparation was not successful, as the synthesis with **Mal-Cl** did not result in any product. The preparation with **Mal-Br** resulted in the ether formation, however, with loss of the aldehyde group in premature cycloadditions. *1) K_2CO_3, 18-crown-6, THF, reflux, o.n.*

from 24 to 48 h did also not result in any product formation (refer to Additional Data, Figure C.23 on page 160 for NMR results). Alternative publications suggest that functionalization of **PhE** structures[57,61,174] at times require slight changes to the above mentioned protocol, i.e., solvent, temperature and, moreover, the requirement of a better leaving group, e.g., bromide instead of chloride. Therefore, **Mal-Br** (Figure 5.4) was prepared according to the same protocol as mentioned for **Mal-Cl**. When **Mal-Br** was employed in the synthesis of **PhE-Mal**, the ether conjugation is successful as can be readily detected by ^{1}H NMR spectroscopy (see Additional Data, Figure C.24 on page 160). However, the aldehyde group, which is fundamental for the light-induced tautomerization, is strongly decreased whilst additional resonances arise that suggest that premature cycloadditions consumed the indispensable functional group. Hence, maleimide appears to be overly reactive and resulted in early cycloaddition either during the synthesis or during the purification procedure.

Consequently, the monomer design was reconsidered and the electron-poor double bond realized via a fumarate moiety (see Figure 5.5). The synthesis of the new monomer **PhE-Fum** is appealing for the preparation of precursors that allow the introduction of various backbones to the monomer as R group. Tethering the fumarate to **PhE** directly without spacer groups is not worthwhile as it would result in an aryl ester which may cleave upon the UV irradiation.[177] Furthermore, the fumarate group allows, in addition to the adjustable backbone structure, a second unit, the group R', which adds an additional variation possibility into the monomer structure (Figure 5.5). The precursors for
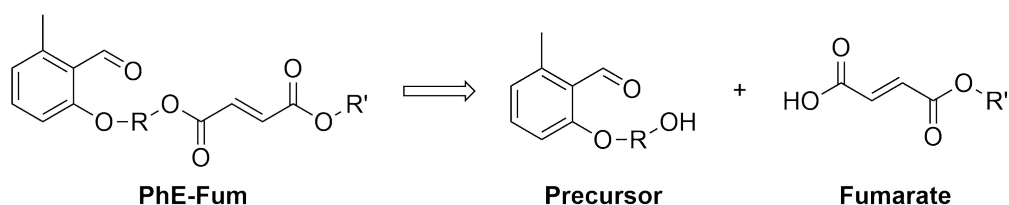
Figure 5.5: Alternative monomer structure and possible retrosynthesis with hydroxy-containing precursors. *R: spacer group; R': aliphatic pendant group.*

the synthesis of step-growth monomers were designed with aromatic and aliphatic units that carry a hydroxy group for further functionalization with fumarates.

The precursors for the future monomers were prepared as described in Figure 5.6 via the condensation between **PhE** and α-halogenide-ω-alcohols. For the synthesis of **Pre1** (Figure 5.6a), the procedure was similar to the synthesis for **PhE-Mal** described above and resulted in the expected product with 52% yield. As the same protocol afforded **Pre2** in less than 5% isolated yield and with low purity (refer to Figure C.25 on page 161), the reaction conditions were adapted. Changing the base from potassium carbonate to caesium carbonate did not enhance the product formation. An explanation for the latter case entails the suggestion that bromoethanol is prone to elimination reactions,[178] and thus an alternative synthesis procedure according to Schuster and coworkers[179] was employed. Thereby, potassium hydroxide is used as the base and the reaction is conducted in ethanol. Unfortunately, the product could again not be fully purified and yields stayed below 5%. Despite the low yield, **Pre2** was used in the monomer synthesis, which will
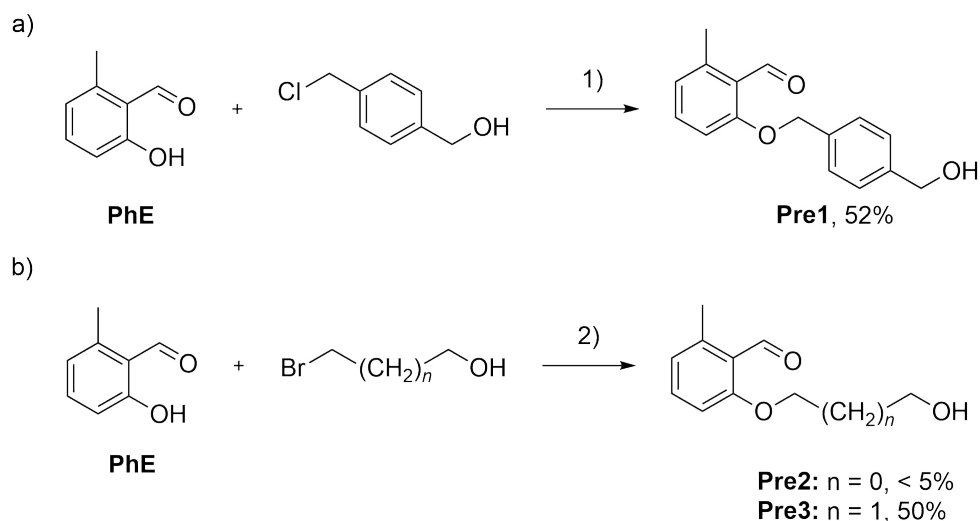
Figure 5.6: Synthesis of monomer precursors **Pre1** (a), **Pre2** and **Pre3** (b). *1) K_2CO_3, 18-crown-6, THF, reflux, 4 d; 2) KOH, EtOH, reflux, o.n.*

be described in detail later, since the impurities may not disturb the next reaction step and the following purification may be more successful at this stage.

Precursor **Pre3** was synthesized as a consequence of the unsuccessful purification of **Pre2**, which further resulted in the unsuccessful synthesis of the corresponding monomer. The synthesis of **Pre3** was also performed according to Schuster *et al.*[179] and gave the product in 50% yield with minor impurities. The impurities proved to be not interfering with the consecutive monomer synthesis and **Pre3** could be employed in the monomer synthesis without further purification.

The fumarate derivative for the last step of the monomer synthesis was chosen to be monoethyl fumarate **Fum** as it is commercially available and was employed in photoenol conjugation previously.[57] The esterification between the precursors **Pre1-3** and **Fum** was performed under *Steglich* conditions with DCC and DMAP (Figure 5.7).[180] The syntheses resulted in yields above 55% for **PhE-Xy** and **PhE-Pr**, yet, **PhE-Et** was not successfully purified.

The monomers **PhE-Xy** and **PhE-Pr** were implemented in polymerization procedures as is described in the next section. **PhE-Et** was not included into the polymerization studies due to the present impurities.

Pre1: R = *p*-xylyl
Pre2: R = ethyl
Pre3: R = propyl

Fum

PhE-Xy: R = *p*-xylyl, 56%
PhE-Et: R = ethyl, 50%
PhE-Pr: R = propyl, 57%
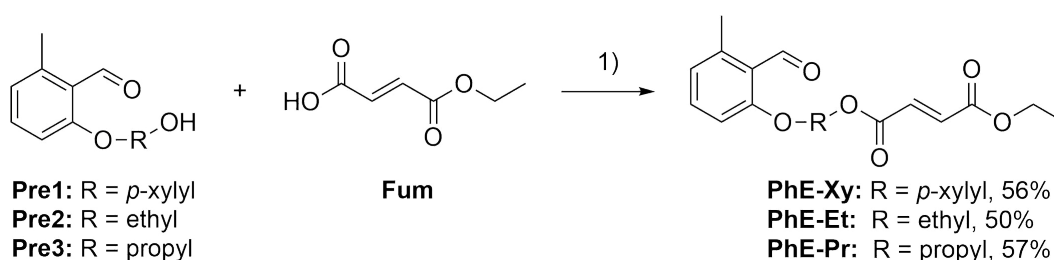
Figure 5.7: Synthetic procedure for the esterification of precursors **Pre1-3** with monoethyl fumaric acid ester **Fum** to the monomers **PhE-Xy**, **PhE-Et** and **PhE-Pr**. *1) DCC, DMAP, DCM, a.t., 4 h.*

5.2 Homopolymerizations of Aliphatic and Aromatic Photomonomers

With the design of the presented monomers, the stoichiometric ratio of functional groups A and B is set to $r = A : B = 1.0$. Thus, choosing a suitable concentration for the step-growth process is critical as the reaction cannot be accelerated by employing excesses of the functional groups. Furthermore, a phenomenon referred to as self-dilution[26] also depends on the initial concentration of the monomer. Self-dilution describes the fact that

the concentration of functional groups is decreased throughout the polymerization. As high conversions are required for obtaining high molar masses in step-growth processes (refer to Chapter 2.5.1 on page 38), the concentration of functional groups can reach a limiting concentration below which the tendency towards cyclization outweighs the chain growth tendency. However, due to the fact that the polymerization is conducted under light irradiation, the reaction kinetics also depend on the Beer-Lambert Law, favoring lower concentrations and thereby increasing the penetration depth of the light. The concentration of the polymerization must therefore be carefully chosen to obtain reasonable reaction rates via sufficient irradiation (requires low concentration) with the lowest cyclization tendency (requires high concentration).

In the following, we will have a closer look into the polymerizations of both monomers **PhE-Xy** and **PhE-Pr**, which will now be referred to as **M1** and **M2** (see Figure 5.8), and the resulting homopolymers as **HP1** and **HP2**, respectively.
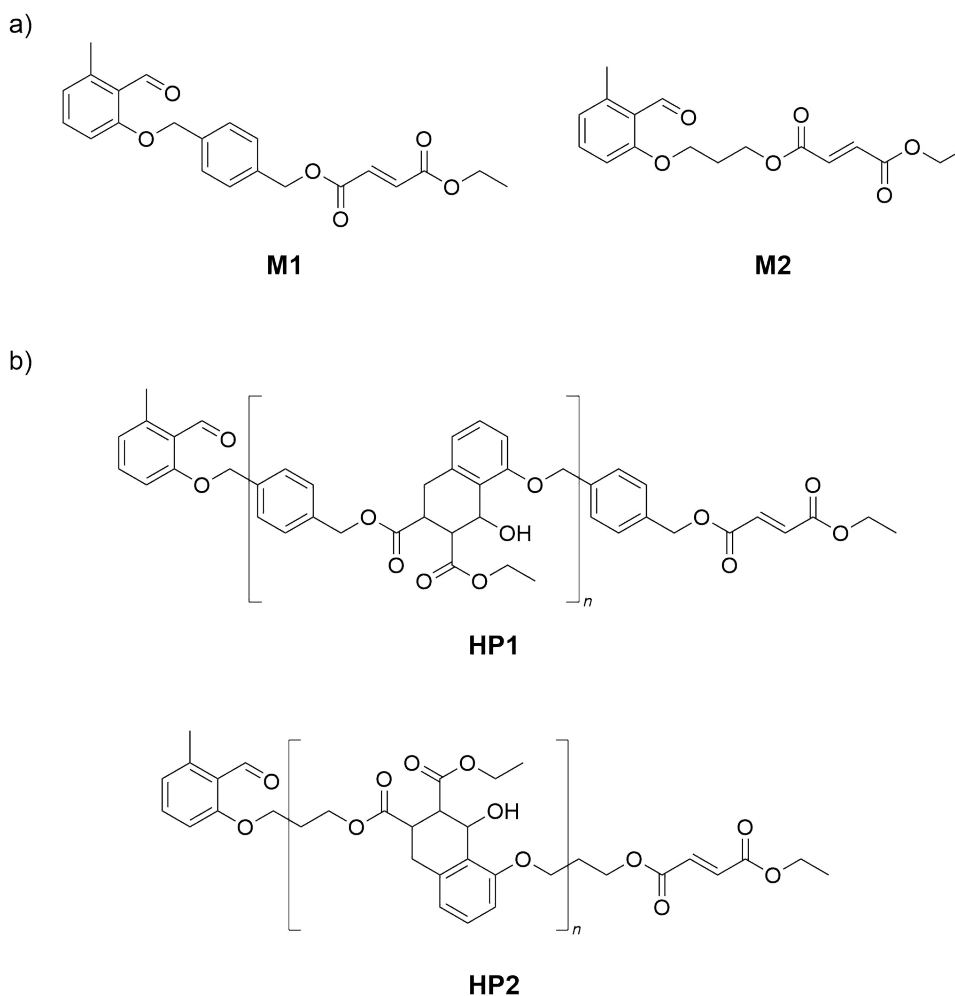
Figure 5.8: Structures of (a) the monomers **M1** and **M2**, and (b) the homopolymers **HP1** and **HP2**. Adapted from Ref. 181. Copyright (2018) American Chemical Society.
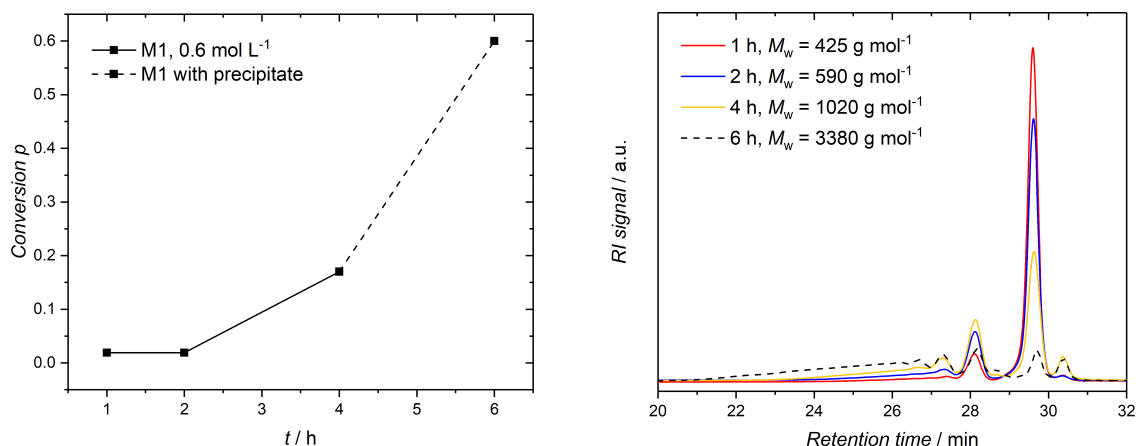
Figure 5.9: Conversion development (left) and SEC traces (right) of the polymerization of **M1** in acetonitrile with an initial concentration of $c = 0.6 \, \mathrm{mol \, L^{-1}}$.

Polymerizations of the monomers **M1** and **M2** were first conducted in acetonitrile. The solvent was purged with argon and the polymerizations were performed under irradiation with $\lambda = 310$ to $400 \, \mathrm{nm}$ ($\lambda_{\max} = 350 \, \mathrm{nm}$). First, polymerizations were conducted with **M1** with concentrations of $0.06 \, \mathrm{mol \, L^{-1}}$ and $0.6 \, \mathrm{mol \, L^{-1}}$ in acetonitrile in order to determine a window of concentrations for kinetic studies. At $0.6 \, \mathrm{mol \, L^{-1}}$, the polymerization resulted in a white precipitate after the reaction time of 4 to 6 h. The precipitate was not soluble in THF, chloroform, DMAc, DMF, dichloromethane or o-chlorobenzene, and could hence not be further characterized. The residual polymer solution was analyzed via NMR spectroscopy to determine the conversion, and SEC (Figure 5.9).

The conversion is determined via NMR spectroscopy (Figure 5.10) by comparing the resonances of the methyl group of the methyl benzaldehyde moiety (a) with the resonances of the cyclohexyl group (b) of the backbone of the polymer by the following equation 5.1.[182]

$$p = \frac{\frac{1}{4} I_\mathrm{P}}{\frac{1}{3} I_\mathrm{M} + \frac{1}{4} I_\mathrm{P}} \tag{5.1}$$

I_P: Integral of polymer backbone

I_M: Integral of monomer functional group

The resonance for the aldehyde proton (c) of the methyl benzaldehyde group is not suitable for deducing the conversion as the proton is rather acidic and is exchanged with deuterium by the analytical solvent. The integral value for the aldehyde moiety is therefore prone to higher errors and was found to be in general lower than expected.
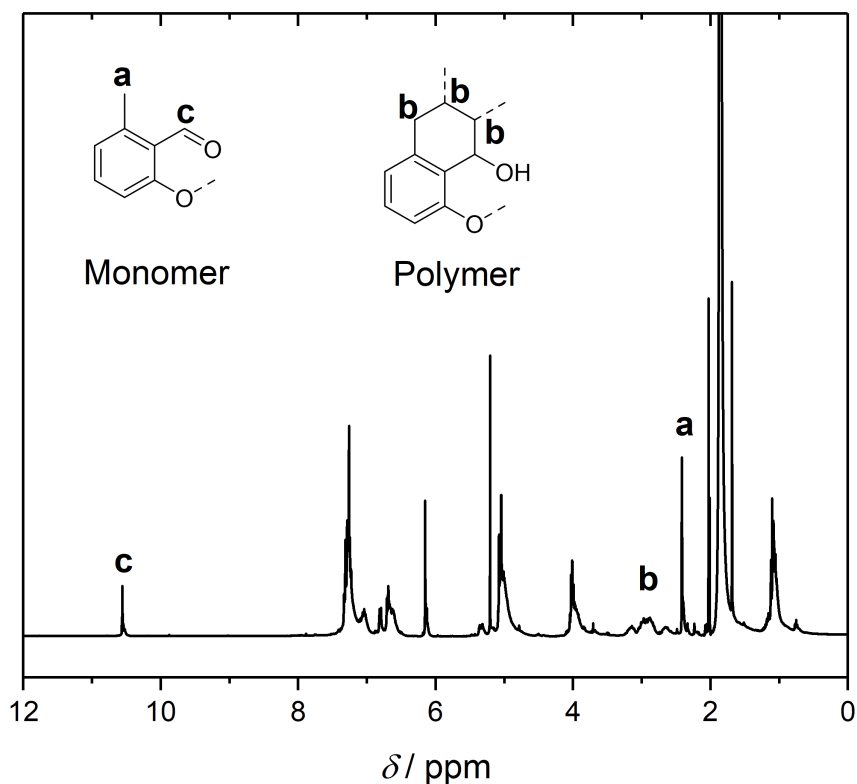
Figure 5.10: ^{1}H NMR spectrum in CDCl$_3$ of the polymerization of **M1** after 4 h in acetonitrile at a concentration of $c = 0.6$ mol L^{-1}. For the determination of the conversion, the integrals of the resonances of the methyl benzaldehyde methyl group (a) and the resonances of the cyclohexyl moiety (b) in the polymer backbone are compared with equation 5.1. The aldehyde resonance (c) is not suitable for the conversion calculation as the proton is easily exchanged with deuterium of the analytical solvent.

The conversion development does not follow the typical kinetics of a step-growth polymerization, which is fast at the beginning and shows a reduced polymerization rate towards high conversions. The polymerization of **M1** proceeds slowly during the first hours and becomes faster after 3 to 4 h of irradiation, clearly evidencing that a concentration of $c = 0.6$ mol L^{-1} is not suitable for the polymerization of **M1**.

The lower concentration of 0.06 mol L^{-1} for **M1** again led to polymer that was insoluble. The polymer for **M1** appears to be insoluble regardless of the polymerization conditions and was not further polymerized in acetonitrile. It was shown that performing the polymerization in dichloromethane enhances the solubility of high molecular weigth species drastically, which will be discussed in detail later in this section.

The monomer **M2** was polymerized in acetonitrile with various concentrations of c = 0.06, 0.1, 0.2 and 0.4 mol L^{-1}. A concentration of $c = 0.4$ mol L^{-1} thereby resulted in insoluble white precipitate after 12 h reaction time, and polymerizations with $c =$ 0.6 mol L^{-1} were not further conducted. The lower concentrations did not result in any

precipitate even after 18 h, suggesting that the aliphatic spacer improves the solubility of the polymer most probably due to a higher flexibility of the chains. However, the polymerizations did not reach conversions higher than 95%, despite the long reaction time of 18 h. Particularly the polymerization with $c = 0.06\,\mathrm{mol\,L^{-1}}$ shows high amount of material with a residual low apparent molecular weight in SEC analysis, which implies that the reaction is prone to cyclization at this concentration. The amount of low molecular weight species decreases with increasing concentration as depicted in Figure 5.11. The SEC results suggest that the higher concentration of $c = 0.2\,\mathrm{mol\,L^{-1}}$ produces the highest amount of polymer (between 26 and 20 min retention time). In all three cases, the amount of monomer (at 30 min retention time, refer to Figure C.27 on page 162) is reduced to a minimum.

Since all attempts to polymerize **M2** in acetonitrile resulted in conversions below 99%, the solvent was exchanged with dichloromethane, which was successfully employed in photoenol polymerizations recently in our group.[57] Here, di-functional monomers were applied in AA- and BB-type step-growth processes. By adapting the ratio between the functional groups A and B, the conversion was pushed to high values, and concentrations below $0.1\,\mathrm{mol\,L^{-1}}$ proved to result in fast reaction kinetics. A concentration study of **M2** with $c = 0.05$, 0.1 and $0.2\,\mathrm{mol\,L^{-1}}$ was conducted in dichloromethane in small batches of 15 mg and the resulting SEC traces are depicted in Figure 5.12. The
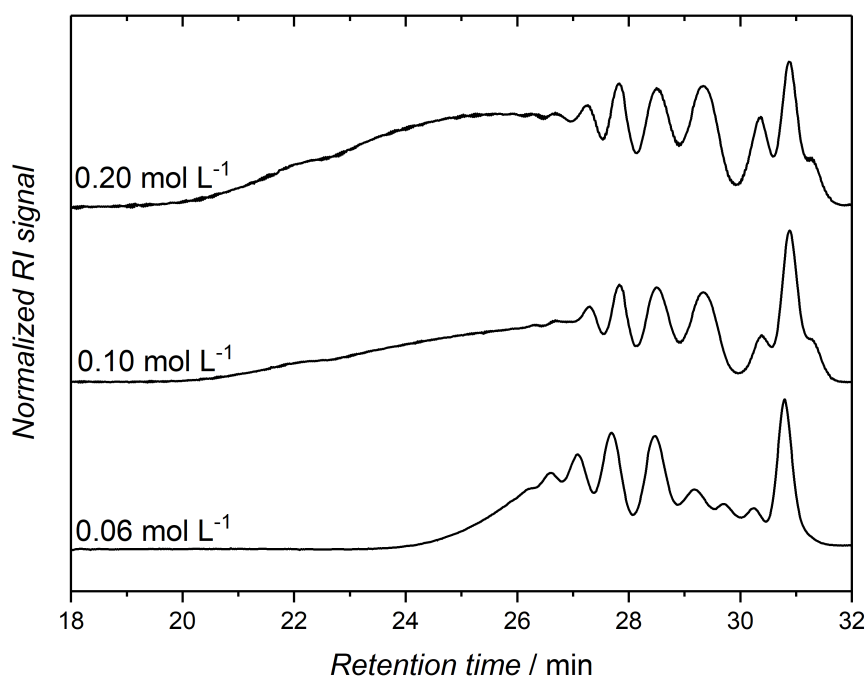
Figure 5.11: SEC traces of the polymerization of **M2** in acetonitrile after 18 h for various concentrations.
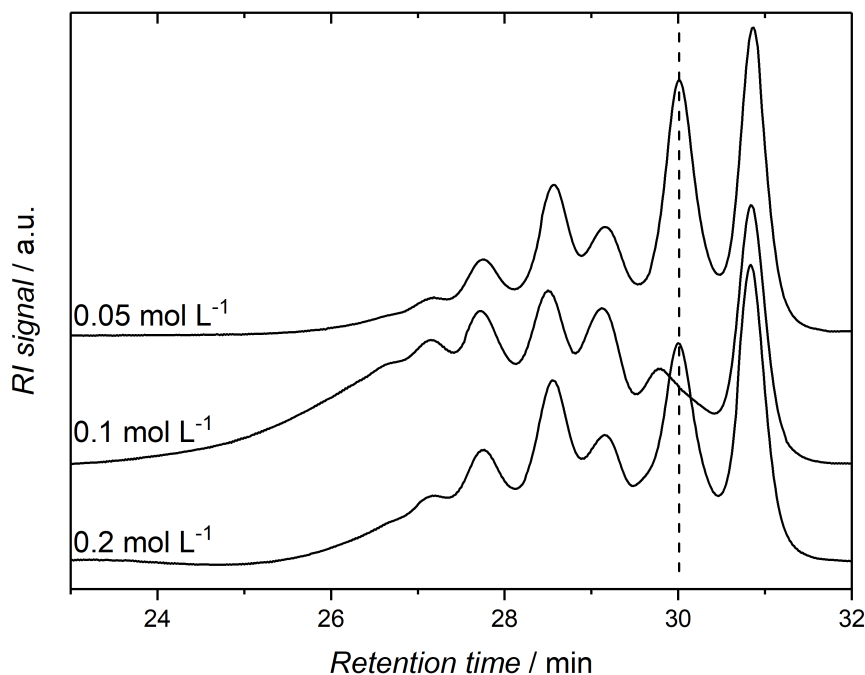
Figure 5.12: SEC traces of the polymerizations of **M2** in dichloromethane (batch size: 15 mg) with various concentrations. The dotted line marks the retention time of the monomer. Adapted with permission from Ref. 181. Copyright (2018) American Chemical Society.

SEC traces show that the monomer is most efficiently consumed with a concentration of $c = 0.1 \, \mathrm{mol \, L^{-1}}$ and furthermore resulted in the highest overall molecular weight with $M_{\mathrm{w}} = 1000 \, \mathrm{g \, mol^{-1}}$. For the concentrations $c = 0.05$ and $0.2 \, \mathrm{mol \, L^{-1}}$, the achieved overall molecular weight is $M_{\mathrm{w}} = 520$ and $900 \, \mathrm{g \, mol^{-1}}$, respectively. All polymerizations contain low molecular weight material below 30 min retention time which may be associated with cyclic species. The conformation of the cyclic products leads to a change in the hydrodynamic radii and thus to a shift in retention time.[183,184] The low concentration of $c = 0.05 \, \mathrm{mol \, L^{-1}}$ may result in slow kinetics and thus to smaller molar masses. The smaller molar masses for the higher concentration $c = 0.2 \, \mathrm{mol \, L^{-1}}$ could result from low penetration depth suggested by Beer-Lambert's law. Consequently, the following polymerizations were conducted at a concentration of $c = 0.1 \, \mathrm{mol \, L^{-1}}$.

Dichloromethane as a solvent also provided soluble polymer for **M1**, which resulted in an insoluble white precipitate when polymerized in acetonitrile earlier. A test reaction was performed between methoxy protected photoenol **PhE-OMe** and diethyl fumarate in dichloromethane and acetonitrile (Figure C.28, page 162) in order to identify side reactions that may occur in acetonitrile and thereby produce insoluble polymer. Yet, both reactions resulted in the same ^{1}H and ^{13}C NMR resonances, and side reactions
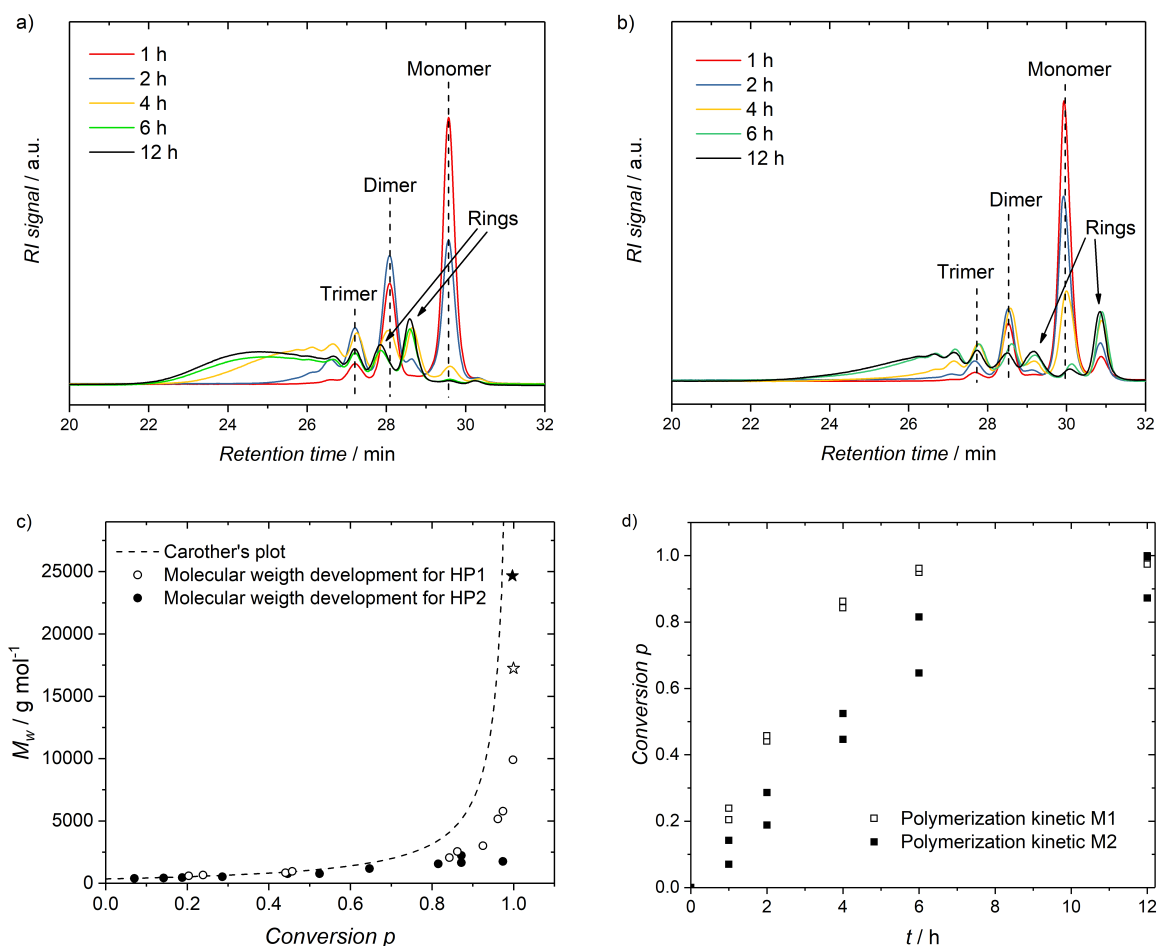
Figure 5.13: SEC traces of **M1** (a) and **M2** (b) polymerized in dichloromethane with $c = 0.1\,\mathrm{mol\,L^{-1}}$; (c) Molecular weight development for the polymers **HP1** (hollow), **HP2** (filled) and after precipitation in methanol (stars) compared to the theoretical Carother's plot (dashed line); (d) Conversion development of the polymerizations of **M1** (hollow) and **M2** (filled). Adapted with permission from Ref. 181. Copyright (2018) American Chemical Society.

were not identified (Figures C.29 and C.30, page 163). It appears that the conditions of the polymerization cannot be realized on a small molecule scale.

The polymers **HP1** and **HP2** were prepared in batches of 100 mg in dichloromethane with a concentration of $c = 0.1\,\mathrm{mol\,L^{-1}}$. Samples were taken at specific time intervals of 1, 2, 4, 6 and 12 h, dried under air and subsequently redissolved in THF or deuterated chloroform for characterization. The SEC traces for both polymerizations are depicted in Figure 5.13a and b, and show a consumption of the monomer along the formation of polymeric material. Likewise, both polymerizations show the formation of small oligomeric material, most probably originating from ring formation.[153,154] While the number of linear dimers and trimers slowly decreases throughout the polymerization, the SEC signals for cyclic, and thus nonreactive oligomers increase and do not show any reduction of intensity. The amount of high molar mass polymer appears to be higher

for the polymerization of **M1**, and a comparison of the molecular weights M_w of the crude polymer mixtures with the theoretical Carother's plot (Figure 5.13c) underpins the assumption of different molecular weight developments. The theoretical values for M_w are calculated via Equation 5.2[182] with $M_M = 350\,g\,mol^{-1}$.

$$M_w = M_M \times \frac{1+p}{1-p} \tag{5.2}$$

M_w: weight-average molecular weight

M_M: molecular weight of monomer

p: fractional conversion

The M_w values for **M2** stay below the theoretical calculations and thereby suggest that **M2** produces more low molecular weight material, e.g., rings. The conversion development plotted against the reaction time (Figure 5.13d) additionally indicates that **M2** reacts slower than **M1**, however reaches high conversions after 12 h. Since the polymerization conversion is high (> 99%), it implies that functional groups are consumed and yet, molecular weigths are low. Thus, the polymerization of **M2** appears to result in either cyclic oligomers, or side reactions render the oligomer end groups non-reactive. In either case, the polymers **HP1** and **HP2** can be isolated from the oligomers via precipitation in methanol at ambient temperature, resulting in polymers with $M_w = 17\,800$ and $24\,700\,g\,mol^{-1}$ for **HP1** and **HP2**, respectively, as is depicted in Figure 5.14. Via SEC analysis, the efficient separation of the high molecular weight polymers for **HP1** (Figure C.31 on page 164) was confirmed, which underlines the efficient separation.

The oligomers that were separated from the polymer via precipitation were further analyzed via ^{1}H NMR spectroscopy in CDCl$_3$ (Figures C.32 and C.33, pages 164 and 165). The spectra of the oligomeric fractions of the polymerizations of both **M1** and **M2** were compared to the NMR spectra of the corresponding monomers. The spectra of the oligomers do not show any residual double bonds, underpinning the formation of cyclic products. Linear oligomers would yield residual double bonds and, thus, longer irradiation times would translate into higher molecular weight polymer. The homocoupling of the photoenol end groups[57] as unwanted side reaction would also have resulted in residual fumarate end groups. Hence, the homocoupling can be neglected as a factor for the generation of low molecular weight polymers.

The differences in cyclization tendencies between **M1** and **M2** is supported by the isolated yield of the polymerizations. While **HP1** is generated with $30\pm5\%$, **HP2** is received with yields of $8\pm2\%$, clearly indicating that less high molecular weight mate-
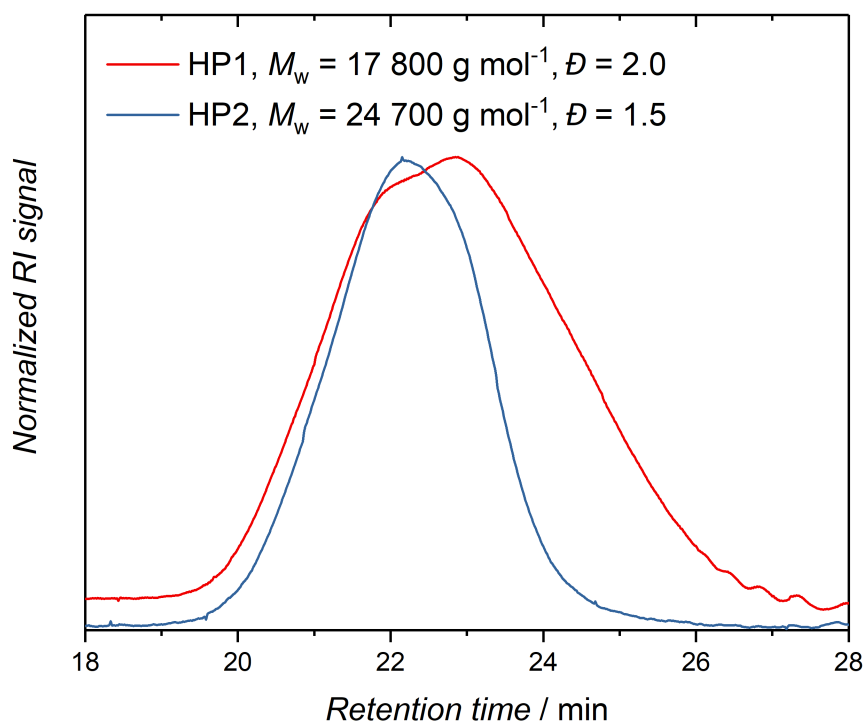
Figure 5.14: SEC traces of **HP1** (blue) and **HP2** (red) after precipitation in methanol. Adapted with permission from Ref. 181. Copyright (2018) American Chemical Society.

rial is produced by the polymerization of **M2**. The cyclization tendencies of monomers for step-growth polymerizations have been described by Kricheldorf,[26] concluding that step-growth polymerizations with monomers containing aliphatic backbones have a lower cyclization tendency compared to aromatic backbones due to the preferred all-trans configuration of aliphatic chains. In the present system, however, the monomers do not match the conclusions of Kricheldorf and the aliphatic monomer appears to have a higher cyclization tendency than the aromatic equivalent.

The presented monomers and polymers offer exceptional possibilities for variations via the backbone and the side chain. Therefore, it is necessary for the structures, especially the esters, to be stable under the polymerization conditions. The change in retention time that was observed for the polymerizations of **M1** and **M2** may also originate from cleaved side and end groups. The structures of the polymers were thus analyzed via the hyphenation of SEC and high-resolution ESI-MS and will be described in detail in the next section.

5.3 SEC-ESI-MS Characterization of Photo-Homopolymers

The homopolymers **HP1** and **HP2** were analyzed via high resolution SEC-ESI-MS with sodium doped solvent (THF/methanol). The crude polymers, before precipitation, were employed in the analysis, as high molecular weight polymers ionize less efficiently than small oligomers. First, **HP1** is characterized between retention times $t = 16$ and 21 min, thereby reducing the signals for double charged species (see Figure C.34 for the chro-
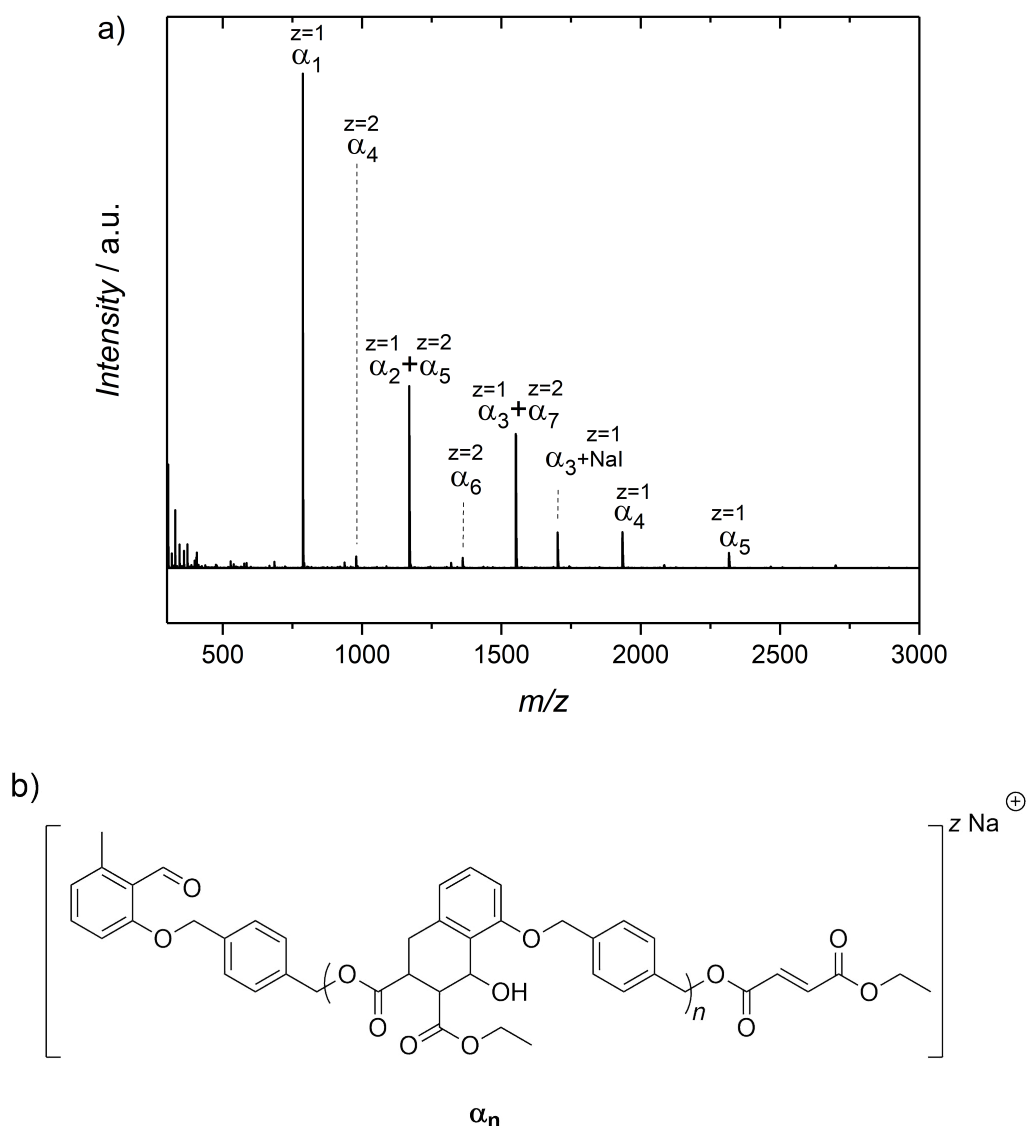
Figure 5.15: (a) SEC-ESI mass spectrum of crude **HP1** integrated from 16 to 21 min; (b) Structures of **HP1** that were identified in the mass spectrum; z corresponds to the charge and equally to the number of sodium counterions. Adapted with permission from Ref. 181. Copyright (2018) American Chemical Society.

matogram). The resulting mass spectrum is shown in Figure 5.15. The spectrum shows species α_n from the monomer to double charged heptamers, as well as background signals. The background spectrum can be found in Figure C.36 on page 166. The double charged and mono charged species can have the same mass, e.g., α_5 and α_2 with 1169.4143 Da. The species can, however, be distinguished by the distances in the isotopic pattern, which is ca. 1 Da for mono charged α_2, but ca. 0.5 Da for α_5. A zoom into the isotopic pattern of the mentioned oligomers is shown in Figure C.37 on page 167.

The mass of the repeating unit of **HP1** was identified as $m/z = 382.142$ Da and fits to each species identified. Theoretical calculations support the suggested structure in Figure 5.15b and are in excellent agreement with the experimental values. A list of all experimental and theoretical values can be found in Table C.2 on page 168. Structures with cleaved end or pendant groups were not identified and we can assume that the structure of **HP1** is stable under the polymerization conditions. Cyclic oligomers cannot be distinguished from the linear oligomers in mass spectrometry as the species have the same mass.

The SEC-ESI mass spectrum of crude **HP2** is shown in Figure 5.17, integrated from 17 to 22 min (see Figure C.35, page 166 for chromatogram) along with the identified structures. The most prominent species are the oligomers of the homopolymer A_n with a repeating unit of $m/z = 320.126$ Da, however, various other structures were detected. The additional detected masses were assigned to the structures B_n, which lack the **PhE** end group, and structures C_n that have lost both the **PhE** and the **Fum** end group.

Species B_n are 148.053 Da smaller than the intact oligomers A_n. A ring-closure side reaction is depicted in Figure 5.16 that results in a molecule with the exact mass $m/z = 148.053$ Da. The mechanism shown here describes a rearrangement with a cyclic six-membered transition state which yields a dioxine heterocycle. The mechanism is described as a radical mechanism due to the UV-light irradiation which may produce radical species, yet the reaction may as well be concerted. The cleaved photoenol group yields in an ethyl ester end group.
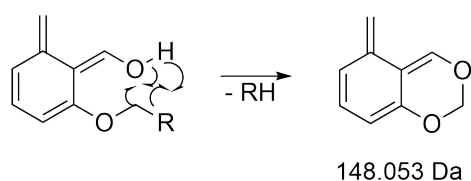
148.053 Da

Figure 5.16: Proposed mechanism for the cleavage of the **PhE** end group which results in a molecule with the required mass $m/z = 148.053$ Da.

a)

b)

Figure 5.17: (a) SEC-ESI mass spectrum of **HP2**, integrated from 17 to 22 min retention time. (b) Structures of **HP2** that were identified in the mass spectrum. Adapted with permission from Ref. 181. Copyright (2018) American Chemical Society.
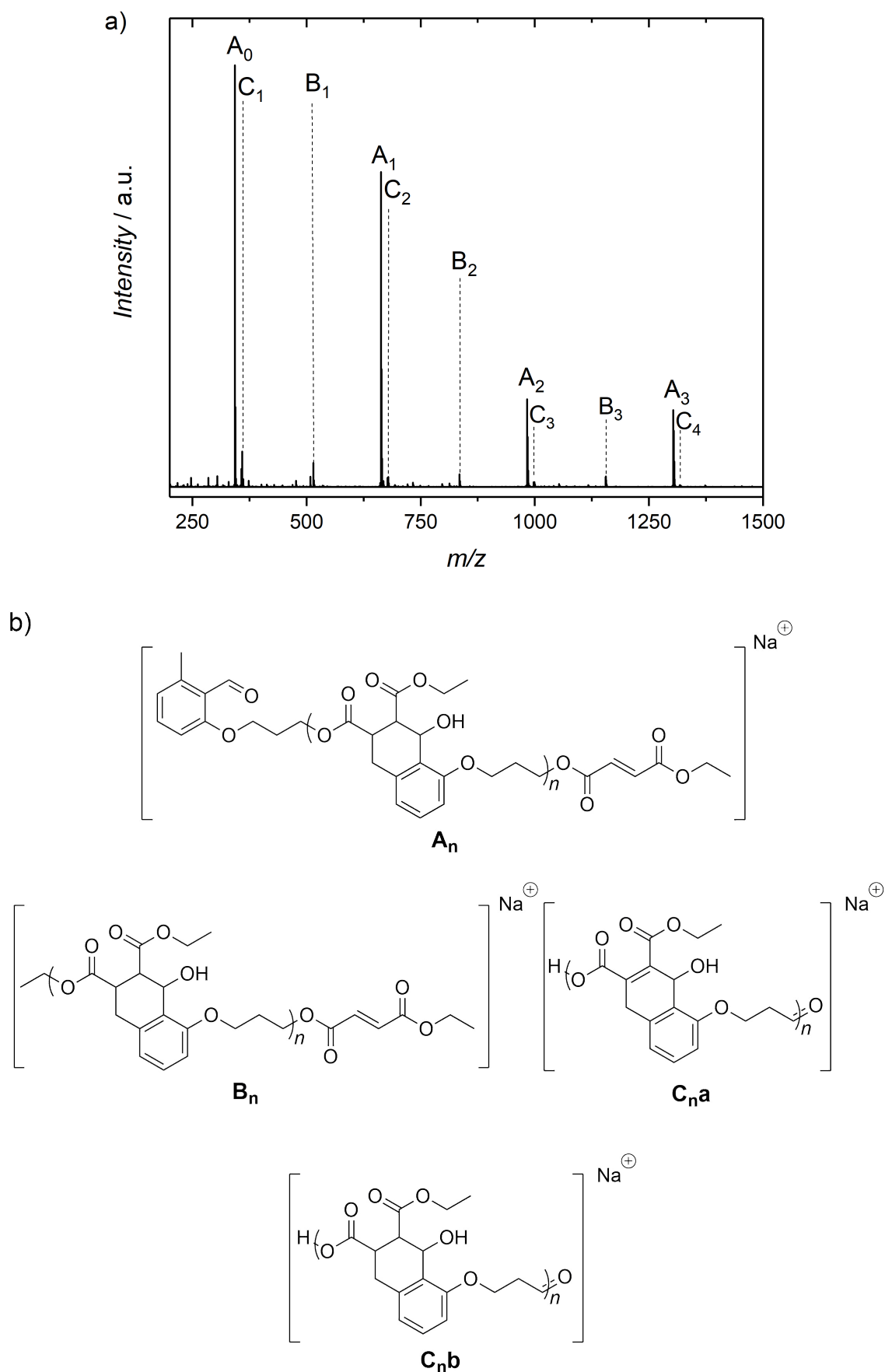
In addition, the oligomers lose the **Fum** end group and result in the species C_n. The isotopic pattern of the C_n oligomers, however, does not match the patterns for A_n and B_n. If the pattern consists of two structures with a mass difference of ca. 2 Da, the isotopic pattern will resemble the theoretical simulations (refer to Figure C.38 on page 167). It is suggested that the structure $C_n b$ may lose the two most acidic protons in the cyclohexyl unit and yield the double bond of structure $C_n a$, thereby creating the unique isotopic pattern. The ester bonds of the pendant ethyl groups appear to be stable as for **HP1**, since there is only one species C_n detected for every A_n. If the side chains had been cleaved, the *m/z* values of the oligomers would show a degradation pattern with masses in the distance of every missing pendant group.

The masses of every individual species match perfectly the theoretical values as can be seen in Table 5.1.

Table 5.1: Theoretical and experimental *m/z* values of **HP2** found in Figure 5.17a. Adapted from Ref. 181. Copyright (2018) American Chemical Society.

Species	$(m/z)_{theo}$	$(m/z)_{exp}$	$\Delta(m/z)$
A_0	343.1152	343.1150	0.0002
$C_1 a$	357.0945	357.0940	0.0005
$C_1 b$	359.1098	359.1096	0.0002
B_1	515.1888	515.1887	0.0001
A_1	663.2412	663.2405	0.0007
$C_2 a$	677.2205	677.2194	0.0011
$C_2 b$	679.2361	679.2354	0.0007
B_2	835.3148	835.3137	0.0011
A_2	983.3672	983.3668	0.0004
$C_3 a$	997.3454	997.3465	0.0011
$C_3 b$	999.3606	999.3621	0.0015
B_3	1155.4407	1155.4400	0.0007
A_3	1303.4932	1303.4933	0.0001
$C_4 a$	1317.4719	1317.5037	0.0319
$C_4 b$	1319.4754	1319.4881	0.0127

The end group stability of the photo-generated polymers **HP1** and **HP2** as well as the cyclization tendencies and reaction kinetics vary widely. The most obvious difference between the systems is the backbone structure. **HP1** contains a xylene backbone whilst **HP2** contains a propyl group. The backbone structure appears to have an influence on the end group stability of the polymer and results in the release of small molecules. As mentioned earlier, a release of small molecules is not desirable for the polymerizations in MOFs. While non-reactive oligomers and side products can be removed by precipitation in conventional polymerization processes, the polymerization in MOF channels requires absolute stability as small molecules may block the pores and disturb the polymerization procedure. So far, it seems that **M1** is fulfilling the requirements for MOF polymerizations, yet **M2** appears to be not suitable.

Albeit, the side reactions of the end group may originate from small impurities rather than the backbone structure. To exclude any possibility of catalysis of the side reactions by impurities in the monomer, copolymerizations were performed with both monomers **M1** and **M2** and again, SEC-ESI-MS was applied to characterize the polymer structures.

5.4 Photo-Copolymerization and Detailed SEC-ESI-MS Characterization

Copolymerizations of **M1** and **M2** were performed in dichloromethane for 12 h with a concentration of $c = 0.1 \, \text{mol} \, \text{L}^{-1}$ and varying monomer ratios $r = \text{M1:M2} = 0.75, 0.50$ and 0.25 mol%. The resulting copolymers are termed **CP1**, **CP2** and **CP3**, respectively. Conversions reached over 99% for all three copolymerizations. The composition of the copolymers was determined via NMR spectroscopy as depicted in Figure C.39 on page 168. The xylene moiety of **M1** is associated with resonances between 7.3 and 7.5 ppm. The value for the integral decreases with increasing amount of **M2** in the copolymerization. The percentage of **M2** units was calculated as $9 \pm 1\%$, $39 \pm 7\%$ and $60 \pm 3\%$ for **CP1**, **CP2** and **CP3**, respectively, which supports the conclusion stated above that **M2** polymerizes more slowly than **M1**. The copolymers were readily precipitated in methanol and resulted in yields of 22-30%. The SEC graphs of the precipitated copolymers are shown in Figure 5.18.

The crude copolymers were analyzed via SEC-ESI-MS in order to determine the structure and stability of the end groups. If minor impurities in monomer **M2** were able to catalyze the end group fragmentation, a copolymerization between the monomers **M1** and **M2** would also result in the side reaction of the end group, although independent of
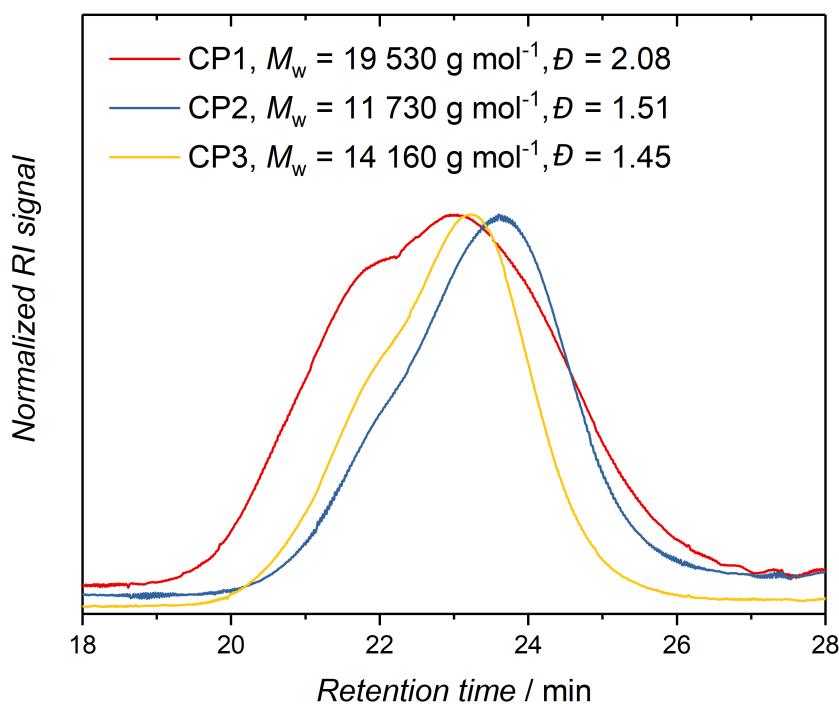
Figure 5.18: SEC traces of the copolymers **CP1**, **CP2** and **CP3**. Adapted with permission from Ref. 181. Copyright (2018) American Chemical Society.

the backbone structure of the terminal monomer unit of the chains. For the examination of the structures of the copolymers, the SEC-ESI mass spectrum of **CP1** will be discussed in detail, and is depicted in Figure 5.19a. The spectrum shows the masses for the copolymer structures $A_n\alpha_m$ and the homopolymer species A_n and α_n. The spectra for **CP2** and **CP3** (Figures C.42 and C.43 on page 170) only contain low intensity signals for α_n species. Due to the low intensitiy, the concentration of any degradation products of α_n oligomers may be below the detection limit. The spectrum of **CP1** provides sufficient intensity for the detailed characterization for both A_n and α_n species. In Figure 5.19, the degradation products for A_n, namely B_n, are not assigned for clarity. Oligomers C_n could not be identified, most probably due to insufficient concentrations. The spectrum of **CP1** supports the observation that the stability of the end groups depends on the backbone structure. Only species A_n and $A_n\alpha_m$ containing **M2** repeating units result in corresponding structures B_n and $B_n\alpha_m$ with cleaved **PhE** end groups. The repeating unit between the oligomers with intact end group and oligomers with fragmented end group is $m/z = 148.053$ Da as was already observed for homopolymer **HP2**. The exact masses for the assigned structures for the copolymers are listed in Table 5.2 and are compared to the experimental values. The experimental and theoretical values are in good agreement, and support the suggested structures for the copolymers.
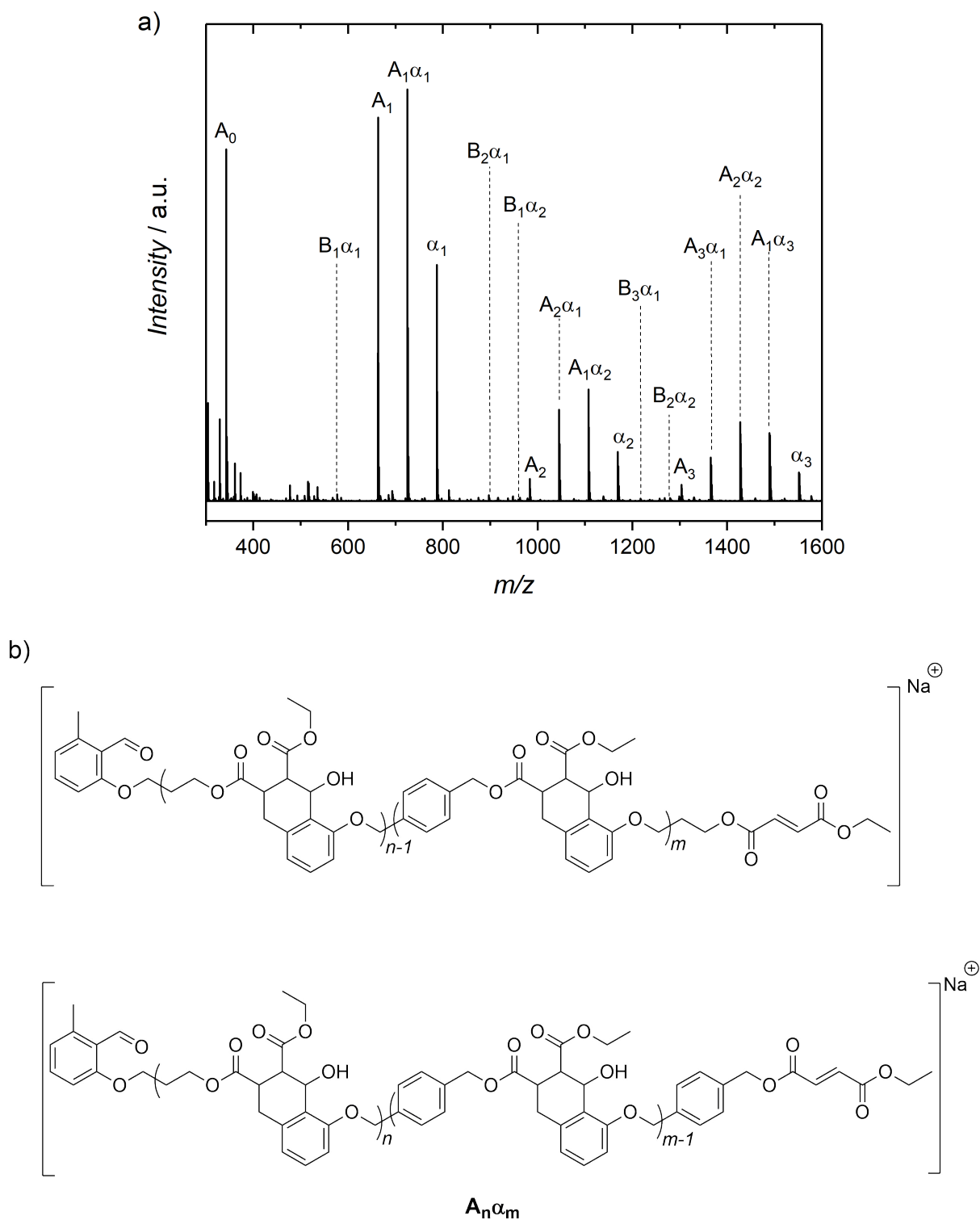
Figure 5.19: (a) SEC-ESI mass spectrum of copolymer **CP1**, integrated from 16 to 22 min retention time. (b) Structures $A_n\alpha_m$ of the copolymer with intact end groups. Adapted with permission from Ref. 181. Copyright (2018) American Chemical Society.

Table 5.2: Theoretical and experimental *m/z* values of **CP1** found in Figure 5.19a. Adapted from Ref. 181. Copyright (2018) American Chemical Society.

Species	$(m/z)_{theo}$	$(m/z)_{exp}$	$\Delta(m/z)$
A_0	343.1152	343.1147	0.0005
B_1	515.1888	515.1887	0.0001
$B_1\alpha_1$	577.2044	577.2035	0.0009
A_1	663.2412	663.2404	0.0008
$A_1\alpha_1$	725.2568	725.2559	0.0009
α_1	787.2725	787.2712	0.0013
A_1 + NaI	813.1338	813.1354	0.0016
B_2	835.3148	835.3126	0.0022
$B_2\alpha_1$	897.3304	897.3283	0.0021
$B_1\alpha_2$	959.3461	959.3441	0.0020
A_2	983.3672	983.3668	0.0004
$A_2\alpha_1$	1045.3828	1045.3812	0.0016
$A_1\alpha_2$	1107.3985	1107.3970	0.0015
B_3	1155.4407	1155.4393	0.0014
α_2	1169.4141	1169.4121	0.0020
$B_3\alpha_1$	1217.4564	1217.4544	0.0020
$B_2\alpha_2$	1279.4720	1279.4699	0.0021
A_3	1303.4932	1303.4918	0.0014
$B_1\alpha_3$	1341.4877	1341.4855	0.0022
$A_3\alpha_1$	1365.5088	1365.5070	0.0018
$A_2\alpha_2$	1427.5245	1427.5231	0.0014
$A_1\alpha_3$	1489.5401	1489.5385	0.0016
α_3	1551.5558	1551.5534	0.0024

The repeating unit of the herein presented polymers are unique in terms of the DA cycloadduct neighboring a phenyl group as well as the alternation of aliphatic and aromatic regions in the backbone. The thermal properties, namely glass transition temperature T_g and melting point T_m, have therefore not yet been investigated for this specific

cycloadduct structure. A comparison with the well-established polymers used in industry is, because of the unique structure, hardly possible, yet, polyethylene terephthalate (PET) is a polymer that also provides alternating aromatic and aliphatic backbone segments. PET is known to form amorphous to crystalline morphologies and features T_g values ranging from 67 to 81 °C.[185] The homopolymers **HP1** and **HP2**, and the copolymers **CP1**, **CP2** and **CP3** were analyzed via differential scanning calorimetry (DSC) in the range from -50 to 300 °C with a heating/cooling rate of $10 \, \text{K min}^{-1}$. The T_g values were determined in the second heating cycle in the order of 92.2 (**HP2**) > 81.3 (**HP1**) = 81.3 (**CP2**) > 81.2 (**CP1**) > 75.4 °C (**CP3**) (Figure C.44 on page 171). The polymers therefore feature T_g values comparable with semi-crystalline and crystalline PET. The melting temperature T_m was not reached for any of the homopolymers or copolymers and lies above 300 °C.

The thorough analysis via homo- and copolymerization of **M1** and **M2** suggests that **M1** is suitable for polymerizations in confined environments.

5.5 Theoretical Calculations of Binding Energies of Photomonomers in MOFs

For polymerizations inside MOF channels, the MOF structure has to be chosen carefully, as the pores may not be too small for the monomer to diffuse into the structure, however, large pores result in lower control over the polymerization system.[103] Therefore, calculations were performed by the group of Prof. Wenzel from the KIT. Two MOF structures were investigated: Cu-BDC-dabco and Cu-BPDC-dabco. The structures of the linkers are depicted in Figure 5.20.
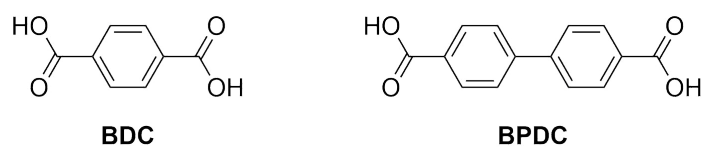
Figure 5.20: Linkers of the MOFs Cu-BDC-dabco and Cu-BPDC-dabco.

DSC measurements were performed by R. V. Schneider from the group of M. A. R. Meier.
Theoretical calculations were performed by J. Helfferich from the group of W. Wenzel.
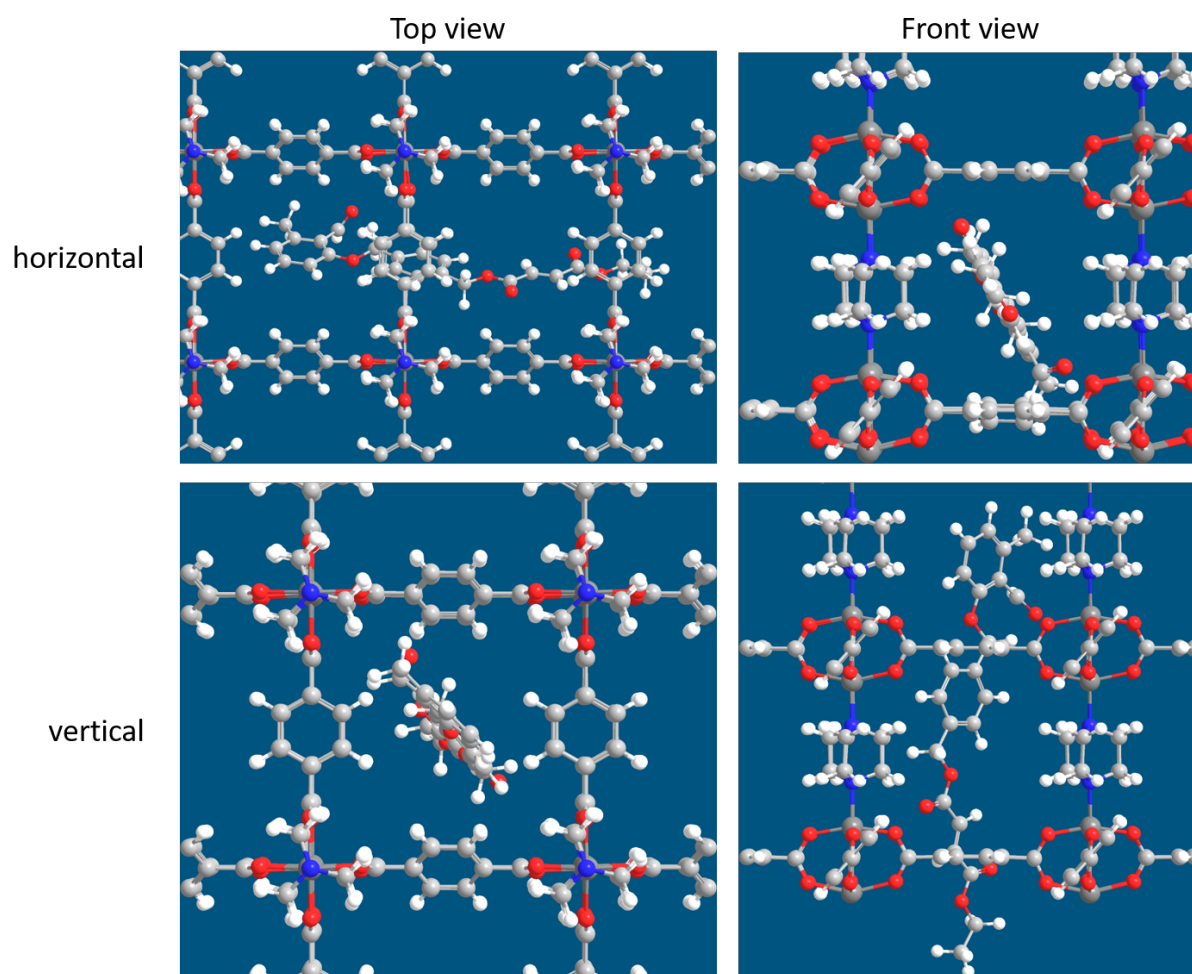
Figure 5.21: Position of **M1** in Cu-BDC-dabco in horizontal (top) and vertical (bottom) orientation. For **M2** in Cu-BDC-dabco refer to Figure C.45 on page 172. *Grey:* carbon; *white:* hydrogen; *red:* oxygen; *blue:* nitrogen.

Table 5.3: Binding energies (in eV) of each monomer in the MOF structures Cu-BDC-dabco and Cu-BPDC-dabco in vertical and horizontal configuration.

Monomer	Vertical configurations		Horizontal configuration	
	Cu-BDC-dabco	Cu-BPDC-dabco	Cu-BDC-dabco	Cu-BPDC-dabco
M1	-0.05994	0.06515	-0.49902	-0.04352
M2	-0.25837	0.00751	-0.41797	-0.06206

To gain a deeper understanding of the molecular configurations, quantum-chemical calculations were performed using the MOPAC2016 software[186] with the semi-empirical PM7 method.[187] Each monomer was inserted into both MOF structures in either horizontal or vertical configuration (Figure 5.21) and the binding energies of the monomers in the MOF structure were calculated (Table 5.3).

The binding energies of the monomers are negative in almost all cases. A negative binding energy is favored by the system and is an indicator for the successful absorption of the molecule into the structure. For the vertical orientation in Cu-BPDC-dabco (Figure 5.22), the binding energies are indeed positive, but small. The energies are comparable with $k_B T$ at ambient temperature (0.29 $k_B T$ for **M1** and 2.5 $k_B T$ for **M2**). Therefore, a significant amount of monomer is expected to diffuse into the structure, given that the concentration of monomer in the surrounding solution is high.

Furthermore, the binding energies in the horizontal orientation are lower in all cases, suggesting that the horizontal orientation is preferred by both monomers. Judging by eye from the optimized configuration, the monomers may not be able to move from horizontal to vertical position in the smaller Cu-BDC-dabco. The vertical configuration may be accomplished in Cu-BPDC-dabco, however, as soon as two or more monomers react with each other, the probability of the structures to change from horizontal to vertical position decreases.
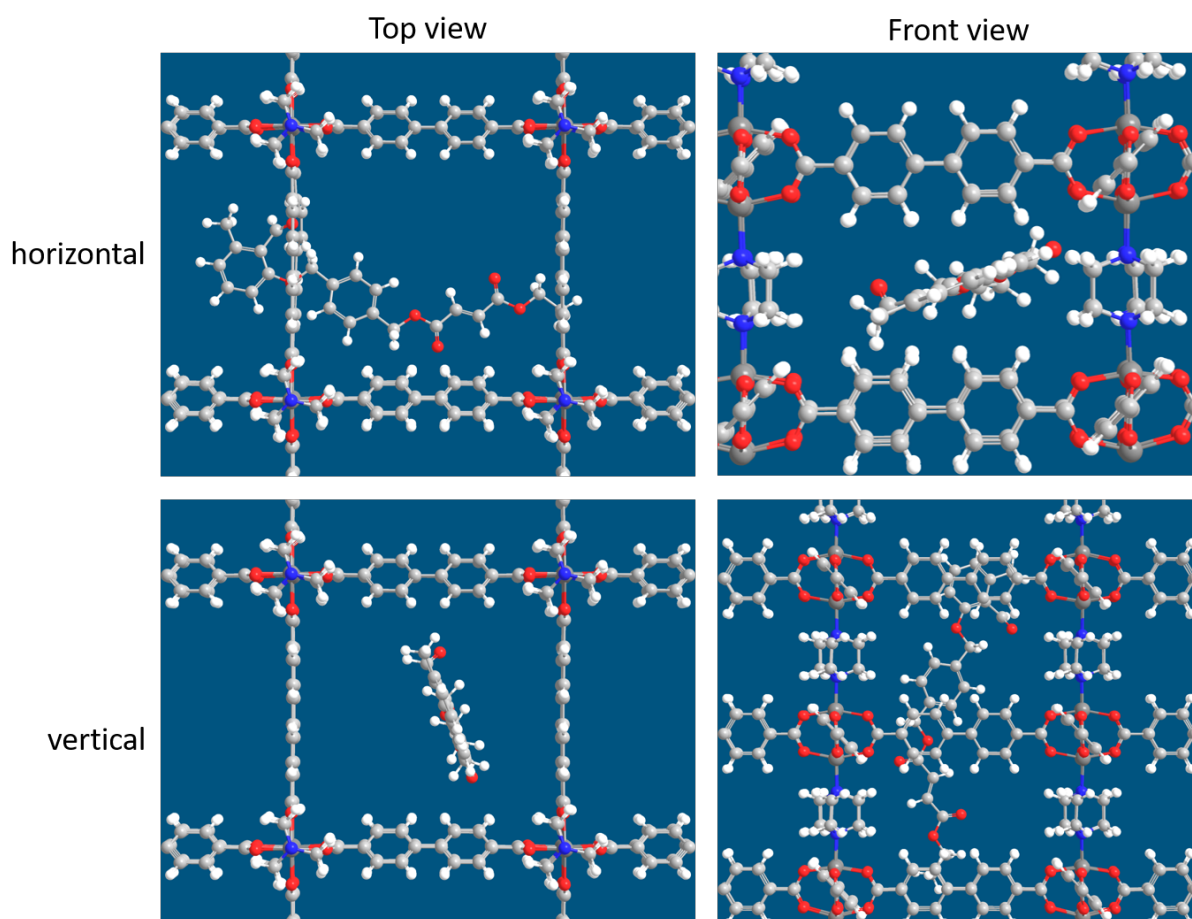
Figure 5.22: Position of **M1** in Cu-BPDC-dabco in horizontal (top) and vertical (bottom) orientation. For **M2** in Cu-BPDC-dabco refer to Figure C.46 on page 172. *Grey:* carbon; *white:* hydrogen; *red:* oxygen; *blue:* nitrogen.

5.6 Summary

The development of a light-induced step-growth polymer was successful by employing photo-induced DA reactions via the photoenolization of α-methyl benzaldehydes. Two monomers were synthesized, which vary in backbone structure and that undergo step-growth polymerization in dichloromethane with conversions >99%. The polymerization processes were thoroughly investigated by SEC-ESI-MS and revealed differences in end group stability. In SEC-ESI-MS, the monomer with an aliphatic backbone structure shows small intensities of species with fragmented end groups. Additionally, the aliphatic monomer possesses a higher tendency towards cyclization, resulting in low polymerization yields (<10%). The aromatic monomer did not show any evidence of end group fragmentation and, in fact, has a lower cyclization tendency, hence, the polymerization resulted in higher isolated yields (ca. 30%). The pendant groups of both aromatic and aliphatic polymers were stable throughout the polymerization process. Furthermore, the polymers with the unique DA repeating unit provide T_g values comparable with commercially available PET.

The space requirement for the monomers was calculated in Cu-BDC-dabco and Cu-BPDC-dabco. It was found that the monomers can diffuse into both Cu-BDC-dabco and Cu-BPDC-dabco. Moreover, the monomers prefer to organize along the dabco-layers of the MOF structures. In general, the polymerization may be possible in both structures, yet, Cu-BDC-dabco may result in a heavily reduced flexibility of the monomers, which could hinder a successful polymerization.

Conclusion and Outlook

The goal of functionalizing a SURMOF scaffold with a bifunctional photoinitiator was achieved (Figure 6.1) and the resulting functional SURMOFs characterized via ToF-SIMS and IRRAS. The functionalization does not hinder the loading of the structures with MMA, as verified by QCM analysis. However, the diffusion of the monomer into SURMOF structures had to be realized via a gas phase approach as the immersion ap-
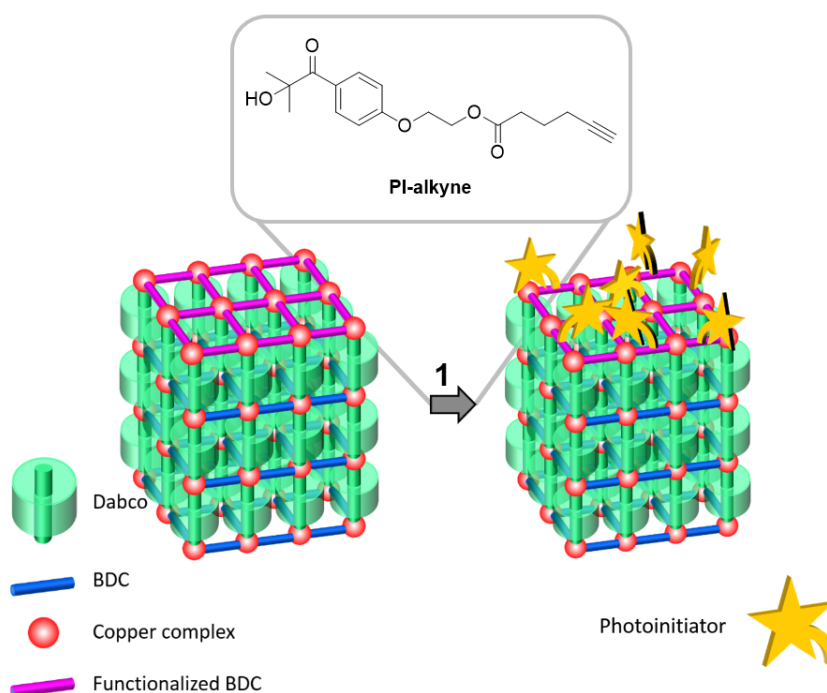
Figure 6.1: Functionalization of Cu-BDC-dabco with **PI-alkyne**. *1) [Cu(CH$_3$CN)$_4$]PF$_6$, THF, a.t., 8 h.*

proach that was employed in MOF powder systems by Kitagawa and coworkers was not compatible with MOF thin films.

The amount of polymer that can theoretically be obtained from SURMOF polymerizations was determined at the single-digit µg range, which is not sufficient for SEC analysis or NMR spectroscopy. Via high resolution ESI-MS, it is possible to detect PMMA in the double-digit ng range. Thus, the analysis of PMMA generated in SUR-MOFs can be achieved via ESI-MS. For future investigations, it will be likely possible to characterize the initiation and termination processes that occur in SURMOF polymerization procedures. Via the formation of block copolymers in a λ-orthogonal fashion, it was evidenced that the initiation and termination reactions in polymerizations with **PI-alkyne** can be observed via mass spectrometry. In an equal manner, the polymers generated in SURMOF frameworks should include the structure depicted in Figure 6.2.
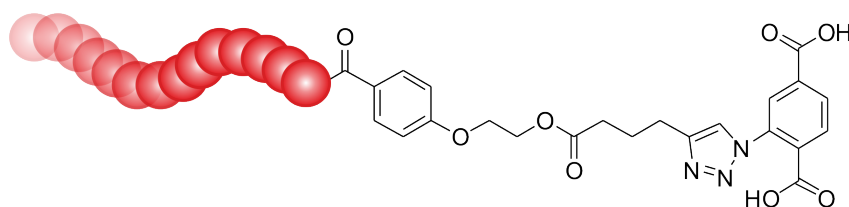
Figure 6.2: Schematic structure of PMMA (red) with the SURMOF-linker BDC attached to the initiator.

For the observation of polymerization processes in SURMOFs, a Cu-BDC-dabco sample was prepared on a QCM substrate and the sample functionalized in the topmost layer with **PI-alkyne**. A model polymerization was performed with MMA in the functionalized SURMOF sample *in situ* via QCM. After loading the sample with the monomer, the polymerization was initiated by irradiation with UV-light (λ_{max} = 366 nm). The mass of the sample increased significantly beyond the maximum capacity of the framework channels. ToF-SIMS clearly evidenced that the polymerization occurred inhomogeneously at solely specific spots in the structure. Furthermore, the polymer was generated on top of the topmost SURMOF layer rather than inside the framework channels, resulting in insoluble PMMA bubbles on the SURMOF structure. Since the polymer was not soluble, it could not be analyzed via ESI-MS. It is questionable if a polymerization can be achieved solely inside the SURMOF structure via the gas phase approach. An atmosphere of monomer/inert gas mixture is required for the monomer to diffuse into the structure. If the atmosphere is changed to pure inert gas after the loading procedure, the monomer diffuses rapidly from the structure, as was ob-

served with a blind sample via QCM. However, a constant monomer atmosphere above the sample may in fact always lead to polymerization outside the SURMOF structure. Still, the initiation and termination processes of MOF polymerizations have not yet been investigated via mass spectrometry. Thus, polymerizations in MOF powder might be of interest for future investigations. The termination of the radical chains may depend on the work-up and release procedure of the polymer from the framework. The chains may terminate upon contact with air or solvents, or may terminate with each other in combination and disproportionation reactions after the release from the MOF. Understanding the termination in detail may lead to the development of specific end group functionalization of the non-terminated chains.

Step-growth polymerizations were investigated in the course of this thesis for potential MOF polymerizations. The herein designed monomers fulfill the requirements for a fast and highly selective reaction in the absence of a catalyst by employing photoenol chemistry and Diels-Alder cycloaddition. The monomers **M1** and **M2** were designed with an aromatic and an aliphatic backbone, respectively, which resulted in differences in polymerization rate and cyclization tendency. The monomer **M1** (Figure 6.3), featuring the aromatic backbone, showed the higher polymerization rate and a lower cyclization tendency, whereas monomer **M2** features a high cyclization tendency and, in addition, end group fragmentation during the polymerization process, which was evidenced via SEC-ESI-MS. The liability of the end group of **M2** was further evidenced by producing copolymers with **M1** and **M2**. It is therefore suggested to employ **M1** in MOF polymerization studies.
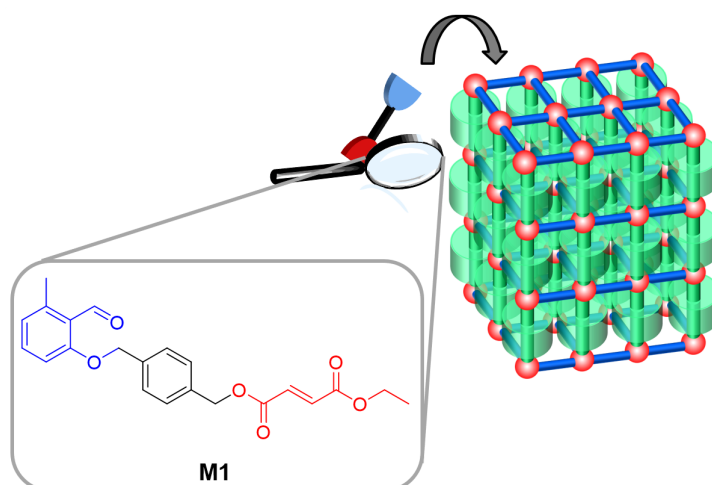
Figure 6.3: Schematic depiction of the photomonomer **M1** for light-induced step-growth polymerization in MOF structures.

119

Via theoretical calculations of the binding energies of the monomers in Cu-BDC-dabco and Cu-BPDC-dabco, one finds that the monomers diffuse into the structure, yet, the flexibility of the monomers in Cu-BDC-dabco may be reduced to an extent where polymerization may be hindered. During the polymerization in MOF structures, the formation of cycles may be suppressed as the end groups of the same chain are unlikely to interact. Hence, the polymerization of step-growth monomers such as **M1** might result in higher yields, as the chains can grow unhindered through the channels of the MOF structures.

In future investigations, the step-growth polymerization of **M1** should be observed in various MOF structures to study the effect of the pore size on the polymerization, as has already been performed for chain polymerizations by Kitagawa and coworkers.[103] For this purpose, the loading of the monomer into the frameworks has to be studied and optimized. Moreover, it is required to investigate the analytical possibilities for the determination of the conversion, e.g., via thermogravimetric analysis. In addition, the formation of cyclic polymers can be detected by the retention time in SEC analysis of the oligomeric structures and can be readily compared with the solution polymerization data presented in Chapter 5.

APPENDIX A

Materials and Equipment

A.1 Materials

Solvents of the grade *per analysis* and absolute solvents have been purchased (VWR, Acros, Sigma Aldrich) and were used without further purification. Solvents were degassed by bubbling inert gas (Ar or N_2). Reagents have been purchased from commercial suppliers (Sigma Aldrich, VWR, Merck, Alfa Aesar, TCI) and have been used without further purification unless otherwise stated. Methyl methacrylate (MMA, Sigma-Aldrich, 99%, stabilized) was freed from inhibitor by passing through a column of activated basic alumina (VWR). PEG-N_3 was purchased from *Creative PEGworks* (M_w 1k). For the SEC-ESI-MS measurements, tetrahydrofuran (THF, Scharlau, multisolvent GPC grade, 250 ppm BHT) and methanol (VWR, chromanorm) were employed as received. Deuterated solvents for NMR experiments were purchased from Sigma-Aldrich and used without additional treatment. Ivocerin® was kindly provided by *Ivoclar Vivadent GmbH* and Irgacure2959® was kindly provided by BASF. Gold-coated silicon wafers were obtained from *PVD Beschichtungen*, Silz, Germany.

A.2 Equipment

Automatic Spray System: The automatic spray system was build by Jonas Wohlgemuth and was introduced earlier.[99] It consists of three MINI-extrusion valves of the MVV series from *ALFRED SCHÜTZE Apparatebau GmbH* that are aligned side-by-

side on a *x-y-z*-axle gantry from *Festo AG & Co. KG*. The samples are held by a vacuum holder system and can be sprayed by the following distances: *x*-axis: $0\ldots200$ mm; *y*-axis: $0\ldots150$ mm; *z*-axis: $0\ldots150$ mm. Sampleholders were indivually 3D-printed by Jonas Wohlgemuth. The following parameters can be set for the coating of surfaces: working distance, speed of moving nozzles, type of nozzles, spray method (line-by-line or frontal centre spray), gas pressure in container, pressure of nitrogen in aspirator unit, ratio of liquid and gas in the nozzles, and concentration of reactants in the liquids.

Excimer Laser: Polymerizations were carried out by an excimer laser system (Coherent XS-500, XeF, 351 nm, frequency variable from 1 Hz to 500 Hz). The polymerizations were performed at a laser energy of 0.35 mJ pulse^{-1} (a custom-build metal filter was implemented to reduce the laser energy) at a frequency of 200 Hz with 90 000 pulses.

Nuclear Magnetic Resonance Spectroscopy (NMR): The NMR spectra were recorded with the following equipment: BRUKER Avance 500 Plus; BRUKER AM 400. The unit of the chemical shift δ is parts per million (ppm). The references of the spectra were the remaining proton signals of the deuterated solvents or the deuterated solvents themselves: chloroform-d$_1$ (^{1}H: 7.26 ppm, ^{13}C: (77.16 ± 0.06) ppm), deuterium oxide (^{1}H: 4.79 ppm), methanol-d$_4$ (^{1}H: 3.31 ppm, ^{13}C: (49.00 ± 0.01) ppm). The multiplicities of the signals were abbreviated as follows: s = singulet, d = doublet, dd = double doublet, dt = double triplet, t = triplet, q = quartet, p = quintet, m = multiplet.

Size Exclusion Chromatography (SEC): SEC measurements were performed on a TOSOH Eco-SEC HLC-8320 GPC System, comprising an autosampler, a SDV 5 µm bead-size guard column (50×8 mm, PSS) followed by three SDV 5 µm columns ($300\times$ 7.5 mm, subsequently 100 1000 105 angstrom pore size, PSS), and a differential refractive index (DRI) detector using tetrahydrofuran (THF) as the eluent at 30 °C with a flow rate of 1 mL min^{-1}. The SEC system was calibrated using linear polymethylmethacrylate (PMMA) standards ranging from 800 g mol^{-1} to 1.82×10^6 g mol^{-1}. Calculation of the molecular weight proceeded via the Mark-Houwink-Sakurada (MHS) parameters for PMMA: K = 129.8×10^{-3} mL g^{-1}, α = 0.688.

Electrospray Ionization-Mass Spectrometry (ESI-MS): Direct infusion mass spectra were recorded on a Q Exactive (Orbitrap) mass spectrometer (Thermo Fisher Scientific, San Jose, CA, USA) equipped with a HESI II probe. The instrument was calibrated in the *m/z* range 74 to 1822 using premixed calibration solutions (Thermo Scientific). A

constant spray voltage of 4.7 kV and a dimensionless sheath gas of 5 were applied. The capillary temperature and the S-lens RF level were set to 320 °C and 62.0, respectively. The samples were dissolved with a concentration of 0.03 mg mL^{-1} in a mixture of THF and MeOH (3:2) containing 100 μmol of sodium trifluoroacetate and infused with a flow of 5 μL/min.

Size Exclusion Chromatography-Electrospray Ionization-Mass Spectrometry (SEC-ESI-MS): Spectra were recorded on a Q Exactive (Orbitrap) mass spectrometer (Thermo Fisher Scientific, San Jose, CA, USA) equipped with a HESI II probe. The instrument was calibrated in the m/z range 74 to 1822 using premixed calibration solutions (Thermo Scientific). A constant spray voltage of 4.6 kV, a dimensionless sheath gas of 8, and a dimensionless auxiliary gas flow rate of 2 were applied. The capillary temperature and the S-lens RF level were set to 320 °C and 62.0, respectively. The Q Exactive was coupled to an UltiMate 3000 UHPLC System (Dionex, Sunnyvale, CA, USA) consisting of a pump (LPG 3400SD), autosampler (WPS 3000TSL), and a thermostated column department (TCC 3000SD). Separation was performed on two mixed bed size exclusion chromatography columns (Polymer Laboratories, Mesopore 250 × 4.6 mm, particle diameter 3 μm) with precolumn (Mesopore 50 × 4.6 mm operating at 30 °C. THF at a flow rate of 0.30 mL min^{-1} was used as eluent. The mass spectrometer was coupled to the column in parallel to an UV-detector (VWD 3400 RS), and a RI-detector (RefractoMax520, ERC, Japan) in a setup described earlier.[152] 0.27 mL min^{-1} of the eluent were directed through the RI-detector and 30 μL min^{-1} infused into the electrospray source after post-column addition of a 100 μmol solution of sodium iodide in methanol at 20 μL min^{-1} by a micro-flow HPLC syringe pump (Teledyne ISCO, Model 100DM, USA). A 20 μL aliquot of a polymer solution with a concentration of 2 mg mL^{-1} was injected onto the HPLC system.

Differential Scanning Calorimetry (DSC): DSC experiments were carried out under nitrogen atmosphere with a DSC821e (Mettler Toledo) calorimeter using 40 μL aluminum crucibles (with pins). An amount of 5 to 10 mg for each sample was measured in two heating circles of −50 to 300 °C with heating and cooling rate of 10 K min^{-1}. The second heating curves were considered for the accurate examination. The glass transition temperature (T$_g$) was defined as the midpoint of the change in heat capacity occurring over the transition. The baseline was measured with an empty 40 μL aluminum crucible.

UV-Vis: UV-Vis absorption spectra were measured on a Varian Cary 300 UV/Vis Spectrometer in dichloromethane at $20\,^{\circ}\mathrm{C}$ with $0.1\,\mathrm{mg\,mL^{-1}}$. Spectra were collected between 800 and 200 nm and were baseline corrected with respect to the pure solvent.

Photoreactor: The photoreactions were performed in a custom-built reactor with a Phillips Cleo Compact PL-L $(5 \times 36\,\mathrm{W})$, 310 to 400 nm, $\lambda_{max} = 350\,\mathrm{nm}$.
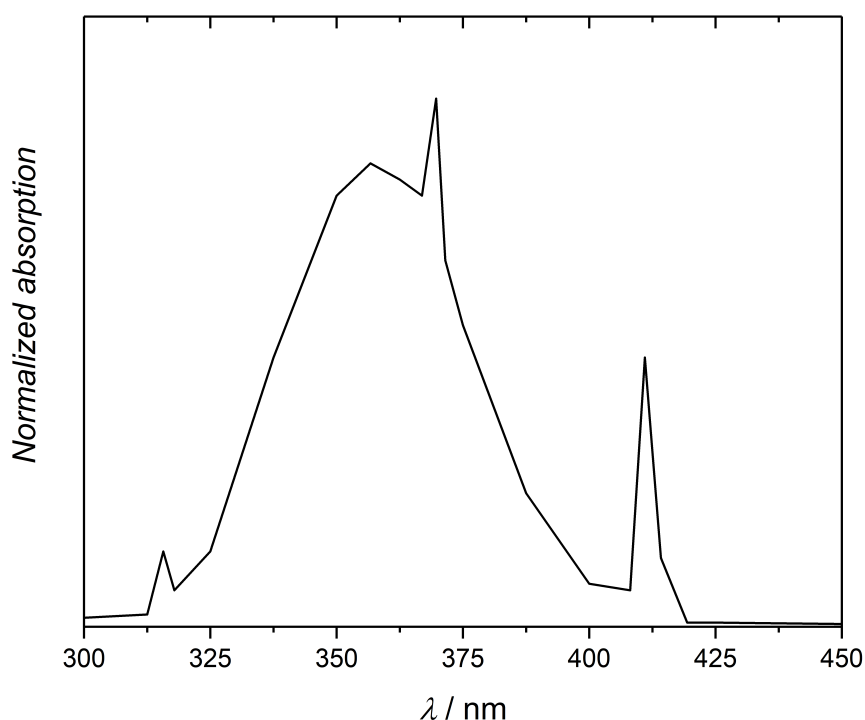
Figure A.1: Emission spectrum of PL-L lamp that was employed for the photo reactions.

Infrared Reflection Absorption Spectroscopy (IRRAS): IRRAS data were recorded using a Biorad Excalibur FTIR spectrometer (FTS 3000) equipped with a grazing incidence reflection unit (Biorad Uniflex) and a narrow band MCT detector. For the IRRAS measurements, a background was recorded, i.e. a gold surface with deuterated MUD, and a baseline-correction was performed.

X-ray Diffraction (XRD): Measurements for out-of-plane (co-planar orientation) were carried out using Bruker D8-Advance diffractometer equipped with a position sensitive

detector (PSD) Lynxeye$^®$ in θ-θ geometry, variable divergence slit and 2.3° Soller-slit was used on the secondary side. Cu-Anode: Cu Kα1, 2-radiation, λ = 0.154018 nm. XRD spectra were recorded from 2 θ = 4° to 20° and were calibrated by the measured gold peak [111] at 18.188°.

Time of Flight-Secondary Ion Mass Spectrometry (ToF-SIMS): ToF-SIMS was performed on a TOF.SIMS5 instrument (ION-TOF GmbH, Münster, Germany) at the Institute of Functional Interfaces, Karlsruhe Institute of Technology (KIT). This spectrometer is equipped with a Bi cluster primary ion source and a reflectron type time-of-flight analyzer. UHV base pressure was $< 5 \times 10^{-9}$ mbar. For high mass resolution, the Bi source was operated in the "high current bunched" mode providing short Bi^{1+} or Bi^{3+} primary ion pulses at 25 keV energy and a lateral resolution of approx. 4 µm. The short pulse length of 1.1 to 1.3 ns allowed for high mass resolution. The primary ion beam was rastered across a $500 \times 500 \, \mu m^2$ field of view on the sample, and 128×128 data points were recorded. Primary ion doses for surface analysis without depth profiling were kept below 10^{11} ions cm^{-2} (static SIMS limit). Spectra were calibrated on the omnipresent C^-, C_2^-, C_3^-, or on the C^+, CH^+, CH_2^+, and CH_3^+ peaks. Based on these datasets, the chemical assignments for characteristic fragments were determined.
Images larger than the maximum deflection range of the primary ion gun of $500 \times 500 \, \mu m^2$ were obtained using the manipulator stage scan mode. For the depth profiling samples, a dual beam analysis was performed: The primary ion source was operated in "bunched" mode with a scanned area of $300 \times 300 \, \mu m^2$ and a C_{60}^+ sputter gun (2000 eV, scanned over a concentric field of $500 \times 500 \, \mu m^2$) was applied to erode the sample. If charge compensation was necessary, an electron flood gun providing electrons of 21 eV was applied and the secondary ion reflectron tuned accordingly.

Quartz Crystal Microbalance (QCM): A quartz crystal microbalance (QCM) from Q-Sense$^®$ was used to record the loading of the SURMOF. Standard QCM sensors have a gold coating on which the MUD SAM and subsequently the SURMOF were grown. The QCM cell is connected to a gas flow system with Ar carrier gas. It is possible to switch instantly between a pure Ar flow and a Ar flow enriched with monomer. By passing the Ar flow through the liquid monomer at ambient temperature, Ar gas containing monomer is prepared. Before each uptake experiment, the sample was activated in the QCM cell in a pure Ar flow at 65 °C overnight.

Syntheses and Preparations

B.1 Syntheses of Initiators and Monomers

2-(4-(2-Hydroxy-2-methylpropanoyl)phenoxy)ethyl hex-5-ynoate (PI-alkyne 2)
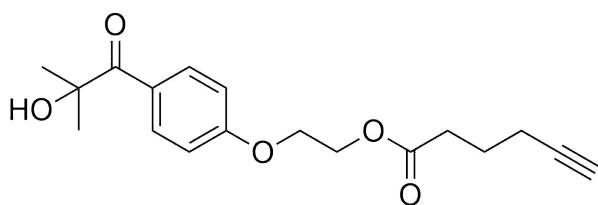
PI-alkyne 2

Hexynoic acid (1.00 eq.), Irgacure2959$^©$ (2.00 eq.) and DMAP (0.15 eq.) were dissolved in dry CH_2Cl_2 (c(Irgacure) = 50 mg mL^{-1}). The reaction mixture was cooled with an ice/water bath to 0 °C. A solution of EDC·HCl (3.00 eq.) in dry dichloromethane (c = 250 mg mL^{-1}) was added dropwise. The reaction mixture was stirred at 0 °C for 1 h and at ambient temperature overnight. Afterwards, the reaction mixture was washed with water (3× with same volume as DCM) and the combined aqueous layers were extracted with DCM (1×). The combined organic layers were dried over Na_2SO_4 and the solvent removed under reduced pressure. Column chromatography (EtOAc:nHex = 3:2) yielded a yellow oil (85%).

^{1}H-NMR (500 MHz, CDCl$_3$): δ (ppm) = 1.61 (s, 6 H, CH$_3$), 1.87 (q, $J = 7.1$ Hz, 2 H, CH$_2$), 1.96 (t, $J = 2.6$ Hz, 1 H, CH), 2.27 (td, $J = 6.9, 2.7$ Hz, 2 H, CH$_2$), 2.51 (t, $J = 7.4$ Hz, 2 H, CH$_2$), 4.24 (m, 2 H, CH$_2$), 6.95 (m, 2 H, ar H), 8.05 (m, 2 H, ar H). ^{13}C-

NMR (125 MHz, CDCl$_3$): δ (ppm) = 17.9 (CH$_2$), 23.6 (CH$_2$), 28.8 (CH$_3$), 32.8 (CH$_2$), 62.5 (CH$_2$), 66.2 (CH$_2$), 69.4 (CH), 76.0 (C4), 83.2 (C4), 114.3 (ar CH), 126.5 (ar C4), 162.4 (ar C4), 173.0 (C=O), 202.7 (C=O). UV-Vis (THF): 272 nm. HR ESI-MS (M+Na$^+$): m/z = 341.1359 (calcd), 341.1357 (found).
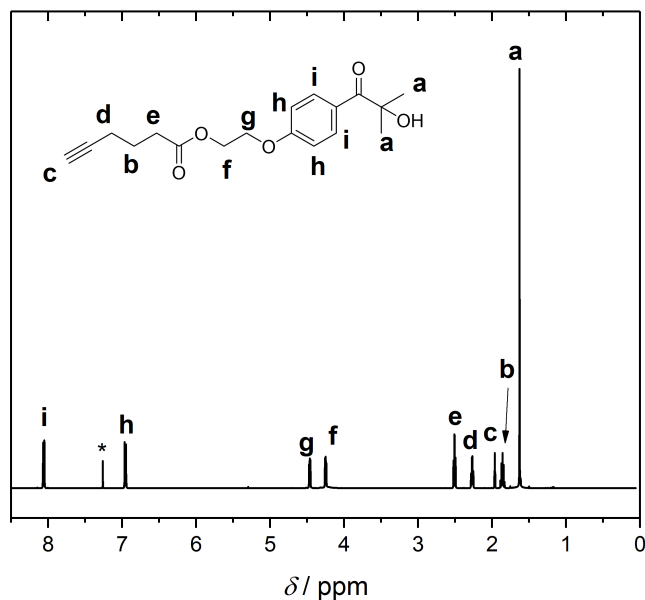
Figure B.1: ^{1}H NMR spectrum of **PI-alkyne 2** in CDCl$_3$.
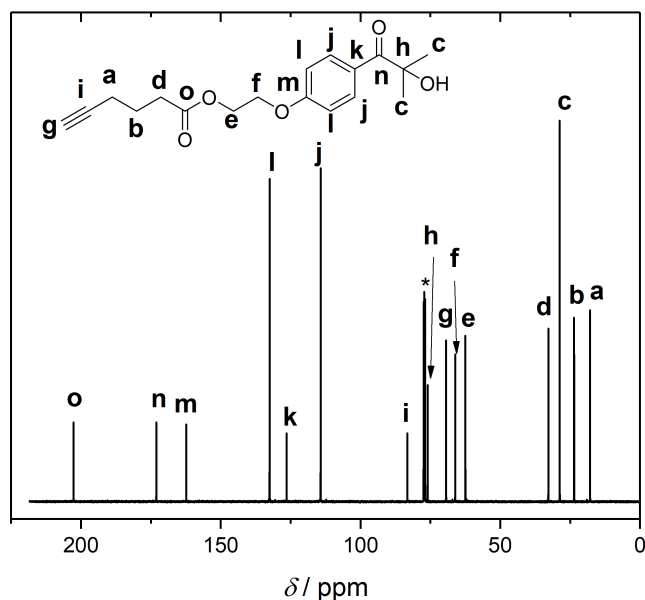
Figure B.2: ^{13}C NMR spectrum of **PI-alkyne 2** in CDCl$_3$.

Test Click Reaction of PI-alkyne
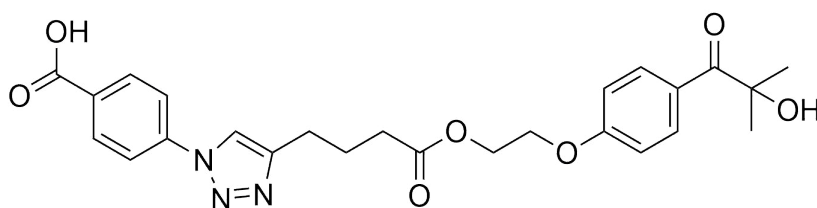
PI-alkyne (163 mg, 0.50 mmol, 1.00 eq.), azidobenzoic acid (100 mg, 0.60 mmol, 1.20 eq.) and $[Cu(CN)_4]PF_6$ (224 mg, 0.60 mmol, 1.20 eq.) were dissolved in 20 mL degassed THF under inert conditions. The reaction mixture was stirred overnight at 70 °C. After cooling to a.t., the solution was diluted with 20 mL EtOAc and washed with sat. aqueous EDTA solution (3×20 mL). The aqueous phase was extracted with 60 mL EtOAc. The combined organic layers were washed with sat. $NaHCO_3$ solution (60 mL) and dried over $MgSO_4$. The solvents were removed under reduced pressure and yielded the crude product (65%). Column chromatography (*n*Hex:EA = 1:4) with acetic acid (5%) did not purify the product completely and resulted in residual acetic acid in the product.

^{1}H-NMR (500 MHz, THF−d_6): δ (ppm) = 1.44 (s, 6 H, CH_3), 2.04 (p, $J = 7.5$ Hz, 2 H, CH_2), 2.45 (t, $J = 7.4$ Hz, 2 H, CH_2), 2.81 (t, $J = 7.5$ Hz, 2 H, CH_2), 4.25 (m, 2 H, CH_2), 4.41 (m, 2 H, CH_2), 6.94 (m, 2 H, ar CH), 7.95 (m, 2 H, ar CH), 8.16 (m, 2 H, ar CH), 8.26 (m, 4 H, ar CH), 8.28 (s, 1 H, triazole-CH).
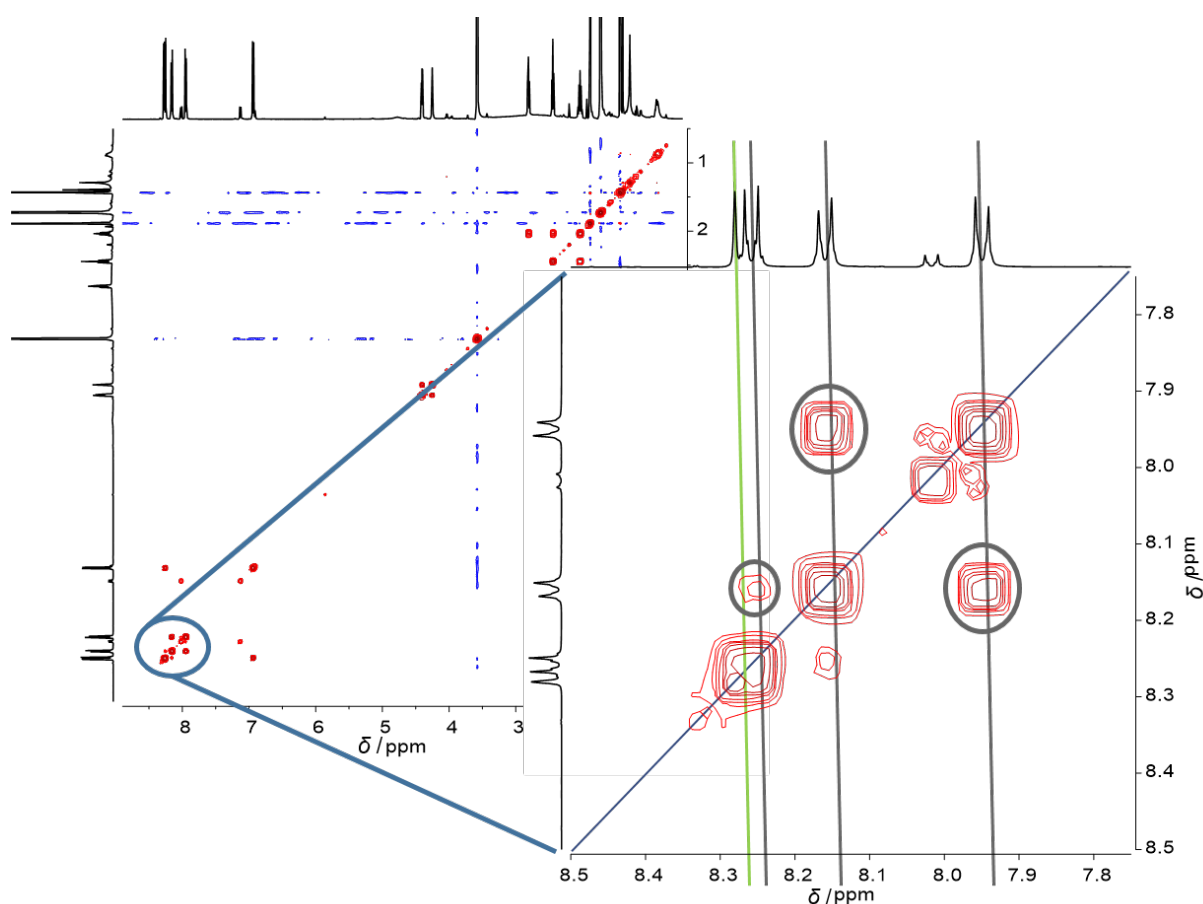
Figure B.3: COSY NMR of the product of the click reaction between PI-alkyne 2 and azidobenzoic acid. The green line represents the resonance of the triazole proton, which does not correlate with any other protons in the molecule.

Visible Light CuAAC with PEG-azide (PEG-PI and PEG-*b*-PMMA)

The synthesis was performed after a literature procedure.[151] PEG-N$_3$ (50 mg, 0.05 mmol, 1.00 eq.), PI-alkyne or PMMA-alkyne (0.06 mmol, 1.10 eq.), Ivocerin (17.1 mg, 0.05 mmol, 1.00 eq.), CuBr$_2$ (11.2 mg, 0.05 mmol, 1.00 eq.) and PMDETA (8.67 mg, 0.05 mmol, 1.00 eq.) were dissolved in 10 mL DMSO (for PMMA-alkyne: 10 mL DMSO/-THF 1:1) and degassed by two freeze-pump-thaw cycles. The solution was irradiated with three LEDs at 410 nm to 420 nm (Avonec / UV-A actinic blue 3 watt) for 24 hour in a custom-build photoreactor. Subsequently, the solution was diluted with 10 mL DCM and filtered over neutral alumina. DCM was evaporated under reduced pressure, and the remaining DMSO was removed by freeze-drying. The macroinitiator or block-copolymer was precipitated in n-hexane with a yield of 50%.

2-Methoxy-6-methylbenzaldehyde (PhE-OMe)

The synthesis was adapted from a literature procedure.[171,188]
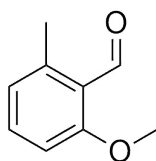
2,3-Dimethyl anisole (5.00 g, 36.7 mmol, 1.00 eq.), copper sulfate pentahydrate (9.35 g, 37.4 mmol, 1.02 eq.) and potassium peroxodisulfate (29.7 g, 110 mmol, 3.00 eq.) were added to a mixture of acetonitrile and water (1:1, 180 mL). The vigorously stirred suspension was placed in an oil bath at 90 °C for 1 h. The mixture was cooled to a.t. and the undissolved copper salt was removed by filtration. DCM (55 mL) was added and the phases separated. The aqueous phase was extracted with DCM (2×35 mL) and the combined organic layers were dried over $MgSO_4$. After the removal of the solvent under reduced pressure, the crude product was purified by column chromatography (silica gel, nHex/EtOAc = 5:1), yielding 3.74 g (68%) of a yellow solid.

^{1}H-NMR (500 MHz, CDCl$_3$): δ (ppm) = 2.57 (s, 3 H, CH$_3$), 3.89 (s, 3 H, OCH$_3$), 6.81 (t, $J = 8.0$ Hz, 2 H, ar CH), 7.38 (t, $J = 8.0$ Hz, 1 H, ar CH), 10.64 (s, 1 H, CHO).

2-Hydroxy-6-methylbenzaldehyde (PhE)

The synthesis was performed according to a literature procedure.[61]
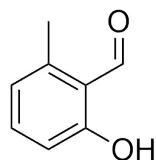
2-Methoxy-6-methylbenzaldehyde (3.74 g, 24.9 mmol, 1.00 eq.) was dissolved in dry DCM (38 mL) and cooled to 0 °C. AlCl$_3$ (20.9 g, 157 mmol, 3.00 eq.) was added and the mixture was stirred overnight. Afterwards, the reaction mixture was quenched with H$_2$O (70 mL, dropwise) at 0 °C. The phases were separated and the aqueous phase was extracted with DCM (3×70 mL). The combined organic layers were dried over $MgSO_4$ and the solvent was removed under reduced pressure. The brown crude product (3.05 g, 22.4 mmol, 90%) was not further purified.

^{1}H-NMR (500 MHz, CDCl$_3$): δ (ppm) = 2.61 (s, 3 H, CH$_3$), 6.76 (dd, $J = 25.3, 7.9$ Hz, 2 H, ar CH), 7.38 (t, $J = 7.9$ Hz, 1 H, ar CH), 10.32 (s, 1 H, CHO), 11.91 (s, 1 H, OH).

1-(3-Chloropropyl)-1H-pyrrole-2,5-dione (Mal-Cl)

The synthesis was performed after a literature procedure.[176]
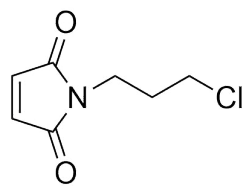
Maleic anhydride (226 mg, 2.31 mmol, 1.00 eq.) was dissolved in DCM (5 mL) together with chloro-3-amino propane hydrochloride (308 mg, 2.31 mmol, 1.00 eq.). Triethylamine (257 mg, 2.54 mmol, 352 μL, 1.10 eq.) was added dropwise to the solution at 0 °C. The solution was stirred at a.t. for 2 h. The solvents were evaporated under reduced pressure and the residue dissolved in DCM (20 mL). Concentrated aqueous HCl (35 μL) was added to the reaction mixture, the phases were separated and the organic phase was washed with aqu. HCl (1 M, 2 × 5 mL). The aqueous phase was extracted with DCM (20 mL) and the combined organic phases were dried over $MgSO_4$. After the solvents were evaporated, the resulting white crystals (300 mg, 1.57 mmol, 1.00 eq.) were dissolved in dry DCM (3 mL) and DMF (20 μL) was added at 0 °C. Oxalylchloride (218 mg, 1.72 mmol, 1.10 eq.) was added dropwise over 30 min and the reaction stirred at a.t. for 2 d. The solvents were evaporated under reduced pressure nad the residue dissolved in DCM. Triethylamine (177 mg, 1.75 mmol, 240 μL, 1.11 eq.) was added and the solution stirred for 30 min at a.t. The solution was washed with aqu. HCl (1 M, 10 mL) and water (2 × 30 mL) and dried over $MgSO_4$. The solvents were evaporated under reduced pressure and the crude product was purified via column chromatography (SiO_2, nhex/EtOAc = 1:1-3:1) and resulted in a white solid (175 mg, 0.91 mmol, 40%).

^{1}H-NMR (500 MHz, CDCl$_3$): δ (ppm) = 2.08 (p, J = 6.7 Hz, 2 H, CH$_2$), 3.52 (t, J = 6.5 Hz, 2 H, CH$_2$Cl), 3.69 (t, J = 6.9 Hz, 2 H, CH$_2$N), 6.72 (s, 2 H, CH=CH).

1-(3-Bromopropyl)-1H-pyrrole-2,5-dione (Mal-Br)

The synthesis was performed after a literature procedure.[176]
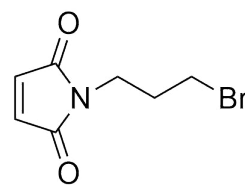
Maleic anhydride (0.50 g, 5.10 mmol, 1.00 eq.) was dissolved in DCM (10 mL) together with bromo-3-amino propane hydrobromide (1.12 g, 5.10 mmol, 1.00 eq.). Triethylamine (0.57 g, 5.60 mmol, 778 μL, 1.10 eq.) was added dropwise to the solution at 0 °C. The solution was stirred at a.t. for 2 h. The solvents were evaporated under reduced pressure and the residue dissolved in DCM (40 mL). Concentrated aqu. HBr (70 μL) was added to the reaction mixture, the phases were separated and the organic phase was washed with aqu. HBr (1 M, 2 × 10 mL). The aqueous

phase was extracted with DCM (40 mL) and the combined organic phases were dried over MgSO$_4$. After the solvents were evaporated, the resulting white crystals (1.19 g, 5.04 mmol, 1.00 eq.) were dissolved in dry DCM (7 mL) and DMF (77 μL) was added at 0 °C. Oxalylchloride (0.75 g, 5.94 mmol, 1.10 eq.) was added dropwise over 30 min and the reaction stirred at a.t. for 2 d. The solvents were evaporated under reduced pressure and the residue (1.27 g, 5.00 mmol, 1.00 eq.) dissolved in DCM. Triethylamine (0.56 g, 5.53 mmol, 760 μL, 1.10 eq.) was added and the solution stirred for 30 min at a.t. The solution was washed with aqu. HCl (1 M, 2 × 10 mL) and water (20 mL) and dried over MgSO$_4$. The solvents were evaporated under reduced pressure and the crude product was purified via column chromatography (SiO$_2$, $n$hex/EtOAc = 1:1) and resulted in a yellow solid (0.38 g, 1.74 mmol, 35%).

^{1}H-NMR (500 MHz, CDCl$_3$): δ (ppm) = 2.17 (p, $J = 6.7$ Hz, 2 H, CH$_2$), 3.36 (t, $J = 6.7$ Hz, 2 H, CH$_2$N), 3.67 (t, $J = 6.9$ Hz, 2 H, CH$_2$Br), 6.72 (s, 2 H, CH=CH).

2-((4-(Hydroxymethyl)benzyl)oxy)-6-methylbenzaldehyde (Pre1)

The synthesis was performed after a literature procedure.[62]

Pre1
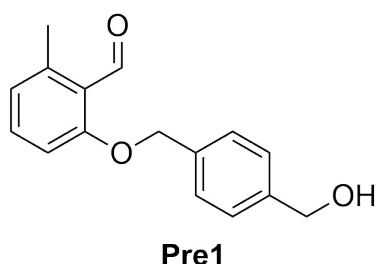
2-hydroxy-6-methylbenzaldehyde **PhE** (1.00 eq.), K$_2$CO$_3$ (1.50 eq.) and 18-crown-6 (0.015 eq.) were dissolved in dry THF ($c_{PhE} = 0.37$ M). The suspension was heated to 80 °C. A solution of 4-(chloromethyl)benzyl alcohol (1.10 eq.) in dry THF (2.0 M) was added dropwise to the hot suspension. The reaction was heated under reflux for 4 d. The reaction mixture was cooled to a.t., filtered and the solvent removed under reduced pressure. The residue was redissolved in EtOAc and washed with water and brine. The organic phase was dried over MgSO$_4$ and the crude product was purified via column chromatography (nHex: EtOAc = 1:1, R_f = 0.50). The product was isolated as a slightly yellow solid (52%).

^{1}H-NMR (400 MHz, CDCl$_3$): δ (ppm) = 2.57 (s, 3 H, CH$_3$), 4.70 (s, 2 H, CH$_2$), 5.14 (s, 2 H, CH$_2$), 6.82 (m, 4 H, ar CH), 6.89 (d, $J = 8.4$ Hz, 1 H, ar CH), 7.34 to 7.42 (m, 5 H, ar CH), 10.71 (s, 1 H, CHO). ^{13}C-NMR (100 MHz, CDCl$_3$): δ (ppm) = 21.6 (CH$_3$, 65.0 (CH$_2$OH), 70.5 (CH$_2$), 110.6 (ar CH), 123.7 (ar C), 124.5 (ar CH), 127.4 (ar. CH), 127.6 (ar CH), 134.5 (ar C), 135.6 (ar CH), 141.1 (ar C), 142.2 (ar C), 162.4

(C-O), 192.5 (C=O). UV-Vis (CH$_2$Cl$_2$): λ_{max1} = 257 nm, λ_{max2} = 318 nm. HR ESI-MS (M+Na$^+$): m/z = 279.0997 (calcd), 279.0985 (found).
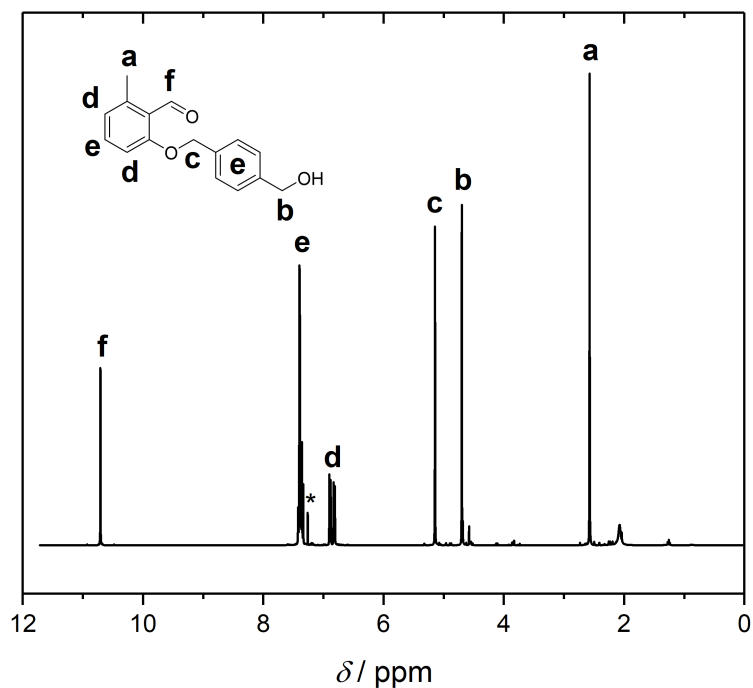
Figure B.4: ^{1}H NMR spectrum of of monomer precursor **Pre1** in CDCl$_3$.
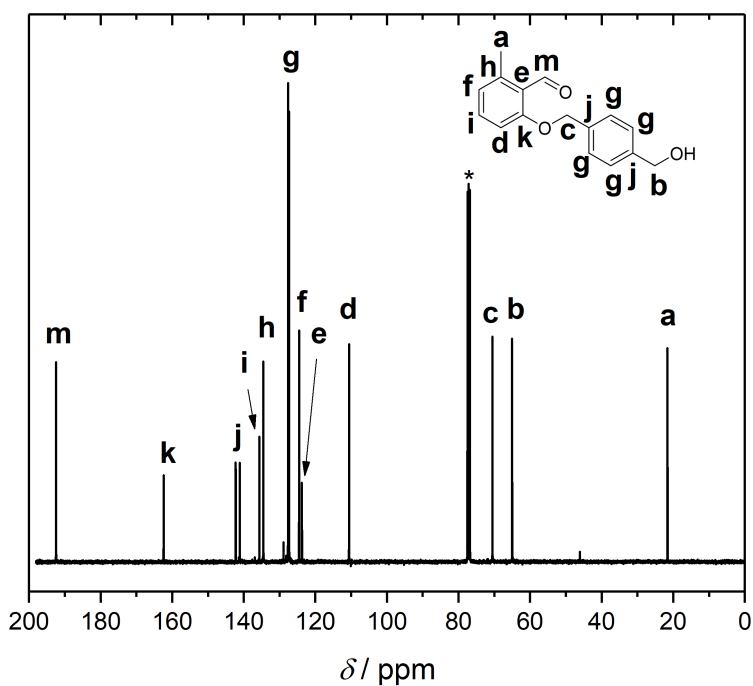
Figure B.5: ^{13}C NMR spectrum of monomer precursor **Pre1** in CDCl$_3$.

2-(3-Hydroxypropoxy)-6-methylbenzaldehyde (Pre3)

The synthesis was adapted from a literature procedure.[179]
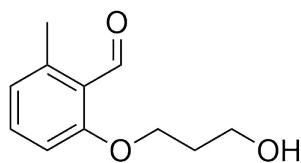
Potassium hydroxide (1.00 eq.) was dissolved in ethanol (1.10 M) and attached to a reflux condenser. Photoenol (1.00 eq.) was added under inert conditions, leading to a yellow precipitation. 3-Bromo-1-propanol was given to the suspension and the reaction was heated under reflux overnight. The suspension was cooled to a.t., filtered, and the filtered solid washed with acetone. The collected liquid filtrate was washed with saturated aq. K_2CO_3 solution and then extracted with chloroform. The organic layer was washed with water and dried over $MgSO_4$. The crude product was purified via column chromatography (*n*Hex: EtOAc = 3:2, R_f = 0.3) and yielded in a yellow oil (50%) with minor impurities.

^{1}H-NMR (400 MHz, CDCl$_3$): δ (ppm) = 2.09 (p, J = 5.9 Hz, 2 H, CH$_2$), 2.56 (s, 3 H, CH$_3$), 3.87 (t, J = 5.9 Hz, 2 H, CH$_2$OH), 4.19 (t, J = 6.0 Hz, 2 H, CH$_2$), 6.79 (d, J = 7.6 Hz, 1 H, ar CH), 6.84 (d, J = 8.4 Hz, 1 H, ar CH), 7.36 (t, J = 8.1 Hz, 1 H, ar CH), 10.61 (s, 1 H, HC=O). ^{13}C-NMR (100 MHz, CDCl$_3$): δ (ppm) = 21.3 (CH$_3$), 32.1 (CH$_2$), 60.0 (CH$_2$OH), 66.2 (CH$_2$), 110.1 (ar CH), 123.3 (ar C), 124.2 (ar CH), 134.8 (ar CH), 142.4 (ar C), 162.2 (C-O), 192.2 (C=O). UV-Vis (CH$_2$Cl$_2$): λ_{max1} = 257 nm, λ_{max2} = 318 nm. HR ESI-MS (M+Na$^+$): m/z = 217.0835 (calcd), 217.0844 (found).
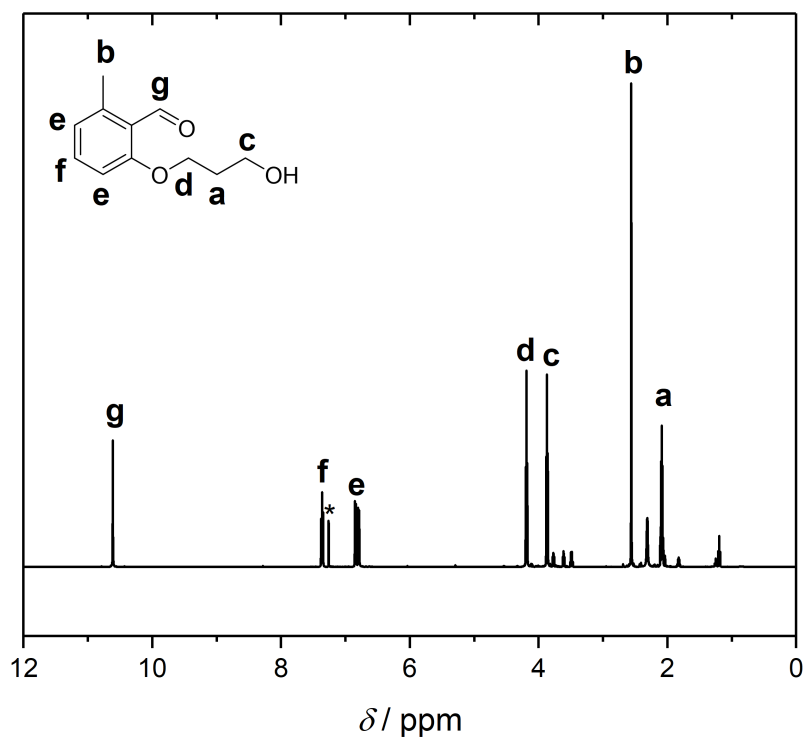
Figure B.6: ^{1}H NMR spectrum of monomer precursor **Pre3** in CDCl$_3$.
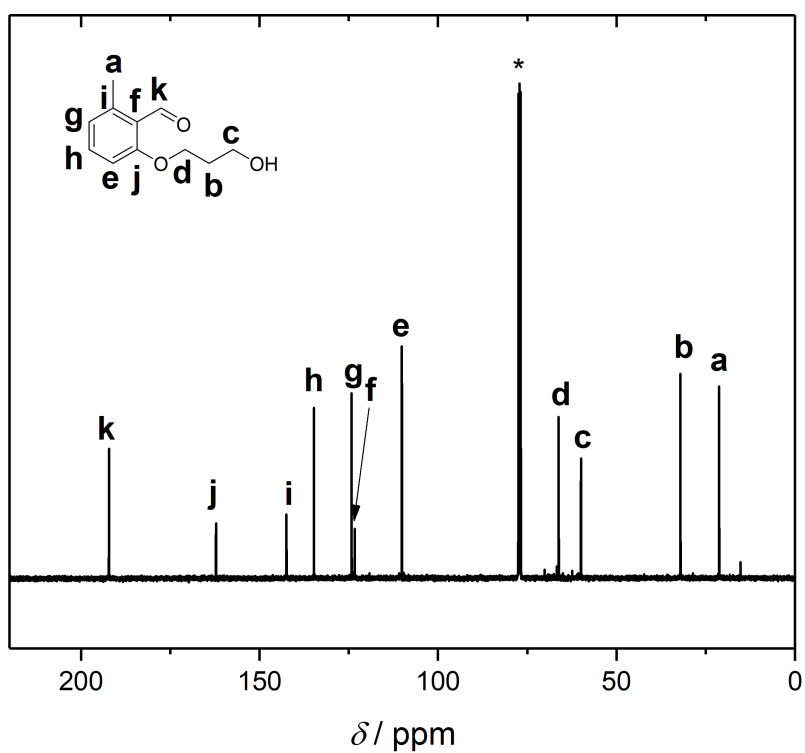
Figure B.7: ^{13}C NMR spectrum of monomer precursor **Pre3** in CDCl$_3$.

Ethyl (4-((2-formyl-3-methylphenoxy)methyl)benzyl) fumarate (PhE-Xy or M1)

The synthesis was performed after a literature procedure.[180]
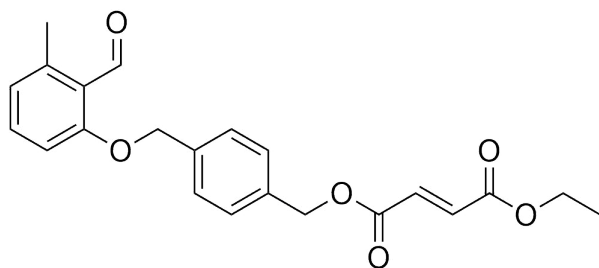
Pre1 (1.00 eq.) was dissolved in dry DCM (0.075 M). Monoethyl fumarate **Fum** (1.30 eq.) and DMAP (0.10 eq.) were added and the solution was cooled to 0 °C. DCC (1.50 eq.) was added in one portion and the reaction was first stirred at 0 °C for 30 min and subsequently for 3 h at a.t. Celite was added to the suspension and the reaction was stirred for an additional 30 min. The suspension was filtered, and the filtrate washed with HCl_{aq} (3.5%) and water. The solution was dried over $MgSO_4$ and the solvent was removed under reduced pressure. The crude product was purified via column chromatography (nHex: DCM = 1:2, R_f = 0.43) and resulted in a white solid (56%).

^{1}H-NMR (400 MHz, $CDCl_3$): δ (ppm) = 1.31 (t, J = 7.1 Hz, 3 H, CH_3), 2.58 (s, 3 H, CH_3), 4.25 (q, J = 7.1 Hz, CH_2), 5.17 (s, 2 H, CH_2), 5.25 (s, 2 H, CH_2), 6.83 (d, J = 7.6 Hz, 1 H, ar CH), 6.87 to 6.89 (m, 3 H, ar CH + HC=CH), 7.34 to 7.45 (m, 5 H, ar CH), 10.73 (s, 1 H, HC=O). ^{13}C-NMR (100 MHz, $CDCl_3$): δ (ppm) = 14.2 (CH_3), 21.6 (CH_3), 61.5 (CH_2), 66.8 (CH_2), 70.3 (CH_2), 110.5 (ar CH), 123.8 (ar C), 124.6 (ar CH), 127.7 (ar CH), 128.8 (ar CH), 133.3 (ar CH), 134.4 (HC=CH), 135.4 (ar CH), 136.8 (ar CH), 141.1 (ar C), 142.3 (ar C), 162.3 (C-O), 164.9 (HCOO), 192.5 (C=O). UV-Vis (CH_2Cl_2): λ_{max1} = 257 nm, λ_{max2} = 318 nm. HR ESI-MS (M+Na$^+$): m/z = 405.1309 (calcd), 405.1303 (found).
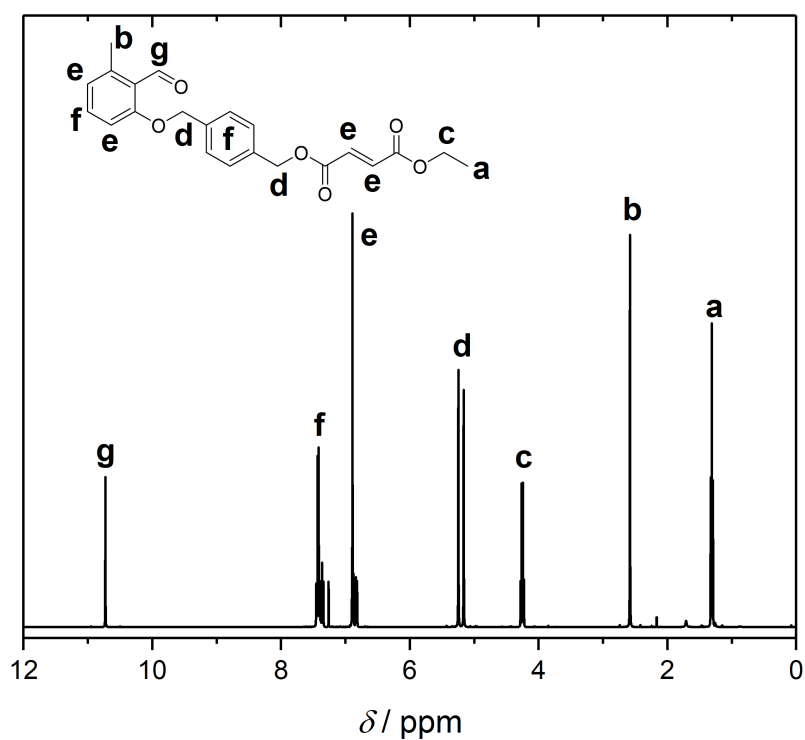
Figure B.8: ^{1}H NMR spectrum of monomer **PhE-Xy** or **M1** in CDCl$_3$.
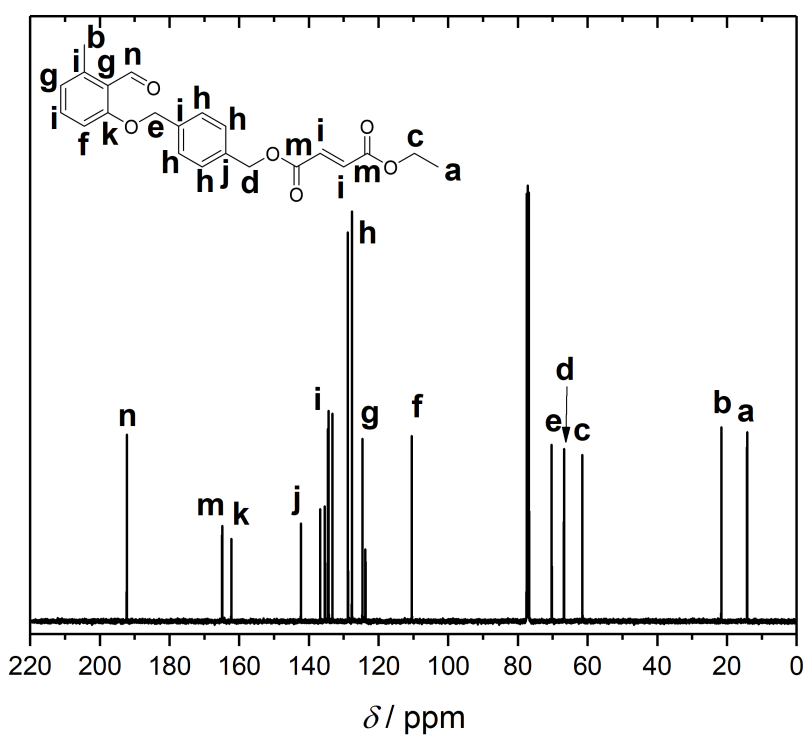
Figure B.9: ^{13}C NMR spectrum of monomer **PhE-Xy** or **M1** in CDCl$_3$.

Ethyl (3-(2-formyl-3-methylphenoxy)propyl) fumarate (PhE-Pr or M2)

The synthesis was performed after a literature procedure.[180]
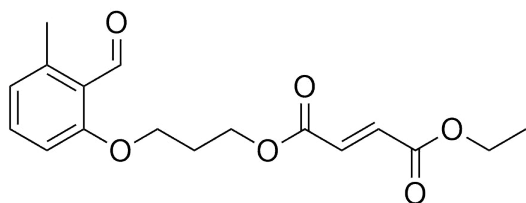
Pre3 (1.00 eq.) was dissolved in dry DCM (0.075 M). Monoethyl fumarate **fum** (1.30 eq.) and DMAP (0.10 eq.) were added and the solution was cooled to 0 °C. DCC (1.50 eq.) was added in one portion and the reaction was first stirred at 0 °C for 30 min and subsequently for 3 h at a.t. Celite was added to the suspension and the reaction was stirred for an additional 30 min. The suspension was filtered, and the filtrate washed with HCl_{aq} (3.5%) and water. The solution was dried over $MgSO_4$ and the solvent was removed under reduced pressure. The crude product was purified via column chromatography (DCM, $R_f = 0.55$) and resulted in a white solid (57%).

^{1}H-NMR (400 MHz, CDCl$_3$): δ (ppm) = 1.30 (t, $J = 7.1$ Hz, 3 H, CH$_3$, 2.23 (p, $J = 6.1$ Hz, 2 H, CH$_2$), 2.55 (s, 3 H, CH$_3$), 4.15 (t, $J = 6.1$ Hz, 2 H, CH$_2$), 4.25 (q, $J = 7.1$ Hz, 2 H, CH$_2$), 4.41 (t, $J = 6.3$ Hz, 2 H, CH$_2$), 6.79 to 6.84 (m, 4 H, ar CH + HC=CH), 7.36 (t, $J = 8.0$ Hz, 1 H, ar CH), 10.65 (s, 1 H, HC=O). ^{13}C-NMR (100 MHz, CDCl$_3$): δ (ppm) = 14.2 (CH$_3$), 18.9 (CH$_3$), 28.6 (CH$_2$), 61.5 (CH$_2$), 62.0 (CH$_2$), 65.0 (CH$_2$), 109.9 (ar CH), 123.5 (ar C), 124.5 (ar CH), 133.2 (ar CH), 134.2 (HC=CH), 135.4 (ar C), 142.2 (ar C), 162.3 (C-O), 164.9 (HCOO), 192.0 (C=O). UV-Vis (CH$_2$Cl$_2$): $\lambda_{max1} = 257$ nm, $\lambda_{max2} = 318$ nm. HR ESI-MS (M+Na$^+$): $m/z = 343.1152$ (calcd), 343.1151 (found).
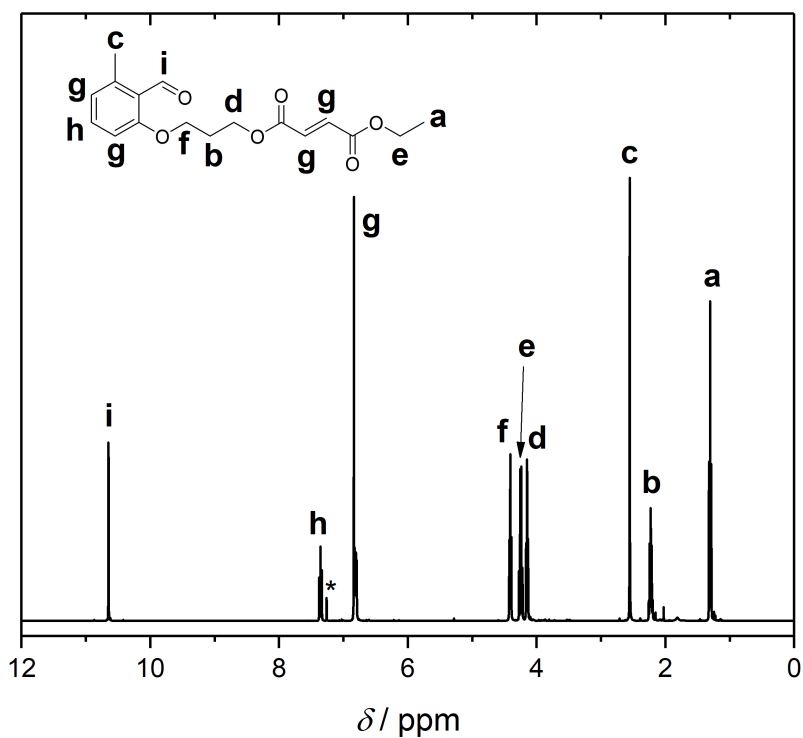
Figure B.10: ^{1}H NMR spectrum of monomer **PhE-Pr** or **M2** in CDCl$_3$.
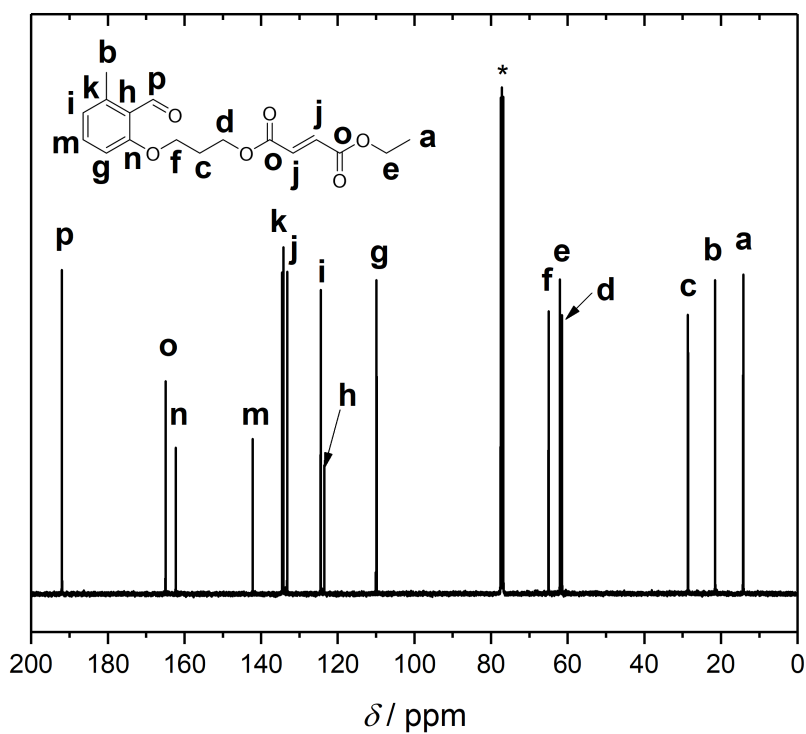
Figure B.11: ^{13}C NMR spectrum of monomer **PhE-Pr** or **M2** in CDCl$_3$.

B.2 Preparation of Surface-Mounted Metal-Organic Frameworks

B.2.1 Preparation of Self-Assembled Monolayers

Gold-coated substrates were immersed in ethanol containing MUD or MHDA (c = 1 mM) for 24 h or 3 d, respectively. The surfaces were subsequently rinsed with ethanol and dried under a flux of nitrogen.

B.2.2 Preparation of Cu-BPDC by Automatic Spraying

Copper acetate in ethanol ($1.0\,\mathrm{mmol\,L^{-1}}$) and BPDC in ethanol ($0.05\,\mathrm{mmol\,L^{-1}}$) were sprayed subsequently onto the MHDA-functionalized surface by a nozzle system[99] described in Chapter 2.4.2, page 30. The spraying times were: 2×15 s for metal solution; 25 s pause; 4×15 s rinsing with ethanol; 2×20 s for linker solution; 25 s pause. After completing the desired number of cycles, the samples were thoroughly rinsed with ethanol and dried in a flux of nitrogen.

B.2.3 Preparation of Cu-BDC-dabco by Automatic Pumping

The SAM-modified substrates were coated with SURMOF according to the procedure described in Chapter 2.4.2, page 29. All employed solutions were tempered at 60 °C. The samples were immersed in copper acetate solution (c = 1 mM in ethanol) for 15 min. After rinsing with pure ethanol for 4 min, the samples were immersed in BDC/dabco-solution ($c_{\mathrm{BDC+dabco}}$ = 0.2 mM in ethanol) for 25 min before an additional rinsing step with pure ethanol for 4 min. The procedure was repeated until the desired thickness was achieved. The samples were thoroughly rinsed with ethanol and dried in a flux of nitrogen.

B.2.4 CuAAC on SURMOFs

The azide-functionalized SURMOFs were activated at 60 °C under vacuum overnight. A solution of [Cu(CH$_3$CN)$_4$]PF$_6$ (5 mg) and **PI-alkyne** (1 mg) in THF (4 mL) was degassed by bubbling nitrogen, and added to the SURMOF under inert conditions. After 8 h, the samples were rinsed with ethanol and dichloromethane and dried with a flux of nitrogen. The successful functionalization was confirmed via IRRAS and ToF-SIMS.

B.3 Polymerization Procedures

Stability Tests of PI-alkyne

PI-alkyne and Ivocerin were each tested in individual polymerizations of MMA. 4 samples were prepared with an initiator concentration of $c_{\text{initiator}} = 0.005\,\text{mol}\,\text{L}^{-1}$. The samples were degassed by bubbling a nitrogen stream through the solution for 30 min. The samples were irradiated at 420 nm for 0.5 h, 1 h, 2 h and 3 h, respectively. The yield was determined gravimetrically by evaporating the monomer.

Additionally, PI-alkyne was dissolved in $CDCl_3$ in an NMR tube and irradtiated with 420 nm for 24 h. Recorded spectra before and after the irradiation confirmed the stability of the functional photoinitiator.

B.3.1 Polymerization in SURMOFs

Loading Benzoin into the SURMOFs

A solution of benzoin in THF (2.40 mM) was dropped onto the SURMOF coated surface. After the solvent had evaporated, the sample was placed into the gas deposition equipment (refer to Figure 3.5 in Chapter 3.2) and purged with nitrogen for 15 min.

Polymerization in SURMOFs

The samples that contained (anchored) photoinitiator were purged with monomer vapours for 10 min by bubbling Ar through the liquid monomer. The glassware was sealed and placed into a UV reactor and irradiated with $\lambda_{\text{max}} = 366\,\text{nm}$ (Benda, NU-4 KL) for 24 h. After the reaction was finished, the substrates were washed with ethanol and dried with nitrogen. Loading of the SURMOFs was confirmed by XRD and ToF-SIMS analysis.

B.3.2 Pulsed-Laser Polymerizations

The PLP samples for both PI-alkyne and PEG-PI were prepared with a concentration of $c_{\text{initiator}} = 3.7 \times 10^{-3}\,\text{mol}\,\text{L}^{-1}$ in MMA (sample volume 0.5 mL) and freed from oxygen by purging with nitrogen for 2 min. Subsequently, the samples were individually placed into the sample holder, which was held at the constant temperature of $0\,^{\circ}\text{C}$ using a thermostat (model: 1196D, VWR, Darmstadt, Germany). After the polymerization, the remaining monomer was evaporated and yielded a conversion of ca. 2%.

B.3.3 Step-Growth Polymerizations

Concentration Studies

a) The monomer (**M1** or **M2**) was dissolved in degassed acetonitrile with a concentration of 0.06, 0.1, 0.2, 0.4 and 0.6 mol L^{-1} in batches of 100 to 150 mg. The samples were stirred under UV-irradiation (λ = 350 nm) for a maximum of 12 h. All polymerization attempts resulted in insoluble polymer after 3 to 4 h.

b) The monomer **M2** was dissolved in degassed DCM with a concentration of 0.05, 0.1 and 0.2 mol L^{-1} in batches of 15 mg. The solutions were stirred under UV-irradiation (λ = 350 nm) for 12 h. The solutions were dried under air and redissolved in either chloroform or THF for analysis. The conversion was determined by ^{1}H NMR.

Homo- and Copolymerization Procedures

The monomer **M1** and/or **M2** (100 mg) were dissolved in degassed DCM with 0.1 mol L^{-1} with the following ratios for M1:M2 = 1.00, 0.75, 0.50, 0.25 and 0.00 mol%. The solutions were irradiated with λ = 350 nm for 12 h. Samples for SEC and NMR were taken at 1, 2, 4, 6 and 12 h. The samples were dried under air and subsequently dissolved in either THF or deuterated CDCl$_3$ for analysis. The conversion p was determined by ^{1}H NMR spectroscopy, comparing the integral of the methyl group of the photoenol unit (2.51 to 2.60 ppm, 3H) with the newly formed CH- and CH$_2$-groups of the cyclohexyl moiety (2.69 to 3.50 ppm, 4H).
The conversion p was calculated with the following formula:

$$p = \frac{\frac{1}{4}I_P}{\frac{1}{3}I_M + \frac{1}{4}I_P} \tag{B.1}$$

I_P: Integral of the polymer from 2.69 to 3.50 ppm
I_M: Integral of the monomer from 2.51 to 2.60 ppm

The polymers were isolated by precipitation in MeOH. The amount of polymer received per 100 mg batch was as follows: **HP1**: 30 $\pm$ 5%; **HP2**: 8 $\pm$ 2%; **CP1**: 27 $\pm$ 3%; **CP2**: 25 $\pm$ 5%; **CP3**: 22 $\pm$ 3%.

B.4 MOPAC Simulations

To predict the monomer conformation inside the MOF structures, a reasonably large supercell needs to be constructed. Due to the large number of atoms in the calculation, we performed semi-empirical quantum chemical calculations using the modified neglect of diatomic overlap (MNDO) approximation[189] with the PM7 parametrization.[187] Starting from a single unit cell of the Cu-BDC-dabco and Cu-BPDC-dabco MOF structures, we have constructed a $2 \times 2 \times 3$ supercell (the longer axis aligned with the orientation of the monomer to be inserted) with periodic boundary conditions. The structure was optimized using the eigenvector.[186]

Similarly, we optimized the structure of the two monomers individually. Each monomer was inserted into each of the two MOF structures in horizontal or vertical orientation, typically reaching from one MOF pore to the next. The binding energy of each configuration was calculated with Equation B.2, where E_{MOF} and $E_{Monomer}$ are the total energies of the empty MOF structure and the monomer, calculated separately, whereas $E_{MOF+Monomer}$ is the total energy of the MOF structure containing the monomer.

$$E_B = E_{MOF+Monomer} - E_{MOF} - E_{Monomer} \tag{B.2}$$

Additional Experimental Data

C.1 Chapter 3
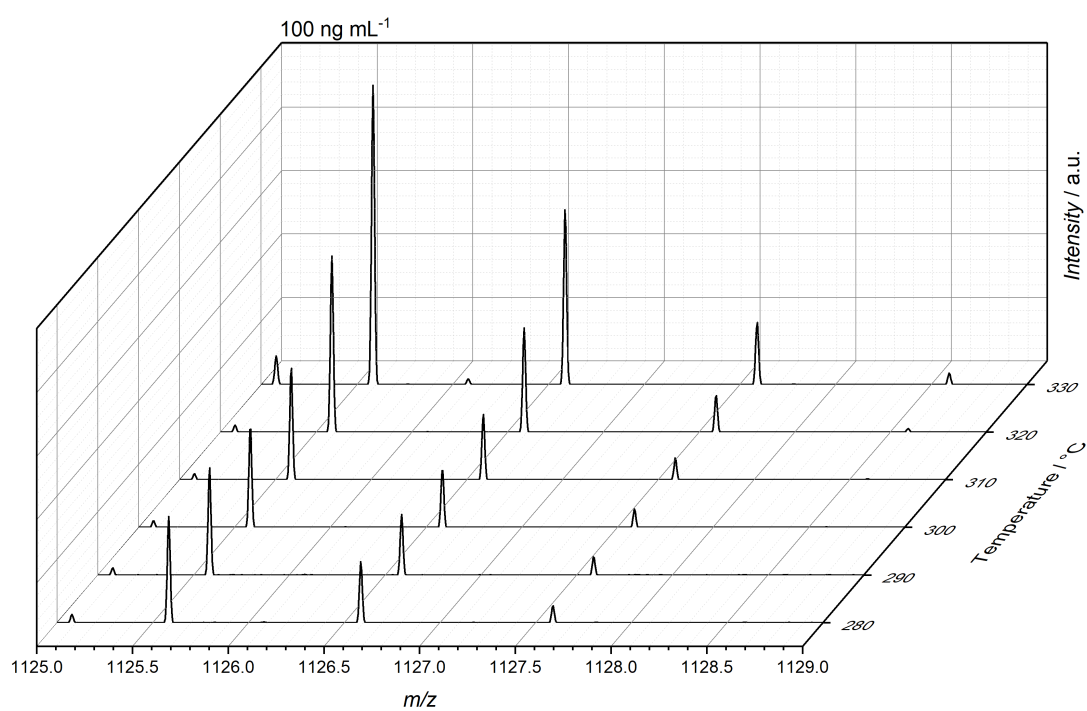
Figure C.1: ESI-mass spectra of PMMA standard with a $c = 100\,\mathrm{ng\,mL}^{-1}$, analyzed with various capillary temperatures.
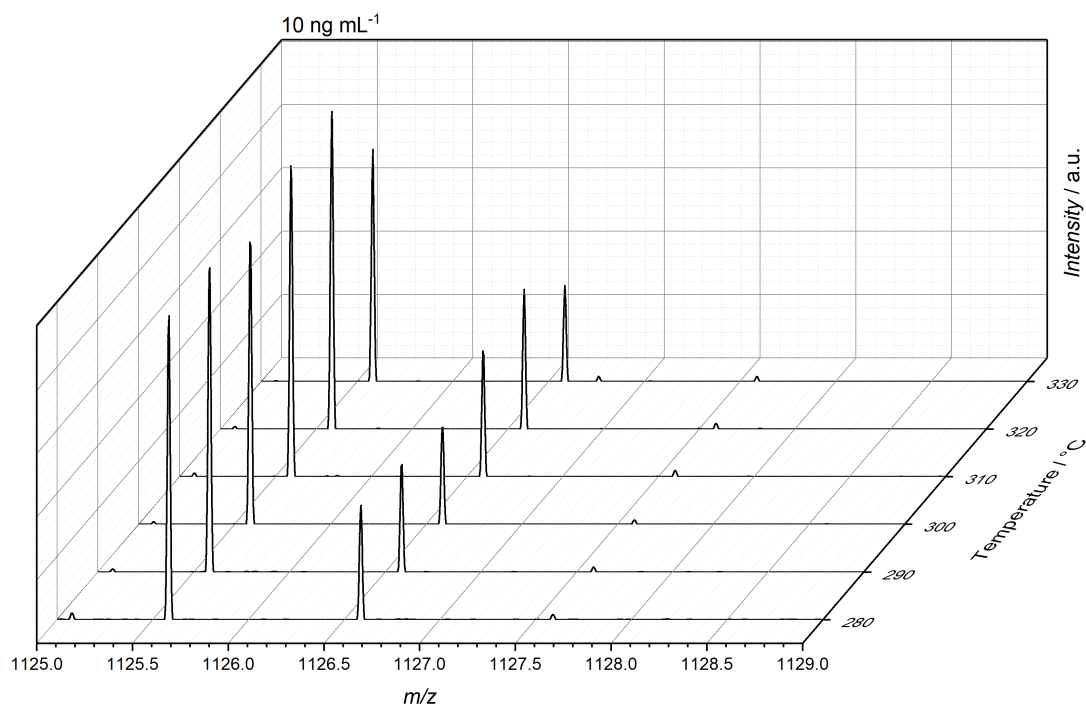
Figure C.2: ESI-mass spectra of PMMA standard with a $c = 10\,\text{ng}\,\text{mL}^{-1}$, analyzed with various capillary temperatures.
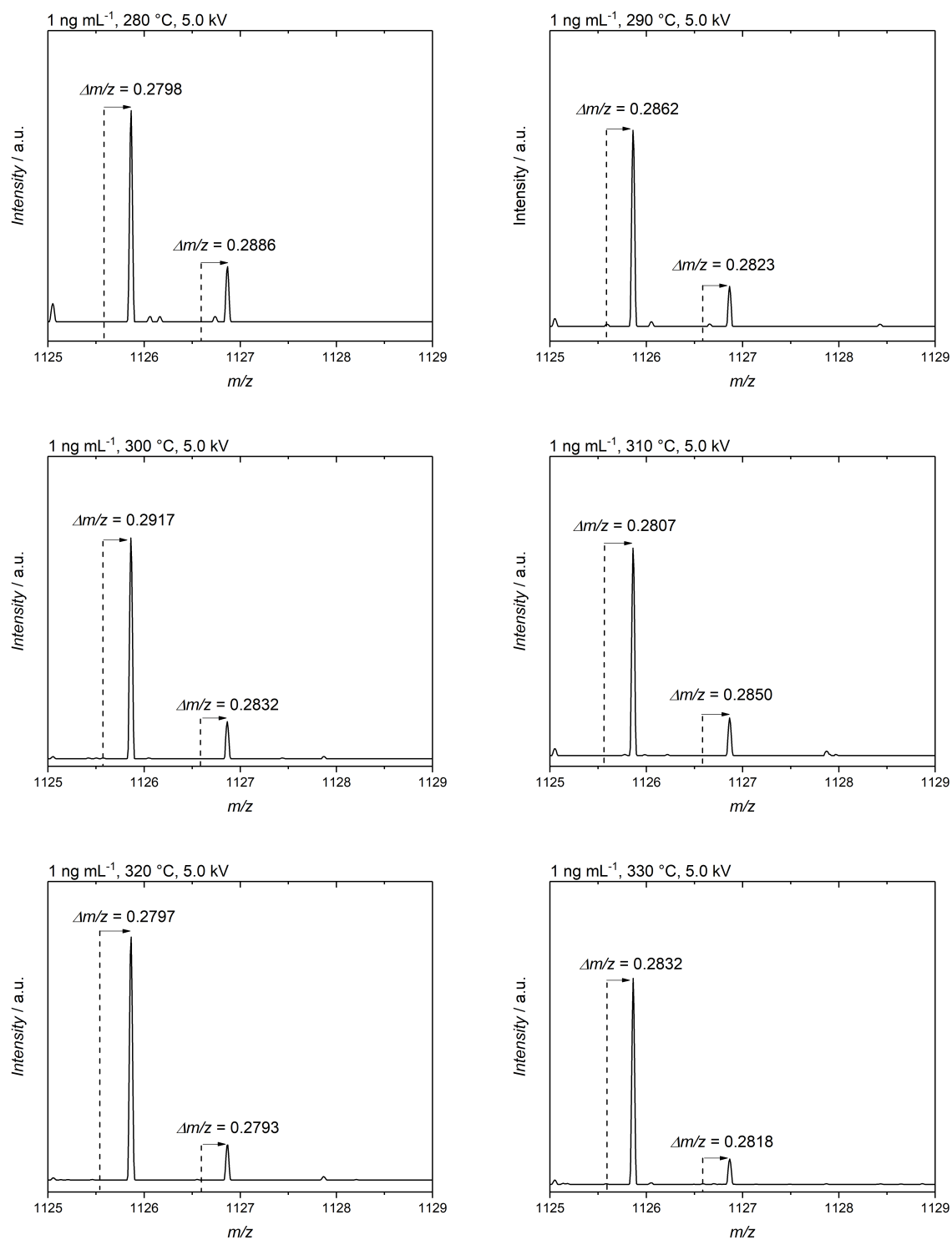
Figure C.3: ESI-mass spectra of PMMA ($c = 1.0 \, \text{ng} \, \text{mL}^{-1}$) with various capillary temperatures and spray voltage of $V = 5.0 \, \text{kV}$.
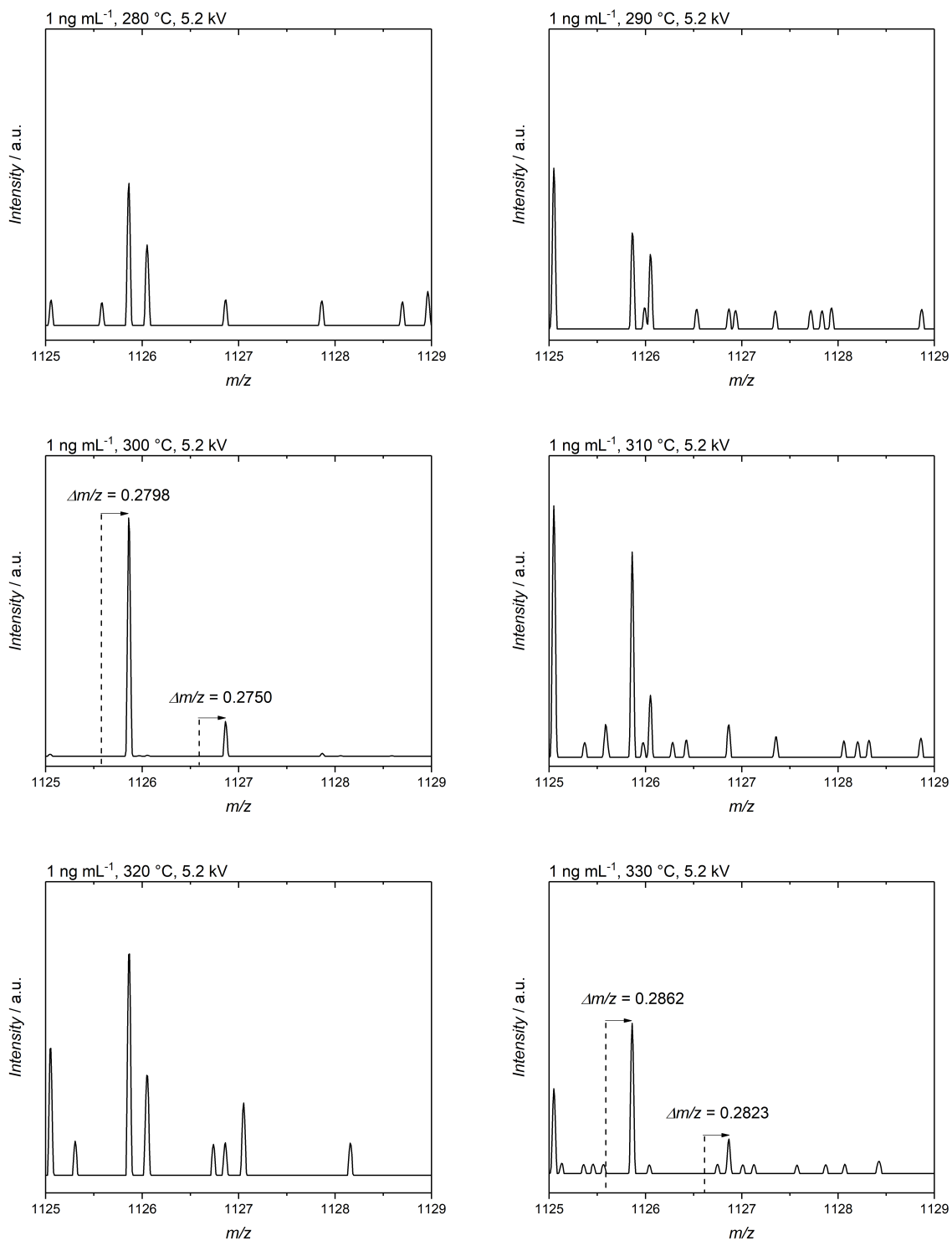
Figure C.4: ESI-mass spectra of PMMA ($c = 1.0\,\text{ng}\,\text{mL}^{-1}$) with various capillary temperatures and spray voltage of $V = 5.2\,\text{kV}$.
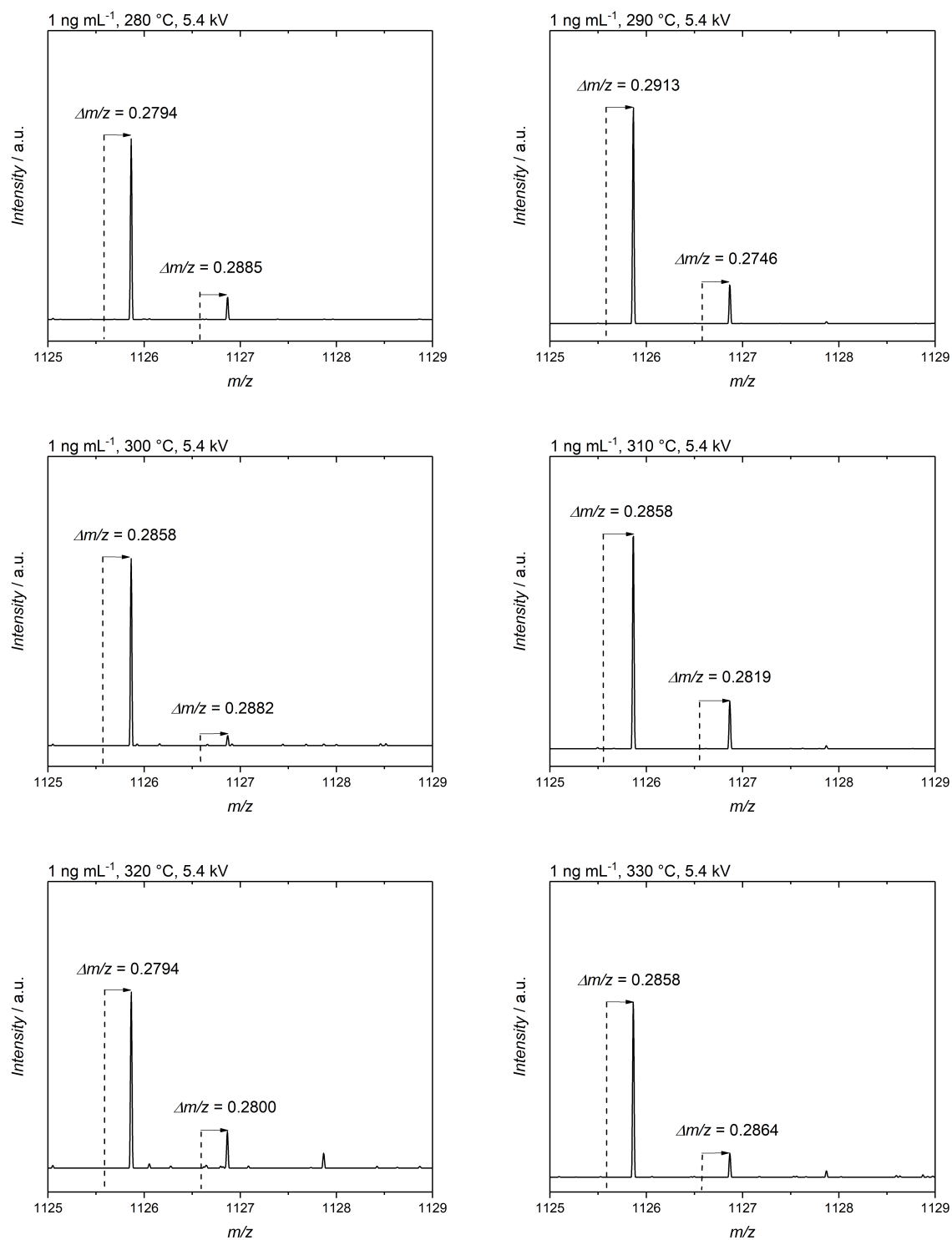
Figure C.5: ESI-mass spectra of PMMA ($c = 1.0\,\mathrm{ng\,mL^{-1}}$) with various capillary temperatures and spray voltage of $V = 5.4\,\mathrm{kV}$.
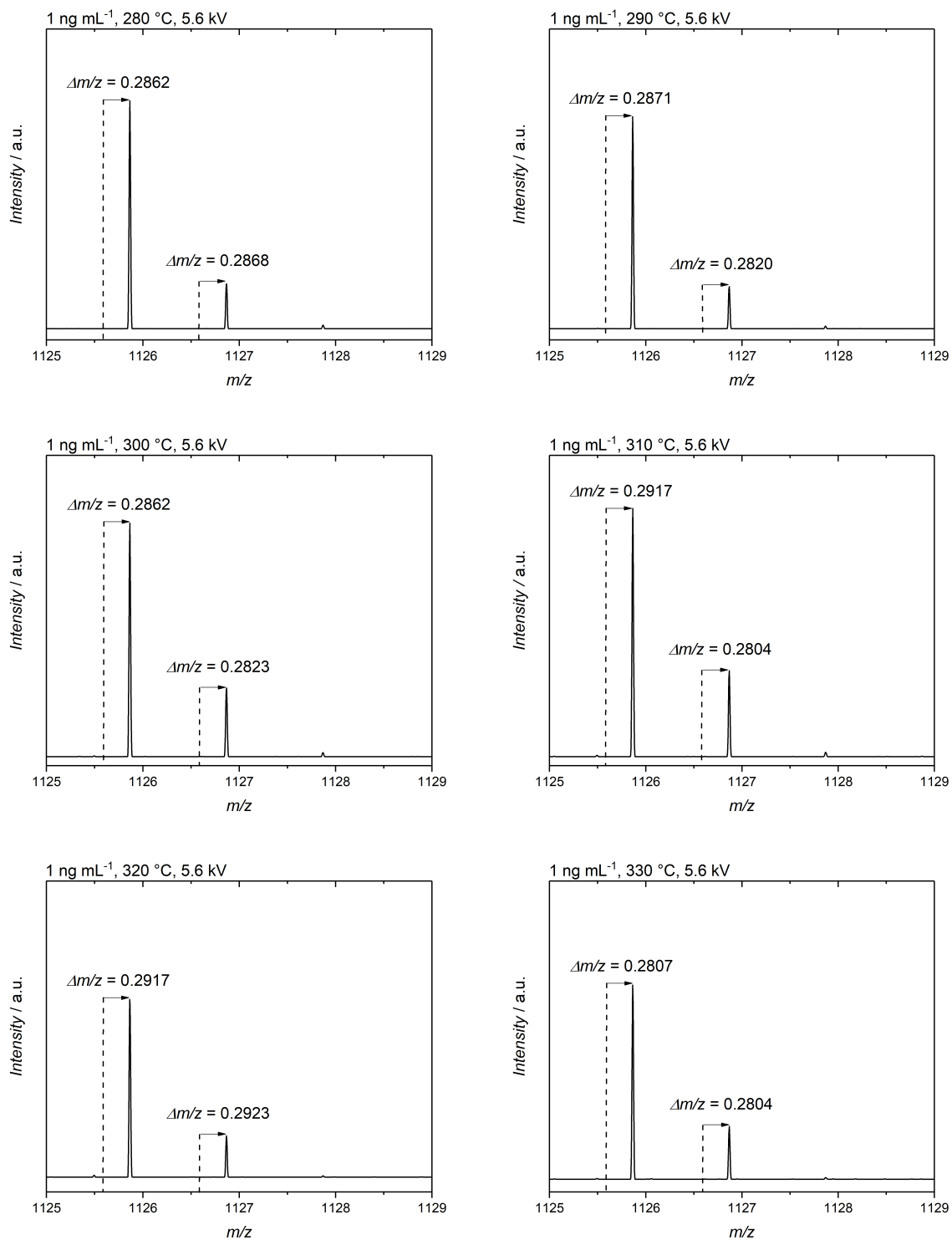
Figure C.6: ESI-mass spectra of PMMA ($c = 1.0\,\mathrm{ng\,mL^{-1}}$) with various capillary temperatures and spray voltage of $V = 5.6\,\mathrm{kV}$.
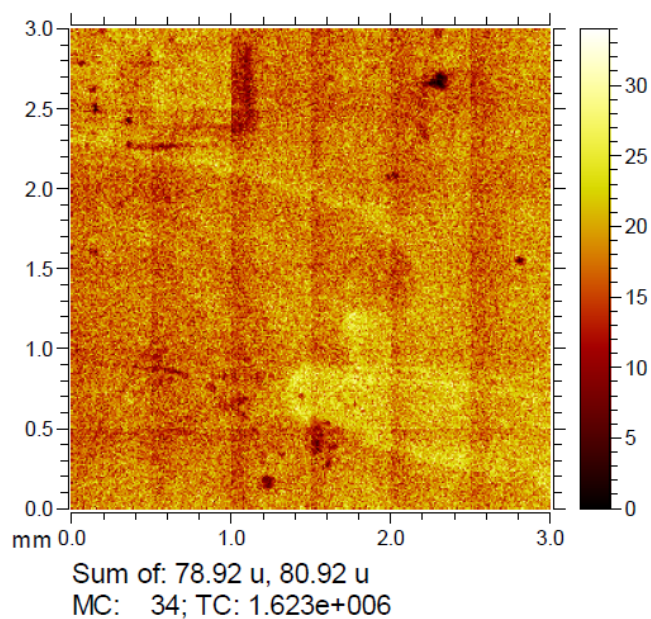
Figure C.7: ToF-SIMS image of Cu-BPDC after the polymerization with bromostyrene via the gasphase approach. Br^- isotopes are equally distributed over the SURMOF surface. Reprinted from the master thesis of S. Hurrle.[141]
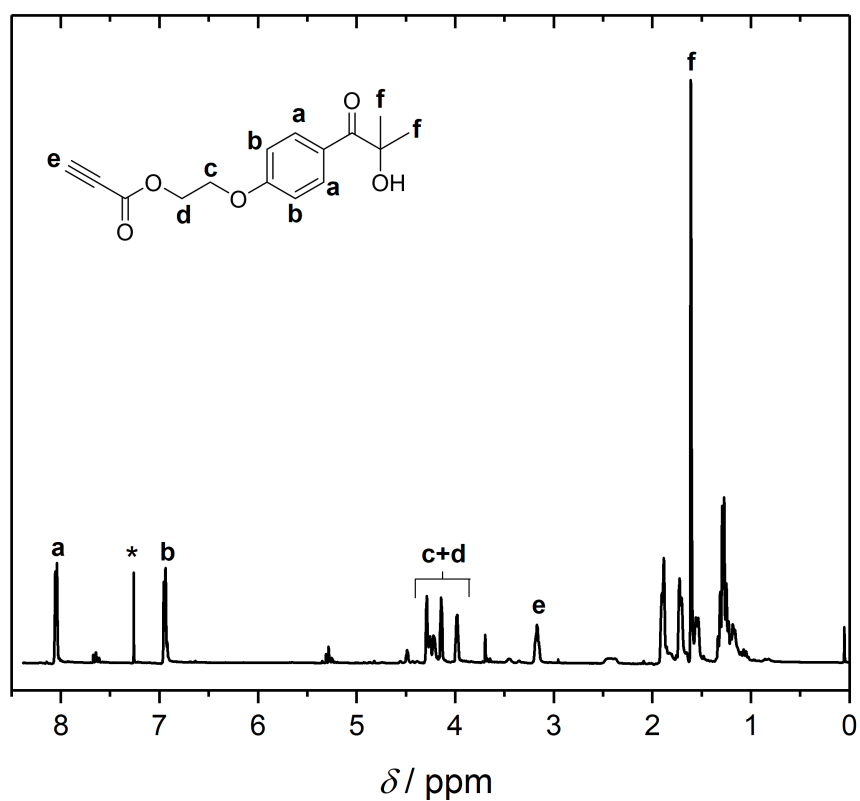
Figure C.8: ^{1}H NMR spectrum in $CDCl_3$ of the crude product of the reaction of **Irgacure2959** and propiolic acid under Steglich conditions with DCC and DMAP.
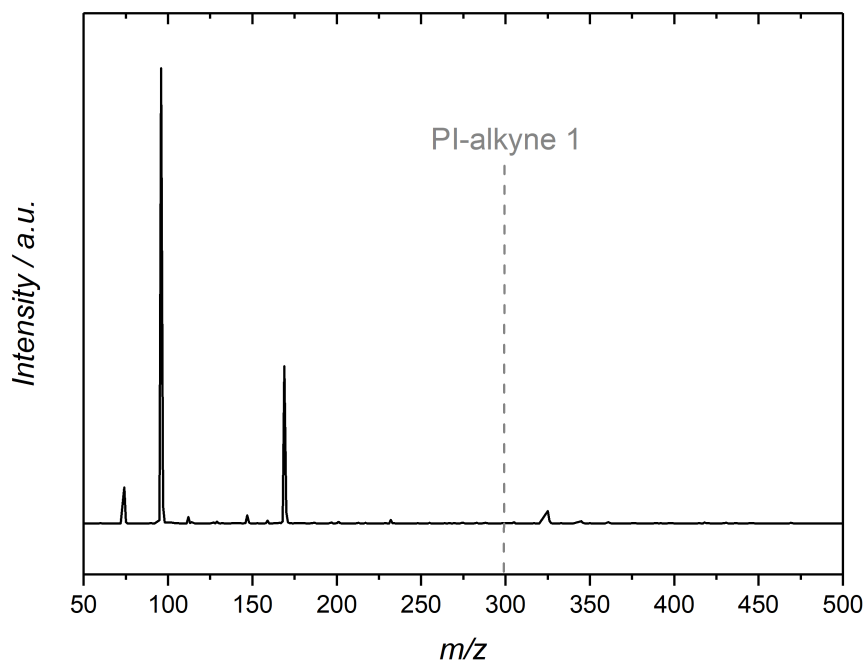
Figure C.9: ESI-mass spectrum of the crude product of the reaction of **Irgacure2959** and propiolic acid under Steglich conditions with DCC and DMAP. The desired mass of the product **PI-alkyne 1** (grey) was not detected.
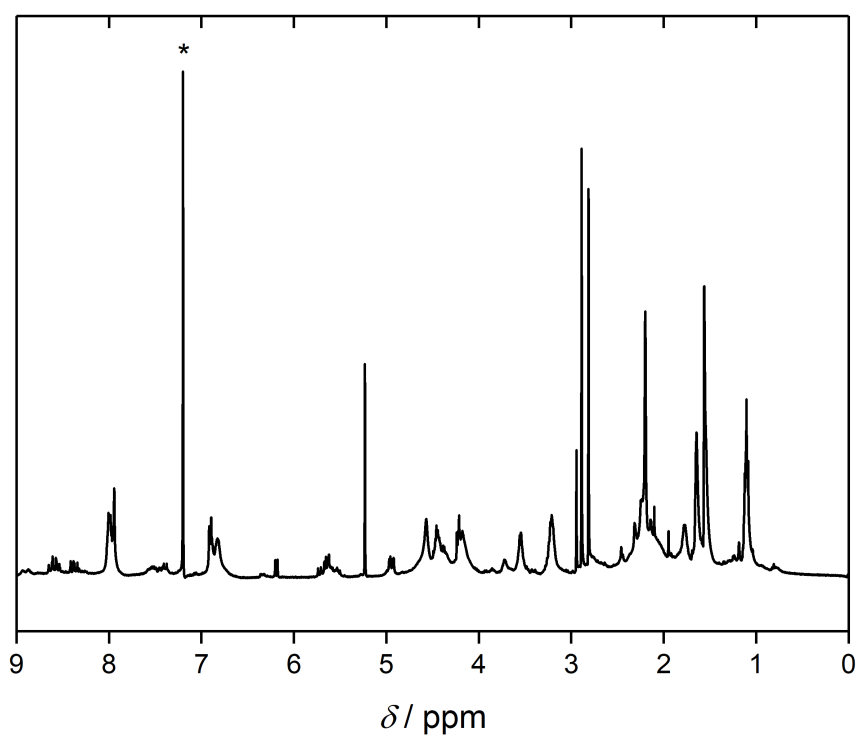
Figure C.10: ^{1}H NMR spectrum in CDCl$_3$ of the crude product of the reaction of **Irgacure2959** and propiolic acid under Steglich conditions with EDC and DMAP.
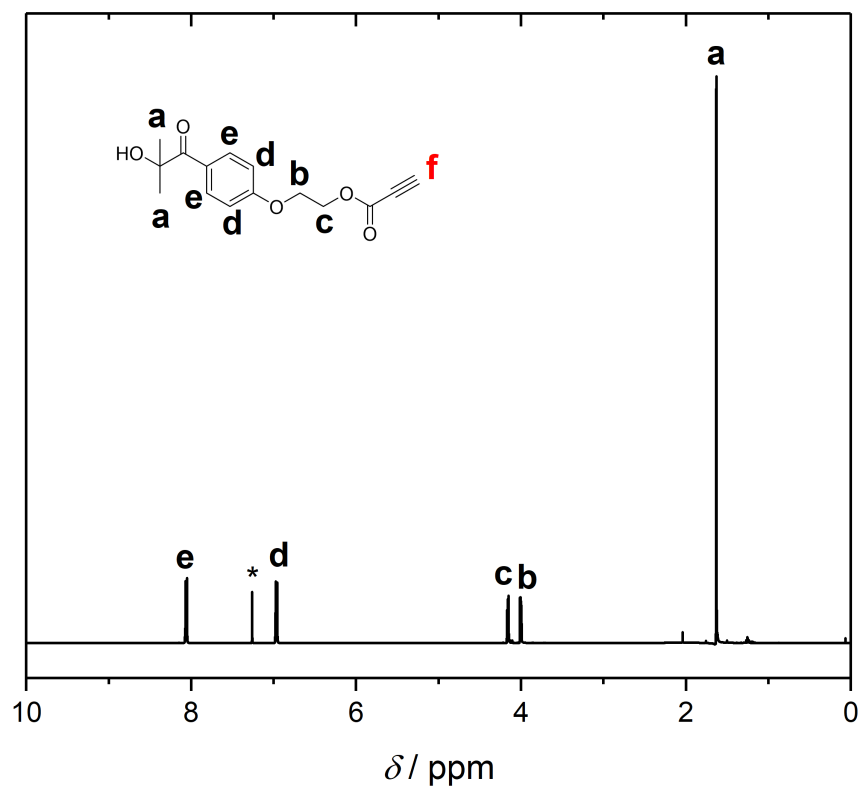
Figure C.11: ^{1}H NMR spectrum in CDCl$_3$ of the product received from the reaction of **Irgacure2959** and propiolic acid. Propiolic acid was transformed into an active ester with CDI. The alkyne proton (red) is not detected.
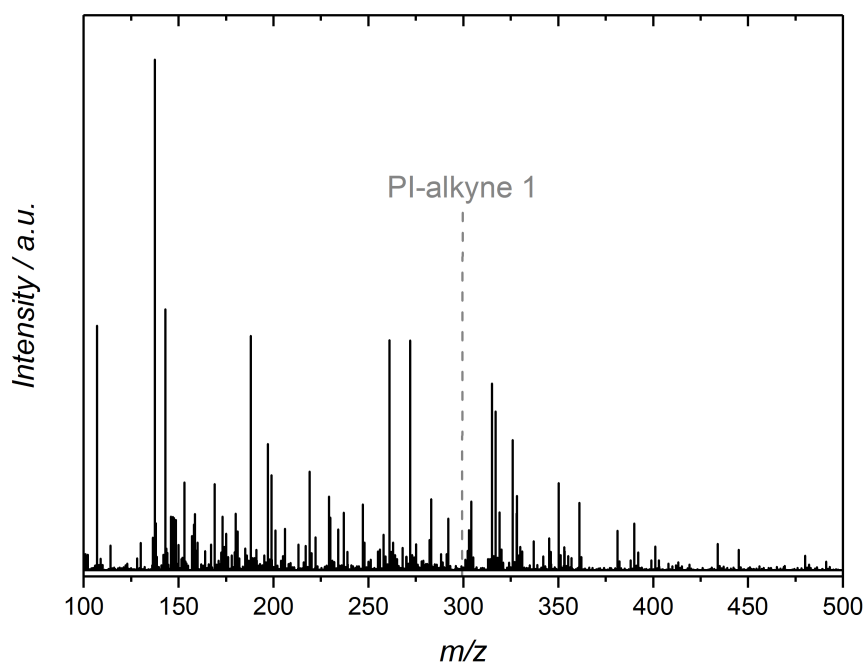
Figure C.12: ESI-mass spectrum of the reaction of **Irgacure2959** with propiolic acid (1.00 eq.), catalyzed via *p*-toluenesulfonic acid.The mass of the desired product **PI-alkyne 1** (grey) is not detected.
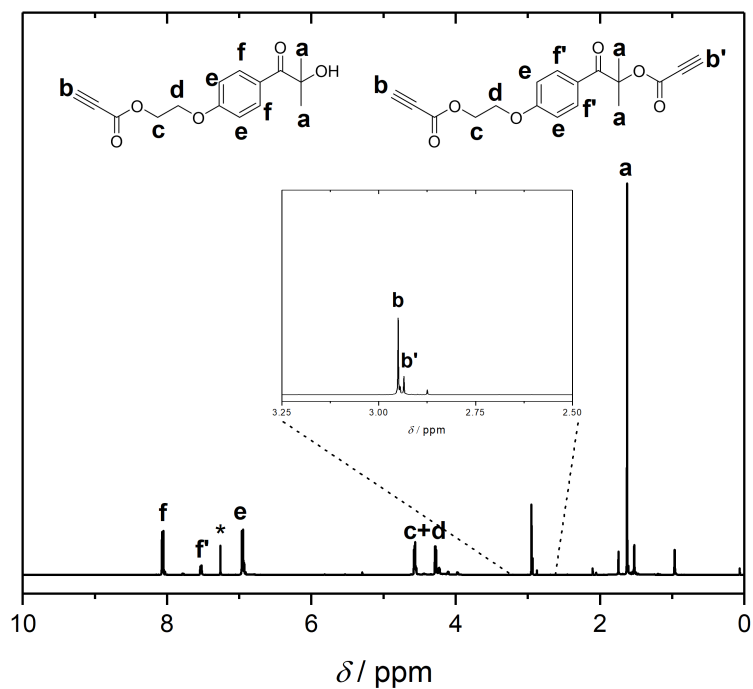
Figure C.13: ^{1}H NMR spectrum of the product of the esterification **Irgacure2959** with propiolic acid (3.00 eq.), catalyzed via *p*-toluenesulfonic acid. A second resonance for the terminal triple bond was detected and suggests that the bifunctional product is present with 20%.
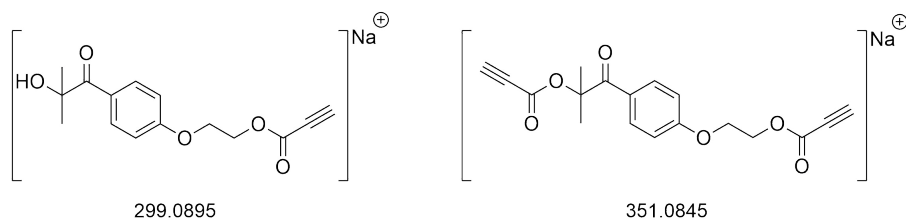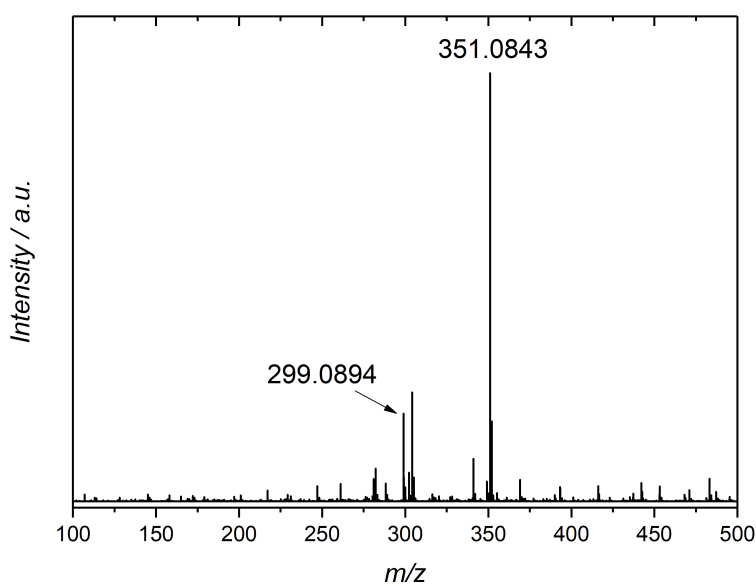
Figure C.14: ESI-mass spectrum of the product of the esterification between **Irgacure2959** and propiolic acid (3.00 eq.), catalyzed by *p*-toluenesulfonic acid. The mass values were assigned to the mono- and bifunctionalized initiator.
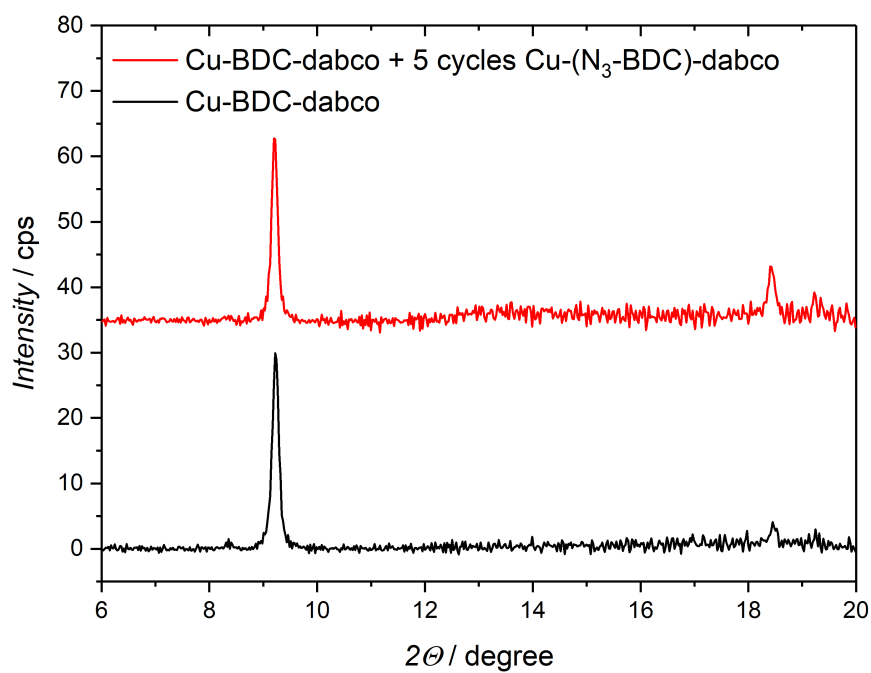
Figure C.15: X-ray diffractograms of Cu-BDC-dabco (40 cycles) + Cu-(N$_3$-BDC)-dabco (5 cycles) before and after the functionalization with **PI-alkyne**.
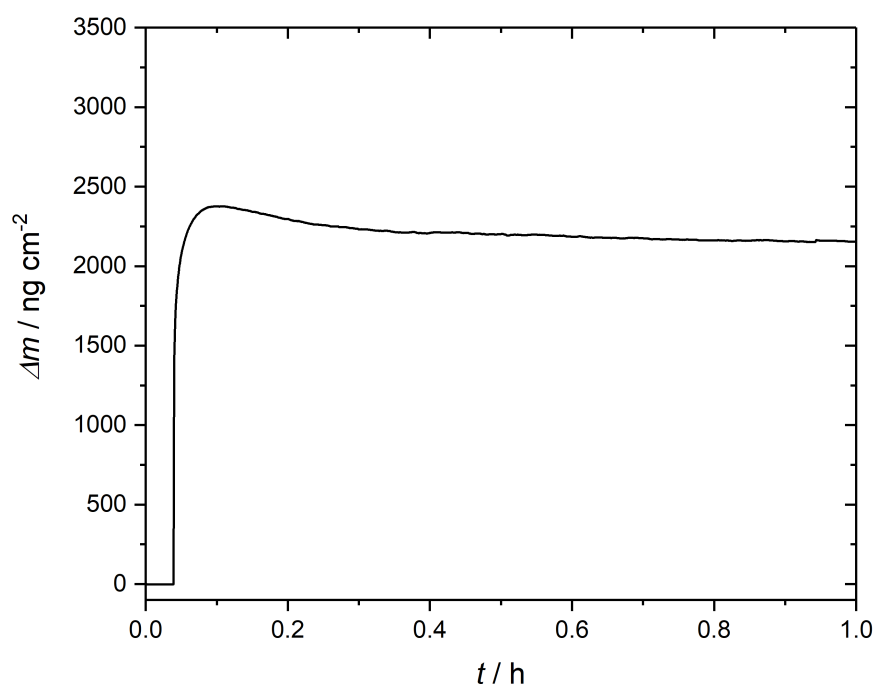
Figure C.16: QCM monitoring of Cu-BDC-dabco (60 cycles) during the loading with MMA, second batch.

C.2 Chapter 4
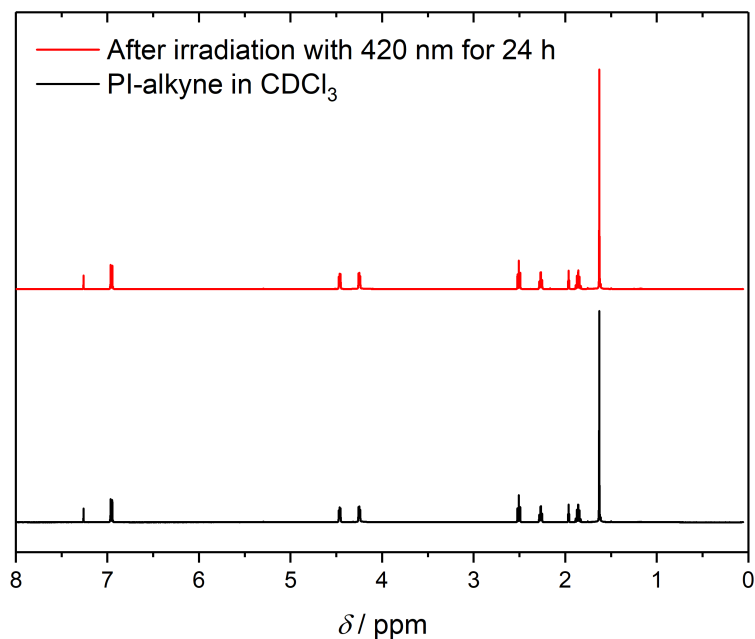
Figure C.17: ^{1}H NMR spectra of **PI-alkyne** in CDCl$_3$ before and after irradiation with 420 nm for 24 h. This figure was adapted with permission from John Wiley and Sons.[144]
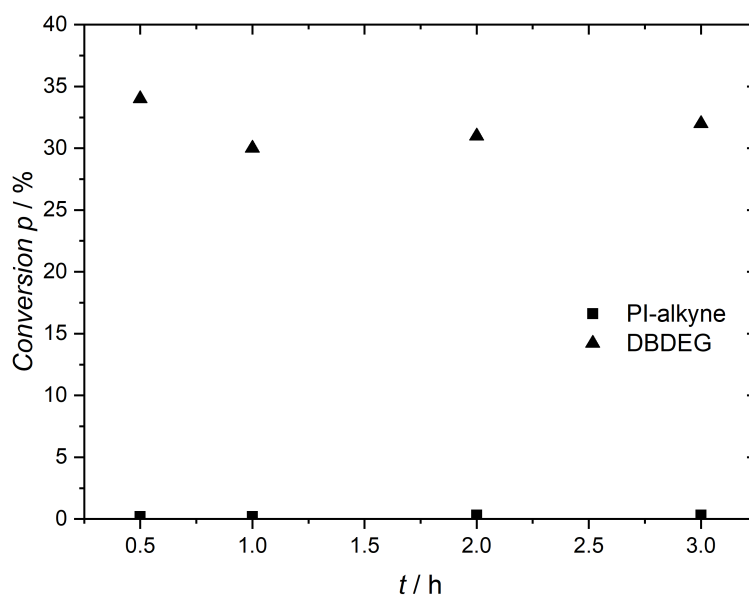
Figure C.18: Results of the polymerizations of MMA with **DBDEG** and **PI-alkyne** at 420 nm. Conversion was determined gravimetically by evaporating the residual monomer. This figure was adapted with permission from John Wiley and Sons.[144]

Table C.1: Theoretical and experimental *m/z* values for the copolymer PEG-*b*-PMMA generated with **PEG-PI** via PLP for pattern B in Figure 4.7. The right column provides the amount in which each species is present in the spectrum, yet other linear combination of the individual contributions may also result in the observed peak patterns. However, the absolute positions of each peak remain intact, confirming the presence of the expected species. Adapted with permission from John Wiley and Sons. [144]

Species	n	m	$(m/z)_{\text{theo}}$	$(m/z)_{\text{exp}}$	$\Delta(m/z)$	amount (eq.)
AB$^{\text{C}}$	15	25	1791.4309	1791.4583	0.0274	0.30
	17	24	1785.4309	1785.4498	0.0189	0.01
	22	22	1795.4440	1795.4570	0.0130	0.60
	31	18	1793.4571	1793.4512	0.0059	0.30
	33	17	1787.4571	1787.4608	0.0037	0.01
2A$^{\text{C}}$	27	17	1783.9185	1783.9519	0.0336	0.01
	32	15	1793.9316	1793.9414	0.0098	0.41
	34	14	1787.9316	1787.9439	0.0123	0.10
A1$^{\text{D}}$	14	25	1789.4153	1789.4567	0.0414	0.30
	21	22	1793.4284	1793.4512	0.0228	0.41
	23	21	1787.4284	1787.4608	0.0324	0.49
	32	17	1785.4415	1785.4498	0.0083	0.01
	37	15	1795.4546	1795.4570	0.0024	0.35
A2$^{\text{D}}$	14	26	1790.4231	1790.4651	0.0420	0.30
	21	23	1794.4361	1794.4467	0.0106	0.41
	23	22	1788.4362	1788.4493	0.0131	0.49
	30	19	1792.4493	1792.4617	0.0124	0.33
	32	18	1786.9510	1786.9591	0.0081	0.01
	37	16	1796.4624	1796.4600	0.0024	0.35
B2$^{\text{DH}}$	0	35	1792.9445	1792.9622	0.0177	0.43
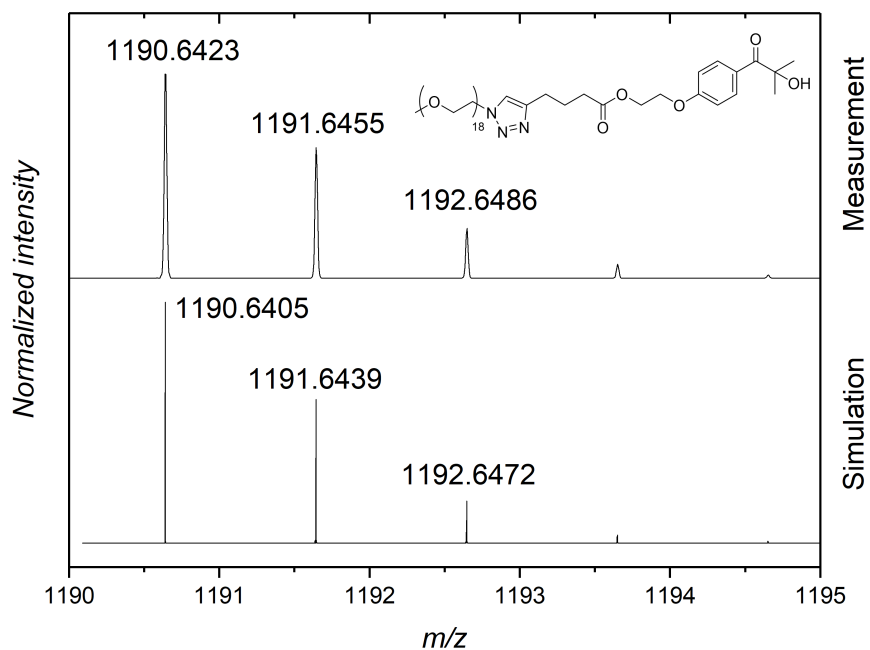
Figure C.19: Theoretical and experimental isotopic pattern distribution of a specific chain length ($n = 18$) of the PEGylated photoinitiator. This figure was adapted with permission from John Wiley and Sons.[144]
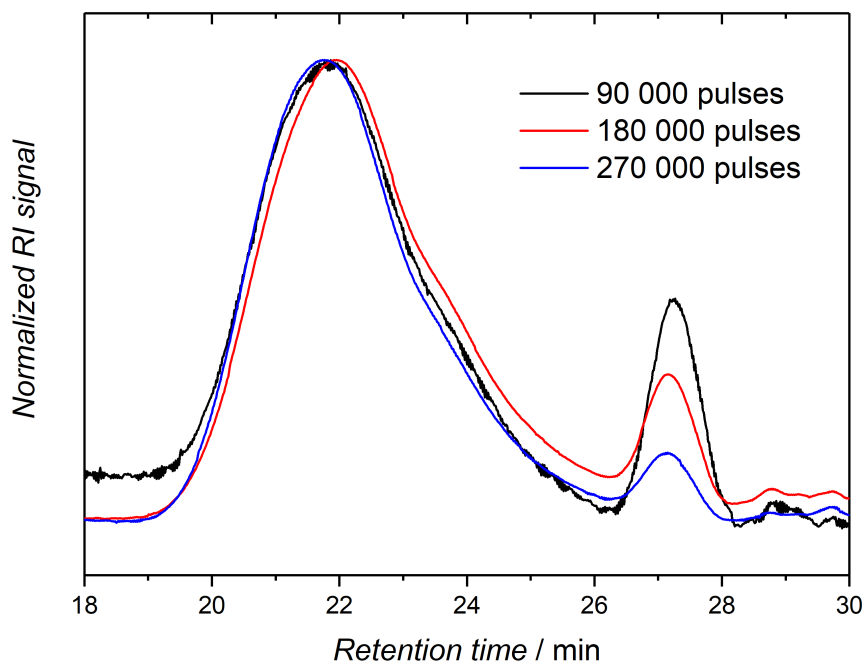
Figure C.20: SEC results of MMA polymerized with **PEG-PI** via PLP. The graph shows that the amount of residual macroinitiator can be reduced by the number of pulses. This figure was adapted with permission from John Wiley and Sons.[144]
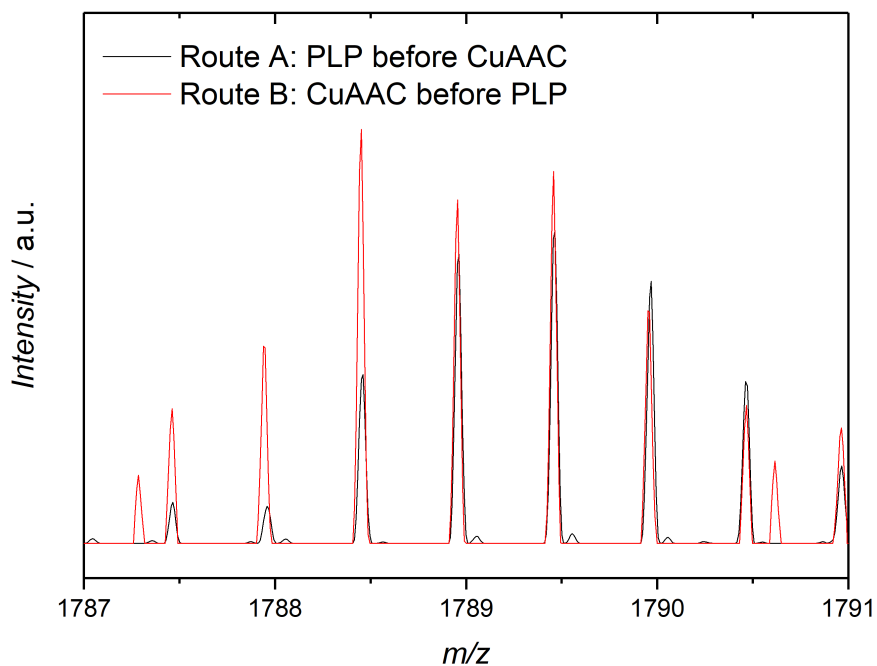
Figure C.21: Illustrative zoom into the spectrum of Figure 4.8 in the mass range m/z = 1787 to 1791. The high-resolution SEC-ESI-mass spectra of PEG-*b*-PMMA synthesized via Route A (black) or Route B (red). The peaks of both spectra have identical m/z values. This figure was adapted with permission from John Wiley and Sons. [144]
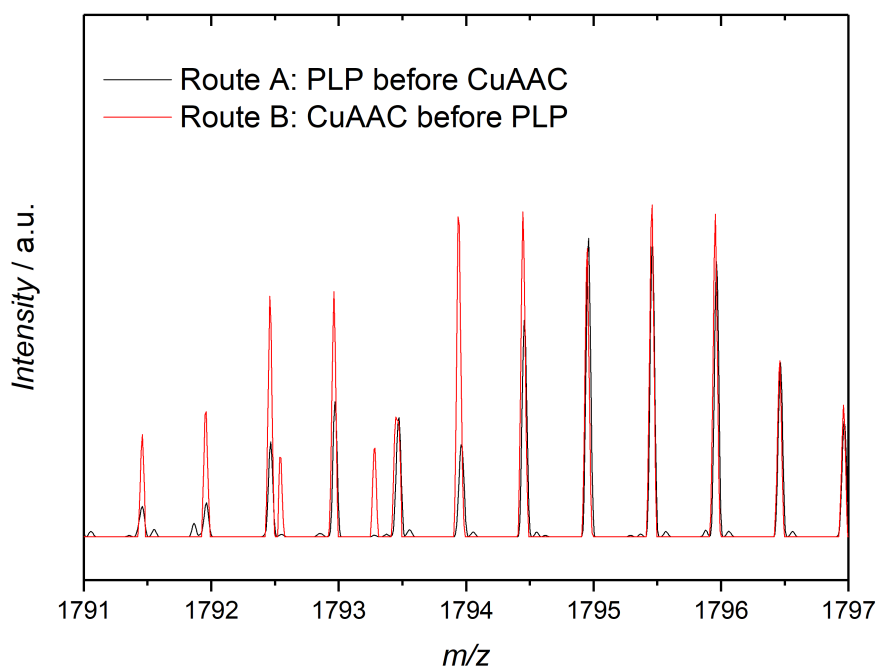
Figure C.22: Illustrative zoom into the spectrum of Figure 4.8 in the mass range m/z = 1791 to 1797. The high-resolution SEC-ESI-mass spectra of PEG-*b*-PMMA synthesized via Route A (black) or Route B (red). The peaks of both spectra have identical m/z values. This figure was adapted with permission from John Wiley and Sons. [144]

C.3 Chapter 5
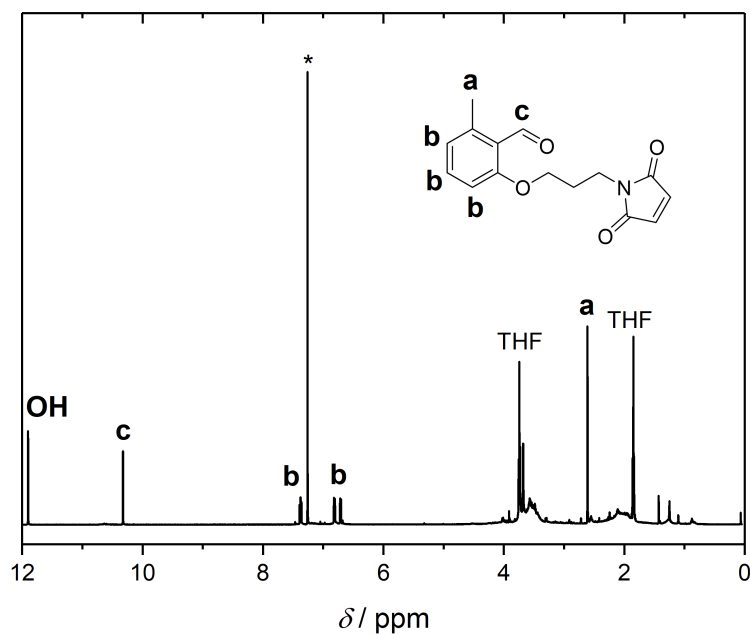
Figure C.23: ^{1}H NMR in CDCl$_3$ spectrum of **PhE-Mal** synthesized with **Mal-Cl**. The NMR spectrum shows resonances for the α-methyl benzaldehyde unit without additional resonances for the maleimide derivative.
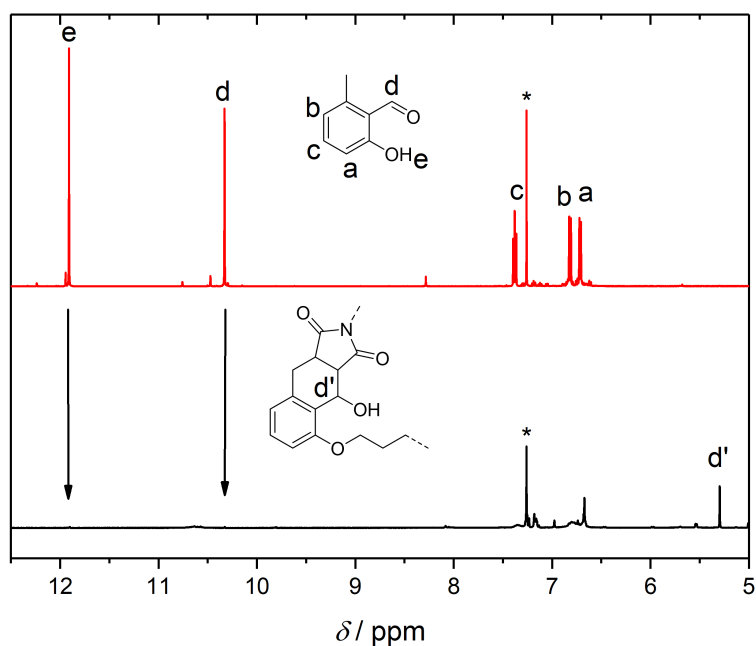
Figure C.24: Zoom into the ^{1}H NMR spectra in CDCl$_3$ of **PhE** before (red) and after (black) the ether synthesis with **Mal-Br**. The ether is successfully formed (resonance e), yet the cycloaddition consuming the aldehyde moiety (resonance d) also occured.
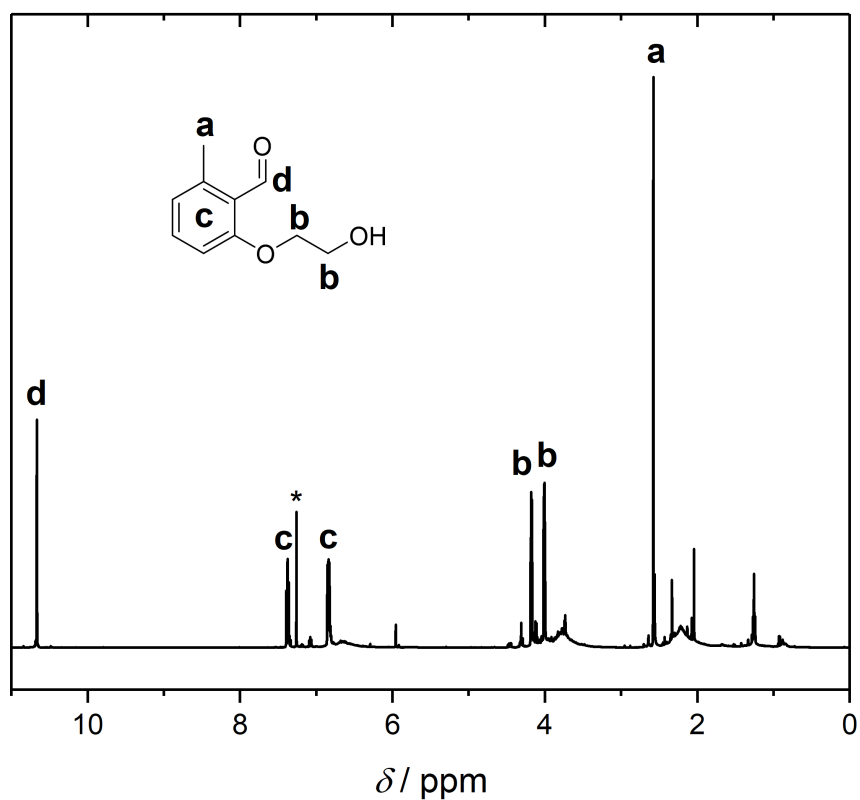
Figure C.25: ^{1}H NMR spectrum in CDCl$_3$ of **Pre2** prepared according to a published procedure.[62] The product could not be purified successfully and, thus, the spectrum shows impurities.
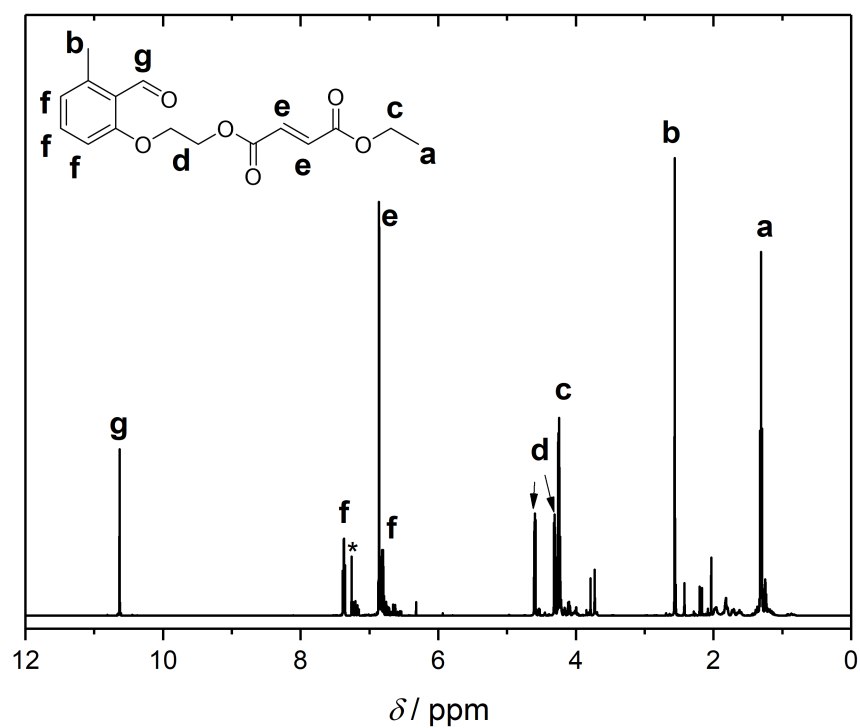
Figure C.26: ^{1}H NMR spectrum in CDCl$_3$ of **PhE-Et** synthesized from crude **Pre2**.

161
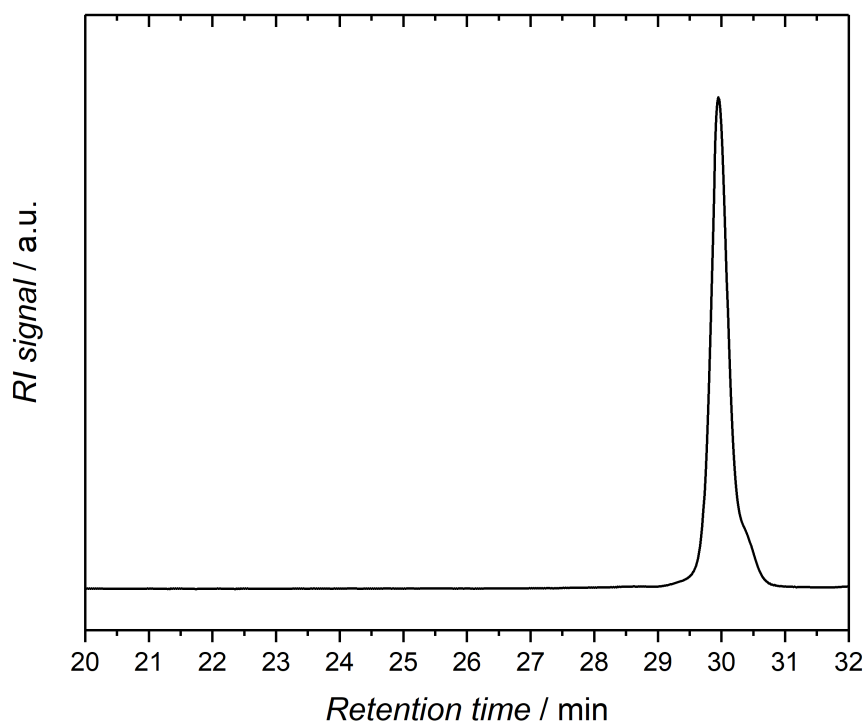
Figure C.27: SEC traces of **M2**.
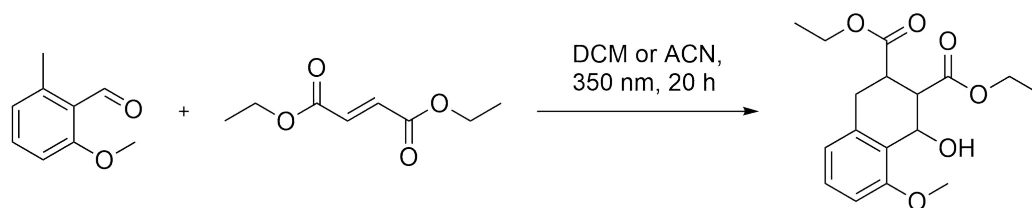
Figure C.28: Test reaction between methoxy protected photoenol **PhE-OMe** and diethyl fumarate in acetonitrile and dichlormethane, respectively. Adapted with permission from Ref. 181. Copyright (2018) American Chemical Society.
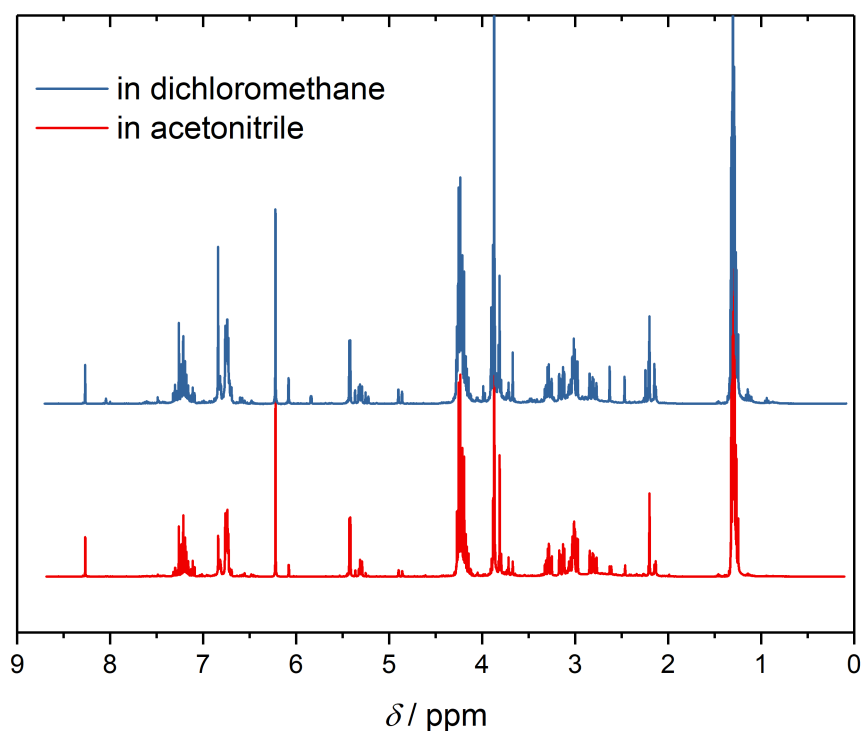
Figure C.29: ^{1}H NMR spectra in CDCl$_3$ of crude test reaction (Figure C.28). Both reactions result in similiar resonances and side reactions cannot be identified. Adapted with permission from Ref. 181. Copyright (2018) American Chemical Society.
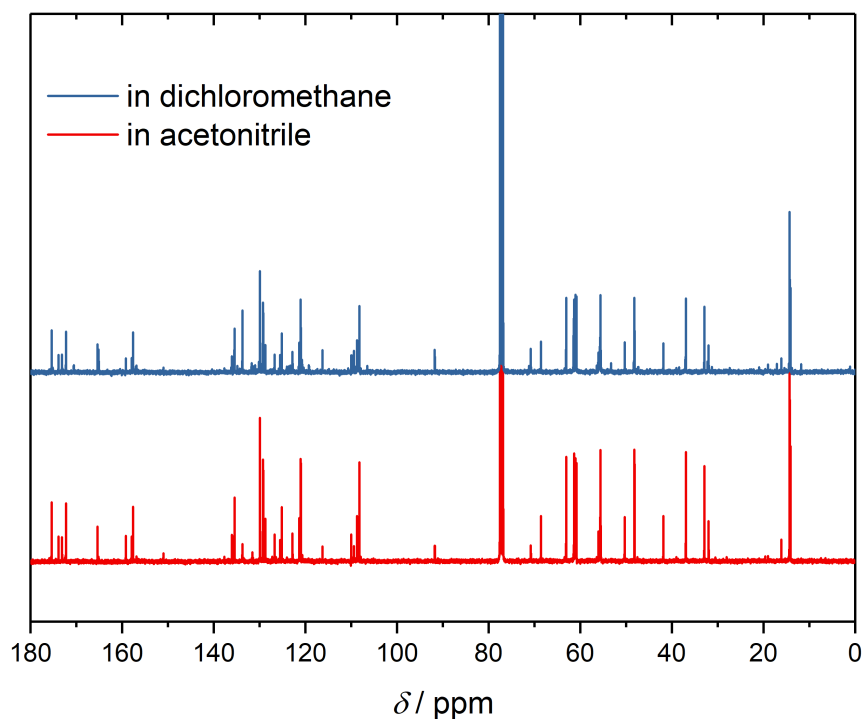
Figure C.30: ^{13}C NMR spectra in CDCl$_3$ of crude test reaction (Figure C.28). Both reactions result in similiar resonances and side reactions cannot be identified. Adapted with permission from Ref. 181. Copyright (2018) American Chemical Society.
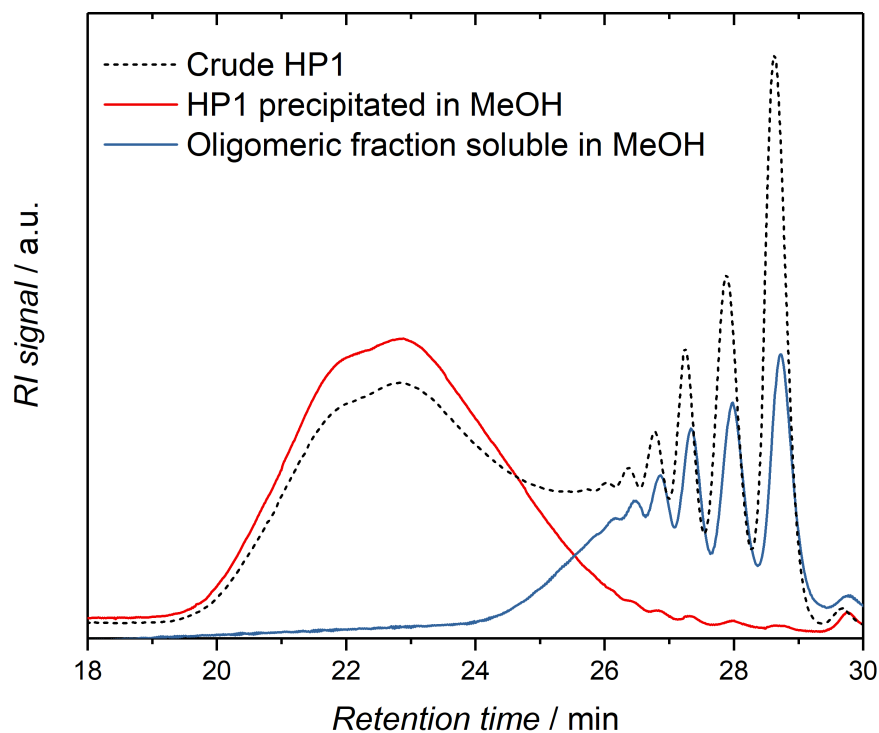
Figure C.31: SEC traces of crude **HP1** (dotted) and after first precipitation in methanol (red) compared to the oligomeric species (blue). Adapted with permission from Ref. 181. Copyright (2018) American Chemical Society.
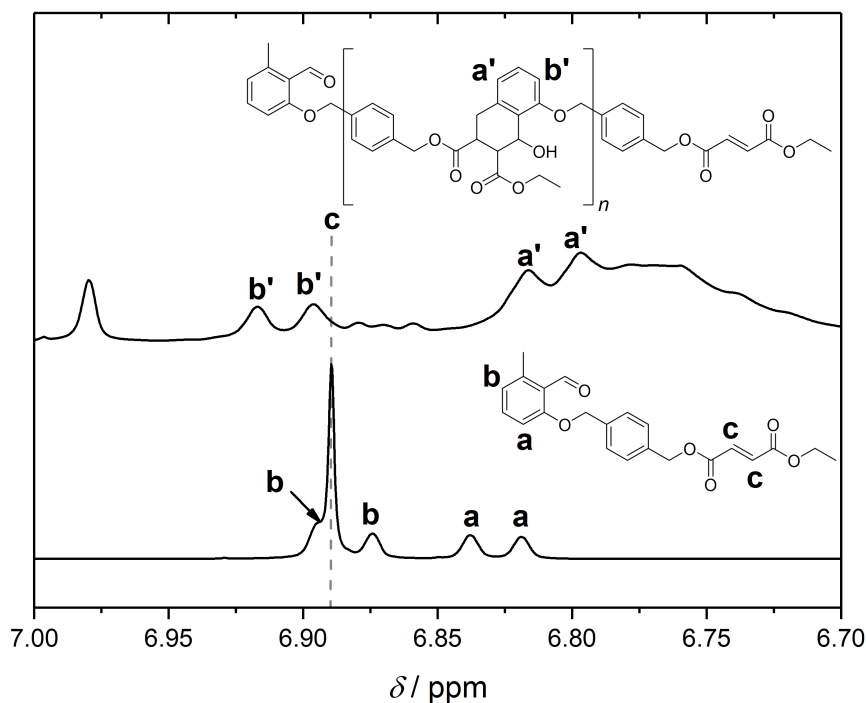
Figure C.32: Zoom into the ^{1}H NMR spectra in CDCl$_3$ of **M1** and the oligomeric fraction that was separated from **HP1**. Adapted with permission from Ref. 181. Copyright (2018) American Chemical Society.
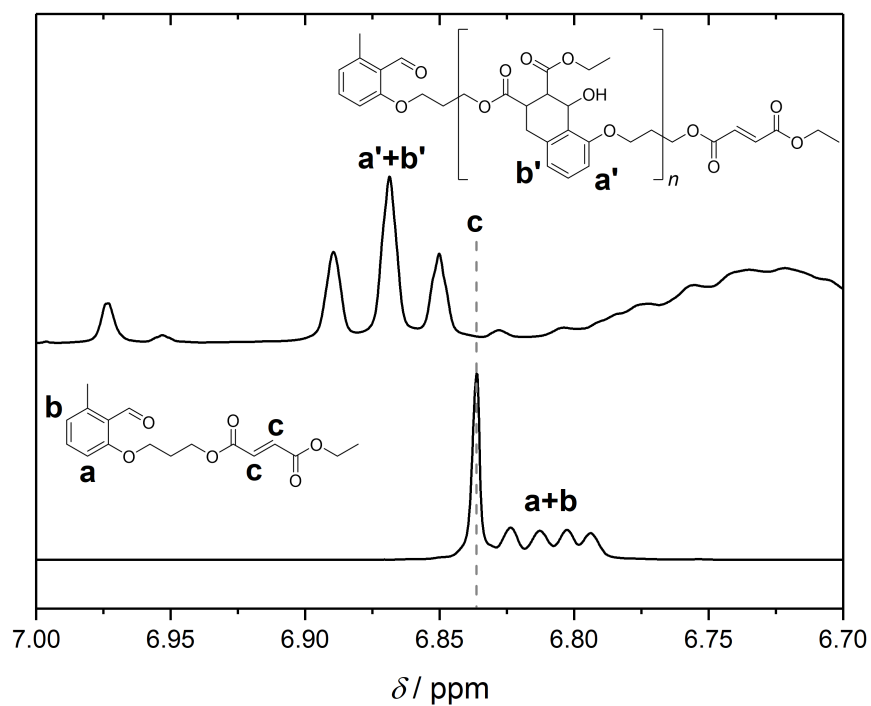
Figure C.33: Zoom into the ^{1}H NMR spectra in CDCl$_3$ of **M2** and the oligomeric fraction that was separated from **HP2**. Adapted with permission from Ref. 181. Copyright (2018) American Chemical Society.
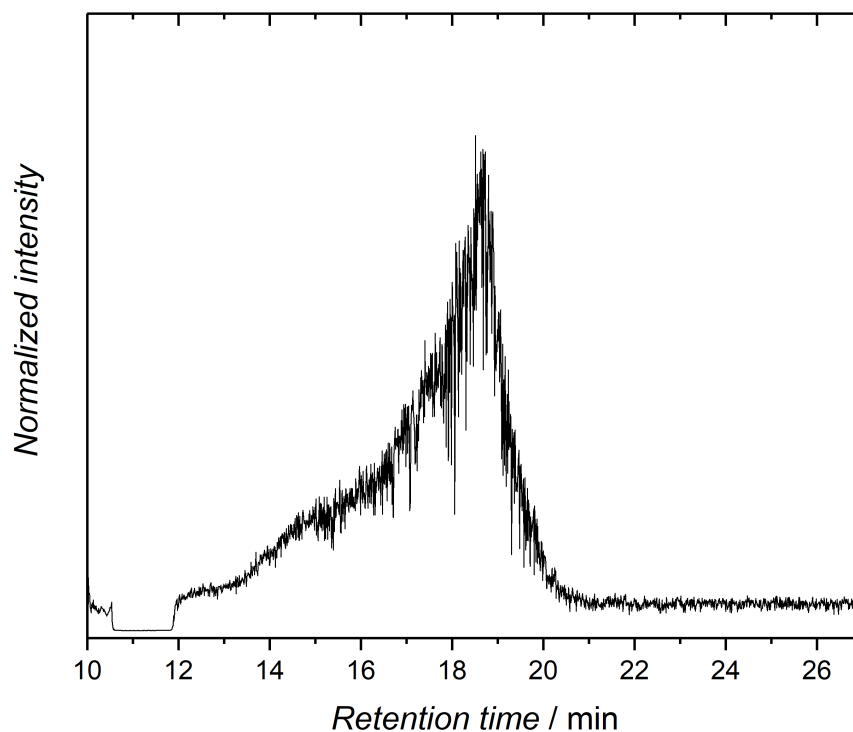
Figure C.34: Chromatogram of **HP1** in SEC-ESI-MS, detected via the ion count of the ESI unit. Adapted with permission from Ref. 181. Copyright (2018) American Chemical Society.
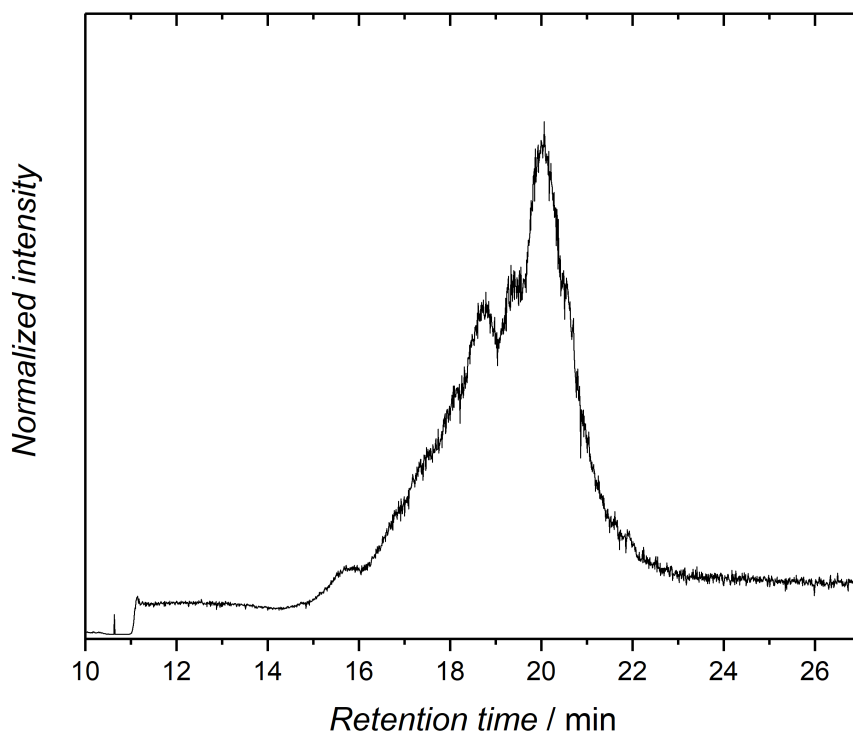
Figure C.35: Chromatogram of **HP2** in SEC-ESI-MS, detected via the ion count of the ESI unit. Adapted with permission from Ref. 181. Copyright (2018) American Chemical Society.
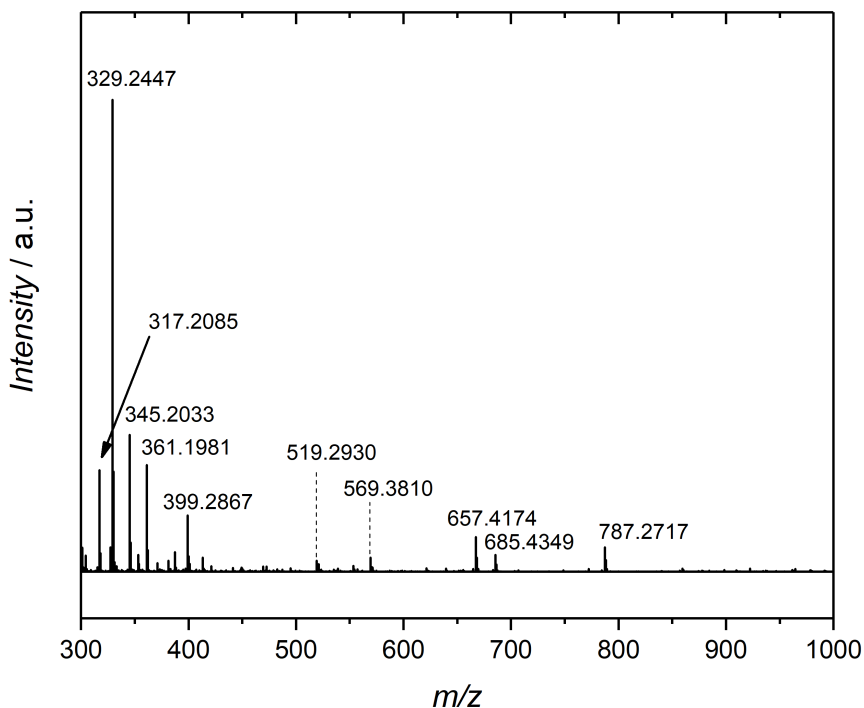
Figure C.36: Background SEC-ESI-mass spectrum, integrated from 22 to 26 min. Adapted with permission from Ref. 181. Copyright (2018) American Chemical Society.
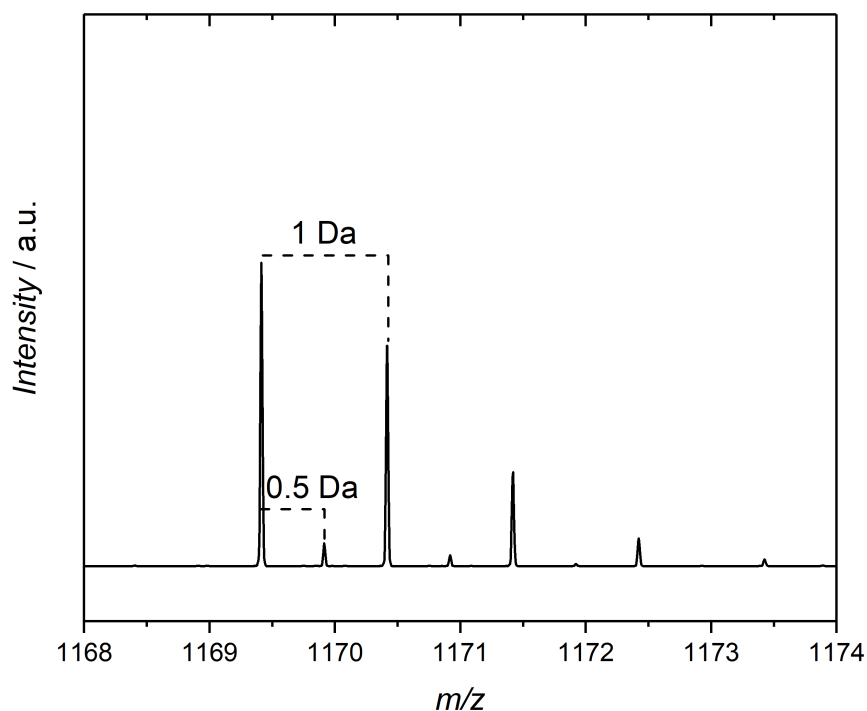
Figure C.37: Zoom into the SEC-ESI-mass spectrum in Figure 5.15 on page 105 showing the isotopic patterns of α_2 and α_5. Both oligomers have the exact same mass, however, can be distinguished by the distances in the isotopic pattern. Adapted with permission from Ref. 181. Copyright (2018) American Chemical Society.
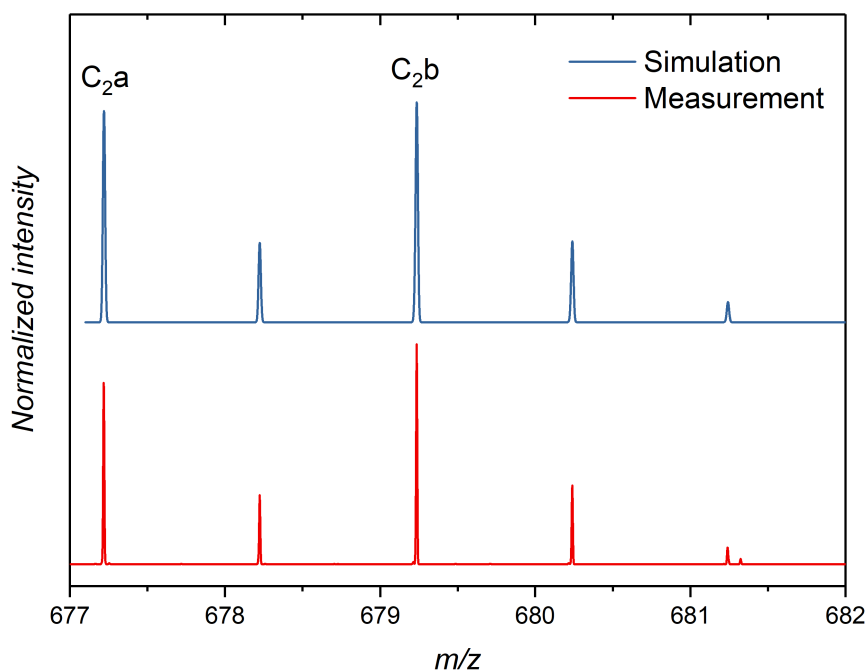
Figure C.38: Zoom into the SEC-ESI-mass spectrum of **HP2** in Figure 5.17a, showing the isotopic pattern of C_2a and C_2b compared to the corresponding simulation. Adapted with permission from Ref. 181. Copyright (2018) American Chemical Society.

Table C.2: Theoretical and experimental *m/z* values of **HP1** found in Figure 5.15a. Adapted from Ref. 181. Copyright (2018) American Chemical Society.

Species	$(m/z)_{theo}$	$(m/z)_{exp}$	$\Delta(m/z)$
α_1	787.2725	787.2724	0.0001
$\alpha_4, z = 2$	978.3433	978.3428	0.0005
α_2	1169.4141	1169.4143	0.0002
$\alpha_5, z = 2$	1169.4141	1169.4143	0.0002
$\alpha_6, z = 2$	1360.4850	1360.4854	0.0004
α_3	1551.5558	1551.5562	0.0004
$\alpha_7, z = 2$	1551.5558	1551.5562	0.0004
α_3 + NaI	1701.4500	1701.4625	0.0125
α_4	1933.6974	1933.7125	0.0151
α_5	2315.8391	2315.8547	0.0156
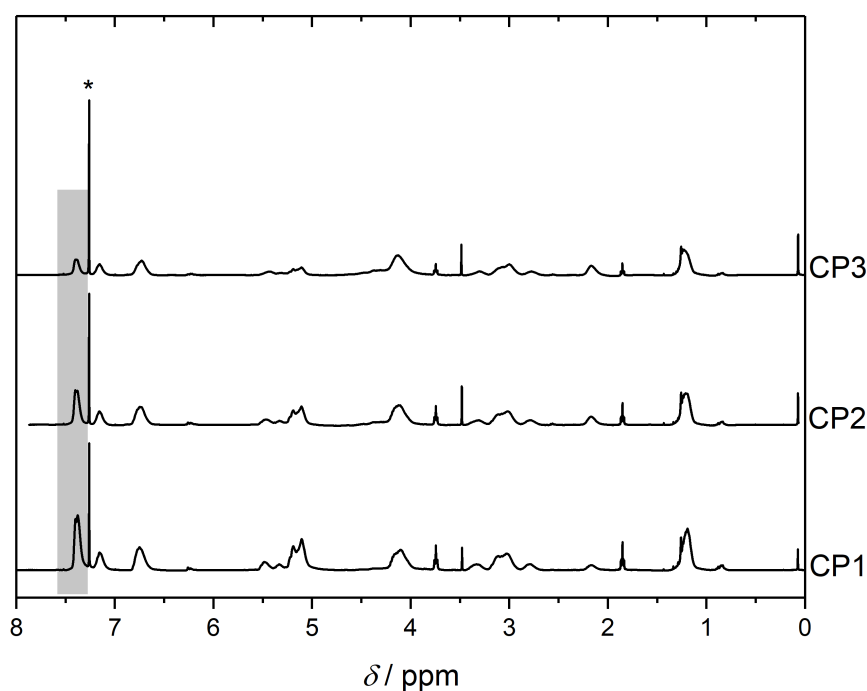
Figure C.39: ^{1}H NMR spectra of copolymers **CP1**, **CP2** and **CP3** in CDCl$_3$. The resonances marked with the grey box are assigned to the xylene backbone of **M1** which can be employed for the calculation of the copolymer composition. Adapted with permission from Ref. 181. Copyright (2018) American Chemical Society.
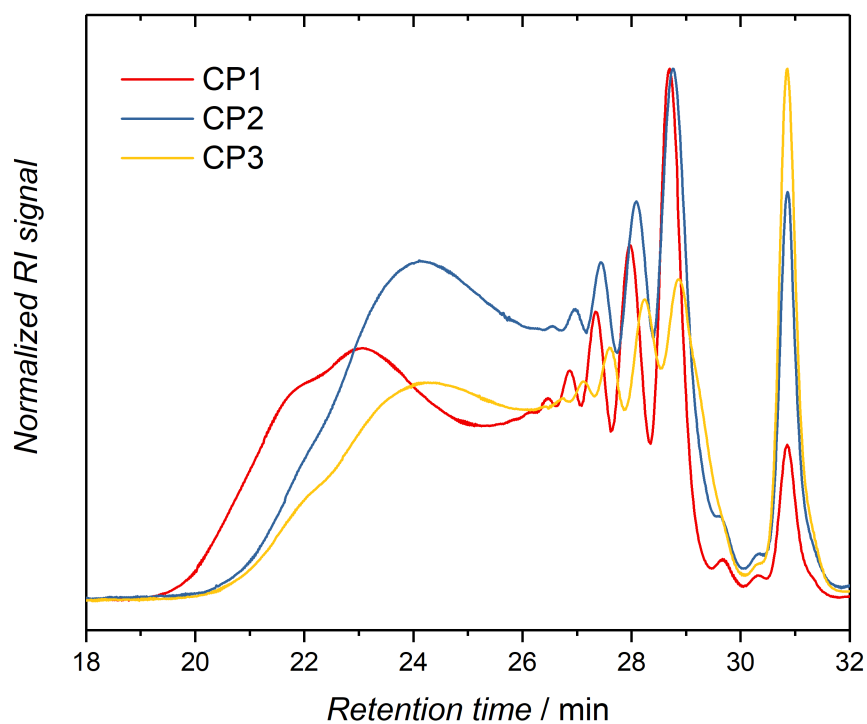
Figure C.40: SEC traces of crude copolymers **CP1**, **CP2** and **CP3**. Adapted with permission from Ref. 181. Copyright (2018) American Chemical Society.
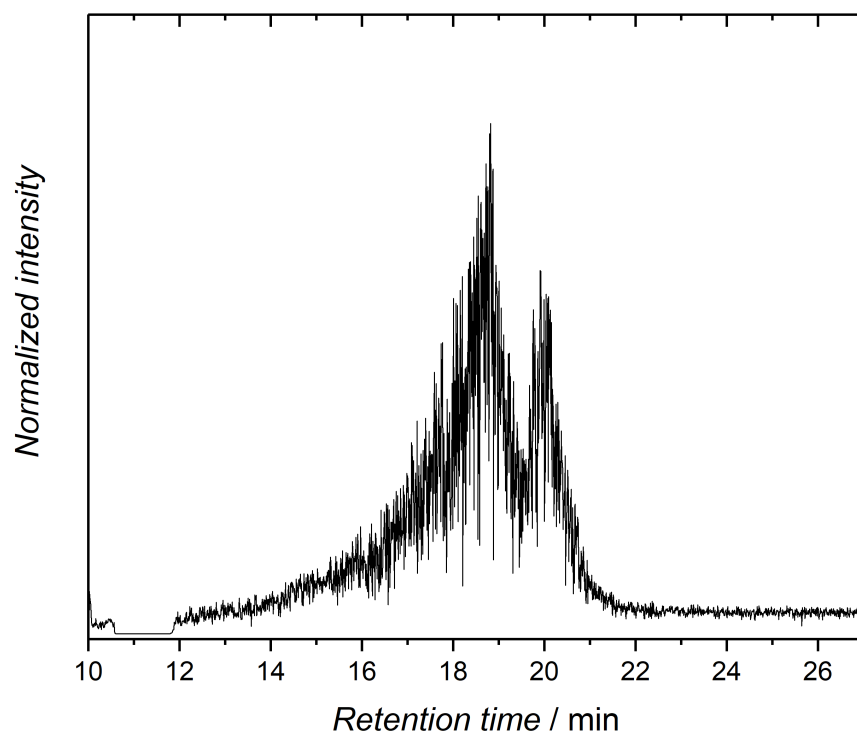
Figure C.41: Exemplary chormatogram for SEC-ESI-MS measurements on copolymers **CP1**, **CP2** and **CP3**, detected via the ion count of the ESI unit. Adapted with permission from Ref. 181. Copyright (2018) American Chemical Society.

169
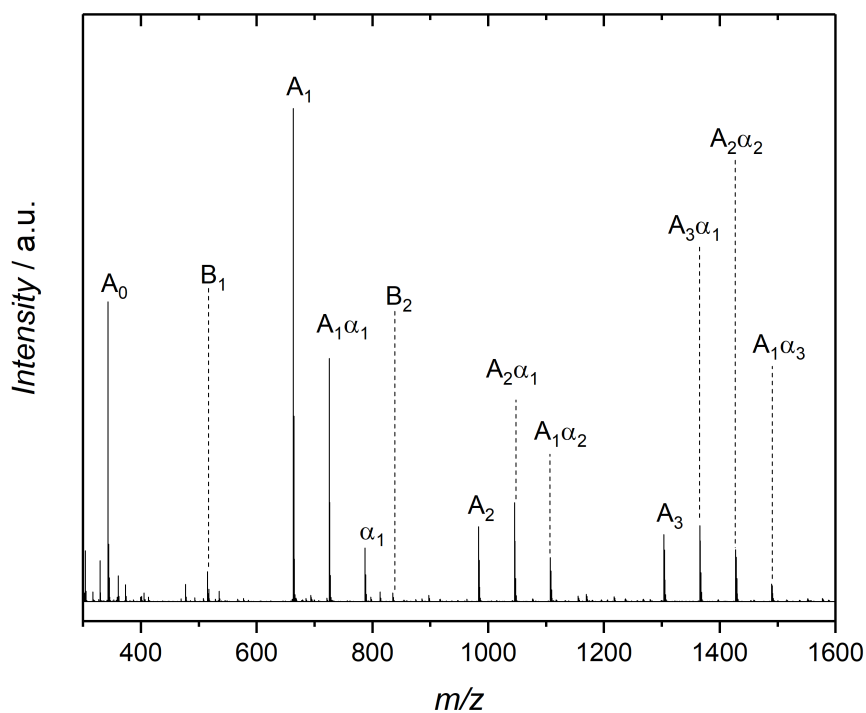
Figure C.42: SEC-ESI-mass spectrum of **CP2**, integrated from 16 to 22 min. Adapted with permission from Ref. 181. Copyright (2018) American Chemical Society.
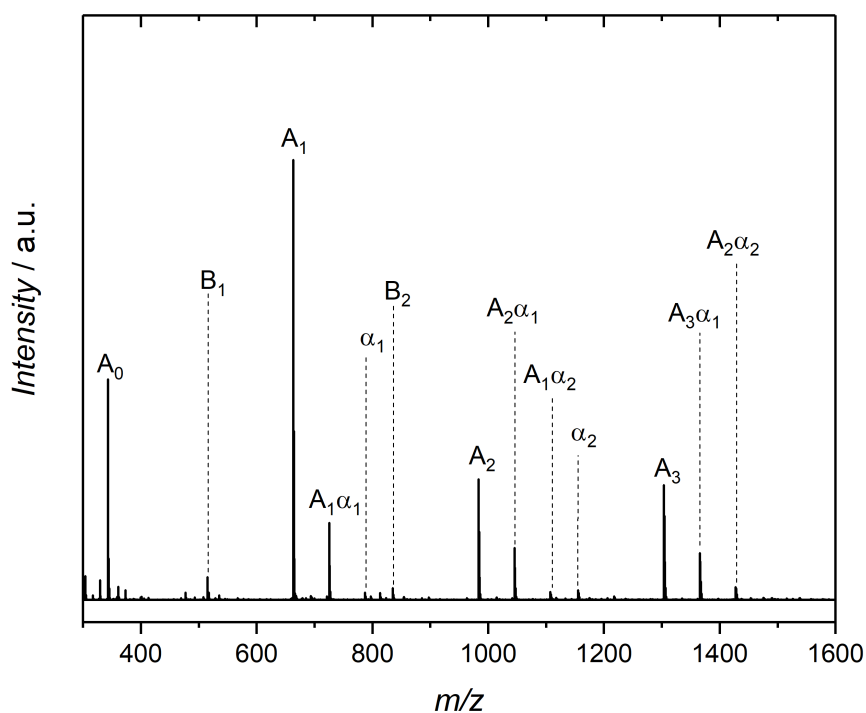
Figure C.43: SEC-ESI-mass spectrum of **CP3**, integrated from 16 to 22 min. Adapted with permission from Ref. 181. Copyright (2018) American Chemical Society.
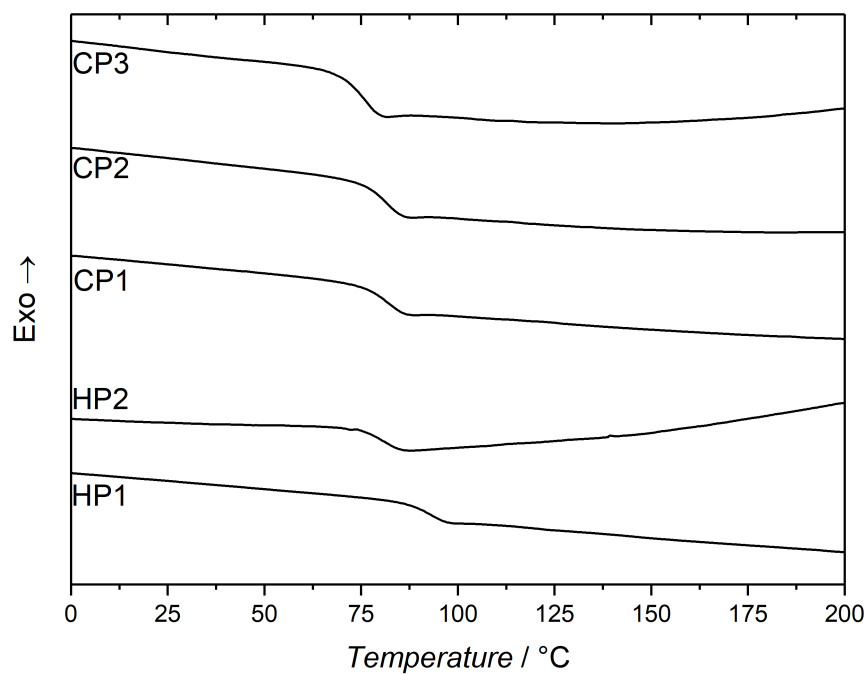
Figure C.44: DSC measurements of the homopolymers **HP1** and **HP2**, as well as the copolymers CP1, **CP2** and **CP3** during the second heating cycle. Adapted with permission from Ref. 181. Copyright (2018) American Chemical Society.
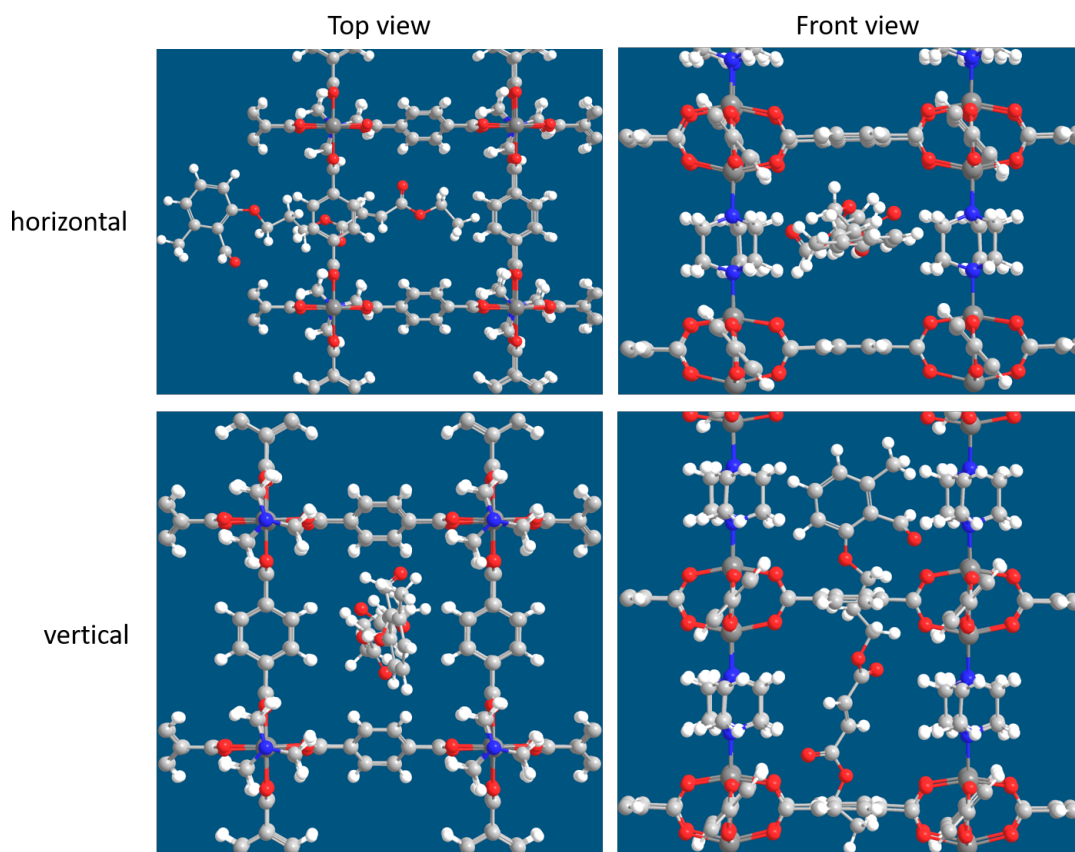
Figure C.45: Position of **M2** in Cu-BDC-dabco in horizontal (top) and vertical (bottom) orientation. *Grey:* carbon; *white:* hydrogen; *red:* oxygen; *blue:* nitrogen.
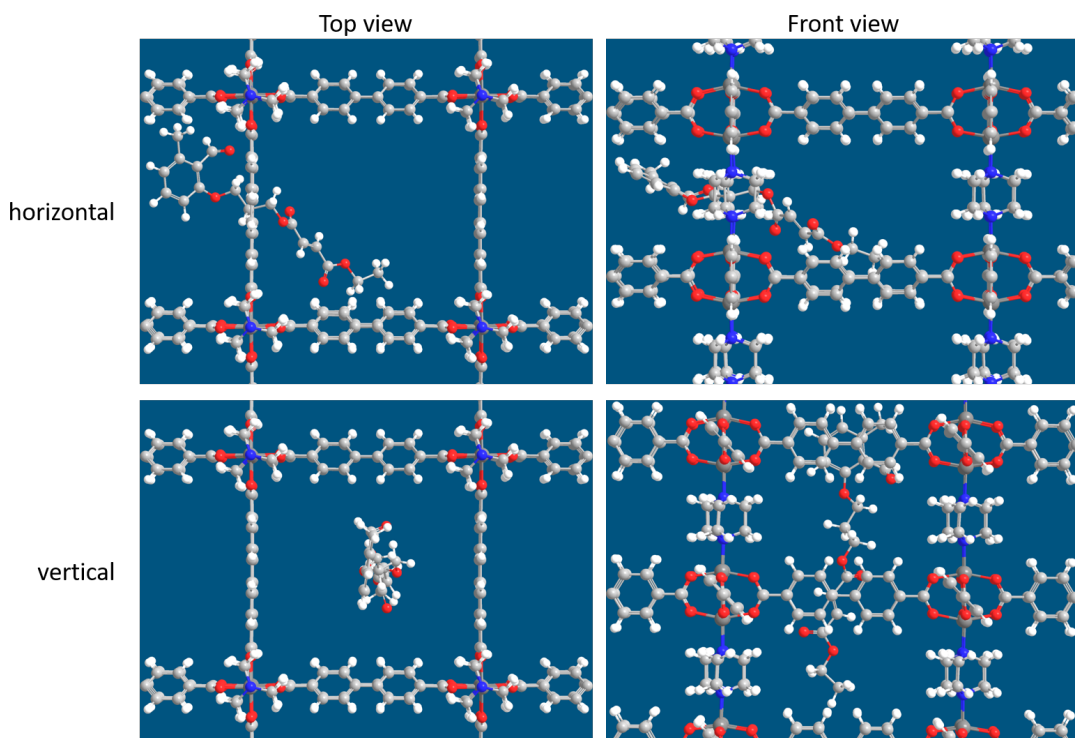
Figure C.46: Position of **M2** in Cu-BPDC-dabco in horizontal (top) and vertical (bottom) orientation. *Grey:* carbon; *white:* hydrogen; *red:* oxygen; *blue:* nitrogen.

List of Abbreviations

°C	degree Celsius
A	area
a	cell edge a
A	energy acceptor
A*	excited energy acceptor
a.t.	ambient temperature
Ac	acetate
ACN	acetonitrile
AO	atomic orbital
aqu.	aqueous
b	cell edge b
BDC	therephthalic acid
BPDC	biphenyldicarboxylic acid
BTC	benzene-1,3,5-tricarboxylic acid
c	concentration
c	speed of light in vacuum
C	mass sensitivity constant
cam	(1R, 3S)-(+)-camphoric acid
cm	centimetre
co-I	co-initiator
COSY	homonuclear correlation spectroscopy

CuAAC	copper-catalyzed azide-alkyne cycloaddition
δ	chemical shift
$Đ$	polydispersity
d	day
d	doublet
D	thickness
D	dissipation
D	energy donor
D*	excited energy donor
DA	Diels-Alder
dabco	1,4-diazabicyclo[2.2.2]octane
DCC	*N,N'*-dicyclohexylcarbodiimide
DCM	dichloromethane
DFT	density functional theory
DHBDC	2,5-dihydroxytherephthalic acid
DLW	direct laser writing
DMAP	4-dimethylaminopyridine
DMF	*N,N*-dimethylformamide
DMSO	dimethyl sulfoxide
E	energy
EA	ethyl acetate
EDC	1-ethyl-3-(3-dimethylaminopropyl)carbodiimide
EDG	electron-donating group
EDTA	ethylenediaminetetraacetic acid
eq.	equivalents
ESI	electrospray ionization
EtOAc	ethyl acetate

eV	electronvolt
EWG	electron-withdrawing group
Φ	quantum yield
ϕ	wave function of atomic orbital
f	frequency
Fum	monoethyl fumarate
g	gram
h	hour
HAP	hydroxy alkyl acetophenone
HKUST-1	$Cu_3(BTC)_2$
HOMO	highest occupied molecular orbital
Hz	hertz
I	integral
IC	internal conversion
ISC	intersystem crossing
IR	infrared
IRRAS	infrared reflection absorption spectroscopy
IUPAC	Union of Pure and Applied Chemistry
k	reaction rate constant
k_B	Boltzmann constant
kJ	kilojoule
kV	kilovolt
λ	wavelength
L	litre
LCAO	linear combination of atomic orbitals
LED	light-emitting diode
LUMO	lowest unoccupied molecular orbital

μL	microlitre
μm	micrometer
m	mass
M	molecular weigth
m	metre
MHDA	16-mercapthexadecanoic acid
mm	millimetre
mM	millimolare ($mmol\,L^{-1}$)
M_n	number-average molecular weight
M	molare ($mol\,L^{-1}$)
M1	ethyl (4-((2-formyl-3-methylphenoxy)methyl)benzyl) fumarate
M2	ethyl (3-(2-formyl-3-methylphenoxy)propyl) fumarate
Mal	maleimide functionality
Mal-Br	1-(3-bromopropyl)-1H-pyrrole-2,5-dione
Mal-Cl	1-(3-chloropropyl)-1H-pyrrole-2,5-dione
MeOH	methanol
mg	milligram
MIL-53	Al(BDC)(OH)
min	minute
mL	millilitre
MMA	methyl methacrylate
MNDO	modified neglect of diatomic overlap
MO	molecular orbital
MOF	metal-organic framework
mmol	millimole
mol	mole
MS	mass spectrometry

MUD	11-mercaptoundecanol
M_w	weight-average molecular weight
ν	wavenumber
N_x	number of x
nHex	n-hexane
ng	nanogram
nm	nanometre
NMR	nuclear magnetic resonance
o.n.	overnight
o	*ortho*-position
p	quintet
p	conversion
para	*para*-position
Ψ	wavefunction of molecular orbital
PEG	polyethyleneglycol
PhE	2-hydroxy-6-methylbenzaldehyde
PhE-OMe	2-methoxy-6-methylbenzaldehyde
PhE-Et	ethyl (2-(2-formyl-3-methylphenoxy)ethyl) fumarate
PhE-Mal	2-(3-(2,5-dioxo-2,5-dihydro-1H-pyrrol-1-yl)propoxy)-6-methylbenzaldehyde
PhE-Pr	ethyl (3-(2-formyl-3-methylphenoxy)propyl) fumarate
PhE-Xy	ethyl (4-((2-formyl-3-methylphenoxy)methyl)benzyl) fumarate
PI	photoinitiator
PI-alkyne 1	2-(4-(2-hydroxy-2-methylpropanoyl)phenoxy)ethyl propiolate
PI-alkyne (2)	2-(4-(2-hydroxy-2-methylpropanoyl)phenoxy)ethyl hex-5-ynoate

PLP	pulsed-laser polymerization
PMMA	poly(methyl methacrylate)
ppm	parts per million
Pre1	2-((4-(hydroxymethyl)benzyl)oxy)-6-methylbenzaldehyde
Pre2	2-(2-hydroxyethoxy)-6-methylbenzaldehyde
Pre3	2-(3-Hydroxypropoxy)-6-methylbenzaldehyde
PS	photosensitizer
PSM	post-synthetic modification
q	quartet
QCM	quartz crystal microbalance
R_f	retardation factor in planar chromatography
s	second
s	singlet
SAM	self-assembled monolayer
SEC	size exclusion chromatography
SIMS	secondary ion mass spectrometry
S_n	singlet state
SOMO	single-occupied molcular orbital
St	styrene
STED	stimulated emission depletion
SURMOF	surface-mounted metal-organic framewok
T	temperature
τ	life time
t	triplet
tBu	*tert*-butyl
THF	tetrahydrofurane
TMS	trimethylsilyl

T_n	triplet state
ToF	time of flight
TS	transition state
UV	ultra-violet
V	volume
V	spray voltage
vis	visible light
vs	versus
X_n	number-average degree of polymerization
XRD	x-ray diffraction

Bibliography

[1] M. D. Lechner, E. H. N., K. Gehrke *Makromolekulare Chemie*; Birkhäuser Verlag: Basel-Boston-Berlin, 2010; Vol. 4.

[2] Odian, G. *Principles of Polymerizations*, 4th ed.; John Wiley & sons, Inc., Hoboken, New Jersey, 2004.

[3] Arshady, R. *Colloid Polym. Sci.* **1992**, *270*, 717–732.

[4] Moad, G.; Rizzardo, E.; Thang, S. H. *Aust. J. Chem.* **2005**, *58*, 379–410.

[5] Shekhah, O.; Wang, H.; Kowarik, S.; Schreiber, F.; Paulus, M.; Tolan, M.; Sternemann, C.; Evers, F.; Zacher, D.; Fischer, R. A.; Wöll, C. *J. Am. Chem. Soc.* **2007**, *129*, 15118–15119.

[6] Lee, Y.-R.; Kim, J.; Ahn, W.-S. *Korean J. Chem. Eng.* **2013**, *30*, 1667–1680.

[7] Bétard, A.; Fischer, R. A. *Chem. Rev.* **2011**, *112*, 1055–1083.

[8] Kitagawa, S.; Kitaura, R.; Noro, S. *Angew. Chem. Int. Ed.* **2004**, *43*, 2334–2375.

[9] Cohen, S. M. *Chem. Rev.* **2012**, *112*, 970–1000.

[10] Uemura, T.; Yanai, N.; Kitagawa, S. *Chem. Soc. Rev.* **2009**, *38*, 1228–1236.

[11] Li, H.; Eddaoudi, M.; Groy, T. L.; Yaghi, O. M. *J. Am. Chem. Soc.* **1998**, *120*, 8571–8572.

[12] Ferey, G. *Chem. Soc. Rev.* **2008**, *37*, 191–214.

[13] Wang, X.-S.; Ma, S.; Forster, P.; Yuan, D.; Eckert, J.; López, J.; Murphy, B.; Parise, J.; Zhou, H.-C. *Angew. Chem. Int. Ed.* **2008**, *47*, 7263–7266.

[14] Furukawa, H.; Ko, N.; Go, Y. B.; Aratani, N.; Choi, S. B.; Choi, E.; Yazay-din, A. O.; Snurr, R. Q.; O'Keeffe, M.; Kim, J.; Yaghi, O. M. *Science* **2010**, *329*, 424–428.

[15] Mueller, U.; Schubert, M.; Teich, F.; Puetter, H.; Schierle-Arndt, K.; Pastre, J. *J. Mater. Chem.* **2006**, *16*, 626–636.

[16] Wang, C.; Li, L.; Tang, S.; Zhao, X. *ACS Appl. Mater. Inter.* **2014**, *6*, 16932–16940.

[17] Bauer, S.; Stock, N. *Chem. unserer Zeit* **2008**, *42*, 12–19.

[18] Dhakshinamoorthy, A.; Garcia, H. *Chem. Soc. Rev.* **2014**, *43*, 5750–5765.

[19] Prince, J. A.; Bhuvana, S.; Anbharasi, V.; Ayyanar, N.; Boodhoo, K. V. K.; Singh, G. *Sci. Rep.* **2014**, *4*.

[20] Schmitt, S.; Silvestre, M.; Tsotsalas, M.; Winkler, A.-L.; Shahnas, A.; Gros-jean, S.; Laye, F.; Gliemann, H.; Lahann, J.; Bräse, S.; Franzreb, M.; Wöll, C. *ACS Nano* **2015**, 4219–4226.

[21] Motakef-Kazemi, N.; Shojaosadati, S. A.; Morsali, A. *Micropor. Mesopor. Mat.* **2014**, *186*, 73–79.

[22] Biemmi, E.; Scherb, C.; Bein, T. *J. Am. Chem. Soc.* **2007**, *129*, 8054–8055.

[23] Liu, B.; Tu, M.; Zacher, D.; Fischer, R. A. *Adv. Funct. Mater.* **2013**, *23*, 3790–3798.

[24] Tu, M.; Wannapaiboon, S.; Fischer, R. A. *Dalton Trans.* **2013**, *42*, 16029–16035.

[25] Heinke, L.; Cakici, M.; Dommaschk, M.; Grosjean, S.; Herges, R.; Bräse, S.; Wöll, C. *ACS Nano* **2014**, *8*, 1463–1467.

[26] Kricheldorf, H. R. *Macromol. Rapid Commun.* **2008**, *29*, 1695–1704.

[27] Wöhrle, D.; Tausch, M. W.; Stohrer, W.-D. *Photochemie*; Wiley-VCH Verlag GmbH & Co. KGaA, 2005; pp 1–4.

[28] Fouassier, J. P.; Lalevée, J. *Photoinitiators for Polymer Synthesis*; Wiley-VCH Verlag GmbH & Co. KGaA, 2012; pp 11–20.

[29] Mueller, J. O.; Guimard, N. K.; Oehlenschlaeger, K. K.; Schmidt, F. G.; Barner-Kowollik, C. *Polym. Chem.* **2014**, *5*, 1447–1456.

[30] Wang, Z.; Kastern, B.; Randazzo, K.; Ugrinov, A.; Butz, J.; Seals, D. W.; Sibi, M. P.; Chu, Q. R. *ACS Sym. Ser.* **2015**, *17*, 4720–4724.

[31] Stohrer, W.-D.; Wöhrle, D.; Tausch, M. W.; Stohrer, W.-D. *Photochemie*; Wiley-VCH Verlag GmbH & Co. KGaA, 2005; pp 5–81.

[32] Fouassier, J. P.; Lalevée, J. *Photoinitiators for Polymer Synthesis*; Wiley-VCH Verlag GmbH & Co. KGaA, 2012; pp 73–88.

[33] Fouassier, J. P.; Lalevée, J. *Photoinitiators for Polymer Synthesis*; Wiley-VCH Verlag GmbH & Co. KGaA, 2012; pp 127–197.

[34] Yang, N. C.; Yang, D.-D. H. *J. Am. Chem. Soc.* **1958**, *80*, 2913–2914.

[35] Büchi, G.; Inman, C. G.; Lipinsky, E. S. *J. Am. Chem. Soc.* **1954**, *76*, 4327–4331.

[36] Colley, C. S.; Grills, D. C.; Besley, N. A.; Jockusch, S.; Matousek, P.; Parker, A. W.; Towrie, M.; Turro, N. J.; Gill, P. M. W.; George, M. W. *J. Am. Chem. Soc.* **2002**, *124*, 14952–14958.

[37] Jockusch, S.; Landis, M. S.; Freiermuth, B.; Turro, N. J. *Macromolecules* **2001**, *34*, 1619–1626.

[38] Ganster, B.; Fischer, U. K.; Moszner, N.; Liska, R. *Macromolecules* **2008**, *41*, 2394–2400.

[39] Moszner, N.; Fischer, U. K.; Ganster, B.; Liska, R.; Rheinberger, V. *Dent. Mater.* **2008**, *24*, 901–907.

[40] Dinda, B. *Essentials of Pericyclic and Photochemical Reactions*; Springer International Publishing, 2017.

[41] Brückner, R. *Reaktionsmechanismen*, 3rd ed.; Springer-Verlag, 2007.

[42] Vollhardt, K. P. C.; Schore, N. E. *Organische Chemie*, 5th ed.; Wiley-VCH, 2011.

[43] Diels, O.; Alder, K. *Justus Liebigs Ann. Chem.* **1928**, *460*, 98–122.

[44] Kolb, H. C.; Finn, M. G.; Sharpless, K. B. *Angew. Chem. Int. Ed.* **2001**, *40*, 2004–2021.

[45] Meldal, M.; Tornøe, C. W. *Chem. Rev.* **2008**, *108*, 2952–3015.

[46] Himo, F.; Lovell, T.; Hilgraf, R.; Rostovtsev, V. V.; Noodleman, L.; Sharpless, K. B.; Fokin, V. V. *J. Am. Chem. Soc.* **2005**, *127*, 210–216.

[47] Straub, B. F. *Chem. Commun.* **2007**, 3868–3870.

[48] Meng, J.-c.; Fokin, V. V.; Finn, M. G. *Tetrahedron Lett.* **2005**, *46*, 4543–4546.

[49] Yang, N. C.; Rivas, C. *J. Am. Chem. Soc.* **1961**, *83*, 2213–2213.

[50] Porter, G.; Tchir, M. F. *J. Chem. Soc. D* **1970**, 1372–1373.

[51] Porter, G.; Tchir, M. F. *J. Chem. Soc. A* **1971**, 3772–3777.

[52] Sammes, P. G. *Tetrahedron* **1976**, *32*, 405–422.

[53] Salem, L.; Rowland, C. *Angew. Chem. Int. Ed. Engl.* **1972**, *11*, 92–111.

[54] Mellows, S. M.; Sammes, P. G. *J. Chem. Soc. Chem. Comm.* **1971**, 21–22.

[55] Blasco, E.; Yameen, B.; Quick, A. S.; Krolla-Sidenstein, P.; Welle, A.; Wegener, M.; Barner-Kowollik, C. *Macromolecules* **2015**, *48*, 8718–8728.

[56] Hiltebrandt, K.; Pauloehrl, T.; Blinco, J. P.; Linkert, K.; Börner, H. G.; Barner-Kowollik, C. *Angew. Chem. Int. Ed.* **2015**, *54*, 2838–2843.

[57] Gegenhuber, T.; De Keer, L.; Goldmann, A. S.; Van Steenberge, P. H. M.; Mueller, J. O.; Reyniers, M.-F.; Menzel, J. P.; D'hooge, D. R.; Barner-Kowollik, C. *Macromolecules* **2017**, 6451–6467.

[58] Langer, M.; Mueller, J. O.; Goldmann, A. S.; Schacher, F. H.; Barner-Kowollik, C. *ACS Macro Lett.* **2016**, *5*, 597–601.

[59] Vigovskaya, A.; Abt, D.; Ahmed, I.; Niemeyer, C. M.; Barner-Kowollik, C.; Fruk, L. *J. Mater. Chem. B* **2016**, *4*, 442–449.

[60] Tischer, T.; Claus, T. K.; Bruns, M.; Trouillet, V.; Linkert, K.; Rodriguez-Emmenegger, C.; Goldmann, A. S.; Perrier, S.; Börner, H. G.; Barner-Kowollik, C. *Biomacromolecules* **2013**, *14*, 4340–4350.

[61] Pauloehrl, T.; Delaittre, G.; Winkler, V.; Welle, A.; Bruns, M.; Börner, H. G.; Greiner, A. M.; Bastmeyer, M.; Barner-Kowollik, C. *Angew. Chem. Int. Ed.* **2012**, *51*, 1071–1074.

184

[62] Hirschbiel, A. F.; Schmidt, B. V. K. J.; Krolla-Sidenstein, P.; Blinco, J. P.; Barner-Kowollik, C. *Macromolecules* **2015**, *48*, 4410–4420.

[63] Claus, T. K.; Telitel, S.; Welle, A.; Bastmeyer, M.; Vogt, A. P.; Delaittre, G.; Barner-Kowollik, C. *Chem. Commun.* **2017**, *53*, 1599–1602.

[64] Hiltebrandt, K.; Kaupp, M.; Molle, E.; Menzel, J. P.; Blinco, J. P.; Barner-Kowollik, C. *Chem. Commun.* **2016**, *52*, 9426–9429.

[65] Mueller, P.; Zieger, M. M.; Richter, B.; Quick, A. S.; Fischer, J.; Mueller, J. B.; Zhou, L.; Nienhaus, G. U.; Bastmeyer, M.; Barner-Kowollik, C.; Wegener, M. *ACS Nano* **2017**, *11*, 6396–6403.

[66] Ishizaki, K.; Komarneni, S.; Nanko, M. *Porous Materials: Process technology and applications*; Springer US, 2013.

[67] Furukawa, H.; Cordova, K. E.; O'Keeffe, M.; Yaghi, O. M. *Science* **2013**, *341*, 1230444.

[68] Liu, B.; Fischer, R. *Sci. China Chem.* **2011**, *54*, 1851–1866.

[69] Farha, O. K.; Hupp, J. T. *Acc. Chem. Res.* **2010**, *43*, 1166–1175.

[70] Chui, S. S.-Y.; Lo, S. M.-F.; Charmant, J. P. H.; Orpen, A. G.; Williams, I. D. *Science* **1999**, *283*, 1148–1150.

[71] Li, H.; Eddaoudi, M.; O'Keeffe, M.; Yaghi, O. M. *Cah. Rev. The.* **1999**, *402*, 276–279.

[72] Liu, D.; Lu, K.; Poon, C.; Lin, W. *Inorg. Chem.* **2013**, *53*, 1916–1924.

[73] Horike, S.; Kitagawa, S. *Metal-Organic Frameworks*; Wiley-VCH Verlag GmbH & Co. KGaA, 2011; pp 1–21.

[74] Hurrle, S.; Friebe, S.; Wohlgemuth, J.; Wöll, C.; Caro, J.; Heinke, L. *Chem. Eur. J.* **2017**, *23*, 2294–2298.

[75] Bordiga, S.; Regli, L.; Bonino, F.; Groppo, E.; Lamberti, C.; Xiao, B.; Wheatley, P. S.; Morris, R. E.; Zecchina, A. *Phys. Chem. Chem. Phys.* **2007**, *9*, 2676–2685.

[76] Yang, J.; Lutz, M.; Grzech, A.; Mulder, F. M.; Dingemans, T. J. *CrystEngComm* **2014**, *16*, 5121–5127.

[77] Qin, W.; Silvestre, M. E.; Kirschhöfer, F.; Brenner-Weiss, G.; Franzreb, M. *J. Chromatogr. A* **2015**, *1411*, 77–83.

[78] Guo, W.; Liu, J.; Weidler, P. G.; Liu, J.; Neumann, T.; Danilov, D.; Wenzel, W.; Feldmann, C.; Wöll, C. *Phys. Chem. Chem. Phys.* **2014**, *16*, 17918–17923.

[79] Mosleh, S.; Rahimi, M. R.; Ghaedi, M.; Dashtian, K.; Hajati, S.; Wang, S. *Chem. Eng. Process. Process Intensif.* **2017**, *114*, 24–38.

[80] Stavila, V.; Volponi, J.; Katzenmeyer, A. M.; Dixon, M. C.; Allendorf, M. D. *Chem. Sci.* **2012**, *3*, 1531–1540.

[81] Campbell, J.; Szekely, G.; Davies, R. P.; Braddock, D. C.; Livingston, A. G. *J. Mater. Chem. B* **2014**, *2*, 9260–9271.

[82] Kramer, M.; Schwarz, U.; Kaskel, S. *J. Mater. Chem.* **2006**, *16*, 2245–2248.

[83] Xie, L.; Liu, S.; Gao, C.; Cao, R.; Cao, J.; Sun, C.; Su, Z. *Inorg. Chem.* **2007**, *46*, 7782–7788.

[84] Murray, L. J.; Dinca, M.; Yano, J.; Chavan, S.; Bordiga, S.; Brown, C. M.; Long, J. R. *J. Am. Chem. Soc.* **2010**, *132*, 7856–7857.

[85] Loiseau, T.; Serre, C.; Huguenard, C.; Fink, G.; Taulelle, F.; Henry, M.; Bataille, T.; Férey, G. *Chem. Eur. J.* **2004**, *10*, 1373–1382.

[86] Horcajada, P.; Serre, C.; Maurin, G.; Ramsahye, N. A.; Balas, F.; Vallet-Regí, M.; Sebban, M.; Taulelle, F.; Férey, G. *J. Am. Chem. Soc.* **2008**, *130*, 6774–6780.

[87] Finsy, V.; Kirschhock, C. E. A.; Vedts, G.; Maes, M.; Alaerts, L.; De Vos, D. E.; Baron, G. V.; Denayer, J. F. M. *Chem. Eur. J.* **2009**, *15*, 7724–7731.

[88] Hindelang, K.; Kronast, A.; Vagin, S. I.; Rieger, B. *Chem. Eur. J.* **2013**, *19*, 8244–8252.

[89] Rubin, H. N.; Reynolds, M. M. *Inorg. Chem.* **2017**, *56*, 5266–5274.

[90] Wang, Z.; Cohen, S. M. *Chem. Soc. Rev.* **2009**, *38*, 1315–1329.

[91] Farrusseng, D.; Canivet, J.; Quadrelli, A. *Metal-Organic Frameworks*; Wiley-VCH Verlag GmbH & Co. KGaA, 2011; pp 23–48.

[92] Tanabe, K. K.; Wang, Z.; Cohen, S. M. *J. Am. Chem. Soc.* **2008**, *130*, 8508–8517.

[93] Wang, Z.; Tanabe, K. K.; Cohen, S. M. *Inorg. Chem.* **2009**, *48*, 296–306.

[94] Gadzikwa, T.; Lu, G.; Stern, C. L.; Wilson, S. R.; Hupp, J. T.; Nguyen, S. T. *Chem. Commun.* **2008**, 5493–5495.

[95] Goto, Y.; Sato, H.; Shinkai, S.; Sada, K. *J. Am. Chem. Soc.* **2008**, *130*, 14354–14355.

[96] Savonnet, M.; Bazer-Bachi, D.; Bats, N.; Perez-Pellitero, J.; Jeanneau, E.; Lecocq, V.; Pinel, C.; Farrusseng, D. *J. Am. Chem. Soc.* **2010**, *132*, 4518–4519.

[97] Gliemann, H.; Wöll, C. *Mater. Today* **2012**, *15*, 110–116.

[98] Arslan, H. K.; Shekhah, O.; Wieland, D. C. F.; Paulus, M.; Sternemann, C.; Schroer, M. A.; Tiemeyer, S.; Tolan, M.; Fischer, R. A.; Wöll, C. *J. Am. Chem. Soc.* **2011**, *133*, 8158–8161.

[99] Arslan, H. K.; Shekhah, O.; Wohlgemuth, J.; Franzreb, M.; Fischer, R. A.; Wöll, C. *Adv. Funct. Mater.* **2011**, *21*, 4228–4231.

[100] Liu, B.; Shekhah, O.; Arslan, H. K.; Liu, J.; Wöll, C.; Fischer, R. A. *Angew. Chem. Int. Ed.* **2012**, *51*, 807–810.

[101] Carothers, W. H. *Chem. Rev.* **1931**, *8*, 353–426.

[102] Uemura, T.; Hiramatsu, D.; Kubota, Y.; Takata, M.; Kitagawa, S. *Angew. Chem. Int. Ed.* **2007**, *46*, 4987–4990.

[103] Uemura, T.; Ono, Y.; Kitagawa, K.; Kitagawa, S. *Macromolecules* **2007**, *41*, 87–94.

[104] Carothers, W. H. *Trans. Faraday Soc.* **1936**, *32*, 39–49.

[105] Uemura, T.; Mochizuki, S.; Kitagawa, S. *ACS Macro Lett.* **2015**, 788–791.

[106] Uemura, T.; Kitagawa, K.; Horike, S.; Kawamura, T.; Kitagawa, S.; Mizuno, M.; Endo, K. *Chem. Commun.* **2005**, 5968–5970.

[107] Hoffmann, E. D.; Strobant, V. *Mass Spectrometry: Principles and Applications*; Wiley-VCH, 2007.

[108] Barner-Kowollik, C.; Falkenhagen, J.; Gruendling, T.; Weidner, S. *Mass Spectrometry in Polymer Chemistry*; Wiley-VCH Verlag GmbH & Co. KGaA, 2011; pp 1–4.

[109] Karas, M.; Bachmann, D.; Bahr, U.; Hillenkamp, F. *Int. J. Mass Spectrom. Ion Processes* **1987**, *78*, 53–68.

[110] Karas, M.; Hillenkamp, F. *Anal. Chem.* **1988**, *60*, 2299–2301.

[111] Stump, M. J.; Fleming, R. C.; Gong, W.-H.; Jaber, A. J.; Jones, J. J.; Surber, C. W.; Wilkins, C. L. *Appl. Spectrosc. Rev.* **2002**, *37*, 275–303.

[112] Yamashita, M.; Fenn, J. B. *J. Phys. Chem.* **1984**, *88*, 4451–4459.

[113] Mann, M.; Meng, C. K.; Fenn, J. B. *Anal. Chem.* **1989**, *61*, 1702–1708.

[114] Fenn, J.; Mann, M.; Meng, C.; Wong, S.; Whitehouse, C. *Science* **1989**, *246*, 64–71.

[115] Bruins, A. P. *J. Chromatogr. A* **1998**, *794*, 345–357.

[116] The Nobel Prize in Chemistry 2002. Nobelprize.org. Nobel Media AB 2014. http://www.nobelprize.org/nobel_prizes/chemistry/laureates/2002/. accessed: 25.02.2018.

[117] Bruins, A. P. *TrAC, Trends Anal. Chem.* **1994**, *13*, 37–43.

[118] Gomez, A.; Tang, K. *Phys. Fluids* **1994**, *6*, 404–414.

[119] Hart-Smith, G.; Blanksby, S. J. *Mass Spectrometry in Polymer Chemistry*; Wiley-VCH Verlag GmbH & Co. KGaA, 2011; pp 5–32.

[120] Spieß, L., Behnken, H., Genzel, C., Schwarzer, R., Teichert, G., Eds. *Moderne Röntgenbeugung : Röntgendiffraktometrie für Materialwissenschaftler, Physiker und Chemiker*, 2nd ed.; SpringerLink : Bücher; Vieweg+Teubner: Wiesbaden, 2009.

[121] Kleber, W.; Bautsch, H.-J.; Bohm, J.; Klimm, D. *Einführung in die Kristallographie*, 19th ed.; Oldenbourg Wissenschaftsverlag GmbH: München, 2010.

[122] Reviakine, I.; Johannsmann, D.; Richter, R. P. *Anal. Chem.* **2011**, *83*, 8838–8848.

[123] Vickerman, J. C., Ed. *ToF-SIMS : surface analysis by mass spectrometry*; IM: Chichester, 2001.

[124] Fearn, S. *An Introduction to Time-of-Flight Secondary Ion Mass Spectrometry (ToF-SIMS) and its Application to Materials Science*; Morgan & Claypool Publishers, 2015.

[125] Kollmer, F. *Appl. Surf. Sci.* **2004**, *231-232*, 153–158.

[126] Brunelle, A.; Touboul, D.; Laprévote, O. *J. Mass Spectrom.* **2005**, *40*, 985–999.

[127] Matsuo, J.; Okubo, C.; Seki, T.; Aoki, T.; Toyoda, N.; Yamada, I. *Nucl. Instrum. Methods Phys. Res., Sect. B* **2004**, *219-220*, 463–467.

[128] Sodhi, R. N. S. *Analyst* **2004**, *129*, 483–487.

[129] Uemura, T.; Nakanishi, R.; Mochizuki, S.; Murata, Y.; Kitagawa, S. *Chem. Commun.* **2015**,

[130] Liu, B.; Ma, M.; Zacher, D.; Bétard, A.; Yusenko, K.; Metzler-Nolte, N.; Wöll, C.; Fischer, R. A. *J. Am. Chem. Soc.* **2011**, *133*, 1734–1737.

[131] Nayab, S.; Trouillet, V.; Gliemann, H.; Hurrle, S.; Weidler, P. G.; Rashid Tariq, S.; Goldmann, A. S.; Barner-Kowollik, C.; Yameen, B. *Chem. Commun.* **2017**, *53*, 11461–11464.

[132] Hirschbiel, A. F.; Geyer, S.; Yameen, B.; Welle, A.; Nikolov, P.; Giselbrecht, S.; Scholpp, S.; Delaittre, G.; Barner-Kowollik, C. *Adv. Mater.* **2015**, *27*, 2621–2626.

[133] Lederhose, P.; Abt, D.; Welle, A.; Müller, R.; Barner-Kowollik, C.; Blinco, J. P. *Chem. Eur. J.* **2018**, *24*, 576–580.

[134] Steinkoenig, J.; Bloesser, F. R.; Huber, B.; Welle, A.; Trouillet, V.; Weidner, S. M.; Barner, L.; Roesky, P. W.; Yuan, J.; Goldmann, A. S.; Barner-Kowollik, C. *Polym. Chem.* **2016**, *7*, 451–461.

[135] Wang, Z.; Liu, J.; Arslan, H. K.; Grosjean, S.; Hagendorn, T.; Gliemann, H.; Bräse, S.; Wöll, C. *Langmuir* **2013**, *29*, 15958–15964.

[136] Tsotsalas, M.; Liu, J.; Tettmann, B.; Grosjean, S.; Shahnas, A.; Wang, Z.; Azucena, C.; Addicoat, M.; Heine, T.; Lahann, J.; Overhage, J.; Bräse, S.; Gliemann, H.; Wöll, C. *J. Am. Chem. Soc.* **2013**, *136*, 8–11.

[137] Agard, N. J.; Prescher, J. A.; Bertozzi, C. R. *J. Am. Chem. Soc.* **2004**, *126*, 15046–15047.

[138] Cychosz, K. A.; Matzger, A. J. *Langmuir* **2010**, *26*, 17198–17202.

[139] Calvez, C. L.; Zouboulaki, M.; Petit, C.; Peeva, L.; Shirshova, N. *RSC Adv.* **2016**, *6*, 17314–17317.

[140] Campbell, J.; Burgal, J. D. S.; Szekely, G.; Davies, R. P.; Braddock, D. C.; Livingston, A. *J. Membr. Sci.* **2016**, *503*, 166–176.

[141] Hurrle, S. Polymerizations in Confined Environments. M.Sc. thesis, Karlsruhe Institute of Technology, 2014.

[142] Bach, R. D. *J. Am. Chem. Soc.* **2009**, *131*, 5233–5243.

[143] Wang, J.; Wang, H.; Ren, H. *Synth. Commun.* **2010**, *40*, 980–983.

[144] Hurrle, S.; Lauer, A.; Gliemann, H.; Mutlu, H.; Wöll, C.; Goldmann, A. S.; Barner-Kowollik, C. *Macromol. Rapid Commun.* **2017**, *38*, 1600598.

[145] Wong, C.-H.; Zimmerman, S. C. *Chem. Commun.* **2013**, *49*, 1679–1695.

[146] Lemieux, G. A.; Bertozzi, C. R. *Trends Biotechnol.* **1998**, *16*, 506–513.

[147] Wendeln, C.; Singh, I.; Rinnen, S.; Schulz, C.; Arlinghaus, H. F.; Burley, G. A.; Ravoo, B. J. *Chem. Sci.* **2012**, *3*, 2479–2484.

[148] Afagh, N.; Yudin, A. *Angew. Chem. Int. Ed.* **2010**, *49*, 262–310.

[149] Tasdelen, M. A.; Taskin, O. S.; Celik, C. *Macromol. Rapid Commun.* **2016**, *37*, 521–526.

[150] Kocienski, P. J. *Protecting groups*; Thieme Stuttgart, 1994; Vol. 3.

[151] Arslan, M.; Yilmaz, G.; Yagci, Y. *Polym. Chem.* **2015**, *6*, 8168–8175.

[152] Gruendling, T.; Guilhaus, M.; Barner-Kowollik, C. *Anal. Chem.* **2008**, *80*, 6915–6927.

[153] Carothers, W. H. *J. Am. Chem. Soc.* **1929**, *51*, 2548–2559.

[154] Carothers, W. H.; Arvin, J. A. *J. Am. Chem. Soc.* **1929**, *51*, 2560–2570.

[155] Soto, M.; Sebastián, R. M.; Marquet, J. *J. Org. Chem.* **2014**, *79*, 5019–5027.

[156] Binauld, S.; Damiron, D.; Hamaide, T.; Pascault, J.-P.; Fleury, E.; Drocken-muller, E. *Chem. Commun.* **2008**, 4138–4140.

[157] Liu, Z.; Ou, J.; Lin, H.; Wang, H.; Liu, Z.; Dong, J.; Zou, H. *Anal. Chem.* **2014**, *86*, 12334–12340.

[158] Lopez, G.; Ameduri, B.; Habas, J.-P. *Macromol. Rapid Commun.* **2016**, *37*, 711–717.

[159] Marvel, C. S.; Chambers, R. R. *J. Am. Chem. Soc.* **1948**, *70*, 993–998.

[160] Vandenbergh, J.; Ramakers, G.; van Lokeren, L.; van Assche, G.; Junkers, T. *RSC Adv.* **2015**, *5*, 81920–81932.

[161] Xu, J.; Boyer, C. *Macromolecules* **2015**, *48*, 520–529.

[162] Sarapas, J. M.; Tew, G. N. *Angew. Chem. Int. Ed.* **2016**, *55*, 15860–15863.

[163] Oelmann, S.; Solleder, S. C.; Meier, M. A. R. *Polym. Chem.* **2016**, *7*, 1857–1860.

[164] Mutlu, H.; de Espinosa, L. M.; Meier, M. A. R. *Chem. Soc. Rev.* **2011**, *40*, 1404–1445.

[165] Mutlu, H.; Barner-Kowollik, C. *Polym. Chem.* **2016**, *7*, 2272–2279.

[166] Estupiñán, D.; Gegenhuber, T.; Blinco, J. P.; Barner-Kowollik, C.; Barner, L. *ACS Macro Lett.* **2017**, *6*, 229–234.

[167] White, J. E. *Ind. Eng. Chem. Prod. RD* **1986**, *25*, 395–400.

[168] Stutz, H.; Illers, K. H.; Mertes, J. *J. Polym. Sci., Part B: Polym. Phys.* **1990**, *28*, 1483–1498.

[169] Kim, M.-R.; Kim, H.-S.; Ha, C.-S.; Park, D.-W.; Lee, J.-K. *J. Appl. Polym. Sci.* **2001**, *81*, 2735–2743.

[170] Huffman, K. R.; Loy, M.; Ullman, E. F. *J. Am. Chem. Soc.* **1965**, *87*, 5417–5423.

[171] Hauser, F. M.; Ellenberger, S. R. *Synthesis* **1987**, *1987*, 723–724.

[172] Das, A.; Lao, E. A.; Gudmundsdottir, A. D. *Photochem. Photobiol.* **2016**, *92*, 388–398.

[173] Winkler, M.; Mueller, J. O.; Oehlenschlaeger, K. K.; Montero de Espinosa, L.; Meier, M. A. R.; Barner-Kowollik, C. *Macromolecules* **2012**, *45*, 5012–5019.

[174] Oehlenschlaeger, K. K.; Mueller, J. O.; Heine, N. B.; Glassner, M.; Guimard, N. K.; Delaittre, G.; Schmidt, F. G.; Barner-Kowollik, C. *Angew. Chem. Int. Ed.* **2013**, *52*, 762–766.

[175] Hirschbiel, A. F.; Konrad, W.; Schulze-Sünninghausen, D.; Wiedmann, S.; Luy, B.; Schmidt, B. V. K. J.; Barner-Kowollik, C. *ACS Macro Lett.* **2015**, *4*, 1062–1066.

[176] Salonen, L.; Bucher, C.; Banner, D.; Haap, W.; Mary, J.-L.; Benz, J.; Kuster, O.; Seiler, P.; Schweizer, W. B.; Diederich, F. *Angew. Chem. Int. Ed.* **2009**, *48*, 811–814.

[177] Höfler, T.; Track, A. M.; Pacher, P.; Shen, Q.; Flesch, H.-G.; Hlawacek, G.; Koller, G.; Ramsey, M. G.; Schennach, R.; Resel, R.; Teichert, C.; Kern, W.; Trimmel, G.; Griesser, T. *Mater. Chem. Phys.* **2010**, *119*, 287–293.

[178] Brokatzky-Geiger, J.; Eberbach, W. *Chem. Ber.* **1984**, *117*, 2157–2192.

[179] Fazio, M.; Durandin, A.; Tkachenko, N.; Niemi, M.; Lemmetyinen, H.; Schuster, D. *Chem. Eur. J.* **2009**, *15*, 7698–7705.

[180] Wu, J.; Jiang, X.; Xu, J.; Dai, W.-M. *Tetrahedron* **2011**, *67*, 179–192.

[181] Hurrle, S.; Goldmann, A. S.; Gliemann, H.; Mutlu, H.; Barner-Kowollik, C. *ACS Macro Lett.* **2018**, 201–207.

[182] Mueller, J. O.; Voll, D.; Schmidt, F. G.; Delaittre, G.; Barner-Kowollik, C. *Chem. Commun.* **2014**, *50*, 15681–15684.

[183] Baeten, E.; Rubens, M.; Wuest, K. N. R.; Barner-Kowollik, C.; Junkers, T. *Reac. Chem. Eng.* **2017**, *2*, 826–829.

[184] Blasco, E.; Tuten, B. T.; Frisch, H.; Lederer, A.; Barner-Kowollik, C. *Polym. Chem.* **2017**, *8*, 5845–5851.

[185] Demirel, B.; Yaraş, A.; Elçiçek, H. *BAÜ Fen Bil. Enst. Dergisi Cilt* **2011**, *13*, 26–35.

[186] Baker, J. *J. Comput. Chem.* **1986**, *7*, 385–395.

[187] Stewart, J. J. P. *J. Mol. Model.* **2013**, *19*, 1–32.

[188] Senthilmurugan, A.; Aidhen, I. S. *Eur. J. Org. Chem.* **2010**, *2010*, 555–564.

[189] Dewar, M. J. S.; Thiel, W. *J. Am. Chem. Soc.* **1977**, *99*, 4899–4907.

Curriculum Vitae

CV not available online.

Acknowledgements

A really big thank-you goes to the Softies, my colleagues from the Soft Matter Lab. Thank you so much for the nice working atmosphere, for our conversations at lunch, and for the crazy photographs! You are the greatest lab colleagues any chemist can hope for.

I would also like to thank all my colleagues from the CBK group for the nice working atmosphere and the beautiful BBQs. I will miss working with you.

Meiner Familie möchte ich für die großartige Unterstützung in all den Jahren danken.

Aber mein größter Dank gilt meinem lieben Mann Thomas. Danke, dass du immer an meiner Seite bist.

„I love being married. It's so great to find that one special person
you want to annoy for the rest of your life."

-Rita Rudner